Volatile element depletion in Earth and carbonaceous chondrites

Inaugural-Dissertation

zur

Erlangung des Doktorgrades

der Mathematisch-Naturwissenschaftlichen Fakultät

der Universität zu Köln

vorgelegt von

Ninja Braukmüller

aus Bremen

Köln, 2019

Berichterstatter: PD Dr. Frank Wombacher
Prof. Dr. Michael Staubwasser
Prof. Dr. Stefan Weyer

Tag der mündlichen Prüfung: 05.12.2019

Table of contents

Abstract **4**

Kurzzusammenfassung **6**

1 Introduction **8**

1.1 SOLAR SYSTEM ABUNDANCES OF THE ELEMENTS 8

1.2 COSMOCHEMICAL CLASSIFICATION OF THE ELEMENTS 9

1.3 CHONDRITE CLASSIFICATION 12

1.3.1 Primary classification parameters *12*

1.3.2 Secondary and tertiary classification parameters *14*

1.4 CHONDRITE COMPONENTS 15

1.4.1 Chondrules *15*

1.4.2 Matrix *16*

1.4.3 Refractory inclusions *16*

1.4.4 Opaque phases *17*

1.5 VOLATILE ELEMENT FRACTIONATION IN THE SOLAR NEBULA 17

1.5.1 Evaporation vs. condensation models *18*

1.5.2 Inheritance model *19*

1.6 VOLATILE ELEMENT LOSS DURING POST-NEBULAR PROCESSES 20

1.7 TERRESTRIAL BUILDING BLOCKS 21

1.8 DETERMINATION OF ELEMENTAL MASS FRACTIONS VIA INDUCTIVELY-COUPLED-PLASMA MASS-SPECTROMETRY (ICP-MS) 22

1.8.1 External calibration *23*

1.8.2 Isotope dilution *24*

2 The chemical composition of carbonaceous chondrites: implications for volatile element depletion, complementarity and alteration **26**

2.1 INTRODUCTION 26

2.2 METHODS 28

2.2.1 Determination of bulk rock compositions using SF-ICPMS *28*

2.2.2 Murchison (CM2) heating experiments *31*

2.3 RESULTS 32

2.3.1 Orgueil (CI), Ivuna (CI), Allende Smithsonian powder (CV), BHVO-2 and BCR-2 ..... *32*

2.3.2 Carbonaceous chondrite compositions relative to CI *33*

2.3.3 Murchison heating experiments *45*

2.4 DISCUSSION 47

2.4.1 Primary volatile element depletion during the protoplanetary disk stage 48
2.4.2 Secondary modifications of the volatile element budget from the meteorite parent bodies 56
2.4.3 Terrestrial and anthropogenic effects on bulk chondrite compositions 59
2.5 CONCLUSIONS 61

3 Earth's volatile element depletion pattern inherited from a carbonaceous chondrite-like source 63

3.1 INTRODUCTION 63
3.2 TERRESTRIAL HOCKEY STICK VOLATILE ELEMENT DEPLETION PATTERN 64
3.3 PLATEAU VOLATILE ELEMENT ABUNDANCES IN BULK EARTH AND CORE 66
3.4 TERRESTRIAL BUILDING MATERIALS AND VOLATILE ELEMENT DEILVERY 68
3.5 METHODS 70
3.5.1 Isotope dilution analysis of S, Se and Te 70
3.5.2 Calculation of core and bulk Earth plateau volatile element abundances 72

4 Determination of Cu, Zn, Ga, Ag, Cd, In, Sn and Tl in geological reference materials and carbonaceous chondrites by isotope dilution ICP-MS 73

4.1 INTRODUCTION 73
4.2 EXPERIMENTAL PROCEDURE 74
4.2.1 Sample selection 74
4.2.2 Reagents and reference solutions 75
4.2.3 Spike calibration 76
4.2.4 Sample preparation 76
4.2.5 Chemical separation 77
4.2.6 Mass spectrometry 79
4.3 RESULTS AND DISCUSSION 80
4.3.1 Interferences 80
4.3.2 Total procedural blanks 81
4.3.3 Uncertainties 81
4.3.4 Geological reference materials 82
4.3.5 Carbonaceous chondrites (Orgueil CI1, Murchison CM2, Allende CV3) 95
4.4 CONCLUSIONS 97

References 98

Appendix A 118

Appendix B 132

Appendix C **134**

Danksagung **136**

Erklärung **137**

Lebenslauf ..... Fehler! Textmarke nicht definiert.

Abstract

Volatile elements such as sulfur, zinc, indium and potassium are depleted relative to the Sun in all known inner solar system materials, including Earth, Mars, Moon and differentiated and undifferentiated meteorites. The Sun comprises 99.8 wt.% of our solar system and is thus representative of its chemical composition. CI chondrites are the only meteorites with an extremely similar chemical composition as the Sun for non-atmophile elements and therefore serve as a reference in cosmochemical studies. The degree of volatile element depletion is different between and even within groups of meteorites and planetary bodies, indicating complex fractionation processes. In this work, volatile element abundances in carbonaceous chondrites are studied to elucidate volatile element fractionation processes in the solar nebula and to assess the potential of volatile element depletion patterns as tracers for planetary building blocks. Furthermore, an analytical protocol for the precise determination of volatile element abundances in geological materials is presented.

Carbonaceous chondrites are primitive material sampling the solar nebula. They are made of two main components (i) chondrules, µm- to mm-sized silicate melt droplets and (ii) matrix, an unequilibrated assemblage of extremely fine-grained minerals. Carbonaceous chondrites are the meteorites that are least depleted in volatile elements. In **Chapter 2,** data for the bulk chemical composition of 27 carbonaceous chondrites of different groups analyzed via sector-field inductively-coupled-plasma mass-spectrometry (SF-ICP-MS) are presented. All studied chondrites show the same characteristic "hockey stick" volatile element depletion pattern, where volatile elements with 50% condensation temperatures between 800 and 500 K are equally depleted relative to CI chondrites. The relative abundances of these 'plateau volatile elements' are characteristic for each group and covariate with the matrix abundances of the respective host chondrites. Hence, all carbonaceous chondrites likely contain a CI-like matrix component which accounts for the majority of volatile elements.

The same "hockey stick" volatile element depletion pattern is observed for the Earth. The silicate Earth exhibits a more fractionated volatile element depletion pattern because core formation led to the redistribution of elements according to their geochemical characters. However, lithophile plateau volatile elements (zinc, indium, chlorine, bromine and iodine) are unfractionated from each other relative to CI chondrites. This abundance plateau accounts for the disputed high abundance of In in the silicate Earth without the need of exotic building blocks

or secondary volatile loss and suggests the accretion of 10-15 wt.% CI-like material before core formation ceased. Finally, the newly recognized hockey stick volatile element depletion pattern allows more accurate estimates of volatile element abundance in the core and bulk Earth, which are provided in **Chapter 3**.

Terrestrial basalts and mantle rocks, lunar rocks and achondrites are much more depleted in volatile elements than carbonaceous chondrites. Abundances of volatile elements in these rocks can only be determined precisely after the addition of enriched isotope tracers and chemical separation. **Chapter 4** comprises a new analytical protocol for the determination of copper, zinc, gallium, silver, cadmium, indium, tin and thallium mass fractions via isotope dilution ICP-MS. Results for 21 reference materials of different lithologies and three carbonaceous chondrites are presented and discussed. The results for Orgueil CI1, Murchison CM2 and Allende Smithsonian CV3 are in good agreement with bulk chemical analyses obtained in Chapter 1.

Kurzzusammenfassung

Das gesamte bekannte Material des inneren Sonnensystems, einschließlich der Erde, des Mondes, des Mars sowie der differenzierten und primitiven Meteoriten, ist relativ zur Sonne verarmt an volatilen Elementen, wie Schwefel, Zink, Indium und Kalium. Die Sonne umfasst 99,8 % der Masse unseres Sonnensystems und ist somit repräsentativ für die chemische Zusammensetzung des gesamten Sonnensystems. CI Chondrite sind die einzigen Meteorite, die für nicht-atmophile Elemente eine sehr ähnliche Zusammensetzung wie die Sonne haben. Deshalb dienen sie in kosmochemischen Untersuchungen als Referenz für die chemische Zusammensetzung des Sonnensystems. Die Verarmung an volatilen Elementen ist in den verschiedenen Meteoriten und planetaren Körpern unterschiedlich stark ausgeprägt, was auf komplexe Fraktionierungsprozesse hindeutet. In dieser Arbeit wird die Verarmung volatiler Elemente in kohligen Chondriten untersucht, um Fraktionierungsprozesse im solaren Nebel besser zu verstehen und das Potential von Verarmungsmustern zur Charakterisierung planetarer Bausteine zu beurteilen. Weiterhin wird ein analytisches Protokoll für die präzise Bestimmung der Massenanteile volatiler Elemente in geologischen Materialien vorgestellt.

Kohlige Chondrite sind Überbleibsel des solaren Nebels und repräsentieren somit ursprüngliches Material aus unserem Sonnensystem. Sie bestehen hauptsächlich aus zwei Komponenten: (i) Chondren, µm-mm große silikatische Schmelztröpfchen und (ii) Matrix, eine unequilibrierte Mischung aus extrem feinkörnigen Mineralen. Kohlige Chondrite zeigen die geringste Verarmung an volatilen Elementen aller bekannten Materialien des inneren Sonnensystems. In **Kapitel 2** wird die chemische Zusammensetzung von 27 kohligen Chondriten aus unterschiedlichen Gruppen präsentiert. Die Daten wurden mittels Sektorfeld ICP-MS gemessen. Alle analysierten kohligen Chondrite zeigen den selben charakteristischen „Hockeyschläger“ Verarmungstrend für volatile Elemente. Volatile Elemente mit 50% Kondensationstemperaturen zwischen 800 und 500 K sind relativ zu CI Chondriten gleich stark verarmt. Die relative Häufigkeit dieser „Plateau-Elemente“ ist charakteristisch für die einzelnen Chondritgruppen und kovariiert mit dem Matrixanteil der Chondrite. Dementsprechend enthalten die analysierten kohligen Chondrite wahrscheinlich eine CI-ähnliche Matrixkomponente, die den überwiegenden Teil der volatilen Elemente enthält.

Das gleiche „Hockeyschläger-Verarmungsmuster“ wird auch in der Erde beobachtet. Der silikatische Teil der Erde zeigt ein stärker fraktioniertes Verarmungsmuster als kohlige

Chondrite, da durch die Kernbildung eine Umverteilung der Elemente gemäß ihrem geochemischen Charakter stattgefunden hat. Die lithophilen volatilen Plateau-Elemente (Zink, Indium, Chlor, Brom und Iod) treten, wie bereits in den kohligen Chondriten beobachte, in relativen CI-chondritischen Häufigkeiten auf. Dieses Häufigkeitsplateau bietet eine einfache Erklärung für die viel diskutierte hohe Indium Häufigkeit im silikatischen Teil der Erde ohne die Notwendigkeit von exotischen Bausteinen oder sekundärem Volatilverlust. Weiterhin deutet das Häufigkeitsplateau daraufhin, dass die Erde 10-15 Gew.% CI-ähnliches Material bereits vor Abschluss der Kernbildungsphase erhalten hat. Der neu entdeckte „Hockeyschläger-Verarmungstrend“ ermöglicht es die Häufigkeiten volatiler Elemente im Kern und der gesamten Erde besser abzuschätzen (**Kapitel 3**).

Terrestrische Basalte und Mantelgesteine, Mondproben und Achondrite sind stärker an volatilen Elementen verarmt als kohlige Chondrite. In solchen Gesteinen können die Massenanteile volatiler Elemente nur nach der Zugabe von angereicherten Isotopentracern und chemischer Separation präzise bestimmt werden. **Kapitel 4** enthält ein neues analytisches Protokoll für die präzise Bestimmung der Massenanteile von Kupfer, Zink, Gallium, Silber, Cadmium, Indium, Zinn und Thallium mittels Isotopenverdünnung und Q-ICP-MS. Ergebnisse für 21 Referenzmaterialien mit unterschiedlichen Lithologien und drei kohlige Chondrite werden präsentiert und diskutiert. Die hier bestimmten Massenanteile in Orgueil CI1, Murchison CM2 und Allende Smithsonian CV3 stimmen sehr gut mit den Gesamtgesteinsanalysen aus Kapitel 1 überein.

Chapter 1

Introduction

1.1 SOLAR SYSTEM ABUNDANCES OF THE ELEMENTS

Our solar system formed 4.568 Ga ago (Bouvier and Wadhwa, 2010) through the gravitational collapse of a cold and dense molecular cloud. The elemental and isotopic composition of the solar system has been inherited from that molecular cloud, where essentially all elements, except H and He were condensed in dust grains. After the collapse the mixture of gas and dust formed a circumstellar disk, the solar nebula, which rotated around the protosun. The solar nebula lasted probably for a few million years (Williams and Cieza, 2011).

The Sun makes up 99.86 % of the mass of the solar system and thus its chemical composition can be considered representative of the solar system. Hence, the elemental abundances of the bulk solar system are determined through the quantitative analysis of absorption lines of the solar photosphere (e.g., Asplund et al., 2009). Chemical analyses of primitive meteorites (e.g., Kallemeyn and Wasson, 1981; Barrat et al., 2012; Palme et al., 2014) have shown that CI carbonaceous chondrites are the only group of primitive meteorites with relative elemental abundances that closely matches the composition of the solar photosphere. Exceptions are the atmophile elements (H, He, N, C, O, Ne, Ar, Kr, Xe) which are underrepresented in CI chondrites and Li which was destroyed by nuclear reactions in the protosun and is thus less abundant than in CI chondrites (**Figure 1.1**). Noble gases cannot be measured directly in the solar photosphere because their ionization potentials are too high and CI chondrites did not incorporate them efficiently. Thus, solar system abundances of the noble gases can only be determined indirectly by helioseismology, solar wind and theoretical consideration (Asplund et al., 2009) and are relatively uncertain. Further information about solar system element abundances can be obtained from comets and interplanetary dust particles (e.g., Brownlee et al., 2012).

When the solar system abundances are plotted versus mass number (**Figure 1.2**) four main features become evident: (i) abundances are generally decreasing with increasing mass number, (ii) elements with even mass numbers have higher abundances than odd mass numbers (zigzag pattern), (iii) Li, Be and B have very low abundances and (iv) there is an abundance peak around

^{56}Fe. These characteristic features had already been recognized and described by Russell (1929), who published the first solar system abundance table based on solar photosphere spectroscopy. The most recent table combining photospheric and meteoritic data is from Wang et al. (2019) and includes updated modern hydrodynamic solar models and a recent CI chondrite compilation (Palme et al., 2014a).

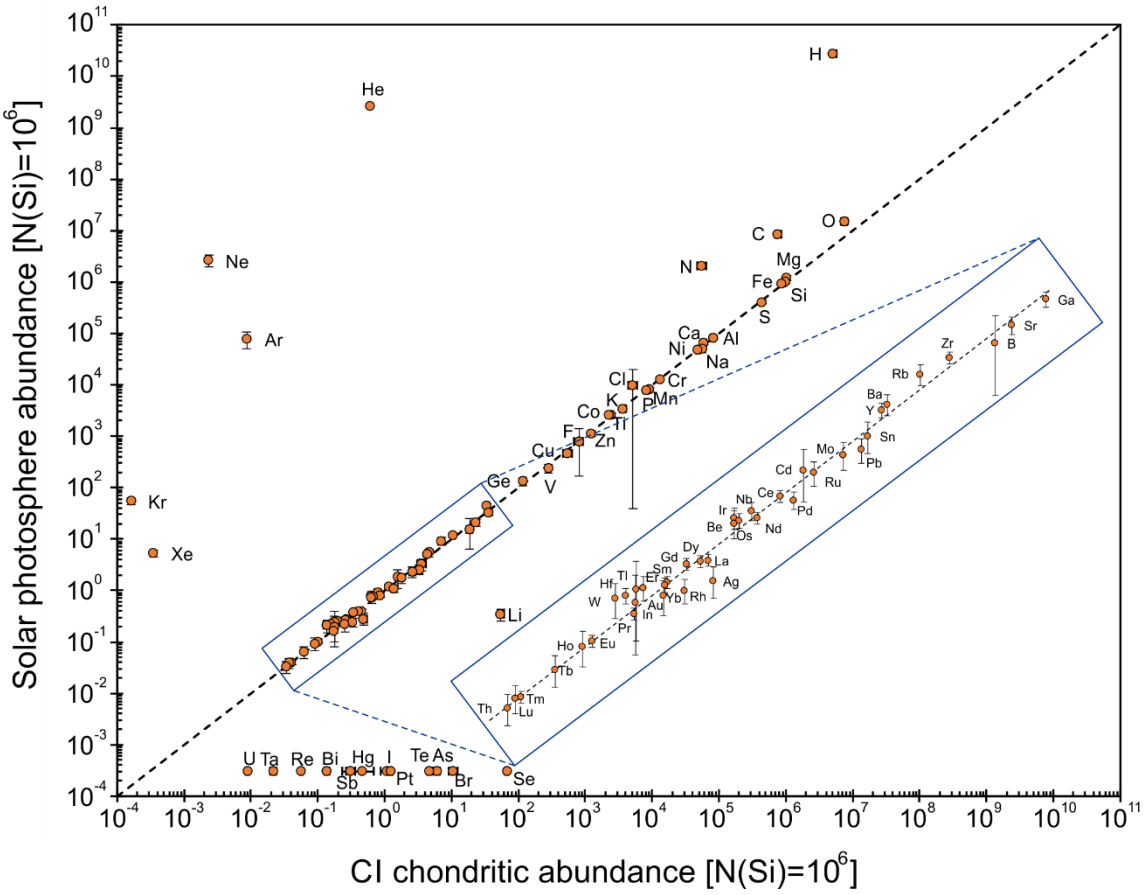

Figure 1.1: Comparison of photospheric and CI chondrititc element abundances in logarithmic space. Abundances are normalized to 10^6 Si atoms. Data points along the black line indicate identical abundances in the solar photosphere and CI chondrites. Elements plotting below the diagonal line are depleted in the solar photosphere, while elements above it are depleted in CI chondrites. No photospheric abundances are available for U, Ta, Re, Bi, Sb, Cs, Hg, I, Pt, Te, As, Br and Se. They were set arbitrarily at 3×10^{-4}. Data: Wang et al. (2019).

1.2 COSMOCHEMICAL CLASSIFICATION OF THE ELEMENTS

The cosmochemical classification of elements is based on elemental volatility, which is quantified by the 50% condensation temperature (50% T_C) of the elements (Grossman, 1972; Anders and Grevesse, 1989; Lodders, 2003). The 50% T_C is defined as the temperature at which half of an element is condensed in a solid phase from a gas of solar composition at canonical conditions (10^{-4} bars total pressure). Major elements such as Ca, Mg, Fe and Si condense as silicates and metal while trace elements typically condense in solid solutions with major elements.

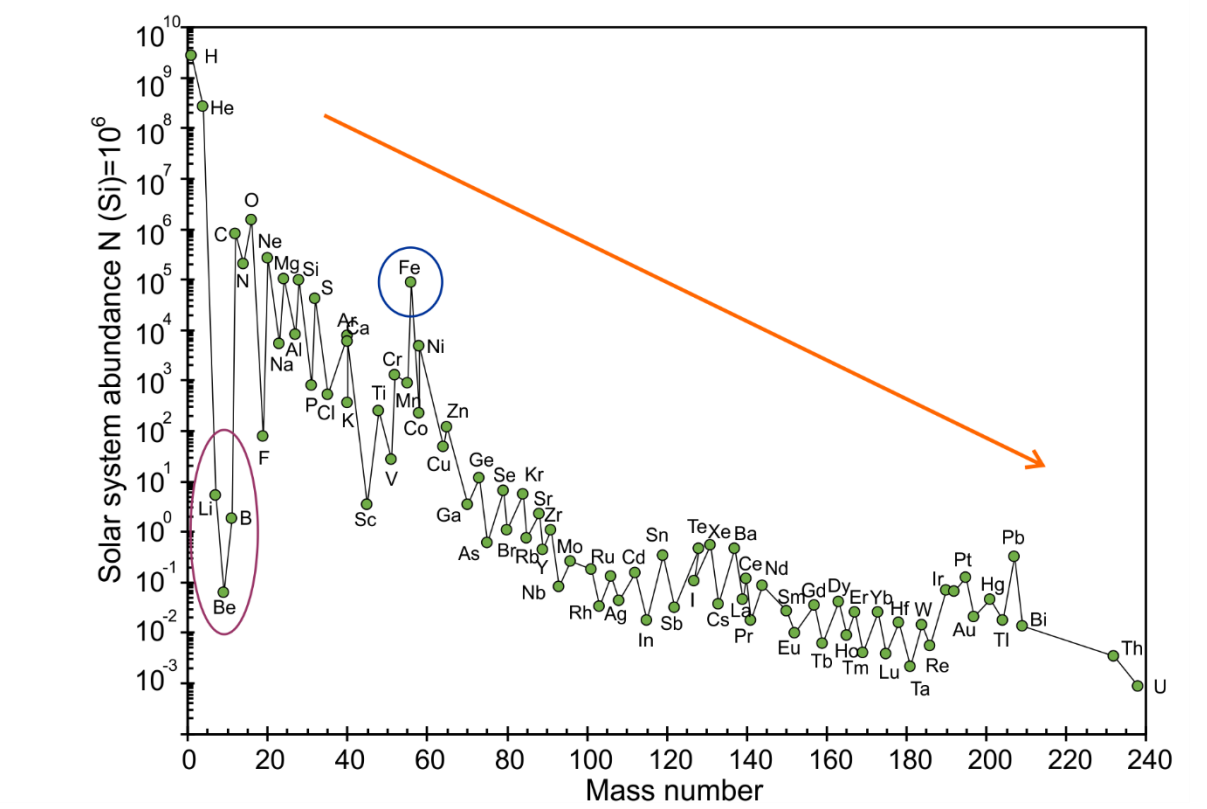

Figure 1.2: Solar system element abundances vs. mass number. With increasing mass number abundances of the elements are decreasing and elements with even mass numbers are more abundant than elements with odd mass numbers (Oddo-Harkins rule). Elemental abundances were set by various nucleosynthetic processes (e.g., Burbidge et al., 1957; Heger et al., 2013). Lithium, Be and B are rarer than expected from the general decreasing abundance trend because they were not produced efficiently in the Big Bang or via cosmic ray interaction. The iron-peak elements Fe, Ni and Co have such high abundances because they have the highest binding energies of all nuclides and thus represent the most stable nucleus configuration.

Based on the 50% T_C the elements are divided into four more or less well defined groups (**Table 1.1**). (1) *Refractory elements* with 50% T_C between 1850-1355 K, which form the first condensates from a solar gas making up ~5% of the total condensable matter (Grossman and Larimer, 1974). (2) *Main component elements* with 50% T_C between 1355-1250 K including Mg, Si and Fe condensing as Mg silicates (forsterite and enstatite) accounting for >90% of the mass of objects in the inner solar system and as FeNi alloy. (3) *Moderately volatile elements* with 50% T_C between 1250-250 K which are often subdivided into elements condensing before and after S, the most abundant volatile element. CI chondrites are the only meteorite group containing the full complement of moderately volatile elements. All other meteorites are more or less depleted in these elements. (4) *Highly volatile elements* with 50% T_C <250 K which are not fully condensed in CI chondrites.

Table 1.1: Cosmochemical classification of the elements based on Palme et al. (2014) and condensation temperatures from (Lodders, 2003). Major and minor elements in bold.

Group	**Lithophile** (silicate, oxides)	**Siderophile/chalcophile** (metal, sulfide)
Refractory elements T_C = 1850-1355 K	Zr, Hf, Sc, Y, Gd, Tb, Dy, Ho, Er, Tm, Lu, Th, **Al**, U, Nd, Sm, **Ti**, Pr, La, Ta, Nb, **Ca**, Yb, Ce, Sr, Ba, Be, V, Eu	Re, Os, W, Ir, Mo, Ru, Pt, Rh
Main component elements T_C = 1355-1250 K	**Mg**, **Si**, **Cr**	**Ni**, Co, **Fe**, Pd
Moderately volatile elements T_C = 1250-1250 K		
T_C > S (664 K)	**Mn**, Li, **K**, **Na**, Cl, B, Rb, Cs, F, Zn	P, As, Au, Cu, Ag, Sb, Ga, Ge, Bi, Pb, Te, Sn, Se, **S**
T_C < S (664 K)	Br, I, Tl	Cd, In Tl, Hg
Highly volatile elements T_C < 250 K	O, N, Xe, Kr, Ar, C, Ne	

The 50% T_C are calculated with complex thermodynamic models taking into account (i) total pressure, (ii) elemental abundances which determine partial pressures in the gas, (iii) distribution of an element between different gases and solid phases and (iv) vapor pressure of the elements (Lodders, 2003). First less complex studies were already carried out in the 1930's by Wildt (1933) and Russell (1934). The most recent study comprising condensation temperatures for all elements was published by Wood et al. (2019). As chapters 2 and 3 were already published before Wood et al. (2019), most condensation temperatures refer to Lodders (2003). Condensation temperature determined by Wood et al. (2019) are similar to those calculated by Lodders (2003) and the classification of elements does not change. Also the elemental abundance patterns of carbonaceous chondrites given in chapter 2 and 3 as a function of the 50% condensation temperature do not change significantly.

Unlike the cosmochemical classification, the geochemical element classification is based on the preferred host phases of the elements as proposed by Goldschmidt (1930). (1) *Lithophile elements* preferentially form or enter silicates and oxides while (2) *siderophile elements* are incorporated into iron metal alloys. (3) *Chalcophile elements* have a strong affinity to sulfides and (4) *atmophile elements* tend to reside as gases in planetary atmospheres.

1.3 CHONDRITE CLASSIFICATION

1.3.1 Primary classification parameters

Meteorites are the solid remains of extraterrestrial meteoroids that survived the passage through Earth's atmosphere and reach Earth's surface. Meteorites whose fall was observed are called *falls*, while those that cannot be associated with any observed fall are named *finds*. Based on their textures meteorites are classified as *differentiated* and *undifferentiated* meteorites. Differentiated meteorites have undergone melting and differentiation and are subdivided into *achondrites*, *stony irons* and *iron meteorites*. Undifferentiated meteorites are called *chondrites* and have never been melted, thus representing remnants of the solar nebula stage. Primary classification parameters of chondrites (and achondrites) are the bulk chemical composition, mineralogy, petrography and oxygen isotopic composition (**Figure 1.3**). Three major chondrite classes can be distinguished: *carbonaceous chondrites (CC), ordinary chondrites (OC) and enstatite chondrites (EC)*. Each class comprises several groups (**Figure 1.4**).

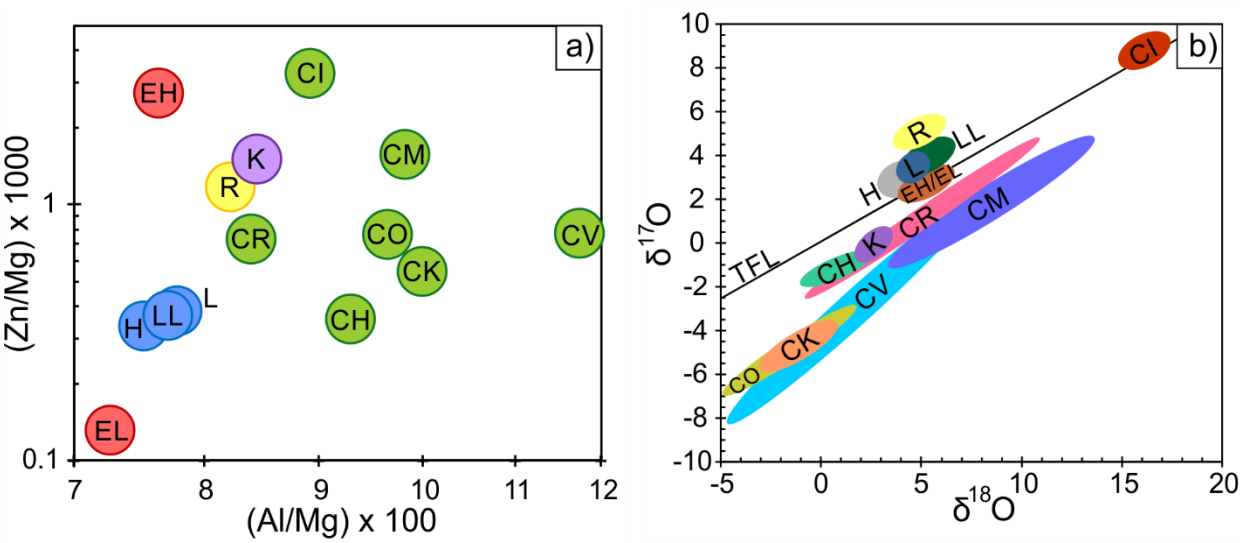

Figure 1.3: Classification of chondrites according to their a) bulk chemical composition and b) bulk oxygen isotope composition. a) All chondrite groups tend to be depleted in volatile elements (Zn) relative to CI, while only carbonaceous chondrites are enriched in refractory elements (Al) relative to CI. Data: (Lodders and Fegley, 1998) b) Carbonaceous (except CI) and K chondrites plot below the terrestrial fractionation line (TFL), while ordinary and R chondrites form well-defined clusters above the TFL. Enstatite and CI chondrite fall directly on the TFL. Data: (Clayton et al., 1984; Clayton et al., 1991; Bischoff et al., 1994; Schulze et al., 1994; Weisberg et al., 1996; Clayton and Mayeda, 1999)

Chondrites of the same group are thought to originate from the same parent body. Carbonaceous chondrites are subdivided into eight groups named after representative meteorites of each group: CI (Ivuna-like), CM (Mighei-like), CR (Renazzo-like), CO (Ornans-like), CV (Vigarano-like), CK (Karoonda-like), CB (Bencubbin-like) and CH (ALH 85085-like). Ordinary chondrites are divided into three groups according to their iron content: H chondrites

(high total iron), L chondrites (low total iron), LL (low total iron and additionally low metallic iron relative to total iron). Enstatite chondrites have either high metallic iron contents (EH) or low metallic iron contents (EL). Two groups of chondrites do not fit into either of the three major chondritic classes: R (Rumuruti-like) and K (Kakangari-like) chondrites.

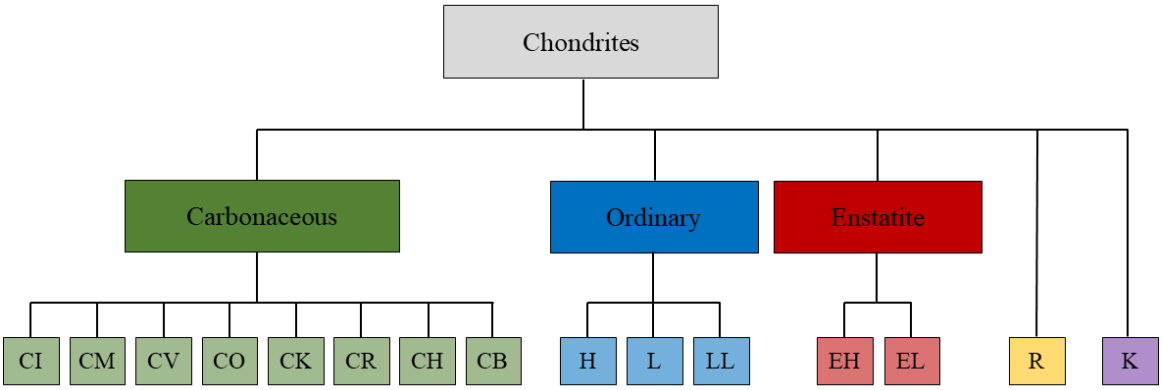

Figure 1.4: Chondrite classification modified after Weisberg et al. (2006)

In the last decade a new classification scheme was introduced based on the distribution of nucleosynthetic anomalies in meteorites. Warren (2011) introduced the terms *carbonaceous (CC)* and *non-carbonaceous (NC)* as taxonomic super-groups based on the well-defined dichotomy in ε^{54}Cr vs. ε^{50}Ti (and ε^{54}Cr vs. Δ^{17}O; not shown) (**Figure 1.5**). Molybdenum isotope anomalies later revealed that the dichotomy also holds for iron meteorites (Burkhardt et al., 2011; Budde et al., 2016a). Based on their ε^{54}Cr, ε^{50}Ti and ε^{94}Mo all meteorite groups are classified as either CC or NC. The CC group currently comprises carbonaceous chondrites, one pallasite (Eagle station Pal) and five iron meteorite groups (IIC, IID, IIF, IIIF and IVB) (Burkhardt et al., 2019). The NC-CC dichotomy seems to be a fundamental and ubiquitous characteristic of the early solar system as revealed by isotopic anomalies for a large number of refractory and main component elements (Ti, Sr, Ca, Cr, Ni, Zr, Mo, Ru, Ba, Nd, Sm, Hf, W and Os). Only volatile elements such as Zn, Cd, Sn, Te and Se do not show clear isotope anomalies thus far (e.g., Fehr et al., 2006; Wombacher et al., 2008; Moynier et al., 2009; Yokoyama and Walker, 2016; Labidi et al., 2018). The dichotomy has been interpreted to be the result of variable mixing of isotopically distinct primordial disk reservoirs inherited from the molecular cloud core (Burkhardt et al., 2019; Nanne et al., 2019).

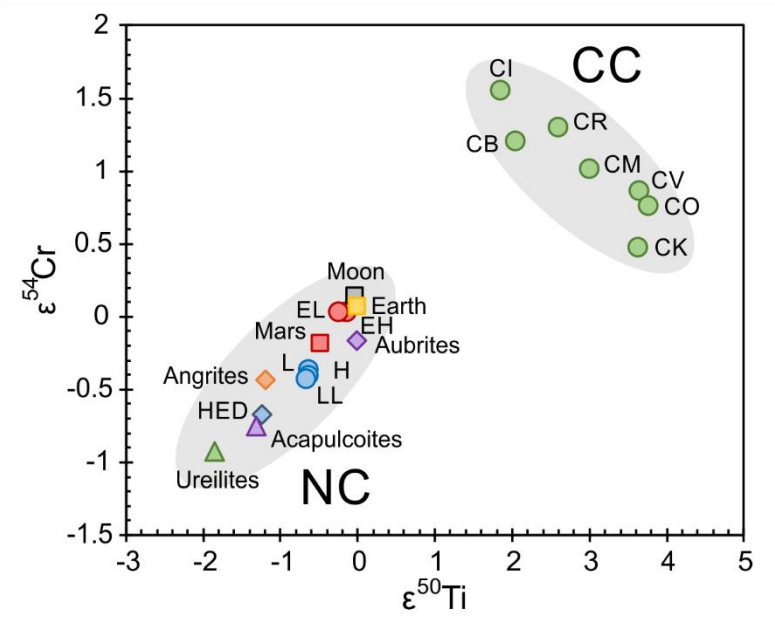

Figure 1.5: Carbonaceous and non-carbonaceous meteorites form well defined clusters in a ε^{50}Ti vs. ε^{54}Cr plot. Data: (Burkhardt et al., 2019 and references therein).

1.3.2 Secondary and tertiary classification parameters

Chondrites are primitive meteorites originating from undifferentiated asteroids. However, no single chondrite can be considered a pristine sample, since all chondrites experienced secondary alteration processes to various degrees mainly on the parent body. Van Schmus and Wood (1967) introduced a classification scheme dividing chondrites into petrologic types 1 - 6 according to the nature and degree of secondary modification. Petrologic type 3 chondrites are considered the least modified by secondary processes (*unequilibrated*). Types 3 to 6 represent increasing chemical equilibrium and textural recrystallization, likely due to thermal metamorphism. Ordinary, CO and CV chondrites of type 3 are further subdivided into 10 subtypes (3.0-3.9), where 3.0 represents the least altered (e.g., Sears et al., 1991). In contrast, chondrites of petrologic type 2 and 1 represent increasing effects of aqueous alteration based on the abundances of hydrous silicates and H, C and N bulk abundances and isotopic compositions (e.g., Browning et al., 1996; Rubin et al., 2007; Alexander et al., 2013). Significant aqueous alteration only occurred on CI, CM and CR parent bodies. Some of these chondrites additionally experienced slight degrees of thermal alteration which led to textural and chemical changes. There is currently no accepted classification for thermally overprinted CI, CM and CR chondrites but Nakamura (2005) and Tonui et al. (2014) proposed four stages according to matrix mineralogy which is related to the temperature at which the thermal overprint occurred.

Many chondrites have also been affected by shock metamorphism due to impacts on the parent body. Stöffler et al. (1991) and Scott et al. (1992) introduced a classification scheme based on shock effects in olivine and plagioclase for ordinary and carbonaceous chondrites. Rubin et al. (1997) extended this classification to orthopyroxene in enstatite chondrites. The classification ranges from S1 (unshocked) to S6 (very strongly shocked).

Terrestrial weathering of meteorite finds can be considered as a tertiary classification parameter. Antarctic meteorites are divided into three groups according to their rustiness (A to C) and the occurrence of evaporate minerals in hand specimens (E) (Grossman, 1994). Hot desert meteorite finds are usually classified with the scheme based on optical microscopy introduced by Wlotzka (1993), ranging from W0 (no visible alteration of minerals) to W6 (massive replacement of silicates by clay minerals and oxides). Typical changes in the bulk chemical composition introduced by terrestrial weathering have been reported by e.g., Al-Kathiri et al. (2005) and Hezel et al. (2011).

1.4 CHONDRITE COMPONENTS

Chondrites basically consist of four different components: (i) chondrules, (ii) matrix, (iii) refractory inclusions and (iv) opaque phases. The relative abundances of these four components are also used for the classification of chondrite classes and groups (see chapter 1.3).

1.4.1 Chondrules

Chondrules are solidified small melt droplets with igneous textures that are the dominant component in most chondrites (except CI). Ordinary and enstatite chondrites contain 60-80 vol.% of chondrules, while chondrule abundances in carbonaceous chondrites are highly variable but characteristic for each group (0-70 vol.%) (Krot et al., 2014). Igneous textures and mineralogical compositions of chondrules indicate that they have been heated to >2000 K and rapidly cooled afterwards within minutes to hours. The cause and setting of this heating event(s) remains enigmatic. Chondrules are compositionally variable, but most contain olivine and/or low-Ca pyroxene embedded in a glassy mesostasis. Recent work has shown that nearly all chondrules in ordinary, carbonaceous and Rumuruti chondrites are mineralogically zoned, with an olivine core surrounded by a low-Ca pyroxene rim (Friend et al., 2016; Barosch et al., 2019). This observation suggests that chondrules behaved as open-systems during their formation interacting with surrounding gaseous SiO to form the low-Ca pyroxene rims. Many chondrules are heavily depleted in volatile elements (e.g., Rubin and Wasson, 1987; Kong and Palme, 1999) attesting to their high-temperature origin. They are among the oldest objects having

formed 1-3 Ma after solar system formation (e.g., Amelin et al., 2002; Kita and Ushikubo, 2012; Becker et al., 2015; Budde et al., 2016b).

1.4.2 Matrix

The matrix is a complex optically opaque mixture of fine-grained (10 nm - 5 µm) silicates, oxides, sulfides, metal, phyllosilicates and carbonates. Together with chondrules it is the second main component in chondrites making up 10-15 vol.% in ordinary chondrites and up to 100 vol.% in carbonaceous chondrites. Enstatite chondrites contain only very little to no matrix (<0.1 to 10 vol.%) (e.g., Scott and Krot, 2014). Because of the fine-grained texture the matrix is most susceptible to aqueous alteration and many minerals have been heavily altered. On the other hand, chemically the matrix may be considered the most primitive component in chondrites having a broadly chondritic composition and being the host phase of presolar grains (e.g., Floss and Haenecour, 2016).

1.4.3 Refractory inclusions

Chondrites contain two types of refractory inclusions: (i) Ca-Al rich inclusions (CAIs) and (ii) amoeboid olivine aggregates (AOAs). Both have first been described in the 1970's in the newly fallen Allende CV3 meteorite (Clarke et al., 1971; Grossman and Steele, 1976). CAIs make up 0.1-3 vol.% in carbonaceous chondrites and only rarely occur in other types of chondrites (<0.1 vol.%) (Hezel and Palme, 2008). They are composed mainly of Ca-, Al-, Mg- and Ti-rich oxides and silicates, such as hibonite, perovskite, melilite, spinel, Al-Ti diopside, anorthite, forsterite, corundum and grossite. These are the minerals that are predicted to condense first from a cooling nebular gas of solar composition. Therefore, some CAIs are thought to be direct condensates which is also reflected in their irregular shape and fluffy textures. They are generally depleted in volatile elements, but strongly enriched in refractory trace elements (e.g., Martin and Mason, 1974; Stracke et al., 2012). Furthermore, CAIs exhibit strong nucleosynthetic isotope anomalies inherited either from presolar grains or the early nebula itself (Burkhardt et al., 2019 and references therein) and are the oldest objects within the solar system (Amelin et al., 2002; Bouvier and Wadhwa, 2010).

AOAs are irregularly shaped fine-grained porous objects that are especially abundant in carbonaceous chondrites (few percent) and rarely occur in ordinary chondrites. They are mainly composed of forsterite and do not show large mineralogical or isotopic variations between groups. Most AOAs also contain a refractory component that is sometimes recognizable as a

CAI, indicating that AOAs formed slightly after CAIs. Like CAIs they are thought to be aggregates of grains that condensed from the solar nebula.

1.4.4 Opaque phases

Opaque phases in chondrites consist of metals, sulfides and oxides. They make up 0-8 vol.% in carbonaceous chondrites (in CH ca. 20 vol.% and in CB chondrites up to 70 vol.%) and 2-10 vol.% in ordinary and enstatite chondrites. There are two kinds of metals in chondrites: (i) grains composed of highly refractory siderophile elements condensing at temperatures >1600 K associated with CAIs and (ii) Fe-Ni-Co grains which are calculated to condense together with the main component oxides. The latter occur mainly within chondrules and sometimes form accretionary rims around them.

It is expected that troilite condenses <650 K by reaction of the nebular gas with metallic Fe, Ni. However, S is readily mobilized during thermal and shock metamorphism on the parent body (e.g., Lauretta et al., 1997) and hence the observed troilite is likely no primary signature, but the result of alteration and recrystallization.

1.5 VOLATILE ELEMENT FRACTIONATION IN THE SOLAR NEBULA

CI chondrites are generally thought to represent the composition of the bulk solar system because of the close agreement of their chemical composition with that of the Sun (see Chapter 1.1). Relative to CI chondrites all other groups of meteorites (chondrites, achondrites and iron meteorites) as well as terrestrial planetary bodies (e.g., Earth, Mars, Moon) are depleted in moderately volatile elements. The depletion and fractionation pattern differ between the different materials. Carbonaceous chondrites are generally least depleted and display a smooth depletion pattern dependent on volatility, meaning that with decreasing 50% T_C the abundances of volatile elements are decreasing (e.g., Wasson and Chou, 1974; Davis, 2006). Ordinary and enstatite chondrites exhibit more complex elemental fractionation pattern. Volatile element depletion patterns in planetary bodies and achondrites are further complicated by igneous differentiation processes that modified the volatile element distribution (see Chapter 1.6). Therefore, studies on volatile element fractionation in the solar nebula focus on carbonaceous chondrites. Evaporation and/or condensation processes are most likely responsible for the primary volatile element depletion in the solar nebula. Alternatively, volatile element depletion was already inherited from the molecular cloud from which the solar system formed.

1.5.1 Evaporation vs. condensation models

Anders (1964) and Larimer and Anders (1967) introduced the first model dealing with volatile element depletion in chondrites, the two-component model. They observed that volatile elements are depleted by constant factors in carbonaceous chondrites relative to CI and concluded that such a pattern could only be obtained by mixing two fractions, one low-temperature component, which contains the full complement of volatile elements (CI chondritic) and one high-temperature component with no volatile elements. Furthermore, Anders (1964) point out that the amount of volatile elements in the different chondrite types covaries with their respective amount of low-temperature minerals. Therefore, he suggested that chondrite matrix is the low-temperature component, while chondrules represent the high-temperature component. Volatile loss from chondrules occurred by evaporation during chondrule formation. The different relative abundances of chondrules and matrix in the different carbonaceous chondrite groups then lead to the different degrees of volatile element depletions observed in carbonaceous chondrites.

At about the same time Wasson and Chou (1974) and Wai and Wasson (1977) introduced the partial condensation model based on the correlation of CI-normalized volatile element abundances with nebular volatility. The basic assumption underlying this theory is that all matter condensed upon cooling of an initially hot gaseous solar nebula with continuous loss of the nebular gas, such that volatile elements could not condense completely. The models by Wasson and Chou (1974) and Wai and Wasson (1977) became widely accepted mainly, because of four arguments. First, the step-wise depletion of volatile elements predicted by the two-component model was not observed in subsequent studies. Second, during evaporation under non-equilibrium conditions stable isotope fractionation would be expected, but was not observed (e.g., Humayun and Clayton, 1995). Third, evaporation experiments could not reproduce the observed volatile element fractionation patterns (Wulf et al., 1995) and fourth, detailed studies of chondrite matrices revealed that their composition is not CI chondritic (e.g., Brearley, 1993; Bland et al., 2005; Abreu and Brearley, 2010). It was also argued that matrix and chondrules have complementary compositions for volatile elements (Bland et al. 2005) and refractory and main component element ratios such as Mg/Si or Ca/Al (e.g., Hezel and Palme, 2008; Hezel and Palme, 2010; Friend et al., 2017; Friend et al., 2018), while bulk chondrite ratios are always CI chondritic. This was taken as an argument against the presence of a CI-like matrix.

Nevertheless, Alexander (2005) re-examined the role of chondrule formation for volatile element depletion in chondrites. By that time presolar material (circumstellar grains and interstellar organic matter) had been detected in most unequilibrated chondrites. Some of these presolar grains are thermally very labile phases and would have been destroyed during a complete vaporization of the solar nebula (Huss et al., 2003; Huss, 2004; Davidson et al., 2014). Furthermore, Alexander (2005) noted that the presolar material occurs in CI chondritic abundances in chondrite matrices and is also related to volatile element abundances in the host chondrite (Huss, 2004). Combined with the constant depletion factors of volatile elements observed by Anders (1964), this suggests that all chondrites accreted a CI-like matrix component (Alexander, 2005). However, the exact mechanisms of volatile element loss during chondrule formation remains enigmatic.

1.5.2 Inheritance model

The model of Yin (2005) suggests that the ubiquitous volatile element depletion in the inner solar system is inherited from the parental interstellar material. Presolar grains and isotope anomalies in chondrites clearly document the preservation of interstellar material in the solar system. Furthermore, volatile element abundances in the interstellar gas phase is anti-correlated with volatile element abundances in carbonaceous chondrites (**Figure 1.6**). It is inferred that elements that are depleted in the interstellar gas phase must be enriched in the dust (e.g., Savage and Sembach, 1996), which is the source of meteorite material.

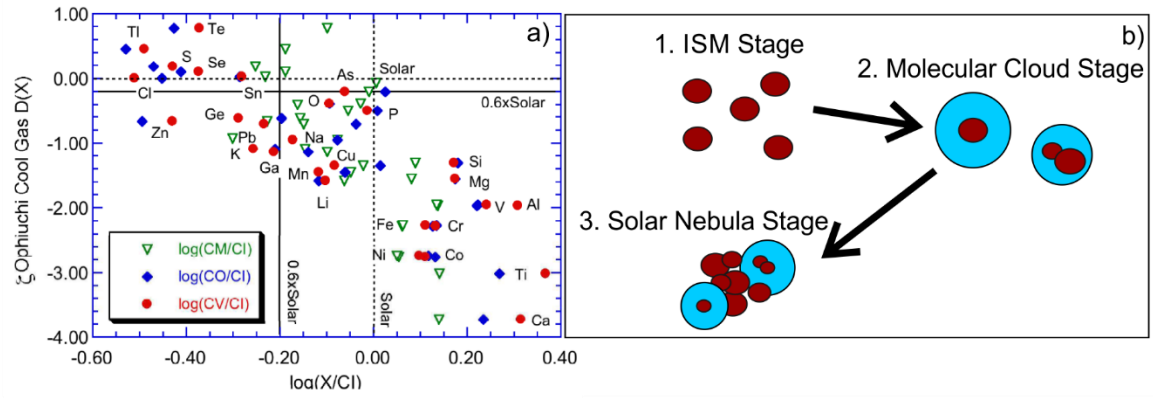

Figure 1.6: Inheritance model modified after Yin (2005). a) Anti-correlated volatile element abundances in carbonaceous chondrites and the interstellar gas. b) Schematic inheritance model. Brown: dust grains. Blue: icy mantles.

In the interstellar medium (ISM) refractory elements are locked in dust grains, while volatile elements reside in the hot ionized gas phase. During the cold and dense molecular cloud stage, volatile elements condense as icy mantles around refractory grains and only H and He remain in the gas phase (**Figure 1.6**). Collapse of the molecular cloud then leads to the rapid formation

of the solar nebula. During the collapse adiabatic compression or the passage of shock waves may take off and largely destroy the icy mantles containing volatile elements. However, the Sun-like composition of CI chondrites requires the local survival of icy mantles, most likely outside the snowline. The heterogeneous volatile element depletion in different reservoirs of the solar nebula can be explained by the accretion of various proportions of grains and icy mantles.

1.6 VOLATILE ELEMENT LOSS DURING POST-NEBULAR PROCESSES

Post-nebular processes such as metal-silicate differentiation, thermal metamorphism, impact vaporization, magma ocean degassing or collisional erosion have been suggested to modify the primary volatile element depletion signatures inherited from the solar nebula (e.g., Herndon and Herndon, 1977; Halliday, 2004; Sahijpal et al., 2007; O'Neill and Palme, 2008; Pringle et al., 2014; Kraus et al., 2015; Hin et al., 2017; Norris and Wood, 2017; Siebert et al., 2018). The different pressure, temperature and fO_2 conditions prevalent during asteroidal and planetary accretion affect elemental volatilities (Schaefer and Fegley, 2010a; Norris and Wood, 2017; Sossi and Fegley, 2018; Sossi et al., 2019). For examples, the more oxidizing conditions during silicate melt evaporation following high energetic impacts change the volatility of Mn (50% T_C = 1158 K) and Na (50% T_C = 958 K). Chondrites and the Earth have constant Mn/Na ratios despite the very different degrees of volatile element depletion under the very reducing conditions in the solar nebula. In contrast, achondrites, Mars and the Moon have super-chondritic Mn/Na ratios reflecting the preferential loss of Na during impact vaporization (O'Neill and Palme, 2008; Siebert et al., 2018). Experimental work coupled with thermodynamic calculations have shown that evaporation from a silicate melt results in highly fractionated or step-like volatile element depletion patterns as observed e.g. in the Moon (Norris and Wood, 2017; Sossi et al., 2019). Furthermore, these post-nebular volatilization processes normally lead to stable isotope fractionation with an enrichment of the heavy isotopes in the residue (e.g., Paniello et al., 2012; Day and Moynier, 2014; Pringle et al., 2014; Kato et al., 2015; Hin et al., 2017; Pringle and Moynier, 2017). The terrestrial volatile element abundances (e.g., chondritic Mn/Na ratio) and the lack of stable isotope fractionation argue against post-nebular volatile element depletion on Earth or its building blocks (Humayun and Clayton, 1995; Wombacher et al., 2008; Nebel et al., 2011; Kato and Moynier, 2017; Pringle and Moynier, 2017; Siebert et al., 2018; Sossi et al., 2018). The highly fractionated volatile element depletion pattern of the bulk silicate Earth and the slight enrichment of heavy Si isotopes is rather

attributed to core formation possibly involving sulfide segregation (O'Neill, 1991; Fitoussi et al., 2009; Righter et al., 2013; Wood et al., 2014; Ballhaus et al., 2017).

Equilibrated chondrites were also affected by post-nebular volatile loss. Thermal metamorphism on asteroid parent bodies either due to the radioactive decay of short-lived radionuclides (e.g., ^{26}Al, ^{60}Fe) or impacts led to the redistribution and loss of some volatile elements, especially in ordinary and enstatite chondrites but also type 3 carbonaceous chondrites are sometimes affected (e.g., Dodd, 1969; Matza and Lipschutz, 1977; Wombacher et al., 2008; Schaefer and Fegley, 2010b).

1.7 TERRESTRIAL BUILDING BLOCKS

The Earth formed through the collision of innumerable planetesimals and planetary embryos (e.g., Chambers, 2004). The sources and nature of these building blocks are tackled by comparing the chemical composition of Earth and chondrites on the one hand and numerical modeling of planetary accretion on the other hand (e.g., Chambers, 2001; Fischer et al., 2018; Brasser et al., 2018). Although it is much more likely that Earth largely accreted from differentiated material (Taylor and Norman, 1990; Fitoussi et al., 2016), chondrites are useful tracers for chemical fractionation trends and different isotopic reservoirs within the protoplanetary disk.

There are basically two competing chondritic models based on the elemental and isotopic evidence from the silicate Earth: (i) the carbonaceous chondrite model and (ii) the enstatite chondrite model. The carbonaceous chondrite model is based on the similarity of lithophile element abundances in the silicate Earth and carbonaceous chondrites (e.g., Dreibus and Palme, 1996; Allègre et al., 2001; Palme and fff, 2014). Refractory lithophile element abundances in the silicate Earth are enriched relative to CI chondrites and within the range of carbonaceous chondrites, while ordinary and enstatite chondrites are depleted in these elements relative to CI (Palme and O'Neill, 2014). Volatile lithophile elements are much more depleted in the silicate Earth than in any chondrite group. However, volatile vs. refractory element ratios, such as K/U or Rb/Sr, show that carbonaceous chondrites follow a single trend and Earth falls on the volatile-depleted end of this trend (Allègre et al., 2001; Palme and O'Neill, 2014). Enstatite and ordinary chondrites, despite also being depleted in volatile elements, deviate from this trend. Thus, the elemental composition of the silicate Earth is most similar to carbonaceous chondrites and cannot be easily reconciled with enstatite or ordinary chondrites.

However, the discovery that carbonaceous chondrites show different nucleosynthetic isotope anomalies than Earth is inconsistent with a carbonaceous chondritic origin of Earth. Nucleosynthetic isotope anomalies reflect the presence of isotopically extremely different presolar material. The presolar material seems to be heterogeneously distributed within the solar system and thus nucleosynthetic anomalies can be considered fingerprints of solar nebular reservoirs (e.g., Carlson et al., 2018). In fact, nucleosynthetic anomalies of several refractory elements (e.g., Ca, Ti, Nd, Cr and Ni) indicate that the vast majority of Earth's building blocks relates to the enstatite chondrite reservoir (e.g., Javoy et al., 2010; Dauphas, 2017). However, terrestrial Nd, Mo and Ru isotope anomalies suggest an endmember composition for Earth, rather than a mixture between enstatite and carbonaceous chondrite-like materials (Boyet and Carlson, 2005; Gannoun et al., 2011; Fischer-Gödde and Kleine, 2017; Render et al., 2017). Hence, Earth's endmember composition requires the accretion of some yet unknown material with even more extreme Nd, Mo and Ru isotope anomalies to balance chondritic contributions. In that case a mix of such unknown materials with material from the carbonaceous chondrite reservoir may reconcile isotopic and elemental observations.

Because of several discrepancies between the composition of chondrites and the Earth such as the superchondritic Fe/Mg ratio and the high $^{142}Nd/^{144}Nd$, non-chondritic models were introduced, assuming that Earth was affected by collisional erosion during the later growth stages, which removed up to 15% of an early formed crust (O'Neill and Palme, 2008; Campbell and O'Neill, 2012; Boujibar et al., 2015).

1.8 DETERMINATION OF ELEMENTAL MASS FRACTIONS VIA INDUCTIVELY-COUPLED-PLASMA MASS-SPECTROMETRY (ICP-MS)

Determination of elemental mass fractions at a high level of precision and accuracy is fundamental in Earth Sciences. In the last 40 years single-collector ICP-MS became the method of choice because of its sensitivity and dynamic range which allows to simultaneously determine the abundances of multiple elements from the sub ppm to major element level (e.g., Houk, 1980; Jenner et al., 1990; Olesik, 2014). After efficient ionization in a plasma ion source, ions are separated according to their mass-to-charge ratio (m/z) for element-specific quantification. Quadrupole ICP-MS (Q-ICP-MS) use a quadrupole mass filter which rapidly scans sequentially through the desired mass range. A higher mass resolution is obtained with a double-focusing sector field ICP-MS (SF-ICP-MS). In double focusing SF-ICP-MS the ions are separated according to their m/z in a magnetic field, while variations in ion kinetic energies

are compensated for by the opposite effects of the magnetic and electrostatic analyzer (e.g., Jakubowski et al., 1998).

1.8.1 External calibration

External calibration is the most commonly applied method for the determination of elemental mass fractions using single-collector ICP-MS. The ion beam intensities of the different isotopes in an unknown sample is compared to an external calibration solution containing known elemental mass fractions. At least three calibration solutions spanning the mass fraction range of all analyzed samples are commonly measured in order to obtain a calibration curve. External calibration requires beam stability throughout the measurement session, but high or variable matrices between sample and calibration solutions can lead to signal drift, i.e. signal enhancement or suppression. Signal drift is mainly induced by salt depositions on the sample cone (e.g., Evans and Giglio, 1993). To monitor and correct signal drift throughout a measurement session, sample, calibration and background solutions are doped with a known amount of an element which has a naturally low mass fraction in the sample. Often, several elements (2-3) covering the whole mass range are used as *internal standards,* because the signal drift is mass-dependent (e.g., Yokoyama et al., 2017). Signal enhancement or suppression arise from the presence of major rock-forming elements such as Mg, Fe, Al and Ca in the sample solution, most likely due to space-charge effects (Gillson et al., 1988; Li et al., 1995). These matrix effects cannot be avoided. Therefore, closely *matrix-matched* calibration solutions should be preferred for quantification.

Spectral isobaric and polyatomic or multiply charged interferences lead to erroneous mass fractions if not accurately corrected for. Isobaric interferences arise when two elements have isotopes of nominally the same mass. Generally, interference-free isotopes should be chosen but isobaric interferences can be corrected mathematically by measuring an interference-free mass for the interfering element followed by the subtraction of the interference contribution from the analyte mass ion beam signal. Polyatomic ions, especially oxides and argides, form in the plasma and can then also overlap on selected mass (e.g., $^{40}Ar^{16}O^{+}$ on $^{56}Fe^{+}$ or $^{140}Ce^{16}O^{+}$ on $^{156}Gd^{+}$). Polyatomic interferences can be diminished using cooled spray chambers and more efficiently by the use of desolvating sample introduction systems (e.g. Apex or Aridus) or by reaction/collision cell techniques. With high-resolution mass spectrometers (SF-ICP-MS) many of the polyatomic interferences at the low to mid-mass range can be resolved from the actual analyte mass. If none of these techniques are available or applicable, polyatomic interferences can also be corrected mathematically by measuring single element solutions containing only

the element which forms the interference and thus determining the oxide formation rate. In general, polyatomic interferences are highly dependent on sample introduction and plasma parameters (e.g., Linge and Jarvis, 2009), which can be individually optimized generating low oxide and double-charged rates.

1.8.2 Isotope dilution

The *isotope dilution* method can be applied for the determination of highly accurate and precise elemental mass fractions (e.g., Stracke et al., 2014). To this end a known amount of an isotope tracer solution with non-natural isotope composition (spike) is equilibrated with a known amount of sample. Once spike and sample are equilibrated no quantitative sample handling is needed. For this reason, isotope dilution can be well combined with the chemical separation of the analyte element from the sample matrix and interfering elements, which also allows for much higher ion beam intensities and hence improved precision. By measuring the isotope ratio of the resulting spike-sample mixture and knowing the isotope composition and mass fraction of the spike, the elemental mass fraction can be calculated with the following equation:

$$mf_{sa} = \frac{\left(\frac{A}{B}\right)_{mix} - \left(\frac{A}{B}\right)_{sp}}{\left(\frac{A}{B}\right)_{sa} - \left(\frac{A}{B}\right)_{mix} \times \left(\frac{A}{B}\right)_{sp}} \times \frac{weight_{sp} \times mf_{sp} \times ab\left(A_{sp}\right) \times atwt(element_{sa})}{weight_{sa} \times ab(B_{sa}) \times atwt\left(element_{sp}\right)}$$

where *A* is the spike isotope and *B* is the reference isotope, *mf* refers to the mass fraction, *weight* to the sample and spike weights, *ab* to the abundance of the spike isotope in the spike or the reference isotope in the sample and *atwt(element)* to the atomic weight of the element. Subscripts *mix*, *sa* and *sp* refer to the sample-spike mixture, the sample and the spike, respectively. One problem arising when isotope ratios are measured with an ICP-MS is the instrumental mass bias. Heavier ions are preferentially transmitted, most likely due to space charge effects in the interface (e.g., Allen et al., 1997; Wombacher and Rehkämper, 2003) resulting in erroneous isotope ratios. The simplest way to correct for mass bias effects in ICP-MS measurements is by external standard sample-standard bracketing. The mass bias is determined from the two standards bracketing the sample or set of samples, assuming that the mass bias is the same for standard and sample solution.

In general isotope dilution combined with chemical separation is considered a superior method for the determination of highly accurate and precise elemental mass fractions via ICP-MS since spectral interferences and matrix effects are largely omitted. Furthermore, extremely low mass

fractions (sub ppb) can be accurately determined as the absence of the matrix alleviates the need for strong sample dilution. However, isotope dilution coupled with chemical separation is an comparatively time consuming method and it can only be applied to elements with two or more naturally occurring isotopes (or in rare cases if suitable radioactive isotopes are available).

Chapter 2

The chemical composition of carbonaceous chondrites: implications for volatile element depletion, complementarity and alteration

2.1 INTRODUCTION

Carbonaceous chondrites represent the most pristine rock samples of our solar system. They are divided into the compositional groups of CI, CM, CR, CO, CV, CK, CH, and CB chondrites. Further discriminating characteristics are distinct abundances of high-temperature components such as chondrules and Ca-Al-rich refractory inclusions (CAIs), opaque phases and the fine grained matrix (e.g., Scott and Krot, 2014), as well as the degree of bulk chondrite alteration. Chondrules are products of transient heating events of unknown origin, and depleted in volatile elements relative to their host bulk chondrite (e.g., Hezel et al., 2018). In contrast, the matrix is enriched in volatile elements relative to the bulk chondrite (e.g., Bland et al., 2005). CI chondrites almost entirely consist of matrix and their relative abundances of non-atmophile elements closely match those of the solar photosphere, attesting to their primitive chemical composition (e.g., Anders and Ebihara, 1982; Anders and Grevesse, 1989). Virtually all other known planetary materials, i.e., other groups of meteorites, the terrestrial planets and the Moon are significantly depleted in volatile elements (e.g. Na, K, Zn, S, Cd) relative to CI.

Over the past 60 years, numerous models have been proposed to explain volatile element depletion in planetary materials. Anders (1964) observed that the abundance of matrix material correlates with the degree of volatile element depletion. Based on this observation he proposed a two-component model, in which all chondrites accreted (i) a volatile-rich CI chondritic matrix and (ii) a high temperature, refractory component (chondrules, CAIs, etc.). In this model, the degree of volatile element depletion would depend on the relative amounts of these two components. However, subsequent investigations have shown that bulk chondrite volatile element depletion correlates with the volatility of the elements as represented by their 50% condensation temperatures (T_C) (Wasson and Chou, 1974). This correlation is in marked conflict with the model from Anders (1964), in which flat volatile element patterns would be expected. Furthermore, many studies (e.g., Brearley, 1993; Alexander, 2005; Bland et al., 2005;

Abreu and Brearley, 2010; Schrader et al., 2014; Howard et al., 2015) demonstrated that chondrite matrix compositions are not CI chondritic. In fact, several refractory and main component element ratios (e.g. Mg/Si, Ca/Al) of matrix and chondrules are complementary to each other, while the bulk chondrite compositions display elemental ratios similar to CI chondrites (Hezel and Palme, 2008, 2010; Friend et al., 2017). This observation led to the conclusion that matrix and chondrules formed from the same reservoir, and cannot be random mixtures of materials from different regions in the solar nebula (Hezel and Palme, 2010; Palme et al., 2015; Ebel et al., 2016).

Wasson and Chou (1974) and Wai and Wasson (1977) proposed partial condensation from a hot solar nebula as the cause of volatile element depletion to explain the decreasing volatile element abundance with decreasing 50% T_C. In their model, a gas of initially solar composition existed in the inner part of the protoplanetary disk. Following the complete condensation of refractory elements, the gas phase containing the volatile elements started to dissipate, while further cooling led to the progressive condensation of the remaining volatile elements. Consequently, volatile element depletion increases with increasing elemental volatility. However, Huss et al. (2003) and Huss (2004) argued that condensation from a hot solar nebula cannot be the primary mechanism for volatile element depletion, as a complete vaporization of the nebula would have destroyed presolar grains, which are commonly found in chondrite matrices.

Thermal metamorphism on the parent body was another suggestion to explain volatile element depletion (e.g., Wasson, 1972), but was quickly discarded, after heating experiments could not reproduce the observed depletion patterns (e.g., Ikramuddin and Lipschutz, 1975; Takahashi et al., 1978; Wulf et al., 1995). More recently, Alexander (2005) argued that volatile element depletion in chondrites is due to evaporation from chondrules and Yin (2005) suggested that volatile depletion may be inherited from the interstellar medium (ISM).

One difficulty regarding studies of volatile element depletion are the limited data available for volatile elements with 50% $T_C < 800$ K and the moderate precision and accuracy of some available data. Takahashi et al. (1978b) pointed out that volatile elements with 50% $T_C < 800$ K seem to be depleted to the same extent in type 3 carbonaceous chondrites. They determined the abundance of eight volatile elements with 50% $T_C < 800$ K. However, their precision was rather poor (5 - 50% RSD, based on the analysis of three Allende Smithsonian replicates). Subsequently, Kallemeyn and Wasson (1981) and Kallemeyn et al. (1991, 1994) analyzed the chemical composition of several carbonaceous chondrite groups by instrumental and

radiochemical neutron activation analysis (INAA and RNAA). They inferred that especially the abundance of volatile elements is a valuable tool to define carbonaceous chondrite groups. However, only a limited set of volatile elements with 50% T_C < 800 K (Zn, Se, Cd, In and Br) was analyzed. Wolf et al. (2005) developed an ICP-MS protocol to determine volatile elements in carbonaceous chondrites. They have quantified nine volatile elements with 50% T_C < 800 K with reasonable precision (<5% RSD, based on the analysis of five Murchison replicates), but only reported data for three carbonaceous chondrites.

Here we present a comprehensive dataset including the bulk chemical compositions of 25 carbonaceous chondrites from six different groups (3x CI; 13x CM; 2x CR, 2x CO, 2x CV and 1x CK) and two ungrouped chondrites (**Table 2.1**). We determined 51 major and trace elements via sector field ICP-MS with a focus on high precision analyses of volatile elements with 50% T_C < 800 K (Cs, Bi, Pb, Zn, Te, Sn, Se, S, Cd, In, Tl). Furthermore, we investigated the putative loss of volatile elements from carbonaceous chondrites upon heating by experimentally heating aliquots of Murchison (CM2) in either O_2 or Ar atmosphere. We combine these datasets to better constrain the processes that can explain the volatile element depletion patterns in carbonaceous chondrites.

2.2 METHODS

2.2.1 Determination of bulk rock compositions using SF-ICPMS

Major and trace element analyses of bulk carbonaceous chondrites were carried out using a Thermo Scientific ElementXR^{TM} sector-field ICP-MS at the University of Bonn/Germany, equipped with an Elemental Scientific SC-2 DX autosampler. Two instrumental set-ups with comparable performances were used: (i) Scott type glass spray chamber and Glass Expansion Micro Mist nebulizer, (ii) Scott type PFA spray chamber and ESI Polypropylene ST nebulizer. Details of the instrumental settings, performance and acquisition parameters are listed in **Table A1**. Results were obtained during several measurement sessions over more than six months, and each sample was analyzed at least twice.

Typically, 50 mg of sample powder were weighed into pre-bombed PFA beakers. Then, 2 ml 14 M HNO_3 and 2 ml 24 M HF were added and the closed beakers placed into Parr® bombs for 24 h at 180°C. Subsequently, samples were dried down, refluxed in 1 ml 14 M HNO_3 and dried down again. To eliminate secondary fluoride precipitates, samples were taken up in 2 ml of 14 M HNO_3 and again placed into Parr® bombs for 24 h at 180°C. After digestion, 500 mg of an internal standard solution containing approximately 60 µg/g Y and 6 µg/g Ho was added

to all samples. The same internal standard solution was added proportionally to blanks, calibration and background solutions. Subsequently, samples were diluted to a solution weight of 100 g (2,000-fold) for trace element analysis. For major element analyses, the same sample solutions were diluted further to a final dilution of 1:10,000. Quantification of the samples has been carried out using external three-point calibration. Two sets of calibration solutions were freshly prepared in 0.28 M HNO_3 from six multi-element solutions and some single element additions matching typical CI and CM chondrite element abundances (Funk, 2015). A set of calibration solutions consists of three solutions, one containing all elements at the nominal concentration of CI or CM chondrites, and two containing the same elemental mix at 25% higher and lower concentrations, respectively. Selenium was included in the measurement routine, although it was not in the calibration solutions. Therefore, Se abundances are only reported relative to CI chondrites (**Table A2**).

A 0.28 M HNO_3 background solution doped with the internal standard was measured prior to every sample and calibration solution to correct for the instrumental background. Prior to the background measurement, the sample introduction system was rinsed for two minutes with 0.56 HNO_3 followed by the background solution for four minutes. The take-up time for sample and calibration solutions was set to 80 s. Background values were always subtracted, although their contribution was generally negligible. Highest contributions were observed for Se, Ag and W (20 - 30%) and In and Bi (typically < 5%, but up to 60% for samples with very low In and Bi concentrations). For all other elements, background contributions were usually below 3%. One or two procedural blanks were processed in parallel during each session. The contributions were insignificant for all elements, except for W in the first and second set of samples digested (up to 10%), which is most likely due to beaker contamination.

External calibration was carried out for Ivuna (CI), Orgueil (CI) and the Allende Smithsonian powder (CV3) during five independent measurement sessions and for the basaltic reference materials BHVO-2 and BCR-2, which were included in two of these sessions. All other samples were analyzed by the sample-standard-bracketing technique relative to the Orgueil sample, which served as a matrix-matched standard. However, results are reported relative to the mean of our Ivuna data (**Table A2**). This is because Ivuna aliquots were more reproducible than Orgueil aliquots (Barrat et al., 2012;**Table A3**, **Table A4**), but we did not have sufficient Ivuna sample for use as a bracketing standard solution throughout all sessions.

Table 2.1: Sample list and water content determined by Karl-Fischer titration

Sample	Group	Fall/Find	W*	Source	Water
Ivuna	CI	Fall		J.-A. Barrat	
Orgueil A	CI	Fall		A. Bischoff	18.14
Orgueil B	CI	Fall		A. Bischoff	
Y-980115	CI	Find	A	NIPR	11.62
Tagish Lake	C2-ungr.	Fall		A. Bischoff	16.54
SCO 06043	CM1	Find	B/Ce	MWG NASA	
MET 01070	CM1	Find	Be	MWG NASA	13.39
Murchison NC	CM2	Fall		E. Strub	10.36
Murchison	CM2	Fall		A. Bischoff	10.81
Mighei	CM2	Fall		Field Museum	10.28
Jbilet Winselwan	CM2	Find	W1	J. Zipfel	
Paris	CM2	Find		J.-A. Barrat	
Cold Bokkeveld	CM2	Fall		NHM London	15.61
Murray	CM2	Fall		Smiths. Inst.	11.64
Nogoya	CM2	Fall		MfN Berlin	14.72
ALH 85013	CM2	Find	A	MWG NASA	14.23
EET 96029	CM2	Find	A/B	MWG NASA	9.80
LON 94101	CM2	Find	Be	MWG NASA	15.99
LON 94102	CM2	Find	Ce	MWG NASA	10.80
Allende Smithsonian	CV3	Fall		Smiths. Inst.	0.08
Allende MS	CV3	Fall		C. Münker	0.45
Vigarano	CV3	Fall		J.Schlüter	2.41
ALH 85002	CK4	Find	A	MWG NASA	0.00
EET 96026	C4/5	Find	B	MWG NASA	0.64
ALHA 77307	CO3.0	Find	Ae	MWG NASA	6.36
Kainsaz	CO3.2	Fall		Meteorite Market	3.97
GRA 95229	CR2	Find	A	MWG NASA	4.43
LAP 02342	CR2	Find	A/B	MWG NASA	2.97

W*: Weathering grade according to MWG and Wlotzka (1993):
A = Minor rustiness; rust haloes on metal particles and rust stains along fractures are minor.
B = Moderate rustiness; large rust haloes occur on metal particles and rust stains on internal fractures are extensive.
C = Severe rustiness; metal particles have been mostly stained by rust throughout.
E = Evaporite minerals visible to the naked eye.
W1 = Small oxide rims around metal and troilite, small oxide veins.

The measured isotopes are listed in **Table A1**. Some of these isotopes suffer from isobaric or molecular interferences. Indium signals, measured at mass 115, were corrected for interferences from ^{115}Sn. To identify possible molecular interferences, five test solutions designed to quantify oxide, hydroxide and argide formation rates were analyzed during most measurement sessions. The magnitude of molecular interferences was observed to be highly variable in different measurement sessions (varying up to 20%), depending on the instrumental set-up. Therefore, we consider it necessary to determine molecular interference rates for each measurement session and do not report values for the elements that were significantly affected by molecular interferences when the test solutions were not analyzed. Most significant was the interference of $^{141}Pr^{16}O^{+}$ on ^{157}Gd, which contributed up to 50% to the signal on mass 157. Data for ^{157}Gd are not reported when the $^{141}Pr^{16}O^{+}$ interference had exceeded 30%.

Uncertainties are reported as the relative standard deviation (RSD) of the mean in percent. The intermediate measurement precision of our ICP-MS method was tested by the repeated measurement of Orgueil, Ivuna and the Allende Smithsonian sample powder. The results of five independent measurement sessions with different set-ups exhibit better than ±10% RSD for all elements (**Table A3** - **Table A5**). The intermediate precision for volatile elements with 50% T_C <800 K is below 3% RSD for Pb, Sn, S, Cd, In and Tl and below 5% RSD for Ag, Zn and Te (**Table A3** - **Table A5**).

In addition, a second Orgueil aliquot was analyzed to evaluate sample homogeneity. Almost all elements agree within 5% between both aliquots, only Zr, Bi, Th, U, and the LREE (La, Ce, Pr, Nd and Sm) exhibit variations >10% (**Table A4).**

In addition to the SF-ICPMS measurements, water contents were determined by Karl-Fischer titration using 5 mg sample powder at the University of Bochum (**Table 2.1**). The method is based on the quantitative reaction of water with iodine. Samples are heated up to 1100°C to release the water and transport it to the titration cell (Behrens et al., 1996). Repeated analyses of an in-house standard containing 5 wt.% water yielded a precision of about ±5% RSD.

2.2.2 Murchison (CM2) heating experiments

A piece of Murchison CM2 chondrite obtained from the Nuclear Chemistry department at Cologne (Murchison NC) was powdered with a small agate ball mill. To study the loss of volatile elements upon heating, approx. 50 mg aliquots of this fine-grained powder were weighed in a quartz glass boat and placed into a tube furnace. The sample aliquots were heated to various temperatures (200 - 1000°C), either in an oxygen or argon gas stream to simulate oxidizing and reducing conditions, respectively. The temperature ramp was set to 5°C/min and the final temperature was held for four hours. After heating, the aliquots were weighed again, digested and analyzed in the same way as the other samples (see Section 2.2.1). An unheated aliquot of Murchison NC was quantified using the calibration solution adapted to CM chondrites and served as a bracketing standard for the analyses of the heated aliquots. The unheated Murchison NC sample has been measured twice at the beginning and the end of the measurement session. The repeatability is excellent, within 2% RSD for all elements except As (7% RSD).

2.3 RESULTS

2.3.1 Orgueil (CI), Ivuna (CI), Allende Smithsonian powder (CV), BHVO-2 and BCR-2

Table A3 - **Table A5** list our results for Orgueil, Ivuna and the Allende Smithsonian powder together with literature data determined by ICP-MS and isotope dilution methods. Orgueil (**Table A4**) shows an overall good agreement with literature data for nearly all elements (Friedrich et al., 2002; Münker et al., 2003; Wolf et al., 2005; Fischer-Gödde et al., 2010; Barrat et al., 2012; Pourmand et al., 2012; Wang et al., 2014). Exceptions are: (i) Th and the fluid mobile elements Na, Rb, Ba and U, which deviate by more than 15%; (ii) Zr and Hf, which deviate substantially from most literature data (Zr >25%, Hf >20%), but are in good agreement with isotope dilution data from Münker et al. (2003) and (iii) Sr, Mo and Bi, which are more than 20% below literature values in all analyzed samples. The most plausible explanation for the deviation of the latter three elements, are inaccurate abundances in the calibration solution. Therefore, we only present relative abundances for Sr, Mo and Bi for all samples.

Our Ivuna data (**Table A3**) agree well with literature data (Lu et al., 2007; Fischer-Gödde et al., 2010; Barrat et al., 2012; Pourmand et al., 2012; Wang et al., 2014) and deviate no more than 15% for all elements. The results for the Allende Smithsonian powder (**Table A5**) are also in good agreement with literature data (Jarosewich et al., 1987; Münker et al., 2003; Wolf et al., 2005; Fischer-Gödde et al., 2010; Barrat et al., 2012; Pourmand et al., 2012; Stracke et al., 2012; Wang et al., 2014). All elements agree within 15% and most within 10%.

We further included two reference materials BHVO-2 and BCR-2 – both terrestrial basalts – for comparison (**Table A6**). Our results generally agree with the published reference values from Jochum et al. (2016). However, as our measurement setup is optimized for chondritic compositions, elements with a much lower concentration in geological material than in carbonaceous chondrites cannot be reliably determined in these two terrestrial reference materials. These elements are: Rh, Te, Re, Ir and Pt, but also elements which are affected by large oxide interferences such as ^{111}Cd ($^{95}Mo^{16}O^{+}$) and ^{109}Ag ($^{93}Nb^{16}O^{+}$). In both measurement sessions the Al concentration obtained for BCR-2 is 60% too low for unknown reasons. Since Al concentrations for Ivuna, Orgueil and BHVO-2 from the same measurement sessions are in good agreement with literature data (**Table A3** - **Table A6**), we are confident that this is an isolated anomaly in BCR-2 and does not affect Al concentrations in other samples.

2.3.2 Carbonaceous chondrite compositions relative to CI

Bulk chondrite element concentrations are listed in **Table 2.2**. **Figure 2.1** to **2.5** display the CI and Fe normalized bulk chondrite compositions. We favored Fe as the normalizing element over the more commonly used Mg because the only CK chondrite that we analyzed has a Mg concentration which is 30% below literature values (Kallemeyn et al., 1991). Normalization to Mg would therefore shift all other elements towards higher values in the CK chondrite. There is no significant difference between the Fe and Mg normalized relative elemental abundances in all other samples (for comparison see **Figure A1**). The elements on the x-axes are listed in sequence of increasing volatility based on 50% T_C calculated by Lodders (2003). For Ag we use the revised 50% T_C of 730 K (Kiseeva and Wood, 2015).

Once normalized to CI compositions and Fe, all chondrites display the same overall element pattern, which is commonly divided into four groups based on 50% T_C (e.g., Lodders, 2003; Palme et al., 2014a, 2014b): (i) refractory elements with 50% T_C 1850 - 1355 K (here Re - Rh) are enriched relative to CI; (ii) main component elements with 50% T_C 1355 - 1250 K (Ni - Cr) form a plateau at roughly CI abundances for all groups; (iii) moderately volatile elements with 50% T_C 1250 - 252 K (P - Hg) have decreasing abundances, correlating with decreasing 50% T_C; (iv) highly volatile elements with 50% T_C <250 K.

In our study the patterns of moderately volatile elements do not show a monotonous depletion across their entire temperature interval (**Figure 2.1** - **2.5**). In fact, the monotonous depletion levels off at around 800 K and all elements with 50% T_C down to 500 K are depleted to the same extent. In the following, we call these elements 'plateau volatile elements', while moderately volatile elements with 50% T_C between 1250 and 800 K are called slope volatile elements. The transition from slope to plateau volatile elements is different for the various chondrite groups and occurs between Ga and Rb for CK chondrites and Tagish Lake; and between Cs and Bi for CM, CO, CV and CR chondrites (**Figure 2.6**). In this study, the plateau volatile element group consists of 11 elements with different geochemical characters: Ag, Bi, Pb, Sn, In, Te, Se, S, Cd, Tl and Zn. Deviations from the median of the plateau volatile element abundances in each chondrite group are below 10% RSD, except in CK chondrites where the deviation is up to 15% (**Table 2.3**).

Table 2.2: Major and trace element abundances in carbonaceous chondrites obtained with SF-ICP-MS.

Sample	Ivuna	Orgueil	Y-980115	**Tagish Lake**	Mighei	Murray
Class	CI1	CI1	CI1	**C2-ungr.**	CM2	CM2
Na	4932	2523	5768	**795**	3613	2013
Mg	95468	96735	105876	**112743**	117704	122393
Al	7967	8328	9068	**11886**	11015	11926
S	49686	45450	62002	**34784**	32539	27301
K	407	410	608	**291**	329	323
Ca	8957	7842	10131	**5681**	13459	12442
Cr	2575	2719	3001	**2994**	3060	3183
Mn	2040	1966	2061	**1523**	1737	1771
Fe	182348	192528	212755	**198132**	211723	218478
Ni	11226	11213	12558	**12172**	12433	13227
P	845	905	1108	**1070**	949	973
Ti	381	415	458	**535**	539	555
V	47.5	50.1	56.3	**65.1**	74.9	67.4
Co	507	515	591	**550**	573	594
Cu	136	146	151	**128**	138	138
Zn	321	337	391	**237**	206	195
Ga	8.7	9.25	9.78	**6.86**	6.79	6.79
As	1.7	1.83	1.96	**1.67**	1.81	1.71
Rb	2.09	1.75	2.64	**1.47**	1.37	1.52
Zr	3.27	4.67	3.87	**4.58**	4.50	4.69
Nb	0.251	0.302	0.308	**0.355**	0.376	0.355
Rh	0.129	0.133	0.146	**0.152**	0.157	0.162
Ag	0.203	0.220	0.290	**0.153**	0.139	0.133
Cd	0.696	0.697	0.0131	**0.536**	0.485	0.423
In	0.0797	0.0813	0.0246	**0.0596**	0.0495	0.0474
Sn	1.48	1.55	1.72	**1.10**	1.03	0.90
Te	2.49	2.63	2.99	**1.86**	1.63	1.56
Cs	0.173	0.158	0.205	**0.126**	0.117	0.117
Ba	2.20	3.04	2.58	**2.34**	2.94	2.88
La	0.189	0.287	0.230	**0.275**	0.276	0.277
Ce	0.503	0.718	0.616	**0.717**	0.729	0.737
Pr	0.0824	0.1099	0.0993	**0.114**	0.117	0.119
Nd	0.428	0.537	0.508	**0.586**	0.591	0.607
Sm	0.144	0.166	0.167	**0.192**	0.198	0.203
Eu	0.0547	0.0590	0.0629	**0.0713**	0.0734	0.0766
Gd	0.212	0.230	0.257	**0.294**	0.313	0.341
Tb	0.0356	0.0387	0.0417	**0.0465**	0.0499	0.0541
Dy	0.243	0.266	0.280	**0.319**	0.339	0.365
Er	0.158	0.173	0.183	**0.202**	0.209	0.221
Tm	0.0243	0.0263	0.0281	**0.0328**	0.0331	0.0341
Yb	0.165	0.180	0.191	**0.214**	0.220	0.226
Lu	0.0242	0.0269	0.0285	**0.0325**	0.0325	0.0347
Hf	0.096	0.132	0.114	**0.139**	0.133	0.138
W	0.0934	0.0902	0.108	***0.219****	*28**	0.123
Re	0.0327	0.0339	0.0388	**0.0448**	0.0478	0.0445
Ir	0.409	0.428	0.405	**0.566**	0.559	0.497
Pt	0.787	0.812	0.973	**0.888**	1.01	0.997
Tl	0.136	0.143	0.00721	**0.107**	0.0892	0.0870
Pb	2.39	2.62	2.78	**1.78**	*4.22**	1.54
Th	0.0251	0.0529	0.0295	**0.0360**	0.0364	0.0366
U	0.0060	0.0135	0.00712	**0.00813**	0.00862	0.00831

Sample	Murchison	Murchison NC	Nogoya	Cold Bokkeveld	Jbilet Winselwan	Paris
Class	CM2	CM2	CM2	CM2	CM2	CM2
Na	875	871	4428	2929	3100	4596
Mg	121196	123113	118801	117003	123729	121863
Al	11438	12091	11873	11329	12395	11831
S	24536	26347	33440	28610	20625	34059
K	496	1411	517	451	518	419
Ca	11759	11525	11676	11773	10076	14082
Cr	3202	3300	3124	3033	3478	3160
Mn	1761	1860	1811	1756	1873	1776
Fe	218752	226411	222964	212063	235763	220044
Ni	12944	13376	14156	12670	14060	12967
P	996	1108	1001	950	1065	982
Ti	564	579	558	541	604	546
V	68.6	70.2	67.2	65.8	72.6	66.8
Co	600	612	604	576	649	590
Cu	136.2	142	149	140	147	140
Zn	192	201	196	190	209	205
Ga	6.81	7.10	6.91	6.78	7.31	6.95
As	1.85	1.90	1.85	1.87	1.94	1.68
Rb	1.63	1.39	1.80	1.68	1.32	1.66
Zr	4.74	4.89	4.86	4.57	5.69	4.59
Nb	0.368	0.389	0.374	0.354	0.391	0.349
Rh	0.166	0.165	0.164	0.159	0.197	0.155
Ag	0.123	0.133	0.237	0.162	0.132	0.133
Cd	0.422	0.422	0.356	0.379	0.498	0.432
In	0.0477	0.0477	0.0444	0.0445	0.0502	0.0490
Sn	0.99	0.92	0.96	0.88	0.94	0.97
Te	1.58	1.60	1.49	1.53	1.69	1.64
Cs	0.125	0.114	0.119	0.118	0.128	0.120
Ba	3.15	10.80	3.71	3.16	6.50	2.95
La	0.286	0.340	0.312	0.291	0.311	0.277
Ce	0.754	0.870	0.806	0.758	0.829	0.728
Pr	0.122	0.135	0.127	0.121	0.131	0.116
Nd	0.630	0.677	0.642	0.613	0.666	0.602
Sm	0.202	0.218	0.208	0.198	0.223	0.201
Eu	0.0775	0.0823	0.0773	0.0748	0.0834	0.0779
Gd	0.315	0.332	0.325	0.305	0.425	0.297
Tb	0.0507	0.0529	0.0517	0.0490	0.0712	0.0489
Dy	0.343	0.362	0.349	0.333	0.494	0.334
Er	0.222	0.233	0.226	0.209	0.297	0.215
Tm	0.0347	0.0358	0.0348	0.0335	0.0397	0.0339
Yb	0.232	0.239	0.229	0.224	0.248	0.226
Lu	0.0342	0.0359	0.0356	0.0331	0.0407	0.0338
Hf	0.139	0.147	0.146	0.135	0.166	0.135
W	0.122	0.122	0.135	0.137	0.149	0.132
Re	0.0409	0.0340	0.0450	0.0438	0.0339	0.0454
Ir	0.538	0.531	0.555	0.517	0.704	0.483
Pt	1.03	1.03	1.05	0.979	0.990	1.00
Tl	0.0853	0.0867	0.0779	0.0796	0.0937	0.0880
Pb	1.50	1.56	*3.65**	*2.74**	1.52	1.50
Th	0.0372	0.0495	0.0436	0.0415	0.0442	0.0340
U	0.00874	0.0161	0.0220	0.0104	0.0145	0.00808

Sample	ALH 85013	EET 96029	LON 94101	LON 94102	SCO 06043	MET 01070
Class	CM2	CM2	CM2	CM2	CM1	CM1
Na	4540	2355	4527	1319	1382	1131
Mg	120750	118046	118707	124398	115140	121547
Al	11824	12130	11289	12536	11893	12103
S	31663	36518	33174	30300	33556	36032
K	384	322	381	368	206	233
Ca	12902	15526	13006	12879	12682	10769
Cr	3113	3277	3080	3342	3170	3228
Mn	1760	1831	1774	1920	1768	1851
Fe	216872	220433	212228	232126	221805	226302
Ni	12931	14781	12750	13991	13245	14000
P	993	973	906	1060	971	1052
Ti	560	542	530	584	553	568
V	66.8	66.6	65.2	70.5	67.1	69.2
Co	578	617	563	632	595	616
Cu	138	137	138	149	141	151
Zn	182	199	194	214	194	203
Ga	6.78	6.78	6.51	7.65	6.96	7.24
As	1.79	1.73	1.79	1.94	1.73	1.91
Rb	1.65	1.49	1.58	1.76	1.44	1.67
Zr	4.78	4.48	4.72	4.68	4.74	4.86
Nb	0.359	0.352	0.359	0.380	0.370	0.369
Rh	0.161	0.164	0.156	0.166	0.163	0.164
Ag	0.115	0.125	0.122	0.138	0.123	0.131
Cd	0.389	0.416	0.405	0.454	0.410	0.419
In	0.0442	0.0474	0.0463	0.0515	0.0465	0.0483
Sn	0.84	0.87	0.86	0.97	0.91	1.00
Te	1.51	1.59	1.57	1.75	1.57	1.65
Cs	0.111	0.120	0.114	0.124	0.114	0.137
Ba	2.78	2.87	2.70	3.02	2.73	3.04
La	0.285	0.288	0.279	0.292	0.297	0.295
Ce	0.751	0.758	0.734	0.782	0.773	0.768
Pr	0.119	0.120	0.117	0.126	0.124	0.125
Nd	0.610	0.619	0.593	0.650	0.629	0.640
Sm	0.208	0.203	0.194	0.215	0.204	0.209
Eu	0.0758	0.0757	0.0722	0.0818	0.0773	0.0789
Gd	0.323	0.318	0.312	0.332	0.320	0.329
Tb	0.0514	0.0501	0.0499	0.0535	0.0517	0.0525
Dy	0.353	0.337	0.338	0.355	0.353	0.357
Er	0.227	0.213	0.218	0.221	0.224	0.224
Tm	0.0348	0.0341	0.0332	0.0358	0.0345	0.0349
Yb	0.230	0.228	0.221	0.244	0.230	0.234
Lu	0.0349	0.0333	0.0345	0.0347	0.0345	0.0355
Hf	0.140	0.134	0.141	0.138	0.142	0.143
W	*0.244**	0.118	0.125	0.129	0.125	*0.346**
Re	0.0464	0.0585	0.0471	0.0419	0.0475	0.0513
Ir	0.512	0.565	0.557	0.491	0.568	0.569
Pt	1.03	1.31	1.02	1.03	1.06	1.05
Tl	0.0770	0.0876	0.0825	0.0942	0.0831	0.0890
Pb	1.29	1.44	1.39	1.56	1.42	1.47
Th	0.0364	0.0354	0.0365	0.0366	0.0398	0.0378
U	0.00807	0.00928	0.00808	0.00875	0.00903	0.00871

Sample Class	**Median CM (n=14)**	Kainsaz CO3	ALHA 77307 CO3	**Median CO (n=2)**	Allende Smiths. CV3	Allende MS CV3
Na	**2642**	3650	1134	**2392**	3160	2684
Mg	**120973**	129570	108428	**118999**	149536	131991
Al	**11883**	12225	11097	**11661**	16669	15866
S	**32101**	16417	16325	**16371**	20756	19212
K	**382**	298	272	**285**	270	263
Ca	**12562**	13280	12783	**13032**	17789	17513
Cr	**3176**	3306	3111	**3209**	3603	3350
Mn	**1775**	1475	1479	**1477**	1465	1334
Fe	**220238**	233250	217135	**225192**	237784	225178
Ni	**13236**	13516	12002	**12759**	14197	13564
P	**988**	1063	1012	**1038**	1040	1041
Ti	**556**	656	601	**629**	806	769
V	**67.3**	81.3	73.5	**77.4**	92.6	94.7
Co	**597**	649	581	**615**	656	633
Cu	**140**	133	128	**130.3**	111	103
Zn	**197**	101	119	**109.8**	123	127
Ga	**6.86**	6.45	6.59	**6.52**	5.23	5.13
As	**1.83**	2.27	2.00	**2.14**	1.57	1.69
Rb	**1.60**	1.31	1.35	**1.33**	1.15	0.972
Zr	**4.73**	5.43	4.92	**5.18**	6.45	6.17
Nb	**0.368**	0.432	0.380	**0.406**	0.503	0.499
Rh	**0.163**	0.185	0.174	**0.180**	0.203	0.204
Ag	**0.132**	0.0719	0.0871	**0.0795**	0.097	0.0832
Cd	**0.420**	0.0222	0.251	**0.251**	0.491	0.265
In	**0.0476**	0.0241	0.0281	**0.0261**	0.0290	0.0290
Sn	**0.93**	0.497	0.621	**0.559**	0.67	0.685
Te	**1.59**	0.964	1.14	**1.051**	1.04	1.04
Cs	**0.119**	0.0831	0.0826	**0.0828**	0.080	0.0535
Ba	**2.98**	3.22	3.11	**3.17**	4.21	6.03
La	**0.290**	0.304	0.249	**0.276**	0.471	0.481
Ce	**0.758**	0.820	0.674	**0.747**	1.212	1.17
Pr	**0.122**	0.135	0.122	**0.128**	0.1909	0.191
Nd	**0.624**	0.721	0.671	**0.696**	0.998	0.974
Sm	**0.204**	0.245	0.220	**0.233**	0.328	0.311
Eu	**0.0773**	0.0901	0.0821	**0.0861**	0.1105	0.110
Gd	**0.321**	0.349	0.367	**0.358**	0.439	0.432
Tb	**0.0515**	0.0596	0.0551	**0.0573**	0.0735	0.0690
Dy	**0.351**	0.413	0.373	**0.393**	0.499	0.459
Er	**0.221**	0.259	0.240	**0.249**	0.304	0.291
Tm	**0.0346**	0.0397	0.0374	**0.0385**	0.0532	0.0511
Yb	**0.229**	0.272	0.250	**0.261**	0.327	0.312
Lu	**0.0346**	0.0404	0.0375	**0.0389**	0.0470	0.0443
Hf	**0.139**	0.160	0.145	**0.152**	0.191	0.178
W	**0.125**	0.142	0.115	**0.129**	0.171	0.136
Re	**0.0452**	0.0706	0.0535	**0.0621**	0.0531	0.0472
Ir	**0.546**	0.770	0.618	**0.694**	0.674	0.702
Pt	**1.03**	1.27	1.14	**1.20**	1.385	1.43
Tl	**0.0868**	0.0421	0.0476	**0.0448**	0.0622	0.0593
Pb	**1.50**	0.766	0.912	**0.839**	1.08	1.06
Th	**0.0369**	0.0415	0.0389	**0.0402**	0.0561	0.0586
U	**0.00874**	0.00947	0.00888	**0.0092**	0.0132	0.0141

Sample	Vigarano	**Median CV**	EET 96026	**ALH 85002**	GRA 95229	LAP 02342	**Median CR**
Class	CV3	**(n=3)**	C4/5	**CK4**	CR2	CR2	**(n=2)**
Na	2378	**2684**	3029	**2666**	2887	1697	**2292**
Mg	125352	**131991**	152989	**102692**	138660	108546	**123603**
Al	14226	**15866**	15821	**12535**	12414	11941	**12178**
S	17147	**19212**	7590	**14547**	10531	9717	**10124**
K	251	**263**	364	**202**	274	247	**261**
Ca	15890	**17513**	16576	**14596**	13554	13245	**13399**
Cr	3253	**3350**	3701	**3421**	3967	3759	**3863**
Mn	1343	**1343**	1565	**1359**	1713	1955	**1834**
Fe	222845	**225178**	245997	**227933**	245942	233253	**239597**
Ni	12935	**13564**	11411	**14880**	14685	12860	**13773**
P	1018	**1040**	1044	**1025**	877	928	**903**
Ti	735	**769**	760	**747**	609	685	**647**
V	82.7	**92.6**	88.1	**89.0**	73.3	72.4	**72.9**
Co	608	**633**	624	**661**	678	609	**644**
Cu	103	**103**	121	**100**	87.0	95.7	**91.3**
Zn	112	**123**	128	**82.8**	63.8	59.1	**61.4**
Ga	5.18	**5.18**	4.80	**4.51**	3.31	3.78	**3.54**
As	2.31	**1.69**	1.27	**1.63**	1.27	1.52	**1.39**
Rb	1.17	**1.15**	1.52	**0.55**	1.00	1.09	**1.04**
Zr	5.85	**6.17**	6.36	**5.61**	5.11	5.01	**5.06**
Nb	0.480	**0.499**	0.549	**0.502**	0.405	0.473	**0.439**
Rh	0.184	**0.203**	0.219	**0.213**	0.197	0.167	**0.182**
Ag	0.1184	**0.0966**	0.0763	**0.0546**	0.0399	0.0401	**0.0400**
Cd	0.0822	**0.2646**	0.0485	**0.214**	0.140	0.135	**0.138**
In	0.0274	**0.0290**	0.0100	**0.0222**	0.0149	0.0148	**0.0149**
Sn	0.708	**0.685**	0.124	**0.423**	0.300	0.302	**0.301**
Te	1.02	**1.04**	0.143	**0.610**	0.551	0.576	**0.563**
Cs	0.0816	**0.0804**	0.0606	**0.0481**	0.0586	0.0584	**0.0585**
Ba	4.97	**4.97**	3.83	**3.11**	2.95	3.24	**3.10**
La	0.396	**0.471**	0.386	**0.297**	0.325	0.265	**0.295**
Ce	1.03	**1.17**	1.02	**0.818**	0.838	0.741	**0.790**
Pr	0.171	**0.191**	0.168	**0.148**	0.134	0.130	**0.132**
Nd	0.897	**0.974**	0.879	**0.810**	0.679	0.702	**0.691**
Sm	0.301	**0.311**	0.290	**0.275**	0.224	0.241	**0.233**
Eu	0.102	**0.110**	0.105	**0.0888**	0.0841	0.0875	**0.0858**
Gd	0.399	**0.432**	0.429	**0.394**	0.350	0.344	**0.347**
Tb	0.0688	**0.0690**	0.0705	**0.0642**	0.0569	0.0572	**0.0570**
Dy	0.466	**0.466**	0.473	**0.436**	0.378	0.386	**0.382**
Er	0.275	**0.291**	0.302	**0.275**	0.242	0.249	**0.245**
Tm	0.0475	**0.0511**	0.0484	**0.0446**	0.0380	0.0402	**0.0391**
Yb	0.301	**0.312**	0.313	**0.285**	0.254	0.277	**0.266**
Lu	0.0430	**0.0443**	0.0481	**0.0475**	0.0377	0.0389	**0.0383**
Hf	0.178	**0.178**	0.190	**0.162**	0.155	0.149	**0.152**
W	0.175	**0.171**	0.175	**0.144**	0.184	0.116	**0.150**
Re	0.0513	**0.0513**	0.0200	**0.0466**	0.0591	0.0479	**0.0535**
Ir	0.645	**0.674**	0.724	**0.619**	0.720	0.583	**0.652**
Pt	1.27	**1.38**	1.26	**1.49**	1.32	1.03	**1.18**
Tl	0.0563	**0.0593**	0.0042	***BDL***	0.0272	0.0275	**0.0274**
Pb	*3.84**	**1.07**	0.0916	**0.75**	0.464	0.469	**0.466**
Th	0.0525	**0.0561**	0.0482	**0.0454**	0.0399	0.0410	**0.0404**
U	0.0156	**0.0141**	0.0112	**0.00978**	0.00957	0.0106	**0.0101**

* contaminated

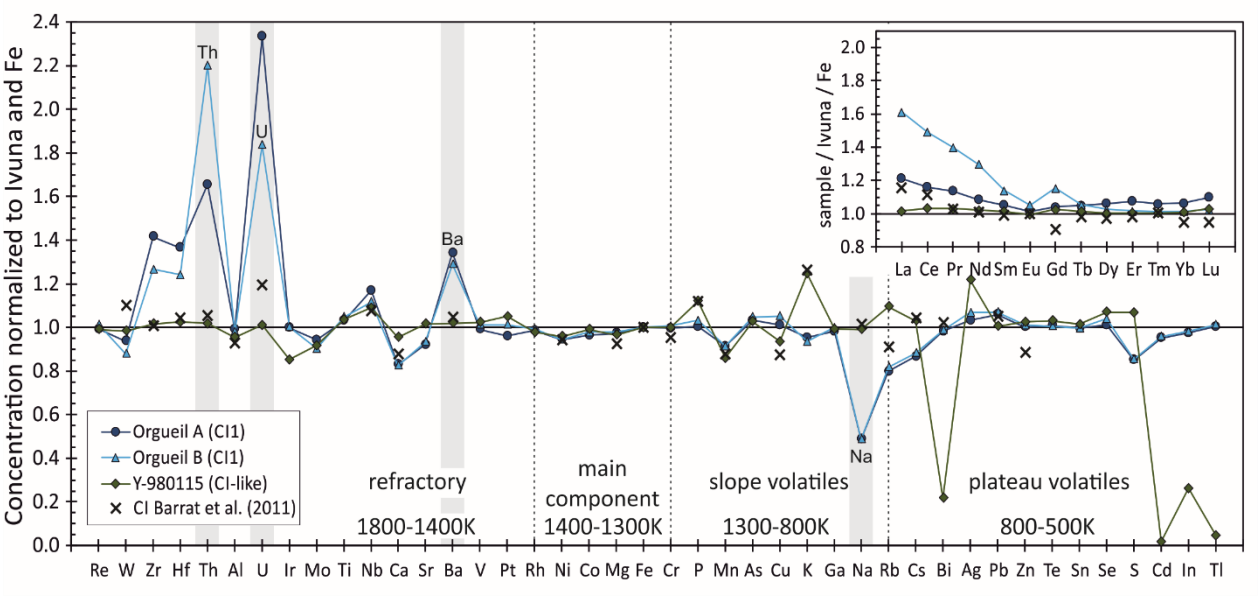

Figure 2.1: Bulk chemical composition of CI chondrite samples relative to Ivuna sample and normalized to Fe. Elements are arranged from left to right in order of decreasing 50% TC (Lodders, 2003; Kiseeva and Wood, 2015). The CI chondritic composition determined by Barrat et al. (2012) is plotted for comparison.

CI chondrite Y-980115

In addition to Orgueil and Ivuna we analyzed the Antarctic sample Y-980115, which is classified as a CI chondrite. Y-980115 has about typical CI element abundances (**Figure 2.1**) but K and Ag are slightly enriched (1.3x CI) and four of the most volatile elements (Bi, In, Cd and Tl) are strongly depleted (Bi: 0.21x CI, In: 0.26x CI, Cd: 0.02x CI, Tl 0.05x CI). The absolute water content of Y-980115 of 11.6 wt.% is significantly below the absolute water content of Orgueil (18.1 wt.%).

CM chondrites

One aim of this study is to test how terrestrial weathering affects the bulk chondrite composition. Therefore, we selected 13 CM chondrites, including five falls (incl. two different pieces of Murchison), six Antarctic finds, one hot desert find and the recently detected Paris meteorite, which was likely collected shortly after its fall (Haack et al., 2012) (**Table 2.1**). The Antarctic CM chondrites include two CM1 and four CM2 chondrites with various degrees of weathering (A to Ce). In addition, we analyzed Tagish Lake, an ungrouped C2 chondrite with strong chemical and textural affinities to the CM group (Friedrich et al., 2002).

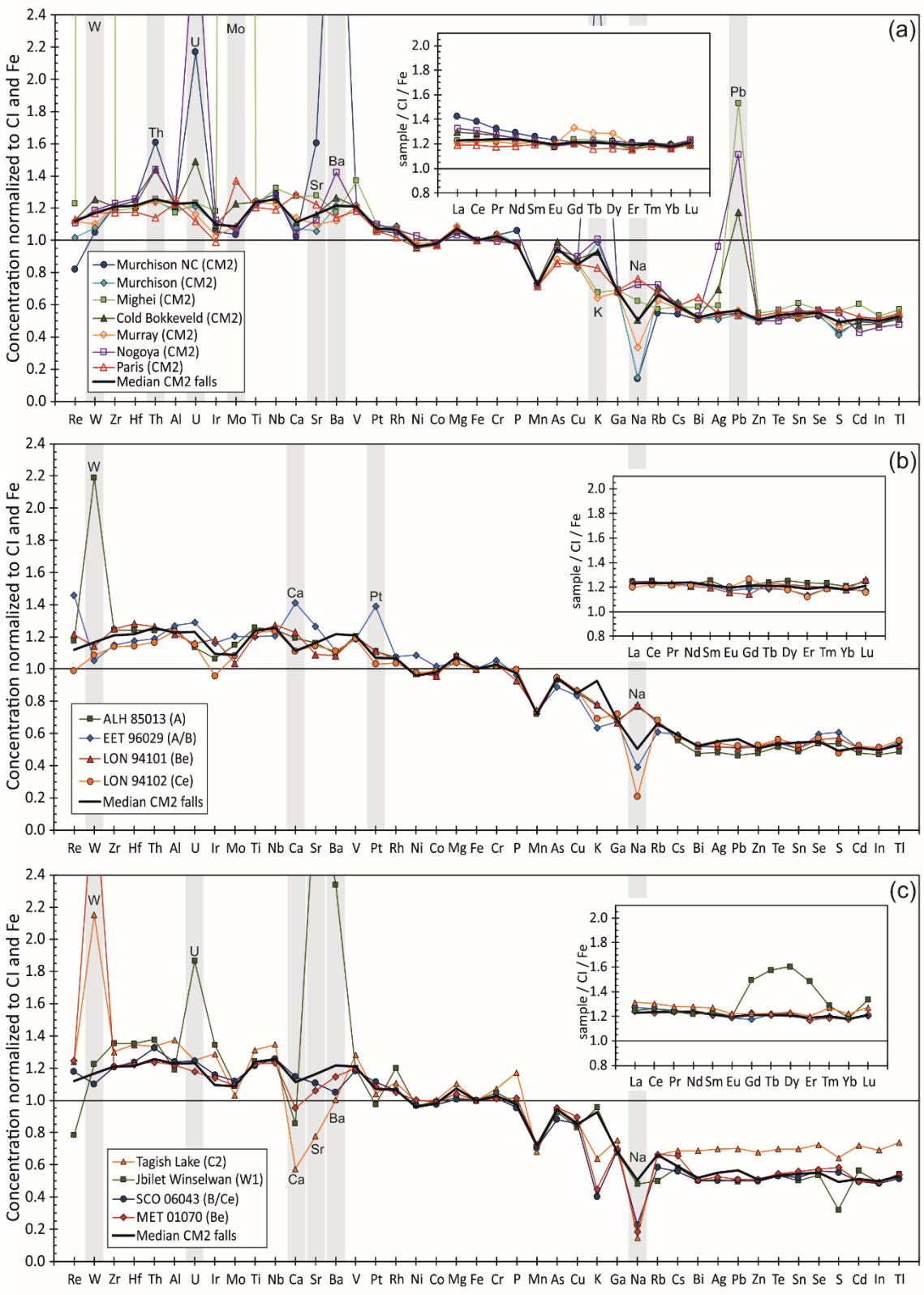

Figure 2.2: Bulk elemental composition of analyzed CM chondrites and Tagish Lake (C2) relative to CI as determined by our Ivuna analysis and normalized to Fe. Elements are arranged from left to right in order of decreasing 50% T_C (Lodders, 2003; Kiseeva and Wood, 2015). (a) CM2 chondrite falls. (b) Antarctic CM2 chondrites with different degree of weathering. (c) Antarctic CM1 chondrites, hot desert find Jbilet Winselwan and C2 chondrite Tagish Lake.

All analyzed CM chondrite samples have generally similar chemical compositions (**Figure 2.2**). We used the seven falls to calculate a representative CM median composition, which can be considered to be almost unaffected by terrestrial weathering. Refractory elements are generally enriched by a factor of 1.2x CI. The plateau volatile elements are homogeneously depleted by a factor of 0.63x CI. Rare Earth element (REE) patterns for the falls are flat except for Nogoya, Murchison NC and Cold Bokkeveld, which show slight light REE enrichments (**Figure 2.2a**). Absolute water contents of the CM chondrite falls vary between 10.3 wt.% and 15.6 wt.%.

A few elements deviate largely from the typical CM patterns in four of the seven CM falls (**Figure 2.2a**): Mighei is enriched in Pb (1.8x CI). Nogoya, and to a lesser degree Cold Bokkeveld, are enriched in Th (1.4x CI both), U (3x CI; 1.5x CI), Ag (1.0x CI; 0.7x CI) and Pb (1.5x CI; 1.2x CI) relative to the median CM composition. Both pieces of Murchison have the same low Na abundance (0.15x CI), but only Murchison NC is additionally enriched in Th (1.6x CI), U (2.2x CI), Sr (1.6x CI), Ba (4x CI) and K (2.7x CI).

The bulk compositions of the Antarctic CM2 samples are similar to the median composition of the CM2 falls with few exceptions. The REE patterns of all Antarctic CM chondrites are flat (**Figure 2.2b, c**). The K and Na abundances deviate significantly from the median. All four Antarctic CM2 samples are more depleted in K (0.63 - 0.78x CI) than the median (0.93x CI). Sodium is less depleted in ALH 85013 and LON 94101 (both 0.77x CI) and more depleted in EET 96029 (0.39 CI) and LON 94102 (0.21x CI) compared to the CM median (0.50x CI). Additionally, EET 96029 is enriched in Re (1.5x CI), Ca (1.4x CI) and Pt (1.4x CI). The Antarctic CM1 chondrites SCO 06043 and MET 01070 have the lowest K and Na abundances of the Antarctic CM samples (**Figure 2.2c**). Further, Ca is depleted in MET 01070 (0.95x CI), but not in SCO 06043. The absolute water contents of Antarctic CMs are in the same range as for the CM2 falls (**Table 2.1**).

The desert find Jbilet Winselwan is highly enriched in U, Sr, Ba, the heavy REEs Gd, Tb, Dy and Er (1.5 - 3x CI), and to a lesser extent in Zr, Hf, Th, Ir, Rh and Lu (1.4x CI) when compared to the median of the CM falls (**Figure 2.2c**). Calcium (0.86x CI) and the volatile elements Rb (0.50x CI,) and S (0.32x CI) are more depleted than the CM median.

The bulk chemical composition of the C2 chondrite Tagish Lake is similar and the REE pattern is indistinguishable from the CM median (**Figure 2.2c**). However, refractory element abundances are generally slightly higher (1.3x CI) and the fluid mobile elements Ca (0.57x CI), Sr (0.78x CI), Ba (1.0x CI) and Na (0.15x CI) are strongly depleted relative to CM median. The

plateau volatile elements are less depleted (0.70x CI) compared to the CM median. Tagish Lake has a slightly higher absolute water content of 16.5 wt.% than CM chondrites.

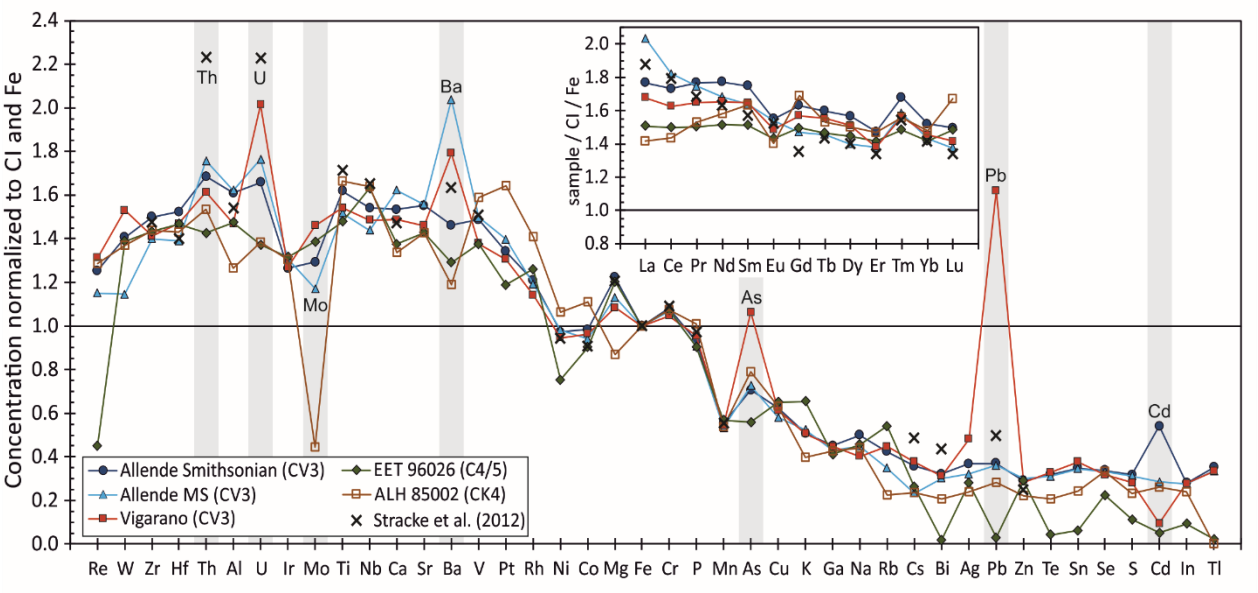

Figure 2.3: Bulk elemental composition of analyzed CV and CK chondrites including EET 96026 (C4/5) relative to CI as determined by our Ivuna analysis and normalized to Fe. Elements are arranged from left to right in order of decreasing 50% T_C (Lodders, 2003; Kiseeva and Wood, 2015). Data from Stracke et al. (2012) for the Allende Smithsonian powder are included for comparison.

The large, non-systematic enrichments of W in Mighei (CM2), ALH 85013 (CM2), MET 01070 (CM1) and Tagish Lake (C2) are most likely the result of high beaker blanks. In case of Mighei, the extreme W enrichment (250x CI) is accompanied by a large Mo enrichment (25x CI). Both enrichments most likely also result from sample preparation.

CV and CK chondrites

In addition to the Allende Smithsonian powder discussed above, we analyzed another Allende split – Allende MS (about 10 g homogenized powder prepared in Münster; Münker et al., 2003) – and the reduced CV3 chondrite Vigarano. The bulk compositions of all three samples are almost identical. Abundances of the refractory elements are strongly variable (1.2 - 1.7x CI) due to the ca. 3 vol.% CAIs in CV chondrites (Hezel et al., 2008). The plateau volatile elements are homogeneously depleted by 0.32x CI (**Figure 2.3**). An exception is Cd, which is enriched in the Allende Smithsonian powder (0.54x CI), but depleted in Vigarano (0.09x CI), relative to the other volatile elements. Vigarano and Allende MS, show enrichments of Ba (1.8x CI; 2.0x CI, respectively), and Vigarano is also enriched in U (2.0x CI), As (1.1 CI) and Pb (1.6x CI).

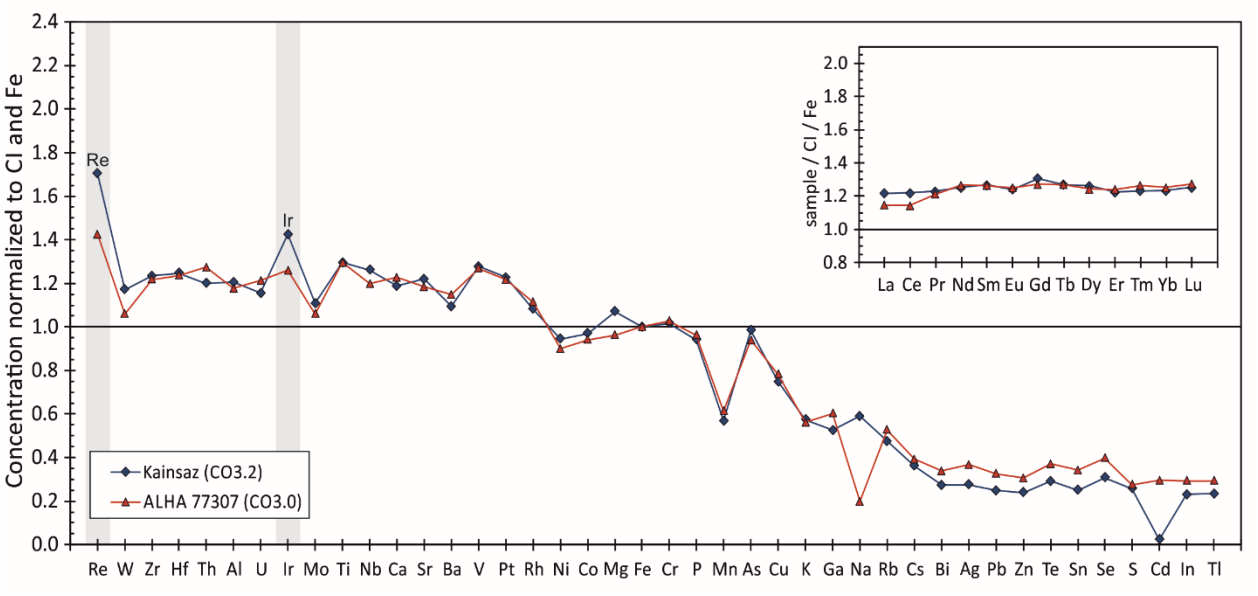

Figure 2.4: Bulk elemental composition of analyzed CO chondrites relative to CI as determined by our Ivuna analysis and normalized to Fe. Elements are arranged from left to right in order of decreasing 50% T_C (Lodders, 2003; Kiseeva and Wood, 2015).

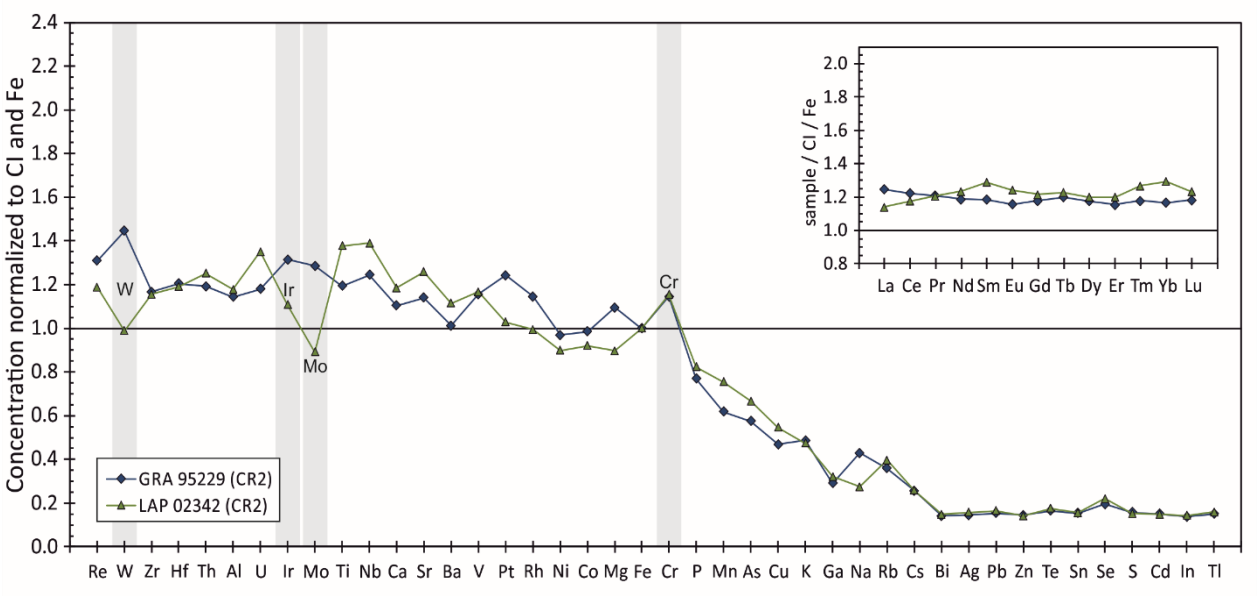

Figure 2.5: Bulk elemental composition of analyzed CR chondrites relative to CI as determined by our Ivuna analysis and normalized to Fe. Elements are arranged from left to right in order of decreasing 50% T_C (Lodders, 2003; Kiseeva and Wood, 2015)

The Antarctic chondrite EET 96026, which strongly resembles CV and CK chondrites in composition (Noronha and Friedrich, 2014), has the same abundance of refractory and main component elements as CV chondrites. Only Re (0.45x CI) and Ni (0.75x CI) are depleted (**Figure 2.3**). Its plateau volatile element abundances are exceptional, as these do not form a plateau, and are significantly more depleted than in all other analyzed CV chondrites (**Figure**

2.3). Only the Zn abundance is similar to CV chondrites. Absolute water contents are <1 wt.% in both Allende samples and EET 96026. Vigarano has a higher water content of 2.4 wt.%.

Overall, the CK chondrite ALH 85002 has fairly similar element abundances as the CV chondrites. Notably, Mo is strongly depleted, and Mg to a lesser degree, relative to CV chondrites (**Figure 2.3**). The plateau volatile elements are consistently more depleted than in CV chondrites (0.25x CI), except for Se, which is at CV level and Tl which is below the detection limit. The sample contains no detectable amount of water.

Rare Earth element patterns of bulk CV and CK chondrites are similar. Most patterns show negative Eu anomalies and all display positive Tm anomalies (**Figure 2.3**). Allende MS is generally enriched in LREE and provides the only CV/CK sample where no Eu anomaly is observed. The fractionation of REEs is smallest in the Antarctic sample EET 96026. The CK chondrite ALH 85002 is depleted in LREE and enriched in Lu.

CO chondrites

The bulk compositions of both CO chondrites are almost identical. Refractory elements are enriched by a factor of 1.2x CI, similar to CM chondrites, whereas the plateau volatile elements are depleted by a factor of 0.25x CI in Kainsaz (CO3.2) and 0.33x CI in the more primitive ALHA 77307 (CO3.0) (**Figure 2.4**). Kainsaz is significantly depleted in Cd (0.02x CI) and also contains less water (4 wt.%) than ALHA 77307 (6.4 wt.%). The Antarctic sample ALHA 77307 is depleted in Na (0.20x CI, compared to 0.59x CI in Kainsaz) (**Figure 2.4**). The REE patterns are flat in both samples.

CR chondrites

The two analyzed CR chondrites are petrographically very similar (Schrader et al., 2011) and also have almost identical bulk compositions (**Figure 2.5**). Generally, refractory elements are enriched by a factor of 1.2x CI, similar to CM and CO chondrites, however, the W abundance is high in GRA 95229 (1.4x CI) and CI-like in LAP 02342 (0.99x CI). Iridium and Mo are less enriched in LAP 02343 (1.1x CI and 0.90x CI, respectively), while Ti and Nb are more enriched (1.4x CI). The REE patterns for both samples are flat (**Figure 2.5**). The main component elements are slightly below CI in LAP 02342 (0.90x CI) but both CR chondrites display a positive Cr anomaly (1.2x CI). The plateau volatile elements are homogeneously depleted in both samples (0.15x CI). The absolute water content of GRA 95229 is 4.4 wt.% and that of LAP 02342 is 3 wt.%.

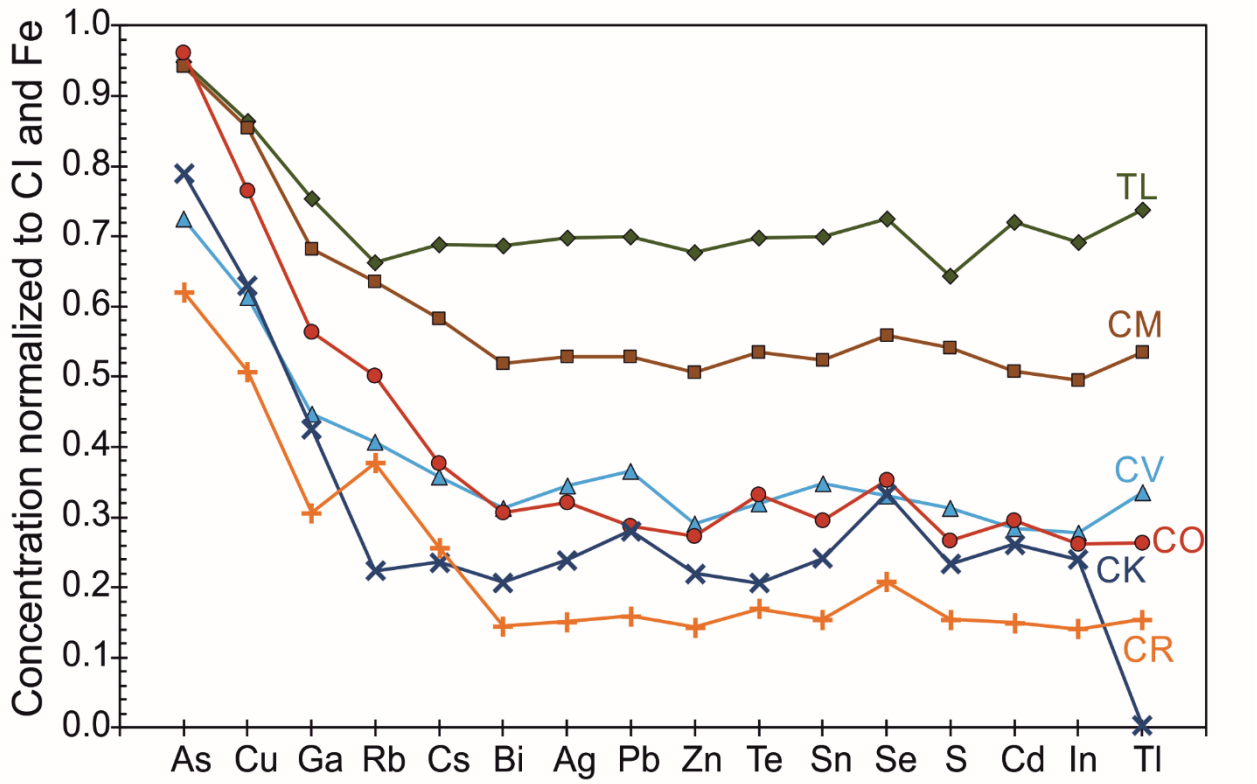

Figure 2.6: Median volatile element depletion relative to CI and normalized to Fe for the different carbonaceous chondrite groups analyzed. Elements are arranged from left to right in order of decreasing 50% T_C (Lodders, 2003; Kiseeva and Wood, 2015). The fluid mobile elements Na and K are not taken into account because their abundances can be severely affected by alteration and weathering processes. TL = Tagish Lake.

2.3.3 Murchison heating experiments

In **Figure 2.7** and **2.8**, element ratios of heated to unheated Murchison samples are displayed. No element loss has been observed up to 400°C (**Table A7**). At higher temperatures and depending on O-fugacity, elements start to evaporate. At reducing conditions Bi, Pb, Sn, Zn, In and Cd are progressively lost with increasing temperature (**Figure 2.8**). Cadmium is already substantially depleted at 600°C. Depletion of the other elements commences in the 800°C run. At oxidizing conditions, the refractory elements Re, Ir and Pt are substantially depleted at 800 and 1000°C (**Figure 2.7b, c**). The chalcophile volatile element Se already starts to evaporate at 600°C (~25% loss), and is almost entirely lost at 1000°C, where only 15% of the initial Se content is left. Sulfur, Tl, Ag and Te are volatilized at both reducing and oxidizing conditions. In the 600 and 800°C runs, S is evaporated to the same extent at both conditions, while in the 1000°C run it is almost completely lost at oxidizing conditions, but not at reducing conditions (**Figure 2.7c**). Thallium shows no volatilization at 600°C at reducing conditions, but is almost completely volatilized at 800°C and 1000°C. At oxidizing conditions, Tl is depleted by 20% at 800°C and 40% at 1000°C. Tellurium is depleted substantially at both reducing (80%) and oxidizing conditions (60%) at 1000°C. Silver is lost at 1000°C at reducing conditions (70%)

and to a lesser extent at oxidizing conditions (15%). Our results confirm previous observations in similar studies, such as those of Matza and Lipschutz (1977) or that of (Wulf et al., 1995).

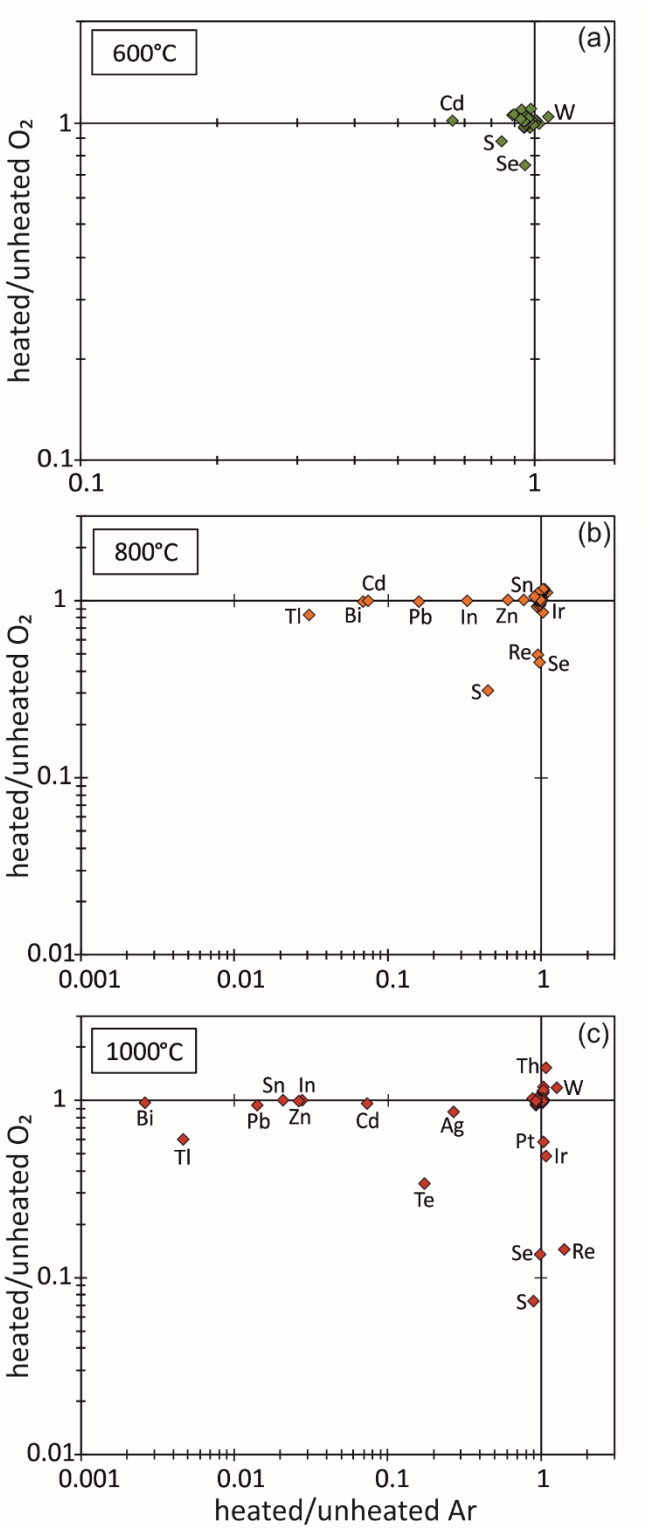

Figure 2.7: Results of heating experiments in either Ar or O_2 atmosphere at (a) 600 °C, (b) 800 °C and (c) 1000 °C.

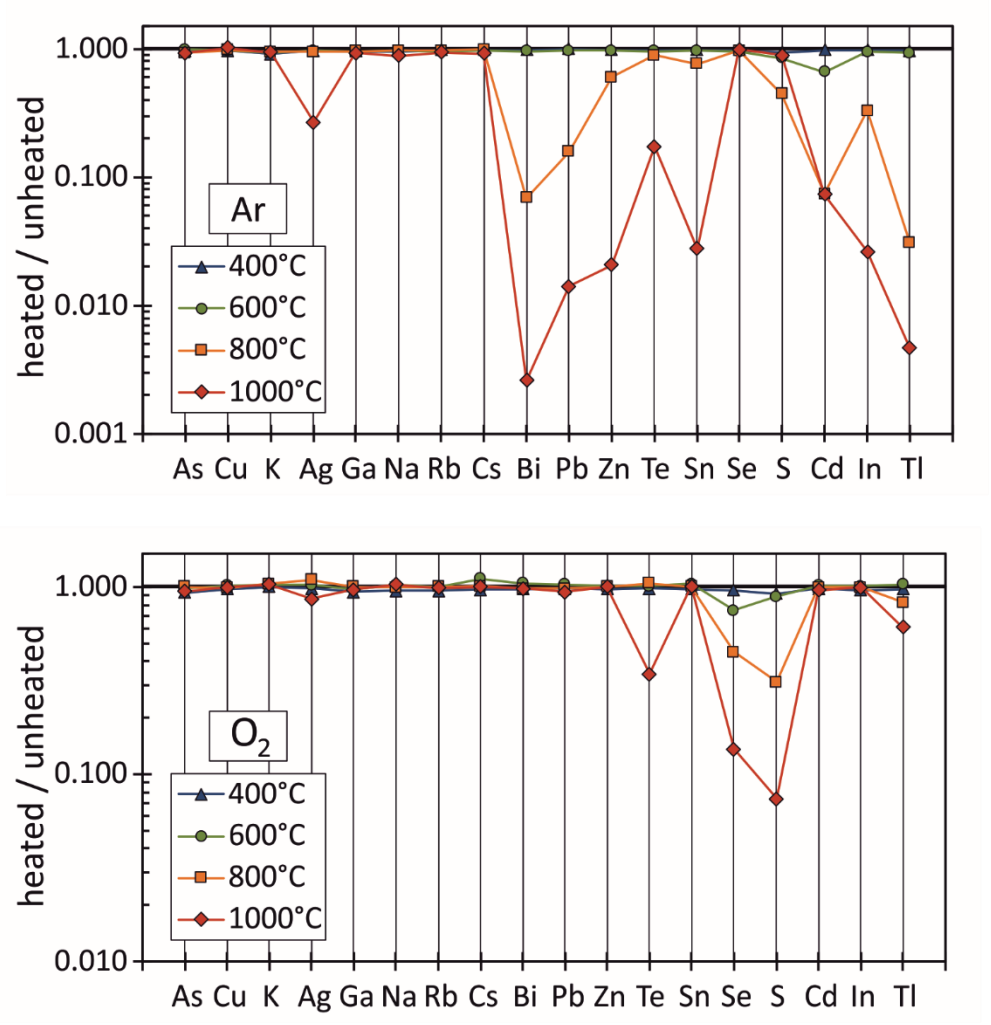

Figure 2.8: Logarithmic representation of volatile element loss during heating experiments at different temperatures in either Ar atmosphere (a) or O_2 atmosphere (b). Elements arranged from left to right in order of decreasing 50% T_C (Lodders, 2003).

2.4 DISCUSSION

It is long known that volatile element abundances decrease with decreasing condensation temperature in most carbonaceous chondrites (e.g., Wasson and Chou, 1974; Wai and Wasson, 1977; Davis, 2006; Palme et al., 2014a; Palme et al., 2014b). It has also been noted that volatile elements with 50% T_C between about 800 K and 500 K in individual chondrites are depleted to the same extent (e.g., Takahashi et al., 1978b; Wolf et al., 1980). The plateau volatile elements as shown in **Figure 2.6** exhibit entirely flat patterns, i.e., the regression through these in each group has a slope of zero within error (**Table 2.3**). This implies that the plateau volatile elements always occur at relative CI chondritic abundances. This observation is a unique characteristic and we therefore propose to recognize the plateau volatile elements as a separate subgroup of the moderately volatile elements, for which we suggest the above introduced designation 'plateau volatile elements'.

2.4.1 Primary volatile element depletion during the protoplanetary disk stage

Each chondrite group has a characteristic depletion of plateau volatile elements (**Figure 2.6**): Tagish Lake (C2) has the highest plateau volatile element abundances, followed in abundance by: CM>CV=CO>CK>CR. This sequence differs from the one reported in Bland et al. (2005), who placed CR chondrites between CMs and CVs. This difference might be related to within-chondrite variabilities. Kallemeyn et al. (1991) reported significant variations in the plateau volatile element depletion among the members of the CR chondrite group (see also Fig. 6 in Wombacher et al., 2008). Hence, some deviation from the above sequence may exist for individual samples.

Table 2.3: Median CI and Fe normalized abundances of plateau volatile elements and slope of the regression through these deduced from data of **Table 2.2**.

Class	CI and Fe normalized abundances		
	Median Bi → Cd	SD	slope
Tagish Lake	0.70	0.02	0.0021
CM	0.53	0.02	-0.0002
CV	0.32	0.03	-0.0034
CO	0.30	0.03	-0.0039
CK*	0.24	0.04	-0.0087
CR	0.15	0.02	0.0003

*without Tl

The plateau volatile element abundances cannot simply be explained by the partial condensation model of Wasson and Chou (1974) and Wai and Wasson (1977) as the depletion trend observed for the slope volatile elements would be expected to continue throughout the plateau volatile elements. We hypothesize that the unfractionated plateau volatile element abundances are best explained by adding material with unfractionated plateau volatile element abundances to each chondrite.

CI-like material in all carbonaceous chondrites

The unfractionated plateau volatile elements would be consistent with the presence of CI-like material in all carbonaceous chondrite groups as suggested by Alexander (2005). **Figure 2.9** shows a remarkably good co-variation of carbonaceous chondrite matrix abundances (in vol.%) with the median of their CI- and Fe-normalized plateau volatile element abundances. Only CKs fall off this trend – this group either has lower volatile abundances or too much matrix material. Chondrules and CAIs are difficult to identify in CK chondrites, due to their high degree of

thermal metamorphism (e.g., Hezel et al., 2008; Chaumard and Devouard, 2016; Dunn et al., 2016). The affinity of CK to CV chondrites makes it plausible to assume that CK chondrites initially contained similar amounts of matrix as CV chondrites. If true, CKs also had matrix contents of about 30 - 40 vol.% and would fall close to the co-variation defined by the other chondrite groups (**Figure 2.9**).

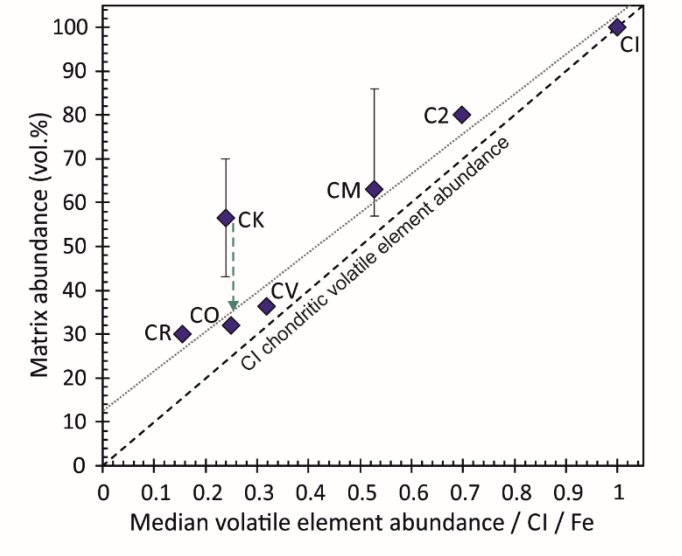

Figure 2.9: Median plateau volatile element abundance vs. matrix content of the analyzed carbonaceous chondrite groups in vol.%. Matrix abundance errors are displayed when reported in the literature. The error bar for CM chondrites spans the range of matrix abundances of the different samples analyzed. For ALH 85002 (CK) no matrix abundance data are available. The symbol therefore represents the average matrix abundance observed in CK chondrites in the literature. Matrix abundances are difficult to determine, and might be off by several %. Matrix abundance values: McSween (1979), Alexander et al. (2007), Wasson (2008), Pizzarello et al. (2012), Marrocchi et al. (2014). The grey dotted line represents the best fit line excluding CK chondrites. The green arrow points towards the assumed original matrix abundance in CK chondrites.

Matrix abundances in CM chondrites vary substantially (**Figure 2.9**), from 55 vol.% in Paris (Hewins et al., 2014) to 85 vol.% in Nogoya (McSween, 1979). This variation should be reflected in variable degrees of plateau volatile depletions, which is not the case. The depletion of plateau volatiles is the same for all CM chondrites (**Figure 2.2**). However, CM matrix abundances correlate positively with the degree of aqueous alteration (McSween, 1979). Based on this observation, McSween (1979) argued that the variations in matrix abundances in CM chondrites result from the degradation of chondrules during aqueous alteration. If true, then the CM primary matrix content can be approximated by the least altered sample, which in our case is Paris with 55 - 63 vol.% (Hewins et al., 2014; Marrocchi et al., 2014). Using these values, all CM chondrites plot close to the covariation defined by the other chondrite groups. Hence, carbonaceous chondrite matrix abundances covariate with plateau volatile element abundances, suggesting a relationship between the CI-like material and chondrite matrices.

However, it is known that the composition of chondrite matrices is not CI chondritic (e.g., Bland et al., 2005; Abreu and Brearley, 2010). Furthermore, the chondrule/matrix complementarity suggests that matrix and chondrules formed from the same reservoir, and cannot be arbitrary mixtures of materials from different regions in the solar nebula (Hezel and Palme, 2010; Palme et al., 2015; Ebel et al., 2016).

In **Figure 2.9**, all carbonaceous chondrite groups plot slightly to the left of the 1:1 line, indicating that the matrix abundances are higher than expected from the plateau volatile element abundances. Therefore, carbonaceous chondrite matrices are possibly mixtures of two components (Jacquet et al., 2016). One component could be CI-like material and the second a volatile element depleted matrix material related to chondrule formation, i.e., that formed contemporaneously with chondrules from the same reservoir. Addition of the CI-like material would then only change the Mg/Si of the bulk matrix, while the bulk chondrite would keep a CI chondritic Mg/Si. This is because CI-like material is mixed with an association of chondrules and fine-grained matrix material that together also has a CI chondritic Mg/Si (**Figure 2.10** and Figure 12 in Jacquet et al., 2016).

To evaluate the possibility of having two matrix components, we carried out mass balance calculations based on Mg and Si concentrations of: (i) chondrules, (ii) chondrule-related matrix, and (iii) CI-like material. The abundance of the CI-like material is constrained by the abundance of the plateau volatile elements in each group. Calculated Mg/Si of the chondrule-related matrix lies between 0.35 and 0.47 (**Figure 2.11**). Bulk Mg and Si concentrations of CM, CV, CO and CR chondrites can be reproduced by the mass balance calculation (**Figure 2.11**). Therefore, the addition of CI-like material to the chondrule-related matrix might explain both: chondrule-matrix complementarity and bulk CI chondritic ratios of plateau volatile elements (**Figure 2.10**). A likely scenario for such an admixture of CI-like material was recently proposed by Goldberg et al. (2015) on the basis of numerical investigations. Certainly, more complex models that take into account refractory and slope volatile element abundances and matrix and chondrule densities are required to further evaluate this model proposed here.

The CI chondritic plateau volatile element ratios suggest that part of the matrix in carbonaceous chondrites – the CI-like material – has never been substantially heated. Partial evaporation would lead to a fractionated volatile element pattern as observed in our heating experiments (**Figure 2.8**). Several authors suggested that carbonaceous chondrites originated from beyond Jupiter (e.g., Wood, 2005; Gounelle et al., 2008; Rubin, 2010; Warren, 2011) where temperatures were too low for a hot solar nebula that could account for the observed depletion trend via partial condensation (Ciesla, 2008). Further, all carbonaceous chondrites contain presolar grains, which cannot survive a hot solar nebula stage (Huss et al., 2003; Davidson et al., 2014). Matrix-normalized abundances of presolar SiC are at CI level for most unheated chondrites (Davidson et al., 2014). Together with the unfractionated plateau volatile element

ratios in carbonaceous chondrites this is a strong evidence for a thermally unprocessed, probably CI-like material.

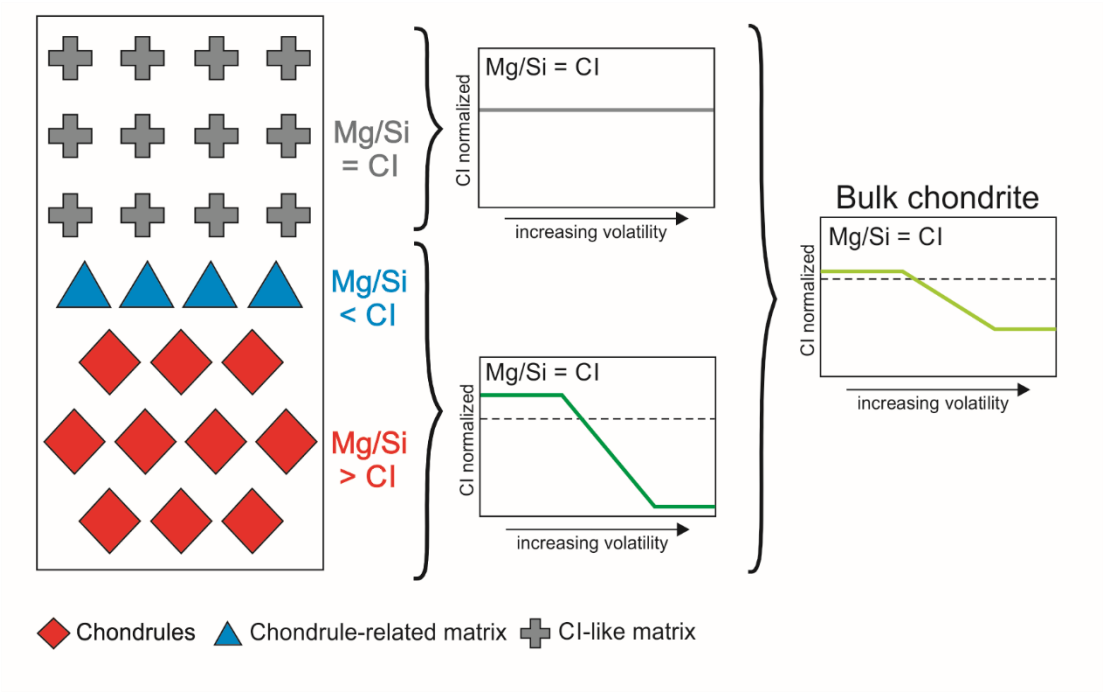

Figure 2.10: Schematic overview of mixing between chondrite components modified after Jacquet et al. (2016). Chondrules and chondrule-related matrix stem from the same reservoir with CI chondritic refractory and main component element ratios (e.g. Mg/Si). They have complementary Mg/Si ratios and both components became depleted in volatile elements during chondrule formation. The addition of CI-like material to the matrix does not affect the bulk Mg/Si ratio, but adds most of the plateau volatile elements to the chondrite.

Partial condensation with dissipation of the vapor phase produces a depletion trend that correlates with volatility (Wasson and Chou, 1974; Wai and Wasson, 1977), and could thereby explain the slope volatile element depletion pattern (from about P to Cs in Fig. 1 - 5). This trend, however, might alternatively be explained by partial recondensation after chondrule formation. We suggest that during chondrule cooling, right after their formation, slope volatile elements partially recondensed, while the plateau volatiles were almost entirely lost. Numerous evidence for evaporation from chondrules have been published (e.g., Kong and Palme, 1999; Alexander, 2004; Davis et al., 2005; Hezel and Palme, 2010; Fedkin et al., 2012). The CI-like material was then added to the matrix after chondrule formation ceased, thereby achieving the plateau volatile element content of the bulk samples. Alternatively, chondrules and the CI-like material formed from the same CI chondritic reservoir, but only a fraction survived as CI-like material with the full complement of plateau volatile elements.

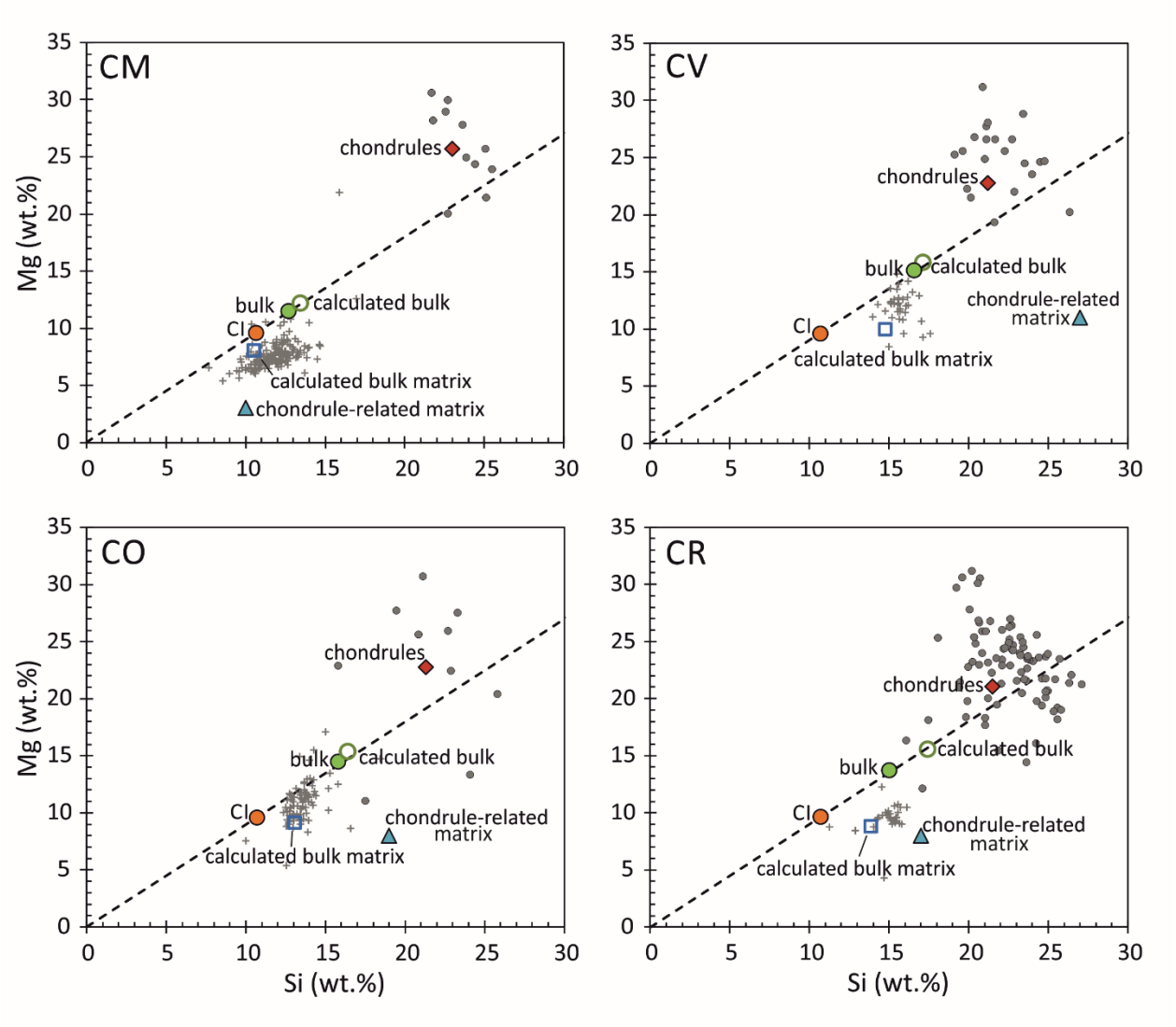

Figure 2.11: Mass-balance calculation for reconciling the presence of CI-like material in chondrite matrices with Mg/Si complementarity between chondrules and bulk matrix. The calculated bulk matrix composition represents mixing of the two matrix components in their respective proportions, while the calculated bulk chondrite composition is the result of mixing all CI-like material with chondrules and chondrule-related matrix. The abundance ratios of CI-like material/chondrule-related matrix are as follows: CM: 3.3, CV: 3, CO: 2.5, CR: 1. Magnesium and Si concentrations for bulk chondrites, bulk matrix and chondrules are taken from Hezel and Palme (2010). Bulk matrix abundances are the same as in **Figure 2.9** and chondrule abundances are from Scott and Krot (2014)

CI-like material and stable isotopes

If all carbonaceous chondrite matrices contain CI-like material, the abundance of this material is expected to correlate with mass-independent isotope variations in the different groups. This is indeed the case for e.g. $\Delta^{17}O$ and $\varepsilon^{54}Cr$ for all groups except for CR chondrites (**Figure 2.12a, b**). The diverse $\Delta^{17}O$ and $\varepsilon^{54}Cr$ compositions of the different groups can actually be explained by two-endmember mixing between chondrules/chondrule-related matrix and the CI-like material. In particular, this two-endmember mixing potentially explains the correlation between $\Delta^{17}O$ and $\varepsilon^{54}Cr$ for carbonaceous chondrites (Warren, 2011). However, values for $\Delta^{17}O$ and $\varepsilon^{54}Cr$ in CR chondrites suggest a considerably higher amount of CI-like material than the

amount deduced here from plateau volatile element abundances and therefore cannot be explained by the same two-endmember mixing.

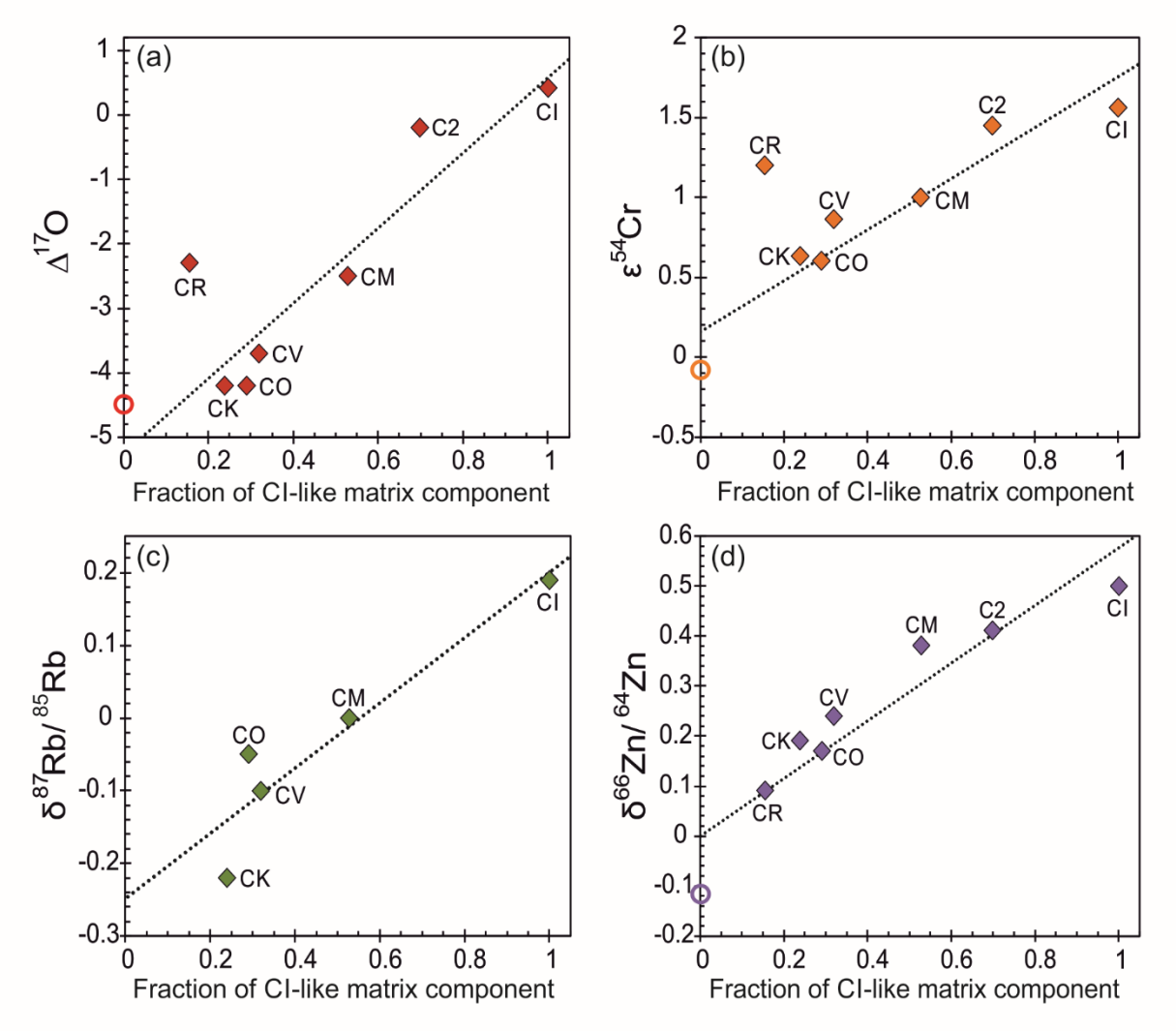

Figure 2.12: Stable isotope compositions in carbonaceous chondrites vs. CI and Fe-normalized plateau volatile element abundance from **Figure 2.6**. Variations of mass-independent (a, b) and mass-dependent isotope systems (c, d) display a linear relationship with the fraction of the CI-like material and thus can be explained by two-endmember mixing between CI-like material and chondrule/chondrule-related matrix. However, high Zn abundances in chondrules suggest more complexity (see text for discussion). Open circles in a, b and d represent the isotope composition of chondrules. $\Delta^{17}O = \delta^{17}O - 0.52\ \delta^{18}O$; $\varepsilon^{54}Cr = 10^4 \times [(^{54}Cr/^{52}Cr)_{sample}/(^{54}Cr/^{52}Cr)_{terrestrial\ standards} - 1]$, normalized to $^{52}Cr/^{50}Cr$; $\delta^{87}Rb = 10^3 \times [(^{87}Rb/^{85}Rb)_{SRM984\ or\ BCR\text{-}2} - 1]$; $\delta^{66}Zn = 10^3 \times [(^{66}Zn/^{64}Zn)_{sample}/(^{66}Zn/^{64}Zn)_{JMC\ Lyon} - 1]$. Data sources: Luck et al. (2005), Trinquier et al. (2007), Yin et al. (2009), Schrader et al. (2011). Pringle et al. (2017), Pringle and Moynier (2017), Mahan et al. (2018).

To test whether the presence of CI-like material in all chondrites is in agreement with the chondrule-matrix complementarity observed for several isotope systems, such as W, Mo and Ca (Becker et al., 2015; Budde et al., 2016a, 2016b; Amsellem et al., 2017), we carried out further mass balance calculations. Based on the concentration of W determined here in CI chondrites (93 ng/g) and the average W concentrations in chondrules (97 ng/g) and bulk matrix (201 ng/g) of Allende (CV3) from Becker et al. (2015) and Budde et al. (2016b), we calculated a W concentration of ~520 ng/g for the chondrule-related matrix. This high W abundance for

the chondrule-related matrix is in line with metal-sulfide separation during chondrule formation (e.g., Bland et al., 2005; Budde et al., 2016a). If we assign an $\varepsilon^{183}W$ value of -1.8 to the chondrule-related matrix, we can roughly reproduce the bulk chondrite $\varepsilon^{183}W$ and the average bulk matrix $\varepsilon^{183}W$ (**Figure A2**). Thus, the proposed model is not in conflict with the chondrule-matrix complementarity suggested by W isotopes.

Regarding mass-dependent isotope compositions of moderately volatile elements, we need to distinguish between slope and plateau volatile elements. Slope volatile element abundances depend only in part on the amount of CI-like material added. The slope volatile elements Cu, Ga and Rb (**Figure 2.12c**) e.g., show increasingly light isotope enrichments with decreasing abundance of the proposed CI-like material (Luck et al., 2003; Kato and Moynier, 2017; Pringle and Moynier, 2017). These trends could be explained by mixing between a heavy CI-like endmember and a light chondrule/chondrule-related matrix endmember similar to the multi-component mixing model suggested by Luck et al. (2003). In our model, chondrules and chondrule-related matrix are expected to be almost devoid of plateau volatile elements. Therefore, the isotope composition of plateau volatile elements should be CI chondritic for all carbonaceous chondrite groups. For $\delta^{114/110}Cd$, no clear variations between carbonaceous chondrites have been resolved, except for occasional variations that are considered to be of secondary origin (Wombacher et al., 2008; Baker et al., 2010b). For $\delta^{82/78}Se$, Vollstaedt et al. (2016) also observed no stable isotope variations, whereas Labidi et al. (2018) suggest that $\delta^{82/78}Se$ in Orgueil (CI) and Murchison (CM) is about 0.2 to 0.3 ‰ heavier than the uniform values observed for other carbonaceous and ordinary chondrites. Likewise, $\delta^{130/125}Te$ displays an offset between CI-CM and CO-CV chondrites (Fehr et al., 2018). More strikingly, Zn stable isotopes in carbonaceous chondrite groups display a trend towards lighter isotope compositions with increasing Zn depletion, as shown in **Figure 2.12d** (Luck et al., 2005; Pringle et al., 2017). Notably, Pringle et al. (2017) have reported light Zn isotope compositions for chondrules in two CV3 chondrites. Therefore, $\delta^{66}Zn$ variations in the different bulk chondrite groups could also be explained by mixing of chondrules/chondrule-related matrix with CI-like material. However, this scenario would imply that a considerable amount of Zn resides in chondrules and chondrule-related matrix. Indeed, Zn concentrations of ~50 µg/g in chondrules of CV chondrites suggests that roughly 25 % of the Zn inventory in CV chondrites stems from chondrules (Palme et al., 2014b; Pringle et al., 2017). Likewise, light Cd isotope compositions and high Cd concentrations of ~100 to 300 ng/g were observed in Allende chondrule separates (Wombacher et al., 2008), which compares with 265 ng/g Cd for bulk Allende. This substantial amount of Zn, Cd and possibly other plateau volatile elements in chondrules should actually

affect the flatness of the plateau, which is surprisingly not the case. Therefore, the inventory of Zn and Cd is apparently not exclusively associated with the CI-like material. The observation that a significant amount of Zn and Cd resides in chondrules either suggests that (i) all plateau volatile elements are hosted to a similar extent in chondrules or (ii) that only the correct mix between chondrules and matrix material results in the observed flat plateau. Notably, Bland et al. (2005) previously suggested that volatile elements are unevenly distributed between chondrules and matrix and that only a complementary mix between chondrules and matrix results in the smooth depletion of volatile elements (a plateau was not recognized in their study).

An unfractionated volatile rich component

In an alternative scenario to the model proposed above, a yet unknown component with flat plateau volatile element abundances and depleted refractory and main component elements could have been added to initially volatile-depleted chondrules and matrix. A plateau volatile element enriched component could indeed have formed during the molecular cloud stage. Yin (2005) shows that in the ISM refractory elements are almost entirely concentrated in dust grains, while plateau volatile elements are completely in the gas phase. Slope volatile elements are partially condensed in dust grains. During the molecular cloud stage, interstellar matter is sufficiently cold for all volatile elements to condense along with ices onto more refractory dust grains (Yin, 2005). When the cold molecular cloud collapses, these ices may be destroyed by adiabatic compression or passage through a shock wave (Yin, 2005). The proportion of accreted dust grains and ices could be different for all chondrite groups and reflects the degree of volatile element depletion. CI chondrites would have to accrete solely grains with a fully complementary budget of icy mantles in order to explain their solar composition in non-atmophile elements. The distribution of elements between dust grains and ices depending on their volatility would thus provide a mechanism to create a refractory element depleted component with CI chondritic volatile element abundances. However, the addition of such a component does not explain the remarkably good co-variation between matrix abundances and volatile element depletion in **Figure 2.9**. It would be a very unlikely coincidence, that this volatile-rich component was always added to the matrices of different carbonaceous chondrite groups at about the same relative proportion.

2.4.2 Secondary modifications of the volatile element budget from the meteorite parent bodies

CM chondrites

Aqueous alteration on the meteorite parent bodies affected most chondrites (Abreu and Brearley, 2010; Brearley, 2014), but was largely isochemical (Bland et al., 2009). Still, the variable Na and K concentrations in all studied CM chondrites (**Figure 2.2**), as well as the anomalously high concentrations of Th, U, Sr, Ba and LREEs in three of the falls (Nogoya, Cold Bokkeveld and Murchison NC), might result from redistributions on the parent body. For actinides and LREEs it is well known that they are easily mobilized by aqueous fluids from phosphates such as apatite and merrillite (Rocholl and Jochum, 1993; Barrat et al., 2012; Pourmand et al., 2012).

The CM chondrite group is particularly suited to study aqueous alteration, as its individual members span a large range of petrologic types. Recently, various alteration scales have been proposed based on texture and mineralogy (Rubin et al., 2007; Howard et al., 2015), as well as on bulk H_2O, H, C and N abundances and isotope compositions (Alexander et al., 2013; Garenne et al., 2014). All three studies agree that Cold Bokkeveld and Nogoya are the most aqueously altered CM falls, followed by Murchison, Mighei and Murray and finally Paris, which is by far the least altered sample. Thus, the changes in mineralogy and H, C and N abundances induced by aqueous alteration are matched by the effects of elemental mobility observed in the bulk composition (**Figure 2.2a**). However, the effects on bulk chemical composition are generally small and only fluid mobile elements are affected, which suggests a systematic migration of small amounts of liquid water through the pore spaces of the parent body (Young et al., 2003). The enrichments of Th, U, Sr, Ba, K and the LREEs in Murchison NC are not reproduced by the other Murchison powder analyzed. It is not clear whether they result from a heterogeneous distribution on the parent body, or are due to terrestrial weathering in the case of Murchison NC.

CO and CV chondrites

Most CO and CV chondrites have been affected by mild thermal metamorphism on the parent body (e.g., Huss et al., 2006; Brearley, 2014). This can lead to the loss or redistribution of the most volatile elements. Laboratory experiments like ours or those of Ikramuddin and Lipschutz (1975) and Tonui et al. (2014) attest that Cd, S and Se are already vaporized at temperatures >400ºC (**Figure 2.7** and **2.8**).

In CO and CV chondrites, thermal metamorphism primarily affects Cd. Wombacher et al. (2008) noted that reduced CV3 chondrites have generally lower Cd/Zn ratios than oxidized CV3 chondrites that yield Cd/Zn similar to or slightly above the chondritic Cd/Zn ratio. This observation agrees with the low Cd/Zn ratio (1000×Cd/Zn = 0.73) we measured in Vigarano ($CV3_{red.}$), as well as the high Cd/Zn ratio (1000×Cd/Zn = 4) in the Allende Smithsonian powder ($CV3_{ox.}$). The Allende MS powder, however, has a chondritic Cd/Zn ratio (1000×Cd/Zn = 2.1) (**Figure 2.3**). In summary, thermal metamorphism apparently led to the redistribution of Cd on the CV parent body.

A similar behavior for Cd is observed for the two CO chondrites (**Figure 2.4**), with the difference that no sample with complementary Cd enrichment is known (Wombacher et al., 2008). In our sample set, the more equilibrated CO3.2 chondrite Kainsaz is strongly depleted in Cd, while the Cd abundance of ALHA 77307 (CO3.0) agrees with the abundances of the other plateau volatiles. Thus, in the case of CO chondrites, thermal metamorphism likely led to the loss of Cd in samples with higher degrees of metamorphism. The low Cd abundance of Kainsaz is consistent with its heavy Cd isotope composition (Baker et al., 2010b) and low water content, since water was most likely also lost during thermal metamorphism. The generally stronger depletion of volatile elements in Kainsaz (0.25x CI) than in ALHA 77307 (0.33x CI) is probably related to the higher amount of matrix in this sample (Scott, 1984). Several heating experiments confirm that a flat depletion pattern for the plateau volatile elements cannot be created by volatilization (e.g., **Figure 2.8**, Ikramuddin and Lipschutz, 1975; Wulf et al., 1995). This is further supported by the observation that heated chondrites such as Y-980115 (**Figure 2.1**) and EET 96026 (**Figure 2.3**) always display an irregular depletion of plateau volatile elements (see also Moriarty et al., 2009; Noronha and Friedrich, 2014; Tonui et al., 2014).

CK chondrites

It has recently been argued that CV and CK chondrites originated on the same parent body (Huber et al., 2006; Greenwood et al., 2010; Wasson et al., 2013). Although refractory and main component element abundances of the CVs and the CK studied here are generally similar, there are three clear differences in their bulk chemical compositions: (i) the marked depletion of Mo (0.44x CI), (ii) the slightly lower plateau volatile element abundances (0.24x CI compared to 0.32x CI in CV chondrites) and (iii) the complete loss of Tl in the CK chondrite ALH 85002.

Strong Mo depletions have also been observed in other CK chondrites (Palme and Rammensee, 1981) and probably result from the oxidized nature of CK chondrites, since Mo behaves much

more volatile under oxidizing conditions at high temperatures (Fegley and Palme, 1985). Whether metamorphic temperatures were sufficiently high enough to volatilize Mo under oxidizing conditions is ambiguous.

The slight difference in plateau volatile element abundances between CV and CK chondrites is attributed to vaporization during impact heating on a CV-CK parent body by Wasson et al. (2013). If true, this should result in a slight fractionation of the plateau volatile elements in these meteorites. Indeed, the plateau for CK chondrites is the most irregular one in our study (**Figure 2.6** and **Table 2.3**). However, it is striking that abundances of the less volatile elements (Ag, Bi, Pb, Zn, Te, Sn and S) are clearly resolvable from those in the CV chondrites, while the more volatiles (Se, Cd and In), which should be affected more severely by thermal metamorphism, are not. One analyzed CK chondrite is certainly insufficient to propose a different origin of CV and CK chondrites, but slightly different plateau volatile element abundances and other small differences (e.g. for Pt and Al) in the elemental composition of our CK sample provide tentative evidence for such a scenario. The complete loss of Tl in the CK chondrite is most likely the result of thermal metamorphism, comparable to the Cd loss observed in CO chondrites.

EET 96026 (CV or CK)

EET 96026 has been re-classified several times (Clayton and Mayeda, 2003; Rochette et al., 2008; Noronha and Friedrich, 2014), as Rumuruti, C4/5 and as CV or CK. Our bulk compositional data for refractory and main component elements strongly support a relationship to CV and CK chondrites. The large depletion of Re (0.45x CI) compared to CV chondrites is very likely a weathering effect, since the low Re/Os is not accompanied by a low $^{187}Os/^{188}Os$ (Fischer-Gödde et al., 2010). The generally stronger depletion of plateau volatiles in EET 96026 compared to CV and CK chondrites together with its irregular pattern (**Figure 2.3**) most likely results from thermal metamorphism on the parent body. According to Tonui et al. (2001), such an extensive loss of plateau volatile elements can only be achieved at temperatures >700°C. Our result therefore supports the finding of Tonui et al. (2001) that EET 96026 should be classified as a heated CV or CK chondrite.

Y-980115 (CI)

Our bulk element data for Y-980115 are in agreement with data reported by Islam et al. (2012), who also observed a general CI-like composition for Y-980115. However, they report anomalous enrichments of Si and Ti, and a H depletion of 20% compared to CI. The low H_2O content determined in our study (**Table 2.1**) supports the depletion of H, but we did not reproduce the Ti enrichment (Si was not measured). Since our Ti value is CI-like as all other refractory elements, we infer the Ti anomaly reported by Islam et al. (2012) might likely be due to sample heterogeneity.

The almost complete loss of the four plateau volatile elements In, Bi, Tl and Cd (**Figure 2.1**) and the low H_2O content confirm that Y-980115 has been thermally altered, as has previously been suggested by Harries and Langenhorst (2011), Burton et al. (2014) and (King et al., 2015) based on mineralogy and a depletion of amino acids relative to CI chondrites. The volatility sequence in Y-980115 is generally comparable with the one in heated CM chondrites with the prominent exception of Zn (Mahan et al., 2018a). However, Mahan et al. (2018) point out that the sequence could also be slightly different in CM chondrites, since variations between the relative element abundances are quite small and overlap within uncertainties. How and when the thermal alteration happened is unknown, but several lines of evidence suggest that the heating period was short (Nakato et al., 2008; Yabuta et al., 2010; Orthous-Daunay et al., 2013). This observation makes either shock heating from impacts (Nakato et al., 2008; Mahan et al., 2018a) or radiative heating (Chaumard et al., 2012) the most likely scenario.

2.4.3 Terrestrial and anthropogenic effects on bulk chondrite compositions

Terrestrial weathering effects

The chemical compositions of the Antarctic chondrites included in this study show little weathering effects. Only the highly mobile alkali elements K, Na and Rb are slightly variable, which agrees with previous reports from Antarctic chondrite samples (Bland et al., 2006). The K and Na variations in the Antarctic CM2 chondrites are even within the inter-group variability of the CM2 falls (**Figure 2.2b**). Further, the magnitude of K and Na variability does not correlate with their host meteorite weathering degrees. Thus, the observed K and Na variations might not even be the result of weathering but of aqueous alteration on the parent body.

Jbilet Winselwan (CM2, W1) is the only hot desert find analyzed in this study. It is enriched in U, Sr and Ba, and depleted in S. This is in excellent agreement with data reported by Göpel et

al. (2015) and Friend et al. (2018), and typical for weathering of hot desert meteorite finds (Al-Kathiri et al., 2005; Hezel et al., 2011).

The depletion of fluid mobile elements (Ca, Sr, Ba, K and Na) in Tagish Lake relative to the CM median indicates that our sample split experienced terrestrial weathering and belongs to the pieces not immediately collected after the fall (Brown et al., 2000; Friedrich et al., 2002). This interpretation is also supported by the significantly lower Sr and Ba concentrations in two samples of Tagish Lake reported by (Friedrich et al., 2002). Leaching experiments by Mittlefehldt and Wetherill (1979) showed that Ca, K and Rb are quickly removed from chondrites within only 1.5 h by distilled water. Because of the strong geochemical similarity of Sr, Ca and Ba, their low contents are most likely the result of leaching at the frozen lake onto which the meteorite fell (Brown et al., 2000).

Bulk chondrite element anomalies caused by anthropogenic influence

Three CM chondrites (Mighei, Cold Bokkeveld, Nogoya) and the CV chondrite Vigarano have anomalously high Pb abundances (**Figure 2.2a, 2.3**). Furthermore, the $^{207}Pb/^{206}Pb$ ratios in these CMs are approximately 0.94, compared to 1.1 in average CM. The CV chondrite Vigarano has a $^{207}Pb/^{206}Pb$ ratio of 0.86 compared to a CV average of 1.01. These Pb anomalies might therefore be the result of an anthropogenic influence: Ethyl-Pb, which has low $^{207}Pb/^{206}Pb$ ratios (e.g. Broken Hill $^{207}Pb/^{206}Pb$=0.96, Doe and Stacey, 1974, Grousset et al., 1994) was added to gasoline and released to the environment after combustion. Anthropogenic lead then contaminated meteorite specimens via the atmosphere and thereby increased their bulk Pb concentrations and changed their $^{207}Pb/^{206}Pb$ ratios (e.g., Tera and Carlson, 1999; Göpel et al., 2015).

The samples Cold Bokkeveld (CM), Nogoya (CM), Vigarano (CV) and Y-980115 (CI) have considerably higher Ag concentrations than other samples of their respective groups. A contamination of specimens with Ag derived from the handling of coins or jewelry is possible, and has been reported earlier (e.g., Greenland, 1967; Kaiser and Wasserburg, 1983). This contamination could explain the high Ag in the museum samples Cold Bokkeveld, Nogoya and Vigarano, which are also contaminated with Pb, but is less likely for the Antarctic sample Y-980115.

2.5 CONCLUSIONS

This study presents a coherent dataset for major and trace elements in carbonaceous chondrites including many volatile elements. The results for volatile elements call for a revision of models that describe the volatile element depletion in the meteoritic building blocks of the Earth. This is because our dataset confirms previous claims (e.g., Takahashi et al., 1978b; Wolf et al., 1980) that volatile elements in carbonaceous chondrites with 50% T_C between about 800 K and 500 K have flat, unfractionated patterns relative to CI chondrites. This characteristic flat depletion pattern is a fundamental characteristic of almost all carbonaceous chondrites and we propose that these elements should be recognized as a subgroup of the moderately volatile elements, namely 'plateau volatile elements'. Elements with condensation temperatures between 1250°K and 800°K are referred to as "slope volatile elements", because their abundances consistently decrease with decreasing condensation temperature.

Abundances of plateau volatile elements for the various carbonaceous chondrite groups reveal discrete degrees of depletions for the different groups. We favor the following scenario to explain the unfractionated patterns of plateau volatile elements as well as the fractionated patterns of slope volatile elements: During the high-temperature event that led to chondrule formation, volatile elements evaporated from chondrule precursor materials. Slope volatile elements partially recondensed, while plateau volatile elements were largely lost from both, chondrules and matrix. After chondrule formation ceased, different amounts of primitive CI-like material were added as part of the matrix, thus explaining the flat plateau volatile element depletion patterns. This model is similar to that of Alexander (2005) and consistent with most isotope systems. A simple mass balance calculation based on Mg and Si concentrations in bulk chondrites, bulk matrix and chondrules approximately reproduces the bulk Mg/Si of (i) chondrules, (ii) chondrule-related matrix, and (iii) the CI-like material. This model can account for both, chondrule-matrix complementarity and unfractionated plateau volatile element abundances. Furthermore, the model eases the chemical restriction that chondrules and bulk matrix have to form from the same reservoir (Hezel and Palme, 2010) While chondrules and the chondrule-related matrix must indeed form from the same reservoir, the CI-like material as part of the matrix may well be derived from another reservoir (Jacquet et al., 2016). However, the above model is challenged by the observation that a substantial amount of Zn, Cd and possibly other plateau volatile elements are hosted in chondrules (Wombacher et al., 2008; Palme et al., 2014b; Pringle et al., 2017) and by trends in plateau volatile element isotope compositions as observed for Zn isotopes (Luck et al., 2005; Pringle et al., 2017). This indicates

that the history of a possible CI-like material as the carrier of the plateau volatile elements is more complex than suggested by the bulk element data alone or, perhaps less likely, that the observed plateau does not result from the presence of CI-like material at all. Whether these issues can be resolved by more complex models remains to be seen. In any case, the flat plateau volatile element abundances and their covariation with matrix abundances in carbonaceous chondrites needs to be taken into account by models for volatile element depletion.

Secondary processes, such as aqueous alteration and thermal metamorphism on the parent body or terrestrial weathering, have only subordinate effects on the bulk composition of carbonaceous chondrites. Antarctic carbonaceous chondrite samples appear to be at least as well preserved as falls. In some cases, thermal overprints led to the fractionation of the plateau volatile elements as most prominently observed in the heated chondrites Y-980115 (CI) and EET 96026 (CV or CK). Despite the fractionated plateau volatile element pattern, the bulk composition of EET 96026 closely resembles CV and CK chondrites and we suggest to re-classify it accordingly.

Chapter 3

Earth's volatile element depletion pattern inherited from a carbonaceous chondrite-like source

3.1 INTRODUCTION

The chemical composition of the terrestrial planets is controlled by the composition of their planetary building blocks. Where data are available, the inner solar system bodies Earth, Moon, Mars and different meteorite parent bodies, are depleted in volatile elements (for example, Cd, In, S and Cl) relative to the bulk solar system composition as represented by CI chondrites (Allègre et al., 2001; Palme and O'Neill, 2014). The volatile element depletion pattern constrains the nature of Earth's building blocks and may serve as a tracer for the delivery of water during Earth's growth (Alexander et al., 2012; Marty, 2012; Wang and Becker, 2013). Although Earth's isotope composition cannot be reproduced by mixing known meteorite groups (Burkhardt et al., 2011; Palme and O'Neill, 2014; Dauphas, 2017; Fischer-Gödde and Kleine, 2017; Render et al., 2017), comparisons between Earth's chemical composition and those of undifferentiated meteorites (chondrites), in particular for volatile elements, suggest that Earth's building blocks experienced similar nebular fractionation processes as carbonaceous chondrites but different to those observed in ordinary and enstatite chondrites (Allègre et al., 2001; Palme and O'Neill, 2014; Sossi et al., 2018). For example, ratios between lithophile volatile and lithophile refractory elements (for example, K/U) for the bulk silicate Earth (BSE) always plot at the volatile-depleted end of a trend defined by carbonaceous chondrites (Allègre et al., 2001). Furthermore, Zn and Rb stable isotope compositions of the BSE follow the carbonaceous chondrite trend of increasingly light isotope compositions with increasing degree of volatile element depletion (Pringle and Moynier, 2017; Sossi et al., 2018).

Earth's primary volatile element depletion pattern is obscured by the additional depletion of siderophile and chalcophile volatile elements in the BSE that is generally attributed to their partitioning into Earth's core (McDonough, 2003; Palme and O'Neill, 2014). However, numerous metal-silicate partitioning experiments have so far been unable to consistently reproduce the siderophile and chalcophile element depletion pattern observed in the BSE (Mann et al., 2009; Wood et al., 2014; Wang et al., 2016; Ballhaus et al., 2017). This is especially true

regarding the abundance of the volatile element In in the BSE, which appears to be overabundant relative to the carbonaceous chondrite-like volatile element depletion pattern (Witt-Eickschen et al., 2009; Wang et al., 2016; Norris and Wood, 2017). Therefore, it was concluded that Earth's volatile element abundances were modified by post-nebular processes, such as vaporization on precursor bodies and possibly during the giant Moon-forming impact, late accretion or collisional erosion (O'Neill and Palme, 2008; Wang and Becker, 2013; Norris and Wood, 2017). Alternatively, it was proposed that volatile element abundances evolved differently in the inner solar system, where the vast majority of Earth's building materials originate (Witt-Eickschen et al., 2009; Wang et al., 2016). There are several arguments against secondary volatile element loss related to Earth's accretion, for example (1) variations in ^{53}Cr induced by the decay of the now extinct ^{53}Mn (half-life of 3.7 Myr) suggest that Mn/Cr fractionation and therefore volatile element depletion in the precursor materials of Earth, Mars and the different meteorite parent bodies occurred early in the protoplanetary disk within about 2 Myr of the formation of calcium–aluminum-rich inclusions (Trinquier et al., 2008), rather than during planetary growth, (2) the chondritic Mn/Na of Earth argues against post-nebular volatile loss as opposed to the high Mn/Na ratio of other differentiated rocky bodies (for example Mars, Moon and achondrites) (O'Neill and Palme, 2008; Siebert et al., 2018) and (3) evaporative loss of volatile elements should lead to stable isotope fractionation that results in an enrichment of heavy isotopes in the residue, which is not observed on Earth (Humayun and Clayton, 1995; Wombacher et al., 2008; Nebel et al., 2011; Pringle and Moynier, 2017; Sossi et al., 2018). As post-nebular volatile element loss was seemingly restricted on Earth, volatile element abundances must mirror the composition of Earth's building blocks. Here we reassess Earth's volatile element depletion pattern based on recently available volatile element data for carbonaceous chondrites (Chapter 2, Clay et al., 2017), complemented by new high-precision S, Se and Te data.

3.2 TERRESTRIAL HOCKEY STICK VOLATILE ELEMENT DEPLETION PATTERN

It is generally assumed that volatile element abundances in carbonaceous and ordinary chondrites decrease gradually with increasing volatility of the elements (as commonly defined by 50% condensation temperatures ($T_{50\%}$)) (Wasson and Chou, 1974; Palme et al., 2014a). However, recent high-precision data (Chapter 2) confirm earlier suggestions (Krähenbühl et al., 1973; Takahashi et al., 1978b) that volatile elements with $T_{50\%}$ <750 K are depleted by a constant factor in carbonaceous chondrites relative to CI chondrites. Thus, CI-normalized

volatile element abundances plotted versus $T_{50\%}$ define a hockey stick depletion pattern for all the investigated carbonaceous chondrite groups (**Figure 3.1**), in which slope volatile elements with $T_{50\%}$ between 1250 and 750 K follow the previously suggested gradual depletion trend, whereas volatile elements with $T_{50\%}$ between 750 and 500 K are essentially unfractionated from each other and are now defined as plateau volatile elements (Chapter 2). Sulfur, Se and Te belong to the plateau volatile elements and our new isotope dilution data confirm their CI-chondritic relative abundances in all the investigated carbonaceous chondrite groups (**Figure B1**). In contrast, ordinary and enstatite chondrite samples display no clear plateau, but more complex volatile element abundance patterns (Wang and Lipschutz, 2005; Wang and Lipschutz, 2007) that result, at least partly, from additional high-temperature processes, as evident by their strongly fractionated Cd and Zn stable isotope compositions in comparison to those of carbonaceous chondrites (Luck et al., 2005; Wombacher et al., 2008; Moynier et al., 2011; Palk et al., 2018).

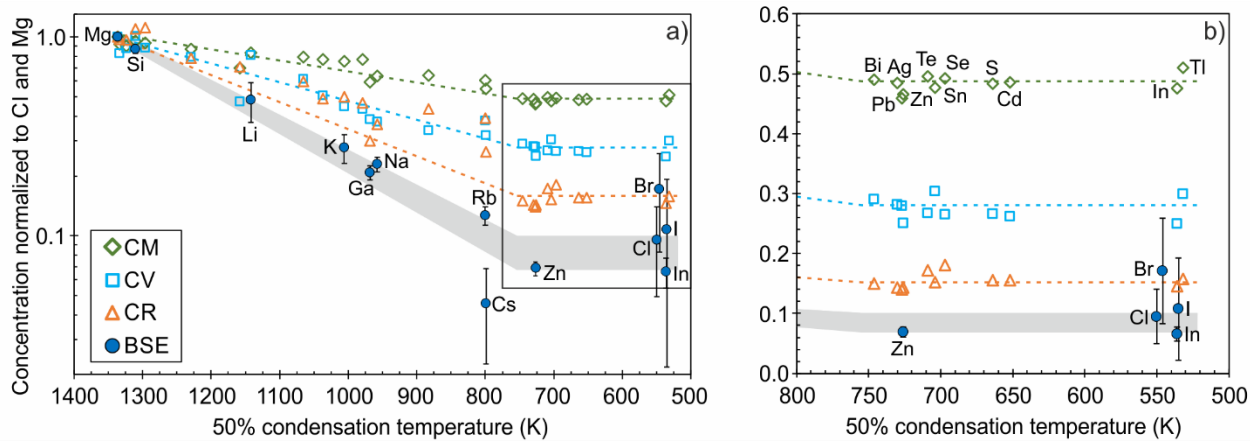

Figure 3.1: Volatile element depletion pattern for different carbonaceous chondrite groups and the bulk silicate Earth (BSE). (a) CI chondrite and Mg normalized volatile element abundances in carbonaceous chondrites and lithophile volatile element abundances in the BSE define a hockey stick depletion pattern in a semilog plot. (b) Zoom-in on plateau region of the hockey stick. Error bars represent the propagated uncertainties of CI chondrite and CM, CV, CR or BSE concentrations, respectively. For data sources see **Table B1**.

The volatile element depletion pattern for Earth can only be deduced from predominantly lithophile volatile element abundances in the BSE. Among the plateau volatile elements, these are In, Zn, Cl, Br and I, the abundances of which have been recently revised in both, the BSE and chondrites (Wang et al., 2016; Clay et al., 2017 and Chapter 2). Importantly, all five elements are unfractionated from each other (CI-like) in the BSE within analytical uncertainty (Witt-Eickschen et al., 2009; Wang et al., 2016; Clay et al., 2017) (**Figure 3.1** and **3.2**). When combined with the abundances of lithophile slope volatile elements in the BSE, this reveals that Earth also displays a hockey stick volatile element depletion pattern (**Figure 3.1**). Recognition of this plateau in Earth's volatile element depletion pattern means that In is no longer

overabundant in the BSE, which obviates the need for terrestrial building blocks with unusual In enrichments (Witt-Eickschen et al., 2009; Wang et al., 2016) or processes, such as melting and volatile loss from precursor bodies or during the Moon-forming impact (Norris and Wood, 2017) to explain Earth's volatile element depletion pattern.

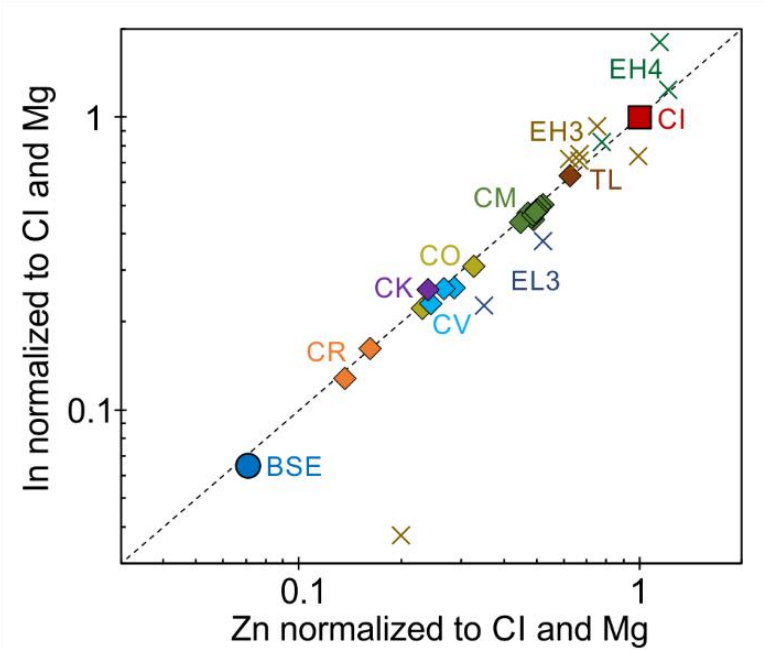

Figure 3.2: Indium and Zn abundances normalized to CI chondrites and Mg in chondrites and the BSE. Carbonaceous chondrites (Chapter 2) and the BSE (Wang et al., 2016) have a CI-chondritic In/Zn ratio as marked by the dashed line, whereas unequilibrated enstatite chondrites (Wang and Lipschutz, 2005) scatter around the CI-chondritic ratio. Because of the large scatter of In abundances in ordinary chondrites, representative In/Zn cannot be inferred (Witt-Eickschen et al., 2009; Wang et al., 2016). Since the In/Zn ratio of the BSE plots on the CI-chondritic ratio, it is concluded that In and Zn both behaved predominantly lithophile during core formation.

3.3 PLATEAU VOLATILE ELEMENT ABUNDANCES IN BULK EARTH AND CORE

Recognition of the hockey stick volatile element depletion pattern allows us to improve estimates of plateau volatile element abundances in bulk Earth and its core (**Table 3.1**). Bulk Earth abundances are derived from the plateau level in the BSE as defined by the lithophile elements Zn and In, whereas the core abundances are calculated from the inferred bulk Earth abundances and the depletions of siderophile and chalcophile elements relative to the BSE plateau level (**Figure 3.3**).

Our estimates of bulk Earth and core abundances hinge on the lithophile behavior of In and Zn during core formation, but metal-silicate partition experiments revealed siderophile tendencies for both elements (Mann et al., 2009; Wang et al., 2016; Mahan et al., 2018b). Therefore, a substantial fraction of In and Zn could have been sequestered into the core, which would drive estimates of their abundances in bulk Earth higher. As In is considered more siderophile than

Zn (Mann et al., 2009; Wang et al., 2016), partitioning of Zn and In into the core, while maintaining CI-chondritic In/Zn ratios in the BSE appears possible only in extreme cases with equilibrium pressures that exceed 30 - 60 GPa during core formation (Mann et al., 2009). Experiments also suggest that In is more siderophile than Cd (Wang et al., 2016), which is depleted by core formation (**Figure 3.3**). If true, In must have become even more depleted during core formation and Earth's building materials must be characterized by a suprachondritic In/Cd ratio to accommodate the observed In/Cd ratio in the BSE (Wang et al., 2016). However, experiments conducted at high sulfur fugacities reveal that Cd is more chalcophile than In (Kiseeva and Wood, 2013; Wood et al., 2014; Righter et al., 2017b). Furthermore, dissolved Si in the metal reduces the In partition coefficient more than that of Cd (Righter et al., 2017a) and Zn (Righter et al., 2018). Such effects could explain the relative abundances of Zn, In and Cd observed in the BSE. Moreover, the lithophile behavior of In and Zn during core formation is supported by the Cs abundance in the BSE (**Figure 3.1**). The slope volatile element Cs plots close to the plateau level or slightly above in different carbonaceous chondrites (**Figure 3.1**). In the BSE, the lithophile element Cs plots within uncertainty at the same level as Zn and In (**Figure 3.1** and **3.3**) and not above. This supports the notion that both Zn and In remained largely in the silicate Earth during core formation and that both elements serve as a robust baseline for the calculation of plateau volatile element abundances in the BSE.

Based on the new hockey stick volatile element depletion pattern, we can re-evaluate plateau volatile element partitioning into the core. To this end, we calculated core and bulk Earth compositions (**Table 3.1**) for two end-member cases: (1) Zn and In did not partition into the core and (2) there are 50 $\mu g\ g^{-1}$ Zn in the core, which is the lower estimate of core formation models based on recent experimental data (Mahan et al., 2018b). The latter results in significantly higher concentrations for siderophile plateau volatile elements in bulk Earth and the core. Differences to previous estimates on bulk Earth and core volatile element abundances (McDonough, 2003) result from (1) the newly recognized plateau region in which volatile element depletion is the same and thus independent from uncertainties in $T_{50\%}$, (2) the observation that Ag belongs to the plateau region (Kiseeva and Wood, 2015 and Chapter 2) and (3) updated chemical compositions for CI chondrites and the BSE (**Table B1**). Our new data confirm that the S abundance in the core cannot contribute substantially to the outer core density deficit (Dreibus and Palme, 1996; McDonough, 2003) and reveal the extent to which Pb and other moderately siderophile and chalcophile plateau volatile elements were sequestered into the core (**Table 3.1** and **Figure 3.3**).

Table 3.1: Bulk Earth and core abundances for plateau volatile elements.

	Bulk Earth [µg/g]			Core [µg/g]			Core/BSE	
	Case 1	Case 2	McDonough (2003)	Case 1	Case 2	McDonough (2003)	Case 1	Case 2
Bi	0.012	0.017	0.010	0.029	0.046	0.030	9.7	15
Ag	0.023	0.034	0.050	0.052	0.086	0.15	5.8	9.5
Pb	0.27	0.40	0.23	0.46	0.86	0.40	2.5	4.6
Zn	35	52	40	0	50	0	-	0.91
Te	0.24	0.35	0.30	0.71	1.06	0.85	65	97
Sn	0.16	0.24	0.25	0.21	0.44	0.50	1.5	3.2
Se	2.2	3.2	2.7	6.5	9.6	8.0	81	120
S	5300	7900	6400	16000	24000	19000	76	113
Cd	0.073	0.11	0.10	0.16	0.27	0.15	5.1	8.6
In	0.0083	0.012	0.007	0	0.013	0	-	1.08
Tl	0.014	0.021	0.014	0.035	0.056	0.030	8.6	14

3.4 TERRESTRIAL BUILDING MATERIALS AND VOLATILE ELEMENT DEILVERY

In carbonaceous chondrites the unfractionated plateau volatile element pattern can be explained by the presence of material with a CI-like composition in their matrices (Jacquet et al., 2016 and Chapter 2). Accordingly, the unfractionated plateau volatile element abundances in Earth most probably reflect the presence of CI-like material within some of Earth's building blocks. The abundances of the dominantly lithophile plateau volatile elements Zn, Cl, Br, I and In in the BSE allow an estimate of the maximum amount of CI-like material in Earth, which is 10-15 wt.% (**Figure 3.3**). The depletion of siderophile and chalcophile volatile elements relative to the plateau implies that the CI-like material was already accreted before core formation and sulfide segregation (O'Neill, 1991; Rubie et al., 2016) ceased. In contrast, the abundances and chondritic ratios of highly siderophile elements and the chalcogens S, Se and Te are best explained by late accretion of ~0.5 wt.% CM-like material (Wang and Becker, 2013) (equivalent to ~0.25 wt.% CI-like material) to a mantle that was virtually completely stripped of highly siderophile elements and chalcogens during core formation (**Figure 3.3**). Plateau volatile elements other than the chalcogens are less chalcophile and siderophile and were therefore affected to a lesser degree by metal or sulfide segregation. The depletion of Pb and Sn, however, is much smaller than predicted by equilibrium partitioning which indicates that the accretion of the CI-like material was biased towards the end of Earth's main accretion phase (Ballhaus et al., 2017), when the composition of Earth's building blocks shifted from reduced refractory matter to more oxidized and volatile-rich material (Schönbächler et al., 2010; Rubie

et al., 2015). Likewise, the overall stronger volatile element depletion of Earth compared to most carbonaceous chondrites is best explained by a mix of early refractory building materials with late volatile-rich materials (Schönbächler et al., 2010). Independent of the exact timing, the recognition that the CM-like material delivered during the late accretion is also characterized by a hockey stick volatile element depletion pattern (**Figure 3.3**), indicates that some of Earth's building materials were chemically similar to carbonaceous chondrites during Earth's main and late accretion phases.

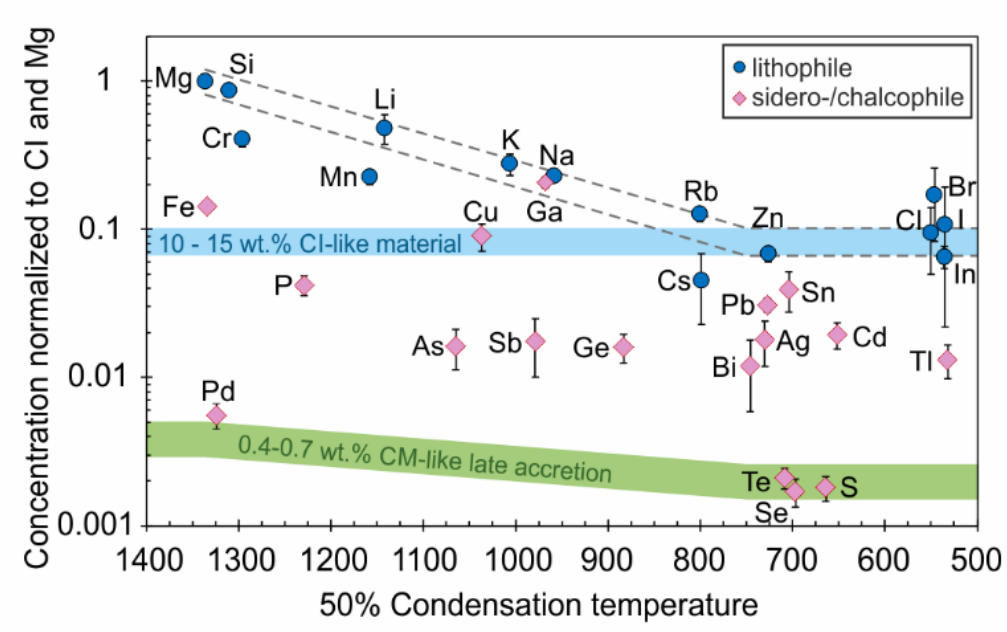

Figure 3.3: Magnesium normalized volatile element abundances in the BSE relative to CI as a function of their 50% condensation temperature (Lodders, 2003; Kiseeva and Wood, 2015; Clay et al., 2017). Lithophile plateau volatile element abundances in the BSE (TC < 750 K) can be explained by the addition of 10-15 wt.% CI-like material within Earth's building blocks before core formation ceased. Sulfur, Se and Te were likely completely stripped of the mantle during this event before late accretion of 0.4 - 0.7 wt.% CM-like material (Wang and Becker, 2013). Error bars represent the propagated uncertainties of CI chondrite and BSE concentrations. For data sources see **Table B1**.

There is an ongoing debate on whether Earth is made of carbonaceous chondrite-like (Allègre et al., 2001; Palme and O'Neill, 2014) or enstatite chondrite-like material (Javoy et al., 2010; Dauphas, 2017). Mass-independent isotope compositions for oxygen and several refractory elements in the BSE are indistinguishable or close to those of enstatite chondrites and clearly different from those of carbonaceous chondrites (Burkhardt et al., 2011; Dauphas, 2017; Fischer-Gödde and Kleine, 2017; Render et al., 2017). Consequently, it was proposed that the vast majority of Earth's building blocks formed in the same region of the solar nebula as enstatite chondrites and cannot comprise significant amounts of carbonaceous chondrites (Dauphas, 2017). In this case, however, a substantial amount of these terrestrial building blocks must be characterized by a hockey stick volatile element depletion pattern, which is so far not observed in enstatite chondrites. Alternatively, the similar mass-independent isotope

composition of Earth and enstatite chondrites results from admixing carbonaceous chondrite material to non-carbonaceous material (Warren, 2011). In this model, Earth's average building material could comprise up to 32 wt.% of carbonaceous chondrite material and still keep the non-carbonaceous isotope compositions for oxygen and refractory elements (Warren, 2011). Earth's endmember composition for Mo, Ru and Nd isotopes (Burkhardt et al., 2011; Fischer-Gödde and Kleine, 2017; Render et al., 2017) would then require the presence of building materials with isotope compositions that are not present in our meteorite collections. The delivery of volatiles, such as water and N_2 by 2-4 wt.% carbonaceous chondrite material (Alexander et al., 2012; Marty, 2012) suggests that at least a fraction of the volatile elements was added by carbonaceous chondrites.

In summary, carbonaceous chondrites and Earth display a unique, hockey stick volatile element depletion pattern in which the most volatile elements are depleted to the same extent. This is in stark contrast to the long-standing model of ever increasing depletion with elemental volatility. As a consequence, abundances of the plateau volatile elements in bulk Earth and in the core were re-evaluated and provide a new framework for studies that constrain terrestrial core formation conditions and planetary differentiation in general.

3.5 METHODS

3.5.1 Isotope dilution analysis of S, Se and Te

Selenium and Te abundances (**Table B2**) were determined by isotope dilution multiple collector-inductively coupled plasma-mass spectrometry (MC-ICP-MS). Sulfur abundances were determined using an Element XR^{TM} sector field ICP-MS (Makishima and Nakamura, 2001; König et al., 2012; Wang et al., 2014). Three isotope tracer solutions (spikes) enriched in ^{34}S, ^{77}Se and ^{125}Te that contained 1,195 ± 26 μg g^{-1} S, 420.1 ± 2.7 ng g^{-1} Se and 56.97 ± 0.83 ng g^{-1} Te (2 s.d. intermediate precision) were used. The intermediate precision given for the spike concentrations refers to repeated calibrations against two commercial Merck and Alfa Aesar element solutions. The isotope tracer solutions were added to ~50 mg of chondrite powders. A mixture of two ml of 14 M HNO_3 and 24 M HF was added for sample digestion and capped beakers were placed onto a hot plate at 120 °C for 48 h. To determine the S content, an aliquot that contained about 15 μg of S was dried down, dissolved in 0.14 M HNO3 and diluted to a final S concentration of about 1 μg g^{-1}.

For Se and Te analyses, the sample solution was dried down, taken up in 2 ml of 6 M HCl and refluxed for 24 h at 80 °C to ensure the complete conversion of Se (VI) and Te (VI) to the 4^{+}

oxidation state (Marin et al., 2001). Solutions were dried down again, taken up in 6 ml of 6 M HCl and refluxed for another 24 h at 80 °C. After cooling, the samples were diluted with ultrapure water (18.2 MΩ*cm) to achieve 36 ml of sample solutions in 1 M HCl. Thiol cotton fibre (TCF) was employed for the separation of Se and Te from sample matrices. The preparation of TCF followed published protocols (Yu et al., 2002; Rouxel et al., 2002; Elwaer and Hintelmann, 2008; Mitchell et al., 2012). Diluted sample solutions were then loaded onto 5 ml polypropylene columns (Rouxel et al., 2002). Although all the major elements pass through these, Se (IV) and Te (IV) have strong affinities for the functional groups on the TCF (Yu et al., 2002). The remaining matrix elements were then eluted with 2 ml of 6 M HCl and 4 ml of H_2O, respectively. Subsequently, the TCF was transferred to 10 ml test tubes and attacked with 0.5 ml of 7 M HNO_3 to elute Se and Te. The test tubes were capped and placed into a boiling water bath for 20 min. Subsequently, samples were diluted by the addition of 4.6 ml of ultrapure water. For Se and Te analyses, the solution was split and 0.25 ml of 10 M HCl was added to both aliquots to ensure that Se and Te remained in the 4^+ state.

For Se and Te isotope ratio measurements, a Neptune MC-ICP-MS equipped with an ESI SC-2 autosampler and a homemade hydride generator were used (Wombacher et al., 2009; König et al., 2012). A 1 μg g^{-1} solution yields about 20 mV for ^{82}Se and 400 mV for ^{128}Te with 10^{11} Ω resistors. The cup configurations include ^{76}Se, ^{77}Se, ^{78}Se and ^{82}Se and ^{124}Te, ^{125}Te, ^{126}Te, ^{128}Te and ^{130}Te, respectively. Each analysis comprised 20 cycles with an integration time of 4.2 s. As Se and, especially, Te can be rather sticky in the sample introduction system, rinsing with 0.56 M HNO_3 takes up to 20 min. The background was determined immediately before every standard and sample analysis. Measured background intensities were subtracted offline from sample signal intensities. Instrumental mass bias was monitored externally by repeated analyses of standard solutions and corrected using the natural $^{77}Se/^{82}Se$ of 0.87447 and $^{125}Te/^{126}Te$ of 0.376688 (Berglund and Wieser, 2011).

The intermediate precision of measurement is given here as two relative standard deviations (RSD) for repeated measurements of the Murchison CM2 chondrite and a slightly weathered piece of the Allende CV3 chondrite (*n* = number of measurements and *d* = number of digestions). Repeated analyses of S yielded ±1.5% (*n*=11 and *d*=4) for Murchison CM2 and ±4.0% (*n*=20 and *d*=8) for Allende CV3. For Se, the intermediate precision was ±1.5% for Murchison CM2 (*n*=5 and *d*=5) and ±2.9% for the weathered Allende CV3 sample (*n*=16 and *d*=14). The intermediate precision for Te was ±2.4% for Murchison CM2 (*n*=5 and *d*=5) and ±4.7% for Allende CV3 (*n*=16 and *d*=14). For S, Se and Te, the precision of the measurement

results from the same aliquot measured in different sessions was generally better than the intermediate precision based on repeated digestions. Thus, the intermediate precision, which includes repeated digestions, very probably comprises sample heterogeneity between different powder aliquots. We decided to use Murchison CM2 for the estimate of the intermediate precisions for samples given in **Table B2**, because the Allende CV3 test sample yielded low S (6,160 μg g^{-1}) and Se (4.5 μg g^{-1}) abundances and may suffer from heterogeneities due to weathering. Procedural blanks for S, Se and Te were variable and always <90 ng for S, <0.6 ng for Se and <0.4 ng for Te. The maximum blank did not contribute significantly to S, up to 0.3% to Se and up to 1.8% to Te for the most depleted CR chondrite sample.

3.5.2 Calculation of core and bulk Earth plateau volatile element abundances

The core and bulk Earth plateau volatile element abundances reported in **Table 3.1** are calculated based on their abundance in the BSE and the uniform depletion of plateau volatile elements relative to CI chondrites (**Figure 3.3**). The extent of plateau volatile element depletion (VED_{BE}) in the bulk Earth is derived from the Mg and CI normalized abundances of the dominantly lithophile plateau volatile elements In and Zn in the BSE, which yields 0.067 for Case 1 and 0.100 for Case 2 (**Table 3.1**). All other plateau volatile elements are depleted relative to this plateau level in a Mg and CI normalized plot (**Figure 3.3**), which suggests that the missing complement of these elements resides in the core. The respective bulk Earth abundances for plateau elements El (μg g^{-1}) are calculated as $El_{BE} = VED_{BE} \times Mg_{BSE} \times (El_{CI}/Mg_{CI}) \times 0.675$, where 0.675 refers to the silicate Earth mass fraction (Lodders and Fegley, 1998). The core element abundances (μg g^{-1}) were then calculated by mass balance as $El_C = (El_{BE} - 0.675 \times El_{BSE})/0.325$.

Chapter 4

Determination of Cu, Zn, Ga, Ag, Cd, In, Sn and Tl in geological reference materials and carbonaceous chondrites by isotope dilution ICP-MS

4.1 INTRODUCTION

Copper, Zn, Ga, Ag, Cd, In, Sn and Tl are classified as volatile elements in cosmochemistry due to their relatively low 50% condensation temperatures, ranging from 1037 to 532 K (Lodders, 2003; Davis, 2006; Palme and O'Neill, 2014). They display chalcophile, siderophile and lithophile tendencies, mainly depending on the oxygen and sulfur fugacity and on pressure and temperature conditions. Volatile element depletion patterns of planetary materials help to constrain the underlying fractionation processes and trace planetary building blocks (e.g., Anders, 1964; Wasson and Chou, 1974; Alexander, 2005; Schönbächler et al., 2010; Wang and Becker, 2013; Wang et al., 2016; Ballhaus et al., 2017). Furthermore, the effects of evaporation and condensation on volatile element abundances and isotope compositions provide key information regarding the formation of our solar system and planetary accretion (e.g., Humayun and Clayton, 1995; Luck et al., 2005; Wombacher et al., 2008; Baker et al., 2010b; Kato et al., 2015; Yang et al., 2015; Norris and Wood, 2017; Pringle and Moynier, 2017; Wang and Becker, 2017; Sossi et al., 2019).

In terrestrial settings the study of volatile trace elements became increasingly important over the last decades (e.g., Newsom et al., 1986; Yi et al., 2000; Witt-Eickschen et al., 2009; Baker et al., 2010a; Barnes and Ripley, 2015; Lorand and Luguet, 2015; Cox et al., 2019). They behave as moderately to highly incompatible elements during magmatic differentiation and thus their abundances and fractionation can give valuable insights into mantle source compositions (Yi et al., 1995; Yi et al., 2000; Norman et al., 2004; Jenner et al., 2012; Kelley et al., 2013; Greaney et al., 2017). However, due to their volatility the effect of possible volatile loss during volcanic outgassing must be taken into account (e.g., Lambert et al., 1988; Baker et al., 2009; Vlastélic et al., 2013; Zelenski et al., 2013).

Despite their great potential in cosmo- and geochemistry there are only fragmentary data on volatile element abundances in geological reference materials available. Analytical challenges include the low natural abundances in silicate rocks (Ag, Cd, In and Tl), especially depleted mantle rocks, and loss during sample preparation (Ag and Sn). To generate high precision trace element abundance data, isotope-dilution inductively-coupled-plasma mass-spectrometry (ID-ICP-MS) is often the method of choice. However, many of these elements suffer from isobaric or polyatomic interferences such as $^{113}Cd^{+}$ on $^{113}In^{+}$, $^{110}Pd^{+}$ on $^{110}Cd^{+}$, $^{93}NbO^{+}$ on $^{109}Ag^{+}$ and $^{138}Ba^{++}$ on $^{69}Ga^{+}$ during ICP-MS analysis. Although these interferences can be monitored throughout the measurement, the involved mathematical corrections lead to larger uncertainties (Jenner et al., 1990; Dulski, 1994; Aries et al., 2000; Linge and Jarvis, 2009). Chromatographic separation of the elements of interest from the rock matrix and interfering elements not only alleviates the interferences, but also allows for higher ion beam intensities and hence improves the trueness of the results.

In this study we determined the mass fractions of Cu, Zn, Ga, Ag, Cd, In, Sn and Tl in 21 geological reference materials (RM) and three carbonaceous chondrites via ID-ICP-MS following digestion and chromatographic separation. So far, only limited high-precision data exist for Ag, Cd, In, Sn and Tl in geological RM (e.g., Yi et al., 1995; Yi et al., 1998; Lu et al., 2007; Makishima et al., 2011; Cotta and Enzweiler, 2013; Wang et al., 2014; Creech et al., 2017; Kirchenbaur et al., 2018). Here, we modified and combined published chemical separation protocols and developed a measurement protocol for high-precision quadrupole ICP-MS (Q-ICP-MS) analyses.

4.2 EXPERIMENTAL PROCEDURE

4.2.1 Sample selection

Twenty-one geological reference materials (RM) with different lithologies, comprising ultramafic rocks, mafic to felsic igneous rocks, one slate and a marine sediment, were analyzed in this study (**Table 4.1**). The sample selection comprises certified reference materials (CRM) and most of the frequently requested materials on the GeoReM database for which a compilation of reference or recommended values exists for many elements (Jochum et al., 2016). In order to compare our results, we included RM for which high-precision isotope dilution data are available for the elements of interest (e.g., Yi et al., 1995; Yi et al., 1998; Makishima et al., 2011; Wang et al., 2014; Kirchenbaur et al., 2018). Furthermore, the three

carbonaceous chondrites Orgueil (CI1), Murchison (CM2) and Allende Smithsonian (CV3) were analysed.

Table 4.1: Reference materials analyzed in this study.

RM	Lithology	Provider
AGV-2	Andesite	USGS
BCR-2	Basalt	USGS
BE-N	Basalt	CRPG
BHVO-1	Basalt	USGS
BHVO-2	Basalt	USGS
BIR-1	Basalt	USGS
BRP-1	Basalt	CPRM
MGL-GAS*	Serpentinite	IAG
DTS-2b	Dunite	USGS
G-2	Granite	USGS
JA-2	Andesite	GSJ
JB-2	Basalt	GSJ
MAG-1	Marine sediment	USGS
MUH-1	Harzburgite	IAG
OKUM	Komatiite	IAG
OU-6	Slate	IAG
PCC-1	Peridotite	USGS
RGM-1	Rhyolite	USGS
UB-N	Serpentinite	CRPG
W-2	Diabase	USGS
WS-E	Dolerite	CRPG

USGS = United States Geological Service,
CRPG = Centre de Recherches Pétrographiques et Géochemiques
IAG = International Association of Geoanalysts
GSJ = Geological Survey Japan
CPRM = Companhia de Pesquisa de Recursos Minerais
* Also known as CGL 001

4.2.2 Reagents and reference solutions

All samples and solutions were prepared in the clean lab facilities at the Universität zu Köln. Hydrochloric (10 mol l^{-1}), hydrofluoric (24 mol l^{-1}) and nitric (14 mol l^{-1}) acid used for sample digestion, chemical separation and ICP-MS measurements were distilled by sub-boiling analytical grade (P.A.) acids with Savillex teflon distils once. In order to improve the Sn blank, HCl was further purified by passing it through a column filled with anion exchanger as described in De Laeter and Jeffery (1965) and Kirchenbaur et al. (2018). Hydrobromic acid

(8.55 mol l^{-1}) was distilled once using a teflon elbow distil. For dilution, water from a Milli-Q purification system with a resistivity of 18.2 MΩ*cm was used. Furthermore, hydrogen peroxide (Suprapur® 30% Merck) and L-ascorbic acid (AnalaR Normapur) were applied in this study.

The single element calibration solutions that were used for isotope tracer (spike) calibration and instrumental mass discrimination are listed in **Table C1**. They are traceable to the respective NIST reference solutions. The Sigma-Aldrich In solution was prepared by dissolving high-purity In metal (Kirchenbaur et al., 2018).

4.2.3 Spike calibration

Commercially available spikes for Cu, Zn, Ga, Cd, In, Sn and Tl in metal form were dissolved and initially diluted at the Institut für Geologie at the Freie Universität Berlin. Primary ^{65}Cu, ^{110}Cd, ^{113}In and ^{203}Tl used here are the same as in Wang et al. (2014) and ^{117}Sn and ^{113}In spike solutions were also used by Kirchenbaur et al. (2018). The ^{109}Ag spike solution in 5 % HNO_3 was obtained from Inorganic Ventures. All spike solutions were further diluted to obtain the mass fractions listed in **Table C2**. The diluted solutions were then calibrated against reference solutions (**Table C1**) via reverse isotope dilution. To this end, seven to ten spike-calibration standard mixtures at different ratios were prepared gravimetrically. To ensure equilibration of the spike-standard mixtures screw-top Savillex beakers containing the blends were heated to 120 °C and left on the hotplate for at least 24 h. Silver spike calibration was carried out in new PFA beakers that were exclusively cleaned with 10 % HNO_3, to avoid the formation of insoluble AgCl.

After equilibration the spike-standard mixtures were evaporated to dryness at 90°C and re-dissolved in 0.28 mol l^{-1} HNO_3 (0.28 mol l^{-1} HNO_3 - 0.012 mol l^{-1} HF for Sn) for ICP-MS measurement. Mass fractions for each spike solution refer to the mean calculated from all spike-calibration solution mixtures and the uncertainties are reported as the 2s standard deviation of the seven to ten mixtures (**Table C2**). Only dilutions denominated SSp 1 (Secondary Spike 1) were calibrated against reference solutions. Further dilutions (SSp 2 and SSp 3) were prepared gravimetrically directly from calibrated SSp 1.

4.2.4 Sample preparation

Typically, 100 - 300 mg sample powder was digested and at least three replicate digestions were made for each RM. The carbonaceous chondrites Orgueil (80 mg) and Murchison (50 mg) were only digested once in Parr bombs. Allende Smithsonian was digested twice. Once in the

DAS-30 (125 mg) and once in Parr bombs (70 mg). For all meteorite samples, 10 % aliquots were taken and spiked after digestion.

Tabletop digestion

Tabletop digestion was applied for basaltic samples and closely resembles the procedure described by Kirchenbaur et al. (2018). Approximately 100 mg of sample powder were weighted into 15 ml PFA beakers and subsequently spiked with appropriate amounts of spike solutions. Spiked samples were then digested with 3 ml 14 mol l^{-1} HNO_3 and 3 ml 24 mol l^{-1} HF for 12-24 h at 120°C. After evaporation to dryness at 90°C, samples were dissolved in 1 ml 14 mol l^{-1} HNO_3 and dried down again. The dry down step was repeated twice to get rid of fluorite precipitates. Afterwards samples were dissolved in 5 ml 6 mol l^{-1} HCl and refluxed for 12 h at 120°C. Optically clear solutions were dried down at 90°C and taken up in 3 ml 4.5 mol l^{-1} HCl. The solution was refluxed for 12 h at 120°C and centrifuged before ion exchange separation.

Parr bomb and DAS-30 digestion

Ultramafic rocks, sedimentary rocks, carbonaceous chondrites and felsic samples (SiO_2>56 wt.%) were first dissolved in 3 ml 14 mol l^{-1} HNO_3 and 3 ml 24 mol l^{-1} HF on a hotplate at 120°C for 12 h and evaporated to dryness at 90°C subsequently. Another 3 ml 14 mol l^{-1} HNO_3 and 3 ml 24 mol l^{-1} HF were then added to the samples. Closed beakers were placed into steel-jacketed Parr pressure vessels with Teflon inliners, which were heated in an oven and kept at 180°C for 72 h. After cooling down, solutions were evaporated to dryness at 90°C and treated as described above for tabletop digestion. One Allende sample was digested in a 30 ml PTFE beaker using the PicoTrace DAS-30 pressure digestion system and the same acid mixtures as with the Parr bombs.

4.2.5 Chemical separation

For the chemical separation of Cu, Zn, Ga, Ag, Cd, In, Sn and Tl from rock matrices, a two-step procedure based on the one described in Wang et al. (2014) was applied. All elements were separated from the same sample aliquot using 1.8 ml anion exchange resin AG MP-1 100-200 mesh. Details of the separation procedure are given in **Table 4.2**. The 10 ml of 0.4 mol l^{-1} HCl contain Ga, In and Cu with most of the Fe matrix. The following collection of Ag (4 ml 8 mol l^{-1} HCl), Sn (12 ml 3 mol l^{-1} HF - 2 mol l^{-1} HCl), Zn (10 ml 0.05 mol l^{-1} HCl) and Cd (6 ml 1.4 mol l^{-1} HNO_3) was slightly modified from Loss et al. (1990). Thallium was collected together with Bi in 14 ml 0.5 mol l^{-1} HF.

Table 4.2: Chemical separation procedure.

1	**1.8 ml AG MP-1 anion exchange resin**	
Step	**Acid**	**Volume (ml)**
Resin cleaning	1.4 mol l^{-1} HNO_3	20
Resin conditioning	4.5 mol l^{-1} HCl	10
Sample loading	4.5 mol l^{-1} HCl	3
Elute matrix	4.5 mol l^{-1} HCl	3
Matrix + **Ga, In, Cu**[a]	0.4 mol l^{-1} HCl	10
Wash	8 mol l^{-1} HCl	1
Ag	8 mol l^{-1} HCl	4
Wash	3 mol l^{-1} HF - 2 mol l^{-1} HCl	4
Sn	3 mol l^{-1} HF - 2 mol l^{-1} HCl	12
Wash	0.05 mol l^{-1} HCl	2
Zn	0.05 mol l^{-1} HCl	10
Wash	1.4 mol l^{-1} HNO_3	2
Cd	1.4 mol l^{-1} HNO_3	6
Tl, Bi	0.5 mol l^{-1} HF	14
Resin cleaning	MilliQ	10

[a]Dry down and redissolve in 0.4 ml 8 M HCl + 0.4 ml 1 M ascorbic acid

2	**1.8 ml AG MP-1 anion exchange resin**	
Step	**Acid**	**Volume (ml)**
Resin cleaning	0.56 mol l^{-1} HNO_3	10
Resin conditioning	4.5 mol l^{-1} HCl	10
Load Matrix + Ga, In, Cu	4.5 mol l^{-1} HCl - 1 mol l^{-1} ascorbic acid	0.8
Elute matrix	4.5 mol l^{-1} HCl - 0.05 mol l^{-1} ascorbic acid	5
Ga[b]	2.5 mol l^{-1} HBr	6
In[b]	0.1 mol l^{-1} HCl	5
Wash	0.56 mol l^{-1} HNO_3	2
Cu	0.56 mol l^{-1} HNO_3	10
Resin cleaning	MilliQ	10
Resin cleaning	0.05 mol l^{-1} HCl	10

[b]Add 100 µl H_2O_2 repeatedly during dry down

The 10 ml 0.4 mol l^{-1} HCl fraction containing Ga, In and Cu was taken to dryness and re-dissolved in 0.4 ml 8 mol l^{-1} HCl. In order to elute Fe from the ion exchanger, it has to be reduced from Fe^{3+} to Fe^{2+}. To this end, 0.4 ml 1 mol l^{-1} ascorbic acid was added to the solution (Wang et al., 2014). After approximately 30 minutes the formerly yellow solution became colorless, indicating that all Fe was successfully reduced. The colorless solution was loaded on the same column as in the first step and the Fe matrix was eluted with additional and freshly prepared 5 ml 4.5 mol l^{-1} HCl and 0.05 mol l^{-1} ascorbic acid. Afterwards Ga was collected in

6 ml 2.5 mol l^{-1} HBr, followed by the collection of In in 5 ml 0.1 mol l^{-1} HCl. Finally, Cu was collected in 10 ml 0.56 mol l^{-1} HNO_3.

All element fractions were evaporated to dryness at 90°C and subsequently dissolved in 2 ml (Ag, Cd, Tl, In) or 10 ml (Cu, Zn, Ga) 0.28 mol l^{-1} HNO_3 for ICP-MS analyses. Because Sn is not stable in low molarity HNO_3 (Clayton et al., 2002) 2 ml 0.28 mol l^{-1} HNO_3 - 0.012 mol l^{-1} HF were added to the dry Sn fraction shortly before measurement.

4.2.6 Mass spectrometry

All isotope ratios were determined with a Thermo-Scientific iCapQ quadrupole ICP-MS at the Universität zu Köln (Germany). For all measurements conventional Ni sample and skimmer cones with a 2.8 mm insert were used.

Tin measurements were performed with a cyclonic PFA spray chamber cooled to 2.7°C by a Peltier element and equipped with an Elemental Scientific PFA nebulizer. Ion beam signals for ^{117}Sn, ^{120}Sn and ^{125}Te were collected to monitor the isobaric interference of ^{120}Te on ^{120}Sn.

For Zn and Cu measurements a cyclonic glass spray chamber cooled to 2.7°C equipped with a glass expansion micromist glass nebulizer was used. Ion beam signals were integrated for ^{66}Zn and ^{67}Zn and ^{63}Cu and ^{65}Cu, respectively. Isotope ratio measurements were performed in kinetic energy discrimination mode (KED) with a He cell gas flow rate of 5 ml/min, in order to reduce polyatomic interferences such as $^{27}Al^{40}Ar^+$ on ^{67}Zn or $^{23}Na^{40}Ar^+$ on ^{63}Cu.

For the determination of Ga, Ag, In, Cd and Tl mass fractions the ICP-MS was coupled with an Elemental Scientific ApexQ to keep oxide formation rates low ($CeO^+/Ce^+ < 0.007$) and simultaneously increase signal intensities. To further stabilize the signal, a cyclonic glass spray chamber was interposed between the ApexQ and the ICP-MS and N_2 was added in the ApexQ. Masses for ion beams integrated as well as further measurement details (number of sweeps and main runs, uptake and rinse time) are summarized in **Table C3**.

Background signals (0.28 mol l^{-1} HNO_3 or 0.28 mol l^{-1} HNO_3 - 0.012 ml l^{-1} HF) were measured after each sample to monitor memory effects. Background intensities were usually < 0.1% of sample signals. Only for Tl measurements background intensities contributed up to 3% to the sample signal. Therefore, background subtraction was carried out for Tl measurements.

Instrumental mass bias was monitored by measuring standard solutions of the respective elements. The deviation from the natural isotopic ratios (Meija et al., 2016) was determined and the mean of two standard solutions bracketing three samples was used to correct for the

instrumental mass bias in sample solutions. Isotopic ratios of the standard solutions (usually 12 measurements) were stable throughout each measurement series (relative variations between 0.05 - 0.3%).

Isobaric interference corrections were carried out for ^{110}Cd, ^{113}In, ^{115}In and ^{120}Sn using the monitor masses of ^{105}Pd, ^{111}Cd, ^{118}Sn and ^{125}Te, respectively.

4.3 RESULTS AND DISCUSSION

4.3.1 Interferences

Isobaric and polyatomic interferences can be serious problems during ICP-MS analyses. Here, chemical separation, kinetic energy discrimination and reduced oxide rates by desolvation using the ApexQ diminish interferences. After chemical separation ^{105}Pd/^{110}Cd intensity ratios were usually <0.007, but occasionally reached 0.1. However, such high ^{105}Pd/^{110}Cd were only observed for samples that were loaded on columns that were previously used for carbonaceous chondrites. Palladium sticks heavily to the anion resin and is difficult to remove (Rehkämper and Halliday, 1997). Carbonaceous chondrites have high abundances of Pd compared to terrestrial samples, therefore the anion resin needs to be discarded after carbonaceous chondrites were passed through the separation procedure.

Both In isotopes suffer from isobaric interferences, that were usually <0.005 for ^{111}Cd/^{113}In and <0.07 for ^{118}Sn/^{115}In. Only in BCR-2 the ^{111}Cd/^{113}In intensity ratio was up to 0.06 which results in interference corrections of 3 - 6%. For all other samples the interference correction is <1%. Ultramafic samples occasionally present higher ^{118}Sn/^{115}In intensity ratios of up to 0.5. However, the interfering ^{115}Sn isotope has an extremely low relative abundance (0.34%) which results in negligible corrections. In general, the chemical separation procedure applied here removed interferences efficiently, nevertheless isobaric interference correction was always carried out.

Oxide interferences are a potential problem especially for the two Ag isotopes, which can be affected by $^{91}Zr^{16}O^{+}$ and $^{93}Nb^{16}O^{+}$. Zirconium was completely removed via chemical separation from the Ag fraction, but ^{93}Nb/^{109}Ag intensity ratios reached between 1-5 in some basaltic samples because these samples have Nb/Ag ratios >100. To quantify $^{93}Nb^{16}O^{+}$ production rates, a pure Nb standard solution was measured several times during the measurement series. Because of the use of the ApexQ introduction system NbO^{+}/Nb^{+} was always <0.005 and thus negligible.

4.3.2 Total procedural blanks

Total procedural blanks were determined by ID-ICP-MS together with samples digested in the same series. Results are given in **Table 4.3**. For RM blanks were always subtracted. Blank subtraction was <0.05% for Cu, Ga, Cd and In and between 0.3 - 5% for Zn, Ag, Sn and Tl. Highest total procedural blank contributions were observed in DTS-2b for Cu, Ag, Cd, In and Tl, in PCC-1 for Ga and in RGM-1 for Zn. For carbonaceous chondrites blank subtraction was negligible (< 0.2%) with the highest blank contributions for Zn and Sn.

Table 4.3: Total procedural blanks.

Blank No.	Comment	Cu (µg)	Zn (µg)	Ga (ng)	Ag (ng)	Cd (ng)	In (ng)	Sn (ng)	Tl (ng)
Blank 1	DAS-30	0.0050	0.07	0.66	0.067	0.0140	0.0030	1.26	0.209
Blank 2	Bomb	0.0062	0.08	0.58	0.021	0.0053	0.0023	3.80	0.098
Blank 3	Tabletop	0.0005	0.15	0.29	0.041	0.0050	0.0138	0.42	0.012
Blank 4	Bomb	-	0.58	0.18	0.013	0.0060	0.0006	0.70	0.001
Blank 5	Bomb	0.0024	0.14	0.54	0.025	0.0110	0.0017	0.70	0.014
Blank 6	Tabletop	0.0071	0.01	0.49	0.016	-	0.0028	0.36	0.076
Mean		0.0042	0.17	0.46	0.030	0.0083	0.0040	1.21	0.068
1 s		0.0024	0.19	0.17	0.019	0.0036	0.0044	1.20	0.072
RSD (%)		58	110	37	61	44	110	99	106

4.3.3 Uncertainties

The combined uncertainty for individual mass fractions was calculated via Monte Carlo simulation including the following components: mass fraction of the spike solution, spike and sample weight, repeatability of isotope ratio measurements, mass bias correction, total procedural blank and interference subtractions, molar fraction of spike isotope in spike, molar fraction of reference isotope in sample, atomic weights of spike and sample. Uncertainties of individual measurements were typically between 1-3% for all elements and are given as 2s in **Table 4.4** along with mass fractions of the respective elements.

Three replicates were made for each geological RM (four for BCR-2 and DTS-2b). For some RM only two replicates for Cu mass fractions are available because Cu was lost during column separation in one series. The combined uncertainty of the mean values was calculated in line with Kirchenbaur et al. (2018) and Wang et al. (2014) from the combined measurement uncertainties of individual values of replicates (s_i) and the standard deviation of the replicates (s_r) according to the following equation, where n is the number of replicates:

$$u = \left(\left(\frac{s_r}{\sqrt{n}} \right)^2 + \frac{\sum {s_i}^2}{n} \right)^{\frac{1}{2}}$$

4.3.4 Geological reference materials

Data for reference materials are reported in **Table 4.4**. The accuracy of our data is assessed by comparing the results with literature data (**Figure 4.1 - 4.3**, **Table 4.5**). Copper, Zn and Ga mass fractions for the more common reference materials have been well determined in the literature, but only limited data exist for Ag, Cd, In, Sn and Tl. For comparison, we preferred literature data obtained by isotope dilution ICP-MS and other ICP-MS methods (**Figure 4.1 - 4.3**). Furthermore, we compare our data with recommended values from the GeoRem database and Jochum et al. (2016) and for some more recent RM with values provided in the certificates (MGL-GAS, OKUM,).

Basaltic/mafic and ultramafic igneous reference materials (BCR-2, BE-N, BHVO-1, BHVO-2, BIR-1, BRP-1, JB-2, OKUM, W-2, WS-E)

Mafic samples were digested via tabletop and Parr bomb procedures, except for BIR-1 which was only subjected to tabletop digestion while JB-2 and the ultramafic komatiite OKUM were only digested in Parr bombs. Mass fractions for all elements agree within 5% for both digestion techniques with one exception. In W-2 the Zn mass fraction is much higher for the Parr bomb digestion (81.3 and 84.1 µg g^{-1} Parr bombs (n=2) vs 31.6 µg g^{-1} table top (n=1). The reason for this discrepancy is unclear. Zhang et al. (2012) report a Zn mass fraction of 77.7 µg g^{-1} for W-2, which is closer to the higher Zn mass fractions determined here.

Copper, Zn, Ga, Ag, Cd, In and Tl mass fractions in replicates of basaltic and mafic samples agree mostly within <2% RSD. Tin mass fractions generally agree within 5% RSD and within 7% for W-2 and WS-E. The OKUM komatiite seems to be slightly more heterogeneous for Cu and Zn (4% and 6% RSD, respectively). Our mass fractions for Cu and Zn are 11 and 17% higher than the certified values provided by the IAG.

One replicate of BCR-2 yielded a four times lower Cd mass fraction than the other three replicates (**Table 4.4**). The same replicate had a 40% higher Ag mass fraction (45.9 ng g^{-1} compared to an average of 32.8 ng g^{-1}). Reasons for these discrepancies are unclear but because the other three replicates yielded consistent mass fractions for Cd and Ag, the first one was taken as an outlier and means are only calculated from the other three replicates. For Ag in BCR-2 only an information value is provided by Jochum et al. (2016) which is three times

higher (90 ng g^{-1}) than the mass fraction obtained here. Published Cd mass fractions for BCR-2 are highly variable (see GeoRem database), which might either be the result of heterogeneous distribution or analytical problems. BCR-2 contains extraordinary high amounts of Mo (250 µg g^{-1}) compared to other basaltic RM (e.g., 4 µg g^{-1} in BHVO-2, 2.75 µg g^{-1} in BE-N). If no matrix removal is carried out $^{95}Mo^{16}O^{+}$ may interfere with ^{111}Cd, the only isobaric interference-free Cd isotope. Therefore, the high and variable Cd mass fractions reported in the literature are likely due to analytical biases.

For Tl occasionally higher mass fractions were determined in BE-N and WS-E. In both cases the lower mass fractions could be confirmed by a second replicate. Therefore, the higher values were not considered for the calculations of the average. Interestingly Wang et al. (2014) report similar problems during Tl analysis. For BE-N the information value reported in Jochum et al. (2016) is 36.3 ± 9.2 ng g^{-1} and therefore within uncertainty in agreement with our average for BE-N (28.8 ±2.0 ng g^{-1}). For WS-E the GeoRem information value (210 ng g^{-1}) lies exactly between our data from table top and Parr bomb digestions. However, since we could reproduce the lower Parr bomb value (169 and 167 ng g^{-1}), we report 168 ng g^{-1} as the average Tl mass fraction in WS-E.

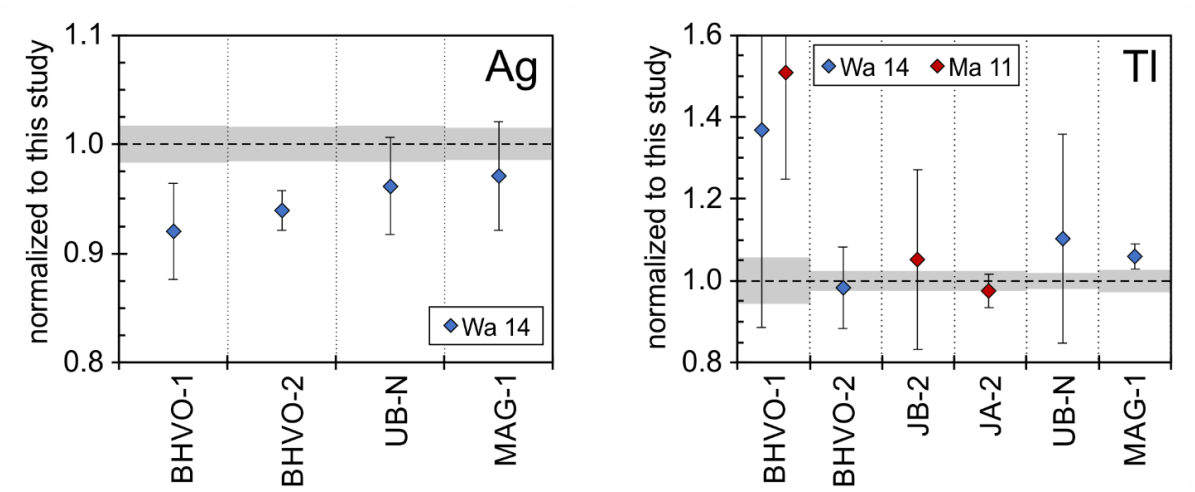

Figure 4.1: Comparison of Ag and Tl mass fractions with available ID data. Literature data were normalized to values determined in this study. Grey boxes denote 2s uncertainties. Wa 14 = Wang et al. (2014), Ma 11 = Makishima et al. (2011).

In comparison to the literature data reported in **Table 4.5** our mass fractions mostly fall within the range of previous data. For Cu, Zn and Ga relative deviations are generally <5% but tending towards slightly higher values (**Figure 4.3**). Silver, Cd, In, Sn and Tl mass fractions agree within 2-5% with literature data obtained via isotope dilution ICP-MS techniques (**Figure 4.1** and **4.2**) (Yi et al., 1995; Yi et al., 1998; Makishima et al., 2011; Cotta and Enzweiler, 2013; Wang et al., 2014; Khan et al., 2015; Kirchenbaur et al., 2018). For many basaltic RM no

isotope dilution data for comparison are available in the literature, especially for Ag, Cd and Tl. Therefore, the here determined mass fractions are often more precise than previous data which are mostly only information values. Furthermore, we report the first Ag mass fraction for OKUM and WS-E and the first Tl mass fraction for BRP-1.

Intermediate and felsic reference materials (AGV-2, G-2, JA-2, RGM-1)

All four felsic RM were digested with Parr bombs only. The determined mass fractions for the three replicates agree well within 5% RSD for all elements. Indium mass fractions even agree within 1% RSD. In comparison to literature data our precision is similar or better especially for Ag, Cd, In and Sn where barely any isotope dilution data exist. Where available, mass fractions of all elements agree within 5% RSD with previous data (**Figure 4.1** - **4.2**). Silver, Cd and In mass fractions are always lower than literature data obtained without isotope dilution (**Table 4.5**).

Ultramafic reference materials (MGL-GAS, DTS-2b, MUH-1, PCC-1, UB-N)

Determination of volatile element mass fractions in non-volcanogenic ultramafic RM is challenging because of their low abundances and nugget effects if trace elements are hosted in trace phases which can be difficult to digest. An incomplete digestion of refractory phases can lead to too low mass fractions (e.g., Meisel and Horan, 2015). Therefore, only limited literature data exist and we report the first Cd mass fractions for MGL-GAS and DTS-2b, first Ag mass fractions for MGL-GAS and MUH-1 and first In, Sn, Tl, Zn and Ga mass fractions for MGL-GAS.

During Parr bomb digestion refractory minerals such as spinel and chromite are not completely dissolved which was visible as black residues after digestion of DTS-2b and MUH-1. However, Kirchenbaur et al. (2018) and Wang et al. (2014) both state that there are no resolvable differences between calculated Cu, Ag, Cd, In, Sn and Tl mass fractions of replicates digested with either Parr bombs or high pressure asher (HPA-S). The higher operation temperature and pressure during HPA-S digestion results in a more efficient dissolution of refractory mineral phases. However, blanks are usually higher than for Parr bomb digestion and recoveries of some elements might be worse because of volatilization (Wang et al., 2014; Kirchenbaur et al., 2018). Therefore, we decided to do Parr bomb digestion only.

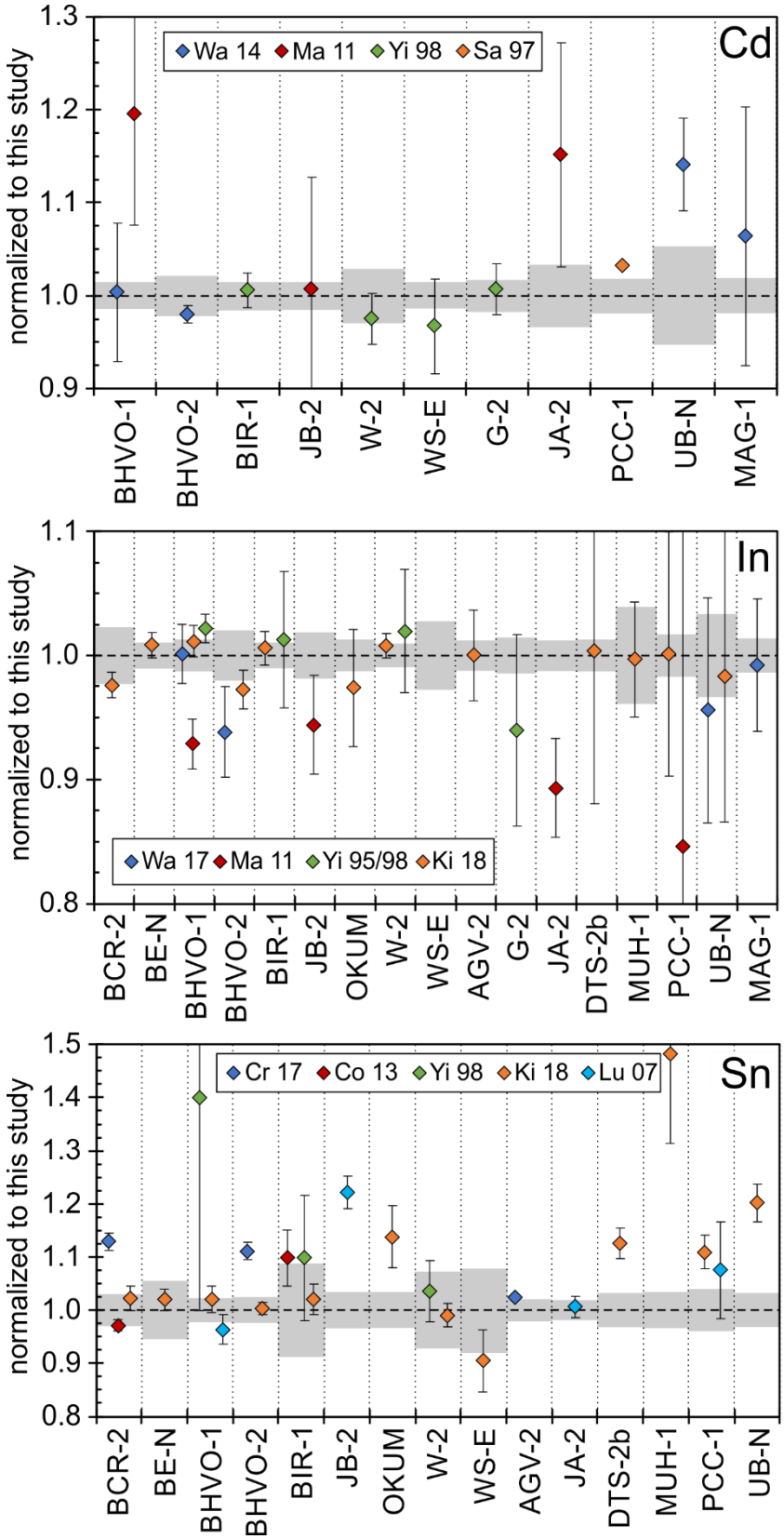

Figure 4.2: Comparison of Cd, In and Sn mass fractions with available ID data. Literature data were normalized to values determined in this study. Grey boxes denote 2s uncertainties. Cr 17 =Creech et al. (2017), Co 13 = Cotta and Enzweiler (2013), Yi 95 = Yi et al. (1995), Yi 98 = Yi et al. (1998), Ki 18 = Kirchenbaur et al. (2018), Lu 07 = Lu et al. (2007), Wa 14 = Wang et al. (2014), Ma 11 = Makishima et al. (2011), Sa 97 = Sands and Rosman (1997).

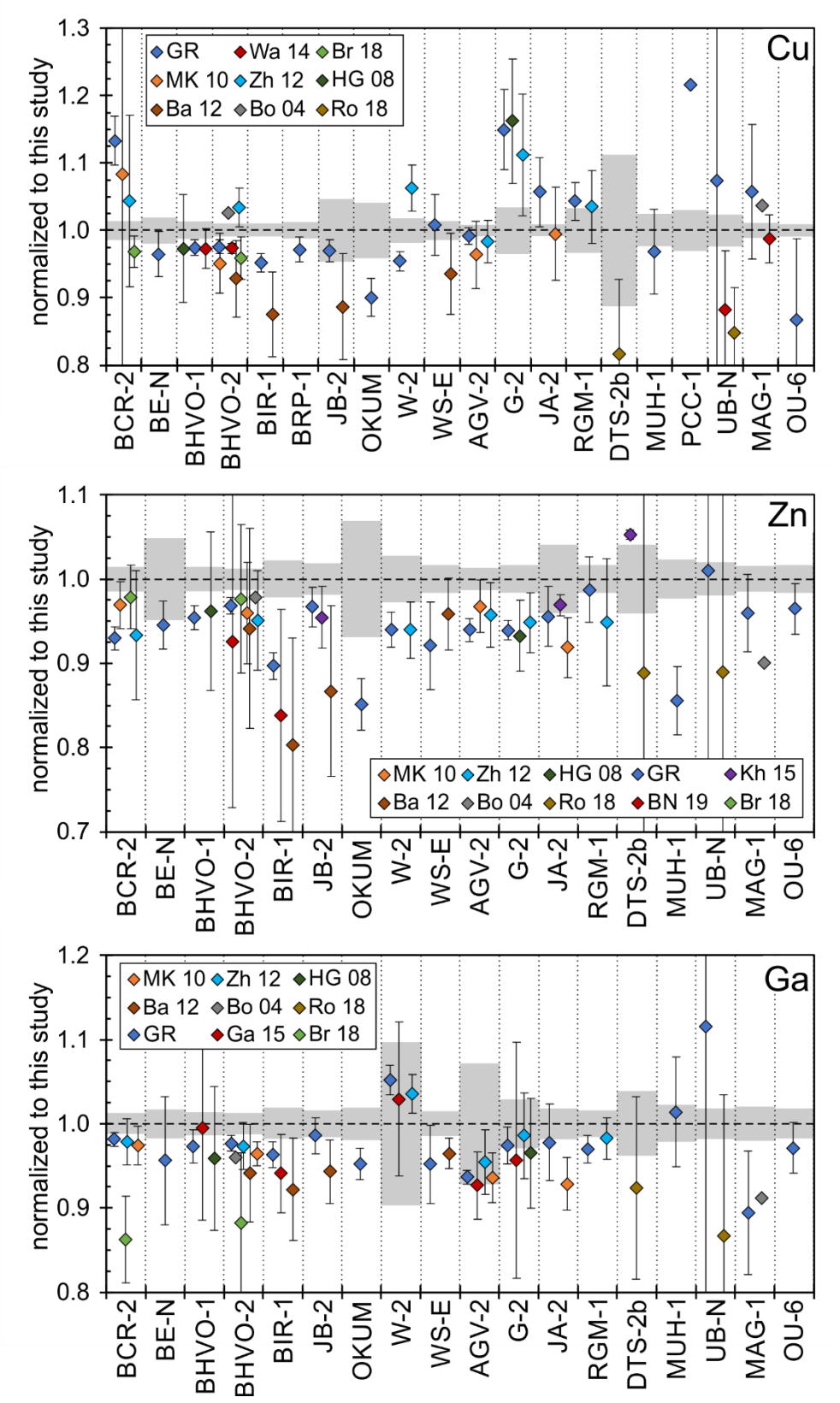

Figure 4.3: Comparison of Cu, Zn and Ga mass fractions with ICP-MS data. Literature data were normalized to values determined in this study. Grey boxes denote 2s uncertainties. GR = GeoRem Database, Wa 14 = Wang et al. (2014), Br 18 = Chapter 2, MK 10= Marx and Kamber (2010), Zh 12 = Zhang et al. (2012), HG 08 = Hu and Gao (2008), Ba 12 = Barrat et al. (2012), Bo 04 = Bouman et al. (2004), Ro 18 = Rospabé et al. (2018), Kh 15 = Khan et al. (2015), BN 19 = Burney and Neal (2019), Ga 15 = Gaschnig et al., 2015).

Table 4.4: Results for geological reference materials.

Sample	Digestion method	Weight (g)	Cu		Zn		Ga		Ag		Cd		In		Sn		Tl	
			µg g^{-1}	2s	µg g^{-1}	2s	µg g^{-1}	2s	ng g^{-1}	2s	ng g^{-1}	2s	ng g^{-1}	2s	µg g^{-1}	2s	ng g^{-1}	2s
BCR-2	Bomb	0.1026	17.15	0.19	137.8	1.5	22.47	0.28	32.94	0.42	198.7	1.7	97.1	1.1	2.114	0.036	269.2	4.6
BCR-2	Tabletop	0.1014	17.51	0.17	139.0	1.6	22.51	0.28	33.24	0.48	213.4	4.9	92.4	0.9	2.129	0.037	272.2	5.0
BCR-2	Tabletop	0.0996	17.43	0.15	140.6	1.6	22.51	0.28	32.26	0.43	200.4	4.0	92.7	0.8	2.064	0.035	269.5	4.9
BCR-2	Bomb	0.1004	17.32	0.16	139.8	1.5	22.47	0.20	(45.91)	0.56	(52.0)	0.4	92.0	0.8	2.038	0.036	268.3	4.7
Mean			17.35	0.22	139.3	1.9	22.49	0.26	32.78	0.64	204.1	8.5	93.5	2.1	2.086	0.061	269.8	5.0
BE-N	Tabletop	0.1009	72.2	0.5	137.0	1.5	18.05	0.23	43.83	1.23	68.5	0.5	73.24	0.66	1.860	0.033	(88.3)	1.7
BE-N	Bomb	0.1011	-	-	128.1	1.5	17.76	0.20	43.82	0.87	73.5	0.6	73.36	0.63	1.862	0.034	30.1	0.6
BE-N	Tabletop	0.0985	70.5	0.6	124.7	1.4	18.15	0.25	43.94	0.89	67.2	0.6	72.29	0.63	1.841	0.160	27.4	0.6
Mean			71.3	1.3	130.0	6.2	17.99	0.29	43.86	1.01	69.7	3.2	72.96	0.69	1.854	0.097	28.8	2.0
BHVO-1	Tabletop	0.1043	141.8	1.1	110.2	1.2	21.89	0.30	48.81	0.65	94.1	1.0	81.8	0.7	1.918	0.035	43.3	0.7
BHVO-1	Bomb	0.0962	-	-	109.3	1.4	51.86	0.25	48.83	0.73	93.3	1.5	83.5	0.7	1.933	0.034	44.2	0.8
BHVO-1	Tabletop	0.1011	139.9	1.1	111.2	1.2	21.95	0.30	48.97	0.97	93.6	1.2	83.5	0.7	1.942	0.035	39.8	0.8
Mean			140.8	1.7	110.2	1.5	21.90	0.29	48.87	0.80	93.7	1.3	82.9	1.0	1.931	0.037	42.4	2.3
BHVO-2	Tabletop	0.0991	132.9	1.1	107.9	1.2	21.85	0.25	47.54	0.67	93.7	1.4	85.7	0.8	1.695	0.030	20.44	0.42
BHVO-2	Tabletop	0.1004	132.3	1.1	107.3	1.2	21.92	0.26	47.06	0.68	96.5	1.3	87.9	0.8	1.707	0.030	20.40	0.40
BHVO-2	Bomb	0.1019	132.4	1.0	106.9	1.1	21.89	0.25	46.85	0.59	94.1	0.8	88.7	0.8	1.725	0.030	20.21	0.36
Mean			132.5	1.1	107.3	1.3	21.88	0.26	47.36	0.72	94.7	2.0	87.4	1.7	1.709	0.041	20.35	0.41
BIR-1	Tabletop	0.1052	126.8	0.9	78.1	0.9	15.95	0.24	31.83	0.42	95.2	1.0	54.00	0.47	0.713	0.013	2.24	0.04
BIR-1	Tabletop	0.1022	126.4	1.0	77.2	0.9	15.93	0.27	32.02	0.45	96.8	1.0	53.85	0.47	0.669	0.011	1.41	0.04
BIR-1	Tabletop	0.0988	127.1	1.0	80.1	0.9	16.27	0.20	31.79	0.49	96.2	1.4	53.58	0.48	0.696	0.012	1.34	0.04
Mean			126.8	1.0	78.5	1.7	16.05	0.29	31.88	0.47	96.0	1.4	53.81	0.52	0.692	0.024	1.66	0.48
BRP-1	Tabletop	0.0985	164.9	1.5	156.9	1.8	24.84	0.29	68.94	0.93	141.7	1.3	120.4	1.1	2.482	0.048	114.6	1.9
BRP-1	Tabletop	0.0968	165.4	1.3	153.3	1.9	24.85	0.25	68.51	0.96	181.8	1.4	119.6	1.1	2.480	0.049	115.3	1.9
BRP-1	Bomb	0.1008	163.6	1.4	151.8	1.7	24.58	0.27	69.02	0.76	141.4	1.6	122.8	1.3	2.469	0.046	115.0	1.9
Mean			164.7	1.7	154.0	3.1	24.71	0.30	68.82	0.92	141.6	1.4	120.9	2.0	2.477	0.059	115.0	2.0
JB-2	Tabletop	0.1006	236	3	114.5	1.3	16.92	0.21	72.8	0.9	140.6	1.2	74.0	0.7	0.577	0.010	35.61	0.61
JB-2	Bomb	0.1059	-	-	115.8	1.5	16.98	0.20	72.8	1.1	140.3	1.5	73.5	0.7	0.608	0.010	35.41	0.63
JB-2	Bomb	0.1078	222	2	112.3	1.2	16.68	0.23	70.8	1.1	138.1	1.3	71.7	0.6	0.579	0.010	34.66	0.64
Mean			229	11	114.2	2.1	16.86	0.26	72.1	1.5	139.6	1.9	73.1	1.3	0.588	0.020	35.23	0.79
OKUM	Bomb	0.0990	-	-	70.3	1.0	9.15	0.14	3.417	0.049	49.2	0.4	33.03	0.30	0.2183	0.0040	15.21	0.26
OKUM	Bomb	0.1008	47.0	0.4	77.6	0.9	9.33	0.15	3.469	0.046	50.5	0.5	32.85	0.30	0.2080	0.0036	15.04	0.27
OKUM	Bomb	0.1018	49.7	0.4	67.7	0.7	9.21	0.15	3.519	0.046	49.5	0.6	33.09	0.54	0.2074	0.0035	14.87	0.28
Mean			48.3	2.0	71.9	4.9	9.23	0.17	3.468	0.067	49.7	0.8	32.99	0.41	0.2112	0.0069	15.04	0.31

Sample	Digestion method	Weight (g)	Cu		Zn		Ga		Ag		Cd		In		Sn		Tl	
			µg g^{-1}	2s	µg g^{-1}	2s	µg g^{-1}	2s	ng g^{-1}	2s	ng g^{-1}	2s	ng g^{-1}	2s	µg g^{-1}	2s	ng g^{-1}	2s
W-2	Bomb	0.1047	112.2	0.9	81.3	0.9	15.1	0.2	42.6	0.6	77.6	0.5	59.28	0.55	1.84	0.03	95.3	1.6
W-2	Bomb	0.0990	-	-	84.1	1.1	18.1	0.2	39.8	0.7	73.7	0.6	59.40	0.53	1.62	0.03	96.2	1.6
W-2	Tabletop	0.0999	109.8	0.9	(31.6)	0.9	18.0	0.2	40.7	0.5	73.9	0.8	59.34	0.57	1.62	0.03	95.6	2.0
Mean			111.0	1.9	82.7	2.2	17.0	1.6	41.0	1.5	75.1	2.2	59.34	0.55	1.69	0.12	95.7	1.8
WS-E	Tabletop	0.1006	65.13	0.53	121.4	1.3	22.80	0.30	46.6	0.6	120.5	1.2	90.23	0.80	20.8	1.4	167.2	2.9
WS-E	Bomb	0.0993	-	-	124.3	1.5	22.57	0.25	53.4	0.7	122.1	1.4	90.52	0.82	19.0	1.2	168.9	2.8
WS-E	Tabletop	0.0999	66.15	0.50	123.7	1.4	22.70	0.33	49.0	0.9	121.0	1.7	90.07	0.78	19.8	1.3	(264.9)	5.1
Mean			65.64	0.89	123.1	2.0	22.69	0.32	49.7	3.3	121.2	1.6	90.28	0.83	19.9	1.5	168.0	3.1
AGV-2	Bomb	0.1036	52.01	0.37	91.7	1.0	21.1	0.3	53.73	0.66	70.25	0.50	43.04	0.39	2.043	0.037	283.8	5.0
AGV-2	Bomb	0.0968	51.81	0.39	92.6	1.2	20.8	0.2	53.51	0.87	68.63	0.55	43.28	0.38	2.003	0.036	288.2	5.1
AGV-2	Bomb	0.1003	52.06	0.34	92.5	1.0	23.7	0.5	54.62	0.75	68.96	0.71	43.95	0.41	2.017	0.035	282.1	6.7
Mean			51.96	0.39	92.3	1.2	21.8	1.6	53.95	0.94	69.28	1.00	43.43	0.50	2.021	0.040	284.7	6.4
G-2	Bomb	0.0996	9.75	0.08	87.9	1.0	23.64	0.26	30.20	0.40	14.56	0.22	27.13	0.24	1.647	0.029	895	20
G-2	Bomb	0.0997	9.73	0.07	89.9	1.2	23.48	0.24	31.20	0.42	14.84	0.16	27.73	0.27	1.683	0.030	908	22
G-2	Bomb	0.1001	9.17	0.06	88.9	1.0	24.70	0.37	29.69	0.40	14.65	0.21	27.52	0.25	1.640	0.029	879	21
Mean			9.55	0.32	88.9	1.4	23.94	0.69	30.36	0.83	14.68	0.24	27.46	0.39	1.657	0.037	894	25
JA-2	Bomb	0.0972	27.44	0.21	65.8	0.7	17.13	0.31	37.07	0.47	61.8	0.4	38.87	0.35	1.546	0.027	367.6	6.5
JA-2	Bomb	0.0985	-	-	70.6	1.0	17.13	0.21	36.17	0.66	65.8	0.8	39.31	0.35	1.544	0.027	362.0	6.5
JA-2	Bomb	0.1046	27.45	0.23	65.9	0.7	17.41	0.24	36.57	0.59	62.6	0.8	39.38	0.38	1.548	0.027	358.8	6.8
Mean			27.44	0.22	67.5	2.7	17.23	0.30	36.60	0.72	63.4	2.1	39.19	0.44	1.546	0.027	362.8	7.8
RGM-1	Bomb	0.0995	10.39	0.08	33.45	0.36	16.68	0.20	90.9	1.2	63.0	0.4	29.85	0.28	4.18	0.10	905	21
RGM-1	Bomb	0.0990	11.03	0.07	33.83	0.69	16.51	0.21	90.4	1.2	62.8	0.5	29.92	0.27	3.98	0.09	906	22
RGM-1	Bomb	0.1072	10.47	0.09	33.62	0.37	16.49	0.30	89.5	1.1	61.2	1.1	29.30	0.27	4.16	0.09	892	31
Mean			10.63	0.34	33.63	0.53	16.56	0.26	90.3	1.4	62.3	1.1	29.69	0.42	4.11	0.14	901	26
DTS-2b	Bomb	0.2015	3.16	0.03	58.3	0.6	1.100	0.011	1.141	0.018	11.59	0.11	2.021	0.018	0.568	0.010	0.697	0.011
DTS-2b	Bomb	0.2019	-	-	52.7	0.8	1.018	0.008	1.149	0.021	9.93	0.09	1.993	0.018	0.559	0.009	0.421	0.008
DTS-2b	Bomb	0.2018	2.58	0.02	53.9	0.6	(2.012)	0.023	1.113	0.025	10.20	0.13	2.059	0.020	0.546	0.010	0.178	0.005
DTS-2b	Bomb	0.3077	2.61	0.03	54.8	0.6	1.059	0.013	1.052	0.050	9.57	0.17	2.021	0.090	0.540	0.010	0.232	0.010
Mean			2.78	0.31	54.9	2.2	1.059	0.040	1.114	0.050	10.32	0.78	2.023	0.025	0.553	0.017	0.382	0.203
MGL-GAS	Bomb	0.2012	7.186	0.059	40.61	0.43	0.921	0.011	13.2	0.2	20.50	0.14	3.470	0.033	0.0458	0.0009	3.62	0.06
MGL-GAS	Bomb	0.1967	-	-	40.45	0.74	0.923	0.012	17.1	0.3	22.02	0.20	3.398	0.037	0.0317	0.0009	3.77	0.07
MGL-GAS	Bomb	0.1016	1.099	0.051	(71.5)	0.80	0.942	0.009	14.4	0.3	20.15	0.22	3.365	0.035	0.0381	0.0008	3.83	0.08
Mean			7.143	0.083	40.53	0.61	0.929	0.015	14.9	1.9	20.89	0.96	3.411	0.061	0.0385	0.0067	3.74	0.12

Sample	Digestion method	Weight (g)	Cu		Zn		Ga		Ag		Cd		In		Sn		Tl	
			µg g^{-1}	2s	µg g^{-1}	2s	µg g^{-1}	2s	ng g^{-1}	2s	ng g^{-1}	2s	ng g^{-1}	2s	µg g^{-1}	2s	ng g^{-1}	2s
MUH-1	Bomb	0.2013	20.00	0.19	52.3	0.6	1.333	0.014	8.5	0.1	17.66	0.12	6.37	0.06	0.0393	0.0007	3.594	0.060
MUH-1	Bomb	0.1510	19.19	0.16	52.9	0.6	1.365	0.019	9.3	0.1	17.45	0.15	6.27	0.07	0.0389	0.0008	3.589	0.070
MUH-1	Bomb	0.1497	19.96	0.16	50.8	0.5	1.386	0.010	12.3	0.1	17.80	0.27	6.76	0.08	0.0411	0.0009	3.701	0.080
Mean			19.72	0.46	52.0	1.2	1.361	0.029	10.0	1.9	17.64	0.26	6.46	0.25	0.0398	0.0013	3.628	0.092
PCC-1	Bomb	0.2000	8.04	0.09	44.81	0.48	0.581	0.007	(8.57)	0.19	15.40	0.12	3.512	0.038	1.109	0.023	0.612	0.011
PCC-1	Bomb	0.1978	8.49	0.09	45.32	0.77	0.608	0.007	3.81	0.06	15.71	0.13	3.538	0.041	1.048	0.019	0.658	0.012
PCC-1	Bomb	0.1984	8.12	0.08	46.22	0.49	0.617	0.008	3.54	0.05	15.28	0.23	3.588	0.054	1.029	0.018	0.583	0.014
Mean			8.22	0.24	45.45	0.91	0.602	0.019	3.67	0.20	15.46	0.27	3.546	0.057	1.062	0.044	0.618	0.038
UB-N	Bomb	0.1990	26.64	0.19	83.3	1.0	2.647	0.030	46.73	0.61	33.5	0.2	11.39	0.10	0.3327	0.0059	39.25	0.65
UB-N	Bomb	0.1505	25.46	0.16	83.5	0.9	2.728	0.030	46.32	0.69	37.2	0.3	11.91	0.22	0.3180	0.0057	39.03	0.70
UB-N	Bomb	0.0994	26.11	0.19	85.8	0.9	2.691	0.020	47.29	0.52	34.6	0.6	11.22	0.14	0.3320	0.0055	38.78	0.68
Mean			26.07	0.59	84.2	1.6	2.689	0.047	46.78	0.77	35.1	1.8	11.51	0.38	0.3275	0.0097	39.02	0.71
MAG-1	Bomb	0.0997	28.26	0.22	134.0	1.6	22.62	0.38	61.92	0.76	201.1	1.5	75.4	0.7	3.494	0.070	(628)	12
MAG-1	Bomb	0.0992	-	-	136.1	1.7	22.66	0.29	61.56	0.86	201.1	1.8	75.3	0.7	3.496	0.069	749	17
MAG-1	Bomb	0.0993	28.46	0.25	136.3	1.5	23.20	0.25	61.86	0.94	206.8	2.2	76.3	1.2	3.498	0.071	743	20
Mean			28.36	0.28	135.5	2.0	22.82	0.44	61.78	0.88	203.0	3.6	75.6	1.0	3.496	0.070	746	19
OU-6	Bomb	0.0997	46.67	0.35	114.6	1.2	24.71	0.30	15.5	0.2	24.15	0.21	85.0	0.8	2.507	0.050	563	11
OU-6	Bomb	0.1019	-	-	116.5	1.4	24.72	0.29	17.2	0.3	23.98	0.22	84.7	0.8	2.509	0.046	563	13
OU-6	Bomb	0.1020	46.55	0.36	(137.0)	1.6	25.24	0.34	17.9	0.2	25.51	0.32	90.4	0.9	2.521	0.045	563	12
Mean			46.61	0.36	115.5	1.9	24.89	0.42	16.9	1.2	24.55	0.83	86.7	3.2	2.512	0.048	563	12

Values in brackets are taken as outliers and are not used to calculate the mean.

In general replicates for ultramafic RM agree within 3-6 % 2RSD for all elements. However, the variability is larger for Cu, Cd and Tl in DTS-2b (**Table 4.4**), which is the sample with the lowest mass fractions of these elements. Especially the Tl mass fraction is extremely low (0.38±0.20 ng g^{-1}) and blank and background subtractions were up to 3.4 and 9% respectively. For more precise analyses of sub ng g^{-1} Tl mass fractions background signals need to be further diminished. Furthermore, one replicate of DTS-2b yielded a twice as high Ga mass fraction than the other three replicates (**Table 4.4**). Since 1.06 µg g^{-1} is in agreement with GeoRem data for Ga (0.93 µg g^{-1}) we assume that the high replicate is erroneous.

For MGL-GAS, a serpentinite from the Naran Massif in Mongolia, only Zn mass fractions are certified by the IAG and no data for the other elements are reported in GeoRem. Two replicates yielded a Zn mass fraction overlapping with the certified value (**Table 4.5**), while the third replicate yielded an almost two times higher mass fraction (71.5 µg g^{-1} compared to 40.5 µg g^{-1}). Silver and Sn mass fractions vary more than for UB-N, another serpentinite (**Table 4.4**). Silver mass fractions also scatter more in MUH-1 a harzburgite distributed by the IAG since 2015. No information on Ag mass fraction is available on GeoRem, thus the here determined value of 10.0 ng g^{-1} with the rather large RSD of 19% is the currently best estimate. Replicates of MUH-1 for Sn mass fractions are in good agreement (3.3% RSD) but are 30% lower than isotope dilution data from Kirchenbaur et al. (2018) (**Figure 4.2**). The two replicates analyzed by Kirchenbaur et al. (2018) scatter substantially (16% RSD) but even the lower value (54 ng g^{-1}) is still 26% higher than our value (40 ng g^{-1}).

Sedimentary reference materials (MAG-1, OU-6)

The two sedimentary RM were only digested with Parr bombs and mass fractions for replicates agree well within 3% RSD for all elements. In general, OU-6 a Cambrian slate from Wales appears less homogeneous than MAG-1 a marine mud. Silver, Cd and In mass fractions scatter considerably more between OU-6 replicates than between MAG-1 replicates. Furthermore, one digestion of OU-6 yielded a 20% higher Zn mass fraction than the average of the other two replicates, which are in good agreement with literature values (116 µg g^{-1} compared to 111 µg g^{-1} from GeoRem). On the other hand, for MAG-1 one out of three analysis yielded a 15% lower Tl mass fraction, while the higher values agree within error with isotope dilution data reported by Wang et al. (2014). For OU-6 no In data are listed in GeoRem, thus we report the first In mass fractions ever and the first high precision Ag, Cd, Sn and Tl mass fractions.

Table 4.5: Comparison with literature data.

Sample	Reference	Method	Cu		Zn		Ga		Ag		Cd		In		Sn		Tl	
			µg g^{-1}	2u	µg g^{-1}	2u	µg g^{-1}	2u	ng g^{-1}	2u	ng g^{-1}	2u	ng g^{-1}	2u	µg g^{-1}	2u	ng g^{-1}	2u
BCR-2			**17.35**	**0.22**	**139.3**	**1.9**	**22.49**	**0.26**	**32.78**	**0.64**	**204.1**	**8.5**	**93.5**	**2.1**	**2.086**	**0.061**	**269.8**	**5.0**
	GeoRem		19.66	0.72	129.5	1.8	22.07	0.19	(90)		(690)	(290)	(700)		2.28	0.13	267	18
	Kirchenbaur et al. (2018)	ID-MC-ICP-MS											91.27	0.94	2.136	0.048		
	Cotta and Enzweiler (2013)	ID-SF-ICP-MS													2.03	0.02		
	Chapter 2	SF-ICP-MS	16.8	0.4	136	12	19.4	1							2.52	0.06	279	8
	Creech et al. (2017)	DS-MC-ICP-MS													2.36	0.038		
	Hu and Gao (2008)	Q-ICP-MS									750		96		2.2		340	
	Marx and Kamber (2010)	Q-ICP-MS	18.8	6.4	135	4	21.9	0.5			227	46			2.37	0.3	255	4
	Zhang et al. (2012)	Q-ICP-MS	18.1	2.3	130	10	22	0.6									270	40
BE-N			**71.3**	**1.3**	**130.0**	**6.2**	**17.99**	**0.29**	**43.86**	**1.01**	**69.7**	**3.2**	**72.96**	**0.69**	**1.854**	**0.097**	**28.8**	**2.0**
	GeoRem		68.8	2.3	122.9	3.5	17.2	1.3	(40)		(200)		(70)		(1.68)	(0.32)	(36.3)	(9.2)
	Kirchenbaur et al. (2018)	ID-MC-ICP-MS											73.57	0.74	1.887	0.038		
BHVO-1			**140.8**	**1.7**	**110.2**	**1.5**	**21.90**	**0.29**	**48.87**	**0.80**	**93.7**	**1.3**	**82.9**	**1.0**	**1.931**	**0.037**	**42.4**	**2.3**
	GeoRem		137.2	1.6	105	1.5	21.32	0.42	(71)		107	13	(85.1)	(8.1)	2.09	0.15	(46.1)	(3.9)
	Wang et al. (2014)	ID-SF-ICP-MS	137	4					45	2	94	7	83	2			58	28
	Kirchenbaur et al. (2018)	ID-MC-ICP-MS											83.85	1.08	1.969	0.05		
	Yi et al. (1995, 1998)	ID-MC-ICP-MS											84.7	1	2.7	1.08		
	Gaschnig et al. (2015)	SA-ICP-MS					21.8	2.4	202	26.3	140	19.9	88.6	5.7	1.91	0.149	42	2.3
	Makishima et al. (2011)	ID-Q-ICP-MS									112	13	77	2			64	17
	Hu and Gao (2008)	Q-ICP-MS	137	11	106	10	21.0	1.8			100	22	95.0	20.1	2.01	0.16	45.0	5.6
	Lu et al. (2007)	ID-Q-ICP-MS													1.86	0.05		
BHVO-2			**132.5**	**1.1**	**107.3**	**1.3**	**21.88**	**0.26**	**47.36**	**0.72**	**94.7**	**2.0**	**87.4**	**1.7**	**1.709**	**0.041**	**20.35**	**0.41**
	GeoRem		129.3	1.4	103.9	1	21.37	0.2	(89)	(37)	152	49	117	45	1.776	0.059	22.4	1.5
	Wang et al. (2014)	ID-SF-ICP-MS	129	1					44.5	0.8	92.8	0.9	82	3			20	2
	Kirchenbaur et al. (2018)	ID-MC-ICP-MS											85	1.34	1.716	0.02		
	Chapter 2	SF-ICP-MS	127	4	105	4	19.3	1.6							1.73	0.04	21.2	1.8
	Barrat et al. (2012)	SF-ICP-MS	123	7	101	12	20.6	1.2										
	Bouman et al. (2004)	Q-ICP-MS	136		105		21				69		180		2.3		59	
	Burney and Neal (2019)	SA-ICP-MS			99.3	20			100	38	130	50	80	10			10	7.0
	Creech et al. (2017)	DS-MC-ICP-MS													1.90	0.03		
	Hu and Gao (2008)	Q-ICP-MS									95		88		1.8		26	
	Marx and Kamber (2010)	Q-ICP-MS	126	5.6	103	6	21.1	0.3			116	14			1.92	0.2	19	0.5
	Zhang et al. (2012)	Q-ICP-MS	137	4	102	6	21.3	0.6									25	4

Sample	Reference	Method	Cu		Zn		Ga		Ag		Cd		In		Sn		Tl	
			µg g^{-1}	2u	µg g^{-1}	2u	µg g^{-1}	2u	ng g^{-1}	2u	ng g^{-1}	2u	ng g^{-1}	2u	µg g^{-1}	2u	ng g^{-1}	2u
BIR-1			**126.8**	**1.0**	**78.5**	**1.7**	**16.05**	**0.29**	**31.88**	**0.47**	**96.0**	**1.4**	**53.81**	**0.52**	**0.692**	**0.024**	**1.66**	**0.48**
	GeoRem		120.7	1.6	70.4	1.1	15.46	0.23	(41)		77	17	(57.6)	(2.8)	0.701	0.067	2.1	0.7
	Kirchenbaur et al. (2018)	ID-MC-ICP-MS											54.13	0.74	0.706	0.02		
	Yi et al. (1995, 1998)	ID-MC-ICP-MS									96.5	1.8	54.5	3.0	0.76	0.09		
	Gaschnig et al. (2015)	SA-ICP-MS					15.1	0.7	37.8	6.8	94.7	4.5	55.9	4.4	0.7	0.04	1.4	0.3
	Cotta and Enzweiler (2013)	ID-SF-ICPMS													0.76	0.04		
	Barrat et al. (2012)	SF-ICP-MS	111	7	63	8	14.8	0.9										
	Burney and Neal (2019)	SA-ICP-MS			65.8	8.3			37	10	100	50	50	5			1	2
	Hu and Gao (2008)	Q-ICP-MS									95		60		0.69		2.1	
BRP-1			**164.7**	**1.7**	**154.0**	**3.1**	**24.71**	**0.30**	**68.82**	**0.92**	**141.6**	**1.4**	**120.9**	**2.0**	**2.477**	**0.059**	**115.0**	**2.0**
	GeoRem		160	3	142	2	24.8	0.6			(200)	(100)	(130)	(10)	(2.5)	(0.4)	(130)	(20)
	Silveira et al. (2013)	Q-ICP-MS	154		140		23.6				140				2.51			
JB-2			**229**	**11**	**114.2**	**2.1**	**16.86**	**0.26**	**72.1**	**1.5**	**139.6**	**1.9**	**73.1**	**1.3**	**0.588**	**0.020**	**35.23**	**0.79**
	GeoRem		222.1	3.6	110.4	2.6	16.62	0.36	(64)		(300)		(70)	(8)	0.635	0.054	34	3.6
	Makishima et al. 2011	ID-Q-ICP-MS									141	17	69	3			37	8
	Barrat et al (2012)	SF-ICP-MS	203	16	99.0	10	15.9	0.6										
	Khan et al. (2015)	ID-ICP-MS			109	4												
	Lu et al. (2007)	ID-Q-ICP-MS													0.718	0.022		
OKUM			**48.3**	**2.0**	**71.9**	**4.9**	**9.23**	**0.17**	**3.468**	**0.067**	**49.71**	**0.82**	**32.99**	**0.41**	**0.211**	**0.007**	**15.04**	**0.31**
	Kirchenbaur et al. (2018)	ID-MC-ICP-MS											32.13	1.52	0.24	0.014		
	Certificate		43.5	1.2	61.2	1.9	8.79	0.16										
W2			**111.0**	**1.9**	**82.7**	**2.2**	**17.0**	**1.6**	**41.0**	**1.5**	**75.1**	**2.2**	**59.34**	**0.55**	**1.69**	**0.12**	**95.7**	**1.8**
	GeoRem		105.9	1.5	77.7	1.6	17.88	0.31	(70)		74	14	(61)	(4.1)	1.92	0.12	104	13
	Kirchenbaur et al. (2018)	ID-MC-ICP-MS											59.81	0.58	1.674	0.038		
	Yi et al. (1995, 1998)	ID-MC-ICP-MS									73.2	2.0	60.5	3.0	1.75	0.10		
	Gaschnig et al. (2015)	SA-ICP-MS					17.5	1.6	106	8	98.7	13.8	58.5	6.9	1.72	0.13	91.8	7.9
	Hu and Gao (2008)	Q-ICP-MS									91		62		1.67		120	
	Zhang et al. (2012)	Q-ICP-MS	118	4	77.7	2.6	17.6	0.4									120	40
WS-E			**65.64**	**0.89**	**123.1**	**2.0**	**22.69**	**0.32**	**49.7**	**3.3**	**121.2**	**1.6**	**90.28**	**0.83**	**19.9**	**1.5**	**168.0**	**3.1**
	GeoRem		66.2	3	113.4	5.9	21.6	1.0	(<200)		(120)		(89)		(15)	(12)	(210)	
	Kirchenbaur et al. (2018)	ID-MC-ICP-MS											90.48	1.08	18	1.04		
	Yi et al. (1995, 1998)	ID-MC-ICP-MS									117	6	91.5	2	13.9	0.6		
	Barrat et al. (2012)	SF-ICP-MS	61.4	3.7	118	5	21.9	0.4										

Sample	Reference	Method	Cu		Zn		Ga		Ag		Cd		In		Sn		Tl	
			µg g^{-1}	2u	µg g^{-1}	2u	µg g^{-1}	2u	ng g^{-1}	2u	ng g^{-1}	2u	ng g^{-1}	2u	µg g^{-1}	2u	ng g^{-1}	2u
AGV-2			**51.96**	**0.39**	**92.3**	**1.2**	**21.8**	**1.6**	**53.95**	**0.94**	**69.28**	**1.00**	**43.43**	**0.50**	**2.021**	**0.040**	**284.7**	**6.4**
	GeoRem		51.51	0.65	86.7	1.2	20.42	0.17	(90)		184	69	(47.8)	(5.9)	1.83	0.25	275	10
	Kirchenbaur et al. (2018)	ID-MC-ICP-MS											43.43	1.58				
	Gaschnig et al. (2014)	SA-ICP-MS					20.2	0.81	174	13.6	136	9.8	45.3	1.8	1.9	0.122	276	30.9
	Creech et al. (2017)	DS-MC-ICP-MS													2.07			
	Hu and Gao (2008)	Q-ICP-MS									82		48		2.08		320	
	Marx and Kamber (2010)	Q-ICP-MS	50.1	2.5	89.3	2.8	20.4	0.6			121	10			2.24	0.36	265	4
	Zhang et al. (2012)	Q-ICP-MS	51.1	1.6	88.4	3.4	20.8	0.8									290	40
G-2			**9.55**	**0.32**	**88.9**	**1.4**	**23.94**	**0.69**	**30.36**	**0.83**	**14.68**	**0.24**	**27.46**	**0.39**	**1.657**	**0.037**	**894**	**25**
	GeoRem		10.98	0.65	83.5	1.0	23.32	0.52	(40)		(80)		(27.2)	(3)	1.72	0.19	884	26
	Yi et al. (1995, 1998)	ID-MC-ICP-MS									14.8	0.4	25.8	2.0				
	Gaschnig et al. (2014)	SA-ICP-MS					22.9	3.2	118	16	84.3	8.3	27.7	0.4	1.71	0.18	890	45
	Hu and Gao (2008)	Q-ICP-MS	11.1	1.03	82.9	3.5	23.1	1.5			14.0	4.8	28.0	3.1	1.73	0.20	920	54
	Zhang et al. (2012)	Q-ICP-MS	10.62	0.96	84.3	3.0	23.6	1.2										
JA-2			**27.44**	**0.22**	**67.5**	**2.7**	**17.23**	**0.30**	**36.60**	**0.72**	**63.4**	**2.1**	**39.19**	**0.44**	**1.546**	**0.027**	**362.8**	**7.8**
	GeoRem		29.0	1.5	64.5	2.3	16.85	0.77	(43)		(69)	(19)	(36.8)	(3.7)	1.69	0.15	330	13
	Makishima et al. 2011	ID-Q-ICP-MS									73	9	35	1			354	14
	Khan et al. 2015	ID-ICP-MS			65.4	0.8												
	Lu et al. (2007)	ID-Q-ICP-MS													1.56	0.03		
	Marx and Kamber (2010)	Q-ICP-MS	27.3	1.9	62	2.2	16	0.5			74	6			1.64	0.32	324	4
RGM-1			**10.63**	**0.34**	**33.63**	**0.53**	**16.56**	**0.26**	**90.3**	**1.4**	**62.3**	**1.1**	**29.69**	**0.42**	**4.11**	**0.14**	**901**	**26**
	GeoRem		11.09	0.31	33.2	1.3	16.06	0.27	(105)		(78)	(19)	(34)		4.34	0.61	990	150
	Hu and Gao (2008)	Q-ICP-MS									66		34		4.07		880	
	Zhang et al. (2012)	Q-ICP-MS	11	0.6	31.9	2.4	16.27	0.4										
DTS-2b			**2.78**	**0.31**	**54.9**	**2.2**	**1.059**	**0.040**	**1.114**	**0.050**	**10.32**	**0.78**	**2.023**	**0.025**	**0.553**	**0.017**	**0.382**	**0.203**
	GeoRem		(3)		(45)	(5)												
	Kirchenbaur et al. (2018)	ID-MC-ICP-MS											2.03	0.25	0.623	0.018		
	Rospabé et al. (2018)	SF-ICP-MS	2.27	0.50	48.8	6.8	0.978	0.106										
	Robin-Popieul et al. (2012)	Q-ICP-MS	3.33		50.2						2.88						0.879	
	Khan et al. 2015	Q-ICP-MS			57.8	0.3												
MGL-GAS			**7.143**	**0.083**	**40.53**	**0.61**	**0.929**	**0.015**	**14.9**	**1.9**	**20.89**	**0.96**	**3.411**	**0.061**	**0.039**	**0.0067**	**3.74**	**0.12**
	Certficate				39	3.0												

Sample	Reference	Method	Cu		Zn		Ga		Ag		Cd		In		Sn		Tl	
			µg g^{-1}	2u	µg g^{-1}	2u	µg g^{-1}	2u	ng g^{-1}	2u	ng g^{-1}	2u	ng g^{-1}	2u	µg g^{-1}	2u	ng g^{-1}	2u
MUH-1			**19.72**	**0.46**	**52.0**	**1.2**	**1.361**	**0.029**	**10.0**	**1.9**	**17.64**	**0.26**	**6.46**	**0.25**	**0.0398**	**0.0013**	**3.628**	**0.092**
	Certificate		19.1	1.2	44.5	1.8	1.38	0.09										
	Kirchenbaur et al. (2018)	ID-MC-ICP-MS											6.44	0.30	0.059	0.01		
PCC-1			**8.22**	**0.24**	**45.45**	**0.91**	**0.602**	**0.019**	**3.67**	**0.20**	**15.46**	**0.27**	**3.546**	**0.057**	**1.062**	**0.044**	**0.618**	**0.038**
	GeoRem		10		42.0		(0.7)		(8)		19		3.7		1.6		2	
	Kirchenbaur et al. (2018)	ID-ICPMS											3.55	0.35	1.176	0.038		
	Makishima et al. 2011	Q-ICPMS ID-IS									90	18	3	0.8			7	6
	Lu et al. (2007)	ID-Q-ICP-MS													1.14	0.10		
	Sands and Rosman (1997)	ID-TIMS									16							
UB-N			**26.07**	**0.59**	**84.2**	**1.6**	**2.689**	**0.047**	**46.78**	**0.77**	**35.1**	**1.8**	**11.51**	**0.38**	**0.328**	**0.0097**	**39.02**	**0.71**
	GeoRem		28	8.49	85	22	3	5			49		15				60	
	Wang et al. (2014)	ID-SF-ICP-MS	23	2					45	2	40	2	11	1			43	11
	Kirchenbaur et al. (2018)	ID-MC-ICP-MS											11.32	1.33	0.393	0.014		
	Rospabé et al. (2018)	SF-ICP-MS	22.1	3.0	74.9	17.1	2.33	0.39										
MAG-1			**28.36**	**0.28**	**135.5**	**2.0**	**22.82**	**0.44**	**61.78**	**0.88**	**203.0**	**3.6**	**75.6**	**1.0**	**3.496**	**0.070**	**746**	**19**
	GeoRem		30	3	130	6	20.4	1.5	80		202	30	(180)		(3.6)		(590)	
	Wang et al. (2014)	ID-SF-ICP-MS	28	1					60	3	216	30	75	4			791	24
	Bouman et al. (2004)	Q-ICP-MS	29.4		122		20.8				173		161		4.24		2090	
OU-6			**46.61**	**0.36**	**115.5**	**1.9**	**24.89**	**0.42**	**16.9**	**1.2**	**24.55**	**0.83**	**86.7**	**3.2**	**2.512**	**0.048**	**563**	**12**
	GeoRem		40.4	4.9	111.4	3.4	24.17	0.73	(<300)		(100)	20			2.67	0.19	(540)	(60)

Values in brackets denote information values on the GeoRem database.

ID-MC-ICP-MS = Isotope Dilution Multicollector ICP-MS, ID-SF-ICPMS = Isotope Dilution Sector Field ICP-MS, DS-MC-ICP-MS = Double Spike Mulricollector ICP-MS, Q-ICP-MS = Quadrupole ICP-MS, SA-ICP-MS = Standard Addition ICP-MS, Q-ICP-MS ID-IS = Quadrupole ICP-MS Isotope Dilution Internal Standard, ID-TIMS = Isotope Dilution Thermal Ionization Mass Spectrometry

4.3.5 Carbonaceous chondrites (Orgueil CI1, Murchison CM2, Allende CV3)

Three different carbonaceous chondrites were digested in Parr bombs and a second Allende Smithsonian (split 8, pos. 7) replicate with the DAS-30. Results are given in **Table 4.6** and **Figure 4.4** and are compared to literature data obtained by state of the art (ID)-ICP-MS analyses and from data compilations (Jarosewich et al., 1987; Lodders, 2003). In Chapter 2 the same the same meteorite samples were analyzed (but different powder aliquots for Allende Smithsonian and Murchison) using external calibration and SF-ICP-MS. The data agree within 10% or better, except Ga which is 10 to 21% higher and In which is 13% lower than in Chapter 2. The In mass fraction for Allende agrees within uncertainty with the isotope dilution data of Wang et al. (2014). Our Ga mass fractions agree better with the other literature data in **Table 4.6** (1-5% relative deviation) and therefore Ga mass fractions from Chapter 2 are probably systematically too low by 1o to 20 % (**Figure 4.4**).

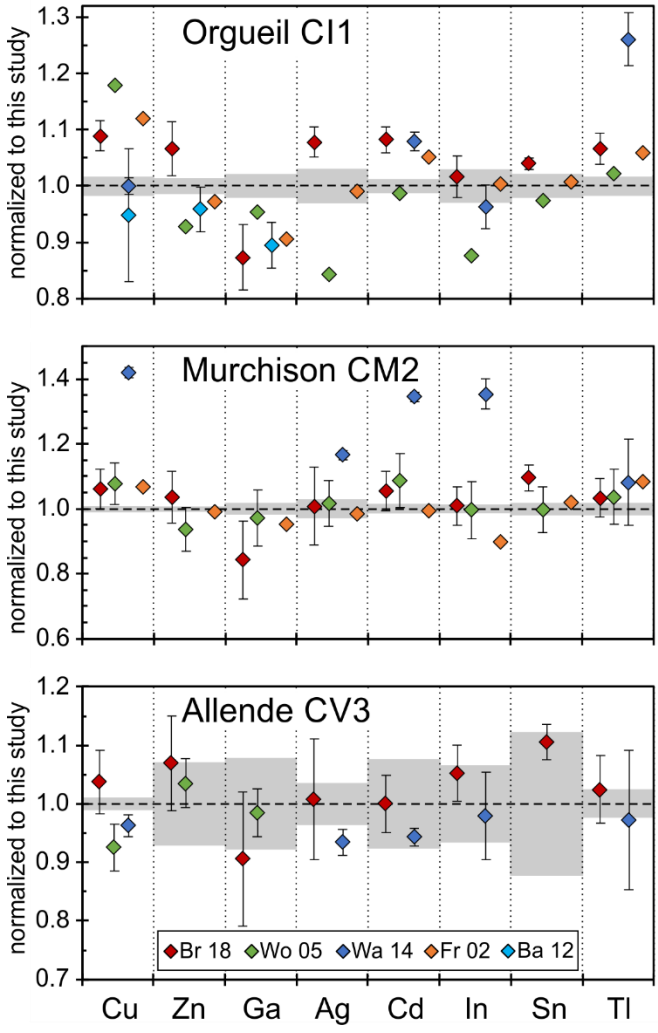

Figure 4.4: Comparison of mass fractions in carbonaceous chondrites with literature data. Literature data were normalized to values determined in this study. Grey boxes denote 2s uncertainties of this study. Br 18 = Chapter 2, Wo 05 = Wolf et al. (2005), Wa 14 = Wang et al. (2014), Fr 02 = Friedrich et al. (2002), Ba 12 =Barrat et al (2012).

Table 4.6: Results for carbonaceous chondrites and comparison with literature data.

Sample	Reference	Method	Cu		Zn		Ga		Ag		Cd		In		Sn		Tl	
			µg g^{-1}	2u	µg g^{-1}	2u	µg g^{-1}	2u	ng g^{-1}	2u	ng g^{-1}	2u	ng g^{-1}	2u	µg g^{-1}	2u	ng g^{-1}	2u
Allende			**107**	**0.9**	**109**	**1.1**	**5.46**	**0.08**	**97.6**	**1.2**	**517.1**	**6.6**	**26.8**	**0.2**	**0.55**	**0.01**	**61.0**	**2.5**
Smithsonian			**108**	**1.1**	**121**	**1.4**	**6.09**	**0.10**	**95.0**	**3.6**	**465.7**	**6.7**	**28.3**	**1.8**	**0.66**	**0.01**	**60.0**	**1.3**
Split 8/7	Wang et al. (2014)	ID-ICPMS	103	2					90	2	463	7	27	2			59	7
	Khan et al. 2015	ID-ICPMS			120	2												
	Barrat et al. (2012)	SF-ICPMS	99	4	119	5	5.68	0.23										
	Jarosewich et al. (1987)		119	38	110	10	6	2			432-580		29	2			53.1	
	Chapter 2	SF-ICPMS	111	6.6	123	9.2	5.23	0.60	97	10	491	24	29.0	1.4	0.67	0.020	62.2	3.6
Murchison			**131**	**0.9**	**189.8**	**2.1**	**8.25**	**0.13**	**126.8**	**2.1**	**400.3**	**5.3**	**47.30**	**0.48**	**0.87**	**0.02**	**83.2**	**1.6**
	Wang et al. (2014)	ID-ICPMS	186	3					148	2	538	8	64	3			90	12
	(Wolf et al., 2005)	Q-ICP-MS	141	9	178	12	8.01	0.69	129	9	435	36	47.1	4.2	0.870	0.061	86.3	7.2
	Friedrich et al. (2002)	Q-ICP-MS/RNAA	140		188		7.85		125		398		42.4		0.890		90.2	
	Chapter 2	SF-ICPMS	136	9.0	192	15	6.81	0.82	123	15	422	25	47.7	2.9	0.990	0.040	85.3	5.1
Orgueil			**134.0**	**1.5**	**316**	**3.6**	**10.6**	**0.24**	**204.4**	**6.2**	**643.6**	**6.9**	**80.0**	**2.2**	**1.490**	**0.028**	**134.2**	**2.4**
	Wang et al. (2014)	ID-ICPMS	134	2							695	12	77	3			169	8
	Lodders (2003)		131	40	318	52	9.57	1.36	203	36	675	90	78	9	1.66	0.32	144	20
	Wolf et al (2005)	Q-ICP-MS	158		293		10.1		172		636		73		1.45		137	
	Friedrich et al. (2002)	Q-ICP-MS/RNAA	150		307		9.6		202		677		80.3		1.5		142	
	Barrat et al. (2012)	SF-ICPMS	127	15	303	12	9.48	0.38										
	Chapter 2	SF-ICPMS	146	3.4	337	16	9.25	0.54	220	5.6	697	16	81.3	3.1	1.55	0.02	143	3.6

4.4 CONCLUSIONS

Copper, Zn, Ga, Ag, Cd, In, Sn and Tl mass fractions were determined in 21 geological RM and three carbonaceous chondrites from the same sample aliquot. All mass fractions were determined via isotope dilution Q-ICP-MS after HNO_3-HF digestion on hotplates and in Parr pressure digestion vessels. We developed an efficient chemical separation protocol to separate the elements of interest from the rock matrix to diminish isobaric and polyatomic interferences and increase ion beam intensities. Further reduction of polyatomic interferences during the ICP-MS analysis is achieved by using an ApexQ for sample introduction (Ga, Ag, Cd, In, Tl) or by using the collision cell mode (Cu, Zn). For many RM this is the first or second time that the mass fractions (in particular Ag, Cd, In, Sn and Tl) were determined at high precision.

Replicate analyses of RM agree in most cases within <5% RSD and means are generally consistent with literature data, thus validating the method. Some ultramafic RM show larger scatter between replicates. It is unclear whether the larger scatter is the result of incomplete sample digestion, sample heterogeneity or the generally low volatile element abundances in these samples. However, since often no literature data are available for these samples, our results are the best estimates currently, despite large uncertainties (up to 50% RSD).

References

Abreu N. M. and Brearley A. J. (2010) Early solar system processes recorded in the matrices of two highly pristine CR3 carbonaceous chondrites, MET 00426 and QUE 99177. *Geochim. Cosmochim. Acta* **74**, 1146–1171.

Al-Kathiri A., Hofmann B. A., Jull A. J. T. and Gnos E. (2005) Weathering of meteorites from Oman: Correlation of chemical and mineralogical weathering proxies with 14C terrestrial ages and the influence of soil chemistry. *Meteorit. Planet. Sci.* **40**, 1215–1239.

Alexander C. M. O., Bowden R., Fogel M. L., Howard K. T., K. H. C. D. and Nittler L. R. (2012) The provenances of asteroids, and their contributions to the volatile inventories of the terrestrial planets. *Science (80-.).* **337**, 721–3.

Alexander C. M. O. D. (2004) Chemical equilibrium and kinetic constraints for chondrule and CAI formation conditions. *Geochim. Cosmochim. Acta* **68**, 3943–3969.

Alexander C. M. O. D. (2005) Re-examining the role of chondrules in producing the elemental fractionations in chondrites. *Meteorit. Planet. Sci.* **40**, 943–965.

Alexander C. M. O. D., Fogel M., Yabuta H. and Cody G. D. (2007) The origin and evolution of chondrites recorded in the elemental and isotopic compositions of their macromolecular organic matter. *Geochim. Cosmochim. Acta* **71**, 4380–4403.

Alexander C. M. O. D., Howard K. T., Bowden R. and Fogel M. L. (2013) The classification of CM and CR chondrites using bulk H, C and N abundances and isotopic compositions. *Geochim. Cosmochim. Acta* **123**, 244–260.

Allègre C., Manhès G. and Lewin É. (2001) Chemical composition of the Earth and the volatility control on planetary genetics. *Earth Planet. Sci. Lett.* **185**, 49–69.

Allen L. A., Leach J. J. and Houk R. S. (1997) Spatial Location of the Space Charge Effect in Individual Ion Clouds Using Monodisperse Dried Microparticulate Injection with a Twin Quadrupole Inductively Coupled Plasma Mass Spectrometer. *Anal. Chem.* **69**, 2384–2391.

Amelin Y., Krot A. N., Hutcheon I. D. and Ulyanov A. A. (2002) Lead isotopic ages of chondrules and calcium-aluminum-rich inclusions. *Science (80-.).* **297**, 1678–1683.

Amsellem E., Moynier F., Pringle E. A., Bouvier A., Chen H. and Day J. M. D. (2017) Testing the chondrule-rich accretion model for planetary embryos using calcium isotopes. *Earth Planet. Sci. Lett.* **469**, 75–83.

Anders E. (1964) Origin, age, and composition of meteorites. *Space Sci. Rev.* **3**, 583.

Anders E. and Ebihara M. (1982) Solar-system abundances of the elements. *Geochim. Cosmochim. Acta* **46**, 2363–2380.

Anders E. and Grevesse N. (1989) Abundances of the elements: Meteoritic and solar. *Geochim. Cosmochim. Acta* **53**, 197–214.

Aries S., Valladon M., Polvé M. and Dupré B. (2000) A routine method for oxide and hydroxide interference corrections in ICP-MS chemical analysis of environmental and geological samples. *Geostand. Newsl.* **24**, 19–31.

Asplund M., Grevesse N., Sauval A. J. and Scott P. (2009) The Chemical Composition of the Sun. *Annu. Rev. Astron. Astrophys.* **47**, 481–522.

Baker R. G. A., Rehkämper M., Hinkley T. K., Nielsen S. G. and Toutain J. P. (2009) Investigation of thallium fluxes from subaerial volcanism—Implications for the present and past mass balance of thallium in the oceans. *Geochim. Cosmochim. Acta* **73**, 6340–6359.

Baker R. G. A., Rehkämper M., Ihlenfeld C., Oates C. J. and Coggon R. (2010a) Thallium isotope variations in an ore-bearing continental igneous setting: Collahuasi Formation, northern Chile. *Geochim. Cosmochim. Acta* **74**, 4405–4416.

Baker R. G. A., Schönbächler M., Rehkämper M., Williams H. M. and Halliday A. N. (2010b) The thallium isotope composition of carbonaceous chondrites - New evidence for live 205Pb in the early solar system. *Earth Planet. Sci. Lett.* **291**, 39–47.

Ballhaus C., Fonseca R. O. C., Münker C., Rohrbach A., Nagel T., Speelmanns I. M., Helmy H. M., Zirner A., Vogel A. K. and Heuser A. (2017) The great sulfur depletion of Earth's mantle is not a signature of mantle–core equilibration. *Contrib. to Mineral. Petrol.* **172**, 1–10.

Barnes S. J. and Ripley E. M. (2015) Highly siderophile and strongly chalcophile elements in magmatic ore deposits. *Rev. Mineral. Geochemistry* **81**, 725–774.

Barosch J., Hezel D. C., Ebel D. S. and Friend P. (2019) Mineralogically zoned chondrules in ordinary chondrites as evidence for open system chondrule behaviour. *Geochim. Cosmochim. Acta* **249**, 1–16.

Barrat J. A., Zanda B., Moynier F., Bollinger C., Liorzou C. and Bayon G. (2012) Geochemistry of CI chondrites: Major and trace elements, and Cu and Zn Isotopes. *Geochim. Cosmochim. Acta* **83**, 79–92.

Becker M., Hezel D. C., Schulz T., Elfers B. M. and Münker C. (2015) Formation timescales of CV chondrites from component specific Hf-W systematics. *Earth Planet. Sci. Lett.* **432**, 472–482.

Behrens H., Romano C., Nowak M., Holtz F. and Dingwell D. B. (1996) Near-infrared spectroscopic determination of water species in glasses of the system MAlSi3O8 (M = Li, Na, K) : an interlaboratory study. *Chem. Geol.* **128**, 41–63.

Berglund M. and Wieser M. E. (2011) Isotopic compositions of the elements 2009 (IUPAC Technical Report). *Pure Appl. Chem.* **83**.

Bischoff A., Geiger T., Palme H., Spettel B., Schultz L., P S., Loeken T., Bland P., Clayton R. N., Mayeda T. K., Herpers U., Meltzow B., Michel R. and Dittrich-Hannen B. (1994) Acfer 217 - a new member of the Rumuruti chondrite group (R). *Meteoritics* **29**, 264–274.

Bland P. A., Alard O., Benedix G. K., Kearsley A. T., Menzies O. N., Watt L. E. and Rogers N. W. (2005) Volatile fractionation in the early solar system and chondrule/matrix complementarity. *Proc. Natl. Acad. Sci. U. S. A.* **102**, 13755–13760.

Bland P. A., Jackson M. D., Coker R. F., Cohen B. A., Webber J. B. W., Lee M. R., Duffy C. M., Chater R. J., Ardakani M. G., McPhail D. S., McComb D. W. and Benedix G. K. (2009) Why aqueous alteration in asteroids was isochemical: High porosity ≠ high permeability. *Earth Planet. Sci. Lett.* **287**, 559–568.

Bland P. A., Zolensky M. E., Benedix G. K. and Sephton M. a (2006) Weathering of chondritic

meteorites. *Meteorites Early Sol. Syst. II*, 853–867.

Boujibar A., Andrault D., Bolfan-Casanova N., Bouhifd M. A. and Monteux J. (2015) Cosmochemical fractionation by collisional erosion during the Earth's accretion. *Nat. Commun.* **6**, 8295.

Bouman C., Elliott T. and Vroon P. Z. (2004) Lithium inputs to subduction zones. *Chem. Geol.* **212**, 59–79.

Bouvier A. and Wadhwa M. (2010) The age of the Solar System redefined by the oldest Pb-b age of a meteoritic inclusion. *Nat. Geosci.* **3**, 637–641.

Boyet M. and Carlson R. W. (2005) 142Nd Evidence for Early (>4.53 Ga) Global Differentiation of the Silicate Earth. *Science (80-.).* **309**, 576–581.

Brasser R., Dauphas N. and Mojzsis S. J. (2018) Jupiter's Influence on the Building Blocks of Mars and Earth. *Geophys. Res. Lett.* **45**, 5908–5917.

Brearley A. J. (1993) Matrix and fine-grained rims in the unequilibrated CO3 chondrite, ALHA77307: Origins and evidence for diverse, primitive nebular dust components. *Geochim. Cosmochim. Acta* **57**, 1521–1550.

Brearley A. J. (2014) *Nebular Versus Parent Body Processing*. 2nd ed., Elsevier Ltd.

Brown P. G., Hildebrand A. R., Zolensky M. E., Grady M., Clayton R. N., Mayeda T. K., Tagliaferri E., Spalding R., MacRae N. D., Hoffman E. L., Mittlefehldt D. W., Wacker J. F., Bird J. A., Campbell M. D., Carpenter R., Gingerich H., Glatiotis M., Greiner E., Mazur M. J., McCausland P. J. A., Plotkin H. and Rubak Mazur T. (2000) The Fall, Recovery, Orbit, and Composition of the Tagish Lake Meteorite: A New Type of Carbonaceous Chondrite. *Science (80-.).* **290**, 320–325.

Browning L. B., McSween H. Y. and Zolensky M. E. (1996) Correlated alteration effects in CM carbonaceous chondrites. *Geochim. Cosmochim. Acta* **60**, 2621–2633.

Brownlee D., Joswiak D. and Matrajt G. (2012) Overview of the rocky component of Wild 2 comet samples: Insight into the early solar system, relationship with meteoritic materials and the differences between comets and asteroids. *Meteorit. Planet. Sci.* **47**, 453–470.

Budde G., Burkhardt C., Brennecka G. A., Fischer-Gödde M., Kruijer T. S. and Kleine T. (2016a) Molybdenum isotopic evidence for the origin of chondrules and a distinct genetic heritage of carbonaceous and non-carbonaceous meteorites. *Earth Planet. Sci. Lett.* **454**, 293–303.

Budde G., Kleine T., Kruijer T. S., Burkhardt C. and Metzler K. (2016b) Tungsten isotopic constraints on the age and origin of chondrules. *Proc. Natl. Acad. Sci.* **113**, 2886–2891.

Burbidge E. M., Burbidge G. R., Fowler W. A. and Hoyle F. (1957) Synthesis of the Elements in Stars. *Rev. Mod. Phys.* **29**, 547–650.

Burkhardt C., Dauphas N., Hans U., Bourdon B. and Kleine T. (2019) *Elemental and isotopic variability in solar system materials by mixing and processing of primordial disk reservoirs*., The Author(s).

Burkhardt C., Kleine T., Oberli F., Pack A., Bourdon B. and Wieler R. (2011) Molybdenum isotope anomalies in meteorites: Constraints on solar nebula evolution and origin of the Earth. *Earth Planet. Sci. Lett.* **312**, 390–400.

Burney D. and Neal C. R. (2019) Method for quantifying and removing polyatomic

interferences on a suite of moderately volatile elements (Zn, Se, Rb, Ag, Cd, In, Sb, Tl, Pb, and Bi) during solution-mode ICP-MS. *J. Anal. At. Spectrom.* **00**, 1–9.

Burton A. S., Grunsfeld S., Elsila J. E., Glavin D. P. and Dworkin J. P. (2014) The effects of parent-body hydrothermal heating on amino acid abundances in CI-like chondrites. *Polar Sci.* **8**, 255–263.

Campbell I. H. and O'Neill H. S. C. (2012) Evidence against a chondritic Earth. *Nature* **483**, 553–558.

Carlson R. W., Brasser R., Yin Q. Z., Fischer-Gödde M. and Qin L. (2018) Feedstocks of the Terrestrial Planets. *Space Sci. Rev.* **214**.

Chambers J. E. (2001) Making More Terrestrial Planets. *Icarus* **152**, 205–224.

Chambers J. E. (2004) Planetary accretion in the inner Solar System. *Earth Planet. Sci. Lett.* **223**, 241–252.

Chaumard N. and Devouard B. (2016) Chondrules in CK carbonaceous chondrites and thermal history of the CV-CK parent body. *Meteorit. Planet. Sci.* **51**, 547–573.

Chaumard N., Devouard B., Delbo M., Provost A. and Zanda B. (2012) Radiative heating of carbonaceous near-Earth objects as a cause of thermal metamorphism for CK chondrites. *Icarus* **220**, 65–73.

Ciesla F. J. (2008) Radial Transport in the Solar Nebula: Implications for Moderately Volatile Element Depletions in Chondritic Meteorites. *Meteorit. Planet. Sci.* **655**, 31.

Clarke R. S., Jarosewich E., Mason B., Nelen J., Gomez M. and Hyde J. R. (1971) Allende, Mexico, Meteorite Shower. *Smithson. Contrib. to Earth Sci.*, 1–53.

Clay P. L., Burgess R., Busemann H., Ruzié-Hamilton L., Joachim B., Day J. M. D. and Ballentine C. J. (2017) Halogens in chondritic meteorites and terrestrial accretion. *Nature* **551**, 614–618.

Clayton R., Andersson P., Gale N. H., Gillis C. and Whitehouse M. J. (2002) Precise determination of the isotopic composition of Sn using MC-ICP-MS. *J. Anal. At. Spectrom.* **17**, 1248–1256.

Clayton R. N. and Mayeda T. K. (1999) Oxygen isotope studies of carbonaceous chondrites. *Geochim. Cosmochim. Acta* **63**, 2089–2104.

Clayton R. N. and Mayeda T. K. (2003) Oxygen isotopes in carbonaceous chondrites. In *Evolution of solar system materials: A new perspective from Antarctic meteorites* National Institute for Polar Research, Tokyo, Japan. pp. 13–14.

Clayton R. N., Mayeda T. K., Goswami J. N. and Olsen E. J. (1991) Oxygen isotope studies of ordinary chondrites. *Geochim. Cosmochim. Acta* **55**, 2317–2337.

Clayton R. N., Mayeda T. K. and Rubin A. E. (1984) Oxygen isotopic compositions of enstatite chondrites and aubrites. *J. Geophys. Res.* **89**, C245.

Cotta A. J. B. and Enzweiler J. (2013) Determination of Cr, Cu, Ni, Sn, Sr and Zn Mass Fractions in Geochemical Reference Materials by Isotope Dilution ICP-MS. *Geostand. Geoanalytical Res.* **37**, 35–50.

Cox D., Watt S. F. L., Jenner F. E., Hastie A. R. and Hammond S. J. (2019) Chalcophile element processing beneath a continental arc stratovolcano. *Earth Planet. Sci. Lett.* **522**, 1–11.

Creech J. B., Moynier F. and Badullovich N. (2017) Tin stable isotope analysis of geological materials by double-spike MC-ICPMS. *Chem. Geol.* **457**, 61–67.

Dauphas N. (2017) The isotopic nature of the Earth's accreting material through time. *Nature* **541**, 521–524.

Davidson J., Busemann H., Nittler L. R., Alexander C. M. O. D., Orthous-Daunay F. R., Franchi I. A. and Hoppe P. (2014) Abundances of presolar silicon carbide grains in primitive meteorites determined by NanoSIMS. *Geochim. Cosmochim. Acta* **139**, 248–266.

Davis A. M. (2006) Volatile Evolution and Loss. *Meteorites Early Sol. Syst. II*, 295.

Davis A. M., Alexander C. M. O., Nagahara H. and Richter F. M. (2005) Evaporation and Condensation During CAI and Chondrule Formation. *Chondrites Protoplanetary Disk* **341**, 432–455.

Day J. M. D. and Moynier F. (2014) Evaporative fractionation of volatile stable isotopes and their bearing on the origin of the Moon. *Philos. Trans. R. Soc. A Math. Phys. Eng. Sci.* **372**, 20130259–20130259.

Dodd R. T. (1969) Metamorphism of the ordinary chondrites: A review. *Geochim. Cosmochim. Acta* **33**, 161–203.

Doe B. R. and Stacey J. S. (1974) The application of lead isotopes to the problems of ore genesis and ore prospect evaluation: A review. *Econ. Geol.* **69**, 757–776.

Dreibus G. and Palme H. (1996) Cosmochemical constraints on the sulfur content in the Earth's core. *Geochim. Cosmochim. Acta* **60**, 1125–1130.

Dulski P. (1994) Interferences of oxide, hydroxide and chloride analyte species in the determination of rare earth elements in geological samples by inductively coupled plasma-mass spectrometry. *Fresenius. J. Anal. Chem.* **350**, 194–203.

Dunn T. L., Gross J., Ivanova M. A., Runyon S. E. and Bruck A. M. (2016) Magnetite in the unequilibrated CK chondrites: Implications for metamorphism and new insights into the relationship between the CV and CK chondrites. *Meteorit. Planet. Sci.* **51**, 1701–1720.

Ebel D. S., Brunner C., Konrad K., Leftwich K., Erb I., Lu M., Rodriguez H., Crapster-Pregont E. J., Friedrich J. M. and Weisberg M. K. (2016) Abundance, major element composition and size of components and matrix in CV, CO and Acfer 094 chondrites. *Geochim. Cosmochim. Acta* **172**, 322–356.

Elwaer N. and Hintelmann H. (2008) Selective separation of selenium (IV) by thiol cellulose powder and subsequent selenium isotope ratio determination using multicollector inductively coupled plasma mass spectrometry. *J. Anal. At. Spectrom.* **23**, 733–743.

Evans E. H. and Giglio J. J. (1993) Interferences in inductively coupled plasma mass spectrometry. A review. *J. Anal. At. Spectrom.* **8**, 1–18.

Fedkin A. V., Grossman L., Ciesla F. J. and Simon S. B. (2012) Mineralogical and isotopic constraints on chondrule formation from shock wave thermal histories. *Geochim. Cosmochim. Acta* **87**, 81–116.

Fegley B. and Palme H. (1985) Evidence for oxidizing conditions in the solar nebula from Mo and W depletions in refractory inclusions in carbonaceous chondrites. *Earth Planet. Sci. Lett.* **72**, 311–326.

Fehr M. A., Hammond S. J. and Parkinson I. J. (2018) Tellurium stable isotope fractionation in

chondritic meteorites and some terrestrial samples. *Geochim. Cosmochim. Acta* **222**, 17–33.

Fehr M. A., Rehkämper M., Halliday A. N., Schönbächler M., Hattendorf B. and Günther D. (2006) Search for nucleosynthetic and radiogenic tellurium isotope anomalies in carbonaceous chondrites. *Geochim. Cosmochim. Acta* **70**, 3436–3448.

Fischer-Gödde M., Becker H. and Wombacher F. (2010) Rhodium, gold and other highly siderophile element abundances in chondritic meteorites. *Geochim. Cosmochim. Acta* **74**, 356–379.

Fischer-Gödde M. and Kleine T. (2017) Ruthenium isotopic evidence for an inner Solar System origin of the late veneer. *Nature* **541**, 525–527.

Fischer R. A., Nimmo F. and O'Brien D. P. (2018) Radial mixing and Ru–Mo isotope systematics under different accretion scenarios. *Earth Planet. Sci. Lett.* **482**, 105–114.

Fitoussi C., Bourdon B., Kleine T., Oberli F. and Reynolds B. C. (2009) Si isotope systematics of meteorites and terrestrial peridotites: implications for Mg/Si fractionation in the solar nebula and for Si in the Earth's core. *Earth Planet. Sci. Lett.* **287**, 77–85.

Fitoussi C., Bourdon B. and Wang X. (2016) The building blocks of Earth and Mars: A close genetic link. *Earth Planet. Sci. Lett.* **434**, 151–160.

Floss C. and Haenecour P. (2016) Presolar silicate grains: Abundances, isotopic and elemental compositions, and the effects of secondary processing. *Geochem. J.* **50**, 3–25.

Friedrich J. M., Wang M.-S. and Lipschutz M. E. (2002) Comparison of the trace element composition of Tagish Lake with other primitive carbonaceous chondrites. *Meteorit. Planet. Sci.* **37**, 677–686.

Friend, Hezel, Barrat, Zipfel, Palme and Metzler (2018) Composition, petrology, and chondrule-matrix complementarity of the recently discovered Jbilet Winselwan CM2 chondrite. *Meteorit. Planet. Sci.* **22**, 1–22.

Friend P., Hezel D. C. and Mucerschi D. (2016) The conditions of chondrule formation, Part II: Open system. *Geochim. Cosmochim. Acta* **173**, 198–209.

Friend P., Hezel D. C., Palme H., Bischoff A. and Gellissen M. (2017) Complementary element relationships between chondrules and matrix in Rumuruti chondrites. *Earth Planet. Sci. Lett.* **480**, 87–96.

Funk C. (2015) Abundances and distribution of chalcogen volatile elements in chondritic meteorites and their components. Universität zu Köln.

Gannoun A., Boyet M., Rizo H. and El Goresy A. (2011) 146Sm-142Nd systematics measured in enstatite chondrites reveals a heterogeneous distribution of 142Nd in the solar nebula. *Proc. Natl. Acad. Sci. U. S. A.* **108**, 7693–7697.

Garenne A., Beck P., Montes-Hernandez G., Chiriac R., Toche F., Quirico E., Bonal L. and Schmitt B. (2014) The abundance and stability of "water" in type 1 and 2 carbonaceous chondrites (CI, CM and CR). *Geochim. Cosmochim. Acta* **137**, 93–112.

Gaschnig R. M., Rudnick R. L. and Mcdonough W. F. (2015) Determination of Ga, Ge, Mo, Ag, Cd, In, Sn, Sb, W, Tl and Bi in USGS Whole-Rock Reference Materials by Standard Addition ICP-MS. *Geostand. Geoanalytical Res.* **39**, 371–379.

Gillson G. R., Douglas D. J., Fulford J. E., Halligan K. W. and Tanner S. D. (1988)

Nonspectroscopic Interelement Interferences in Inductively Coupled Plasma Mass Spectrometry. *Anal. Chem.* **60**, 1472–1474.

Goldberg A. Z., Owen J. E. and Jacquet E. (2015) Chondrule transport in protoplanetary discs. *Mon. Not. R. Astron. Soc.* **452**, 4054–4069.

Goldschmidt V. M. (1930) Geochemische Verteilungsgesetze und kosmische Häufigkeit der Elemente. *Naturwissenschaften* **18**, 999–1013.

Göpel C., Birck J. L., Galy A., Barrat J.-A. and Zanda B. (2015) Mn-Cr systematics in primitive meteorites: Insights from mineral separation and partial dissolution. *Geochim. Cosmochim. Acta* **156**, 1–24.

Gounelle M., Morbidelli A., Bland P. A., Spurny P., Young E. D. and Sephton M. (2008) Meteorites from the Outer Solar System? *Sol. Syst. Beyond Neptune*, 525.

Greaney A. T., Rudnick R. L., Helz R. T., Gaschnig R. M., Piccoli P. M. and Ash R. D. (2017) The behavior of chalcophile elements during magmatic differentiation as observed in Kilauea Iki lava lake Hawaii. *Geochim. Cosmochim. Acta* **210**, 71–96.

Greenland L. (1967) The abundances of selenium, tellurium, silver, palladium, cadmium, and zinc in chondritic meteorites. *Geochim. Cosmochim. Acta* **31**, 849–860.

Greenwood R. C., Franchi I. A., Kearsley A. T. and Alard O. (2010) The relationship between CK and CV chondrites. *Geochim. Cosmochim. Acta* **74**, 1684–1705.

Grossman J. N. (1994) The Meteoritical Bulletin, No 76, 1994 January: The US Antarctic meteorite collection. *Meteoritics* **29**, 100–143.

Grossman L. (1972) Condensation in the primitive solar nebula. *Geochim. Cosmochim. Acta* **36**, 597–619.

Grossman L. and Larimer J. W. (1974) Early chemical history of the solar system. *Rev. Geophys.* **12**, 71–101.

Grossman L. and Steele I. M. (1976) Amoeboid olivine aggregates in the Allende meteorite. *Geochim. Cosmochim. Acta* **40**, 149–155.

Grousset F. E., Quetel C. R., Thomas B., Buatmenard P., Donard O. F. X. and Bucher A. (1994) Transient Pb Isotopic Signatures in the Western-European Atmosphere. *Environ. Sci. Technol.* **28**, 1605–1608.

Haack H., Grau T., Bischoff A., Horstmann M., Wasson J., Sørensen A., Laubenstein M., Ott U., Palme H., Gellissen M., Greenwood R. C., Pearson V. K., Franchi I. A., Gabelica Z. and Schmitt-Kopplin P. (2012) Maribo-A new CM fall from Denmark. *Meteorit. Planet. Sci.* **47**, 30–50.

Halliday A. N. (2004) Mixing, volatile loss and compositional change during impact-driven accretion of the Earth. *Nature* **427**, 505–509.

Harries D. and Langenhorst F. (2011) Sulfides in CM and CM/CI-like chondrites and their record of thermal metamorphism: a FIB-TEM study (abstract). *Meteorit. Planet. Sci.* **74**, 5166.

Heger A., Fröhlich C. and Truran J. W. (2013) Origin of the Elements. In *Treatise on Geochemistry: Second Edition* Elsevier. pp. 1–14.

Herndon J. M. and Herndon M. A. (1977) Aluminum-26 as a planetoid heat source in the early

solar system. *Meteoritics* **12**, 459–465.

Hewins R. H., Bourot-Denise M., Zanda B., Leroux H., Barrat J.-A., Humayun M., Goepel C., Greenwood R. C., Franchi I. A., Pont S., Lorand J. P., Cournède C., Gattacceca J., Rochette P., Kuga M., Marrocchi Y. and Marty B. (2014) The Paris meteorite, the least altered CM chondrite so far. *Geochim. Cosmochim. Acta* **124**, 190–222.

Hezel D. C., Harak M. and Libourel G. (2018) What we know about elemental bulk chondrule and matrix compositions: Presenting the ChondriteDB Database. *Chemie der Erde - Geochemistry* **78**, 1–14.

Hezel D. C. and Palme H. (2008) Constraints for chondrule formation from Ca–Al distribution in carbonaceous chondrites. *Earth Planet. Sci. Lett.* **265**, 716–725.

Hezel D. C. and Palme H. (2010) The chemical relationship between chondrules and matrix and the chondrule matrix complementarity. *Earth Planet. Sci. Lett.* **294**, 85–93.

Hezel D. C., Russell S. S., Ross A. J. and Kearsley A. T. (2008) Modal abundances of CAIs: Implications for bulk chondrite element abundances and fractionations. *Meteorit. Planet. Sci.* **43**, 1879–1894.

Hezel D. C., Schlüter J., Kallweit H., Jull A. J. T., Al Fakeer O. Y., Al Shamsi M. and Strekopytov S. (2011) Meteorites from the United Arab Emirates: Description, weathering, and terrestrial ages. *Meteorit. Planet. Sci.* **46**, 327–336.

Hin R. C., Coath C. D., Carter P. J., Nimmo F., Lai Y.-J., Pogge von Strandmann P. A. E., Willbold M., Leinhardt Z. M., Walter M. J. and Elliott T. (2017) Magnesium isotope evidence that accretional vapour loss shapes planetary compositions. *Nature* **549**, 511–515.

Houk R. S. (1980) Inductively Coupled Argon Plasma as an Ion Source for Mass Spectrometric Determination of Trace Elements. *Anal. Chem.* **52**, 2283–2289.

Howard K. T., Alexander C. M. O. D., Schrader D. L. and Dyl K. A. (2015) Classification of hydrous meteorites (CR, CM and C2 ungrouped) by phyllosilicate fraction: PSD-XRD modal mineralogy and planetesimal environments. *Geochim. Cosmochim. Acta* **149**, 206–222.

Hu Z. and Gao S. (2008) Upper crustal abundances of trace elements: A revision and update. *Chem. Geol.* **253**, 205–221.

Huber H., Rubin A. E., Kallemeyn G. W. and Wasson J. T. (2006) Siderophile-element anomalies in CK carbonaceous chondrites: Implications for parent-body aqueous alteration and terrestrial weathering of sulfides. *Geochim. Cosmochim. Acta* **70**, 4019–4037.

Humayun M. and Clayton R. N. (1995) Potassium isotope cosmochemistry: Genetic implications of volatile element depletion. *Geochim. Cosmochim. Acta* **59**, 2131–2148.

Huss G. R. (2004) Implications of isotopic anomalies and presolar grains for the formation of the solar system. *Antarct. Meteor. Res.* **17**, 132–152.

Huss G. R., Meshik A. P., Smith J. B. and Hohenberg C. M. (2003) Presolar diamond, silicon carbide, and graphite in carbonaceous chondrites: Implications for thermal processing in the solar nebula. *Geochim. Cosmochim. Acta* **67**, 4823–4848.

Huss G. R., Rubin A. E. and Grossman J. N. (2006) Thermal Metamorphism in Chondrites.

Meteorites early Sol. Syst. II, 567–586.

Ikramuddin M. and Lipschutz M. E. (1975) Thermal metamorphism of primitive meteorites I. Variation of six trace elements in Allende carbonaceous chondrite heated at 400-1000°C. *Geochim. Cosmochim. Acta* **39**, 363–375.

Islam M. A., Ebihara M. and Kojima H. (2012) Chemical Compositions and Alteration of Primitive Carbonaceous chondrites. *Lunar Planet. Sci. Conf.* **43**.

Jacquet E., Barrat J.-A., Beck P., Caste F., Gattacceca J., Sonzogni C. and Gounelle M. (2016) Northwest Africa 5958: A weakly altered CM-related ungrouped chondrite, not a CI3. *Meteorit. Planet. Sci.* **51**, 851–869.

Jakubowski N., Moens L. and Vanhaecke F. (1998) Sector field mass spectrometers in ICP-MS. *Spectrochim. acta, Part B At. Spectrosc.* **53**, 1739–1763.

Jarosewich E., Clarke C. R. S. and Barrows J. N. (1987) Allende Meteorite Reference Sample. *Smithson. Contrib. to Earth Sci.*, 1–49.

Javoy M., Kaminski E., Guyot F., Andrault D., Sanloup C., Moreira M., Labrosse S., Jambon A., Agrinier P., Davaille A. and Jaupart C. (2010) The chemical composition of the Earth: Enstatite chondrite models. *Earth Planet. Sci. Lett.* **293**, 259–268.

Jenner F. E., Arculus R. J., Mavrogenes J. A., Dyriw N. J., Nebel O. and Hauri E. H. (2012) Chalcophile element systematics in volcanic glasses from the northwestern Lau Basin. *Geochemistry, Geophys. Geosystems* **13**.

Jenner G. A., Longerich H. P., Jackson S. E. and Fryer B. J. (1990) ICP-MS - A powerful tool for high-precision trace-element analysis in Earth sciences: Evidence from analysis of selected U.S.G.S. reference samples. *Chem. Geol.* **83**, 133–148.

Jochum K. P., Weis U., Schwager B., Stoll B., Wilson S. A., Haug G. H., Andreae M. O. and Enzweiler J. (2016) Reference Values Following ISO Guidelines for Frequently Requested Rock Reference Materials. *Geostand. Geoanalytical Res.* **40**, 333–350.

Kaiser T. and Wasserburg G. J. (1983) The isotopic composition and concentration of Ag in iron meteorites and the origin of exotic silver. *Geochim. Cosmochim. Acta* **47**, 43–58.

Kallemeyn G. W., Rubin A. E. and T J. T. W. (1994) The compositional classification of chondrites: VI. The CR carbonaceous chondrite group. *Geochim. Cosmochim. Acta* **58**, 2873–2888.

Kallemeyn G. W., Rubin A. E. and Wasson J. T. (1991) The compositional classification of chondrites: V. The Karoonda (CK) group of carbonaceous chondrites. *Geochim. Cosmochim. Acta* **55**, 881–892.

Kallemeyn G. W. and Wasson J. T. (1981) The compositional classification of chondrites—I. The carbonaceous chondrite groups. *Geochim. Cosmochim. Acta* **45**, 1217–1230.

Kato C. and Moynier F. (2017) Gallium isotopic evidence for the fate of moderately volatile elements in planetary bodies and refractory inclusions. *Earth Planet. Sci. Lett.* **479**, 330–339.

Kato C., Moynier F., Valdes M. C., Dhaliwal J. K. and Day J. M. D. (2015) Extensive volatile loss during formation and differentiation of the Moon. *Nat. Commun.* **6**, 1–4.

Kelley K. A., Kingsley R. and Schilling J. G. (2013) Composition of plume-influenced mid-ocean ridge lavas and glasses from the Mid-Atlantic Ridge, East Pacific Rise, Galápagos

spreading center, and Gulf of Aden. *Geochemistry, Geophys. Geosystems* **14**, 223–242.

Khan R., Yokozuka Y., Terai S., Shirai N. and Ebihara M. (2015) Accurate determination of Zn in geological and cosmochemical rock samples by isotope dilution inductively coupled plasma mass spectrometry. *J. Anal. At. Spectrom.* **30**, 506–514.

King A. J., Solomon J. R., Schofield P. F. and Russell S. S. (2015) Characterising the CI and CI-like carbonaceous chondrites using thermogravimetric analysis and infrared spectroscopy. *Earth, Planets Sp.* **67**, 1–12.

Kirchenbaur M., Heuser A., Bragagni A. and Wombacher F. (2018) Determination of In and Sn Mass Fractions in Sixteen Geological Reference Materials by Isotope Dilution MC-ICP-MS. *Geostand. Geoanalytical Res.* **42**, 361–377.

Kiseeva E. S. and Wood B. J. (2013) A simple model for chalcophile element partitioning between sulphide and silicate liquids with geochemical applications. *Earth Planet. Sci. Lett.* **383**, 68–81.

Kiseeva E. S. and Wood B. J. (2015) The effects of composition and temperature on chalcophile and lithophile element partitioning into magmatic sulphides. *Earth Planet. Sci. Lett.* **424**, 280–294.

Kita N. T. and Ushikubo T. (2012) Evolution of protoplanetary disk inferred from 26Al chronology of individual chondrules. *Meteorit. Planet. Sci.* **47**, 1108–1119.

Kong P. and Palme H. (1999) Compositional and genetic relationship between chondrules, chondrule rims, metal, and matrix in the Renazzo chondrite. *Geochim. Cosmochim. Acta* **63**, 3673–3682.

König S., Luguet A., Lorand J.-P., Wombacher F. and Lissner M. (2012) Selenium and tellurium systematics of the Earth's mantle from high precision analyses of ultra-depleted orogenic peridotites. *Geochim. Cosmochim. Acta* **86**, 354–366.

Krähenbühl U., Morgan J. W., Ganapathy R. and Anders E. (1973) Abundance of 17 trace elements in carbonaceous chondrites. *Geochim. Cosmochim. Acta* **37**, 1353–1370.

Kraus R. G., Root S., Lemke R. W., Stewart S. T., Jacobsen S. B. and Mattsson T. R. (2015) Impact vaporization of planetesimal cores in the late stages of planet formation. *Nat. Geosci.* **8**, 269–272.

Krot A. N., Keil K., Scott E. R. D., Goodrich C. A. and Weisberg M. K. (2014) *Classification of Meteorites and Their Genetic Relationships*. 2nd ed., Elsevier Ltd.

Labidi J., König S., Kurzawa T., Yierpan A. and Schoenberg R. (2018) The selenium isotopic variations in chondrites are mass-dependent; Implications for sulfide formation in the early solar system. *Earth Planet. Sci. Lett.* **481**, 212–222.

De Laeter J. R. and Jeffery P. M. (1965) The isotopic composition of terrestrial and meteoritic tin. *J. Geophys. Res.* **70**, 2895–2903.

Lambert G., Le Cloarec M. F. and Pennisi M. (1988) Volcanic output of SO2 and trace metals: A new approach. *Geochim. Cosmochim. Acta* **52**, 39–42.

Larimer J. W. and Anders E. (1967) Chemical fractionations in meteorites—II. Abundance patterns and their interpretation. *Geochim. Cosmochim. Acta* **31**, 1239–1270.

Lauretta D. S., Lodders K., Fegley B. and Kremser D. T. (1997) The origin of sulfide-rimmed metal grains in ordinary chondrites. *Earth Planet. Sci. Lett.* **151**, 289–301.

Li G., Duan Y. and Hieftje G. M. (1995) Space-charge effects and ion distribution in plasma source mass spectrometry. *J. Mass Spectrom.* **30**, 841–848.

Linge K. L. and Jarvis K. E. (2009) Quadrupole ICP-MS: Introduction to instrumentation, measurement techniques and analytical capabilities. *Geostand. Geoanalytical Res.* **33**, 445–467.

Lodders K. (2003) Solar system abundances and condensation temperatures of the elements. *Astrophys. J.* **591**, 1220–1247.

Lodders K. and Fegley B. (1998) *The planetary scientist's companion*., Oxford University Press, Oxford.

Lorand J. P. and Luguet A. (2015) Chalcophile and siderophile elements in mantle rocks: Trace elements controlled by trace minerals. *Rev. Mineral. Geochemistry* **81**, 441–488.

Loss R. D., Rosman K. J. R. and De Laeter J. R. (1990) The isotopic composition of zinc, palladium, silver, cadmium, tin, and tellurium in acid-etched residues of the Allende meteorite. *Geochim. Cosmochim. Acta* **54**, 3525–3536.

Lu Y., Makishima A. and Nakamura E. (2007) Coprecipitation of Ti, Mo, Sn and Sb with fluorides and application to determination of B, Ti, Zr, Nb, Mo, Sn, Sb, Hf and Ta by ICP-MS. *Chem. Geol.* **236**, 13–26.

Luck J. M., B. O. D., Barrat J. A. and Albarède F. (2003) Coupled 63Cu and 16O excesses in chondrites. *Geochim. Cosmochim. Acta* **67**, 143–151.

Luck J. M., Othman D. Ben and Albarède F. (2005) Zn and Cu isotopic variations in chondrites and iron meteorites: Early solar nebula reservoirs and parent-body processes. *Geochim. Cosmochim. Acta* **69**, 5351–5363.

Mahan B., Moynier F., Beck P., Pringle E. A. and Siebert J. (2018a) A history of violence: Insights into post-accretionary heating in carbonaceous chondrites from volatile element abundances, Zn isotopes and water contents. *Geochim. Cosmochim. Acta* **220**, 19–35.

Mahan B., Siebert J., Blanchard I., Borensztajn S. and Badro J. (2018b) Constraining compositional proxies for Earth's accretion and core formation through high pressure and high temperature Zn and S metal–silicate partitioning. *Geochim. Cosmochim. Acta* **235**, 21–40.

Makishima A., Kitagawa H. and Nakamura E. (2011) Simultaneous Determination of Cd, In, Tl and Bi by Isotope Dilution-Internal Standardisation ICP-QMS with Corrections Using Externally Measured MoO+/Mo+ Ratios. *Geostand. Geoanalytical Res.* **35**, 57–67.

Makishima A. and Nakamura E. (2001) Determination of total sulfur at microgram per gram levels in geological materials by oxidation of sulfur into sulfate with in situ generation of bromine using isotope dilution high-resolution ICPMS. *Anal. Chem.* **73**, 2547–2553.

Mann U., Frost D. J. and Rubie D. C. (2009) Evidence for high-pressure core-mantle differentiation from the metal–silicate partitioning of lithophile and weakly-siderophile elements. *Geochim. Cosmochim. Acta* **73**, 7360–7386.

Marin L., Lhomme J. and Carignan J. (2001) Determination of selenium concentration in sixty five reference materials for geochemical analysis by GFAAS after separation with thiol cotton. *Geostand. Newsl.* **25**, 317–324.

Marrocchi Y., Gounelle M., Blanchard I., Caste F. and Kearsley A. T. (2014) The Paris CM

chondrite: Secondary minerals and asteroidal processing. *Meteorit. Planet. Sci.* **49**, 1232–1249.

Martin P. M. and Mason B. (1974) Major and trace elements in the Allende meteorite. *Nature* **249**, 333–334.

Marty B. (2012) The origins and concentrations of water, carbon, nitrogen and noble gases on Earth. *Earth Planet. Sci. Lett.* **313**–**314**, 56–66.

Marx S. K. and Kamber B. S. (2010) Trace-element systematics of sediments in the Murray-Darling Basin, Australia: Sediment provenance and palaeoclimate implications of fine scale chemical heterogeneity. *Appl. Geochemistry* **25**, 1221–1237.

Matza S. D. and Lipschutz M. E. (1977) Thermal metamorphism of primitive meteorites - VI-Eleven trace elements in Murchison C2 chondrite heated at 400-1000°C. *Proc. Lunar Sci. Conf.* **8**, 161–176.

McDonough W. F. (2003) *Compositional Model for the Earth's Core*. 3rd ed., Elsevier Ltd.

McSween H. Y. (1979) Alteration in CM carbonaceous chondrites inferred from modal and chemical variations in matrix. *Geochim. Cosmochim. Acta* **43**.

Meija J., Coplen T. B., Berglund M., Brand W. A., De Bièvre P., Gröning M., Holden N. E., Irrgeher J., Loss R. D., Walczyk T. and Prohaska T. (2016) Isotopic compositions of the elements 2013 (IUPAC Technical Report). *Pure Appl. Chem.* **88**, 293–306.

Meisel T. and Horan M. F. (2015) Analytical methods for the highly siderophile elements. *Rev. Mineral. Geochemistry* **81**, 89–106.

Mitchell K., Mason P. R. D., Van Cappellen P., Johnson T. M., Gill B. C., Owens J. D., Diaz J., Ingall E. D., Reichart G. J. and Lyons T. W. (2012) Selenium as paleo-oceanographic proxy: A first assessment. *Geochim. Cosmochim. Acta* **89**, 302–317.

Mittlefehldt D. W. and Wetherill G. W. (1979) Rb-Sr studies of CI and CM chondrites. *Geochim. Cosmochim. Acta* **43**, 201–206.

Moriarty G. M., Rumble D. and Friedrich J. M. (2009) Compositions of four unusual CM or CM-related Antarctic chondrites. *Chemie der Erde - Geochemistry* **69**, 161–168.

Moynier F., Dauphas N. and Podosek F. A. (2009) A search for 70Zn anomalies in meteorites. *Astrophys. J.* **700**, L92–L95.

Moynier F., Paniello R. C., Gounelle M., Albarède F., Beck P., Podosek F. and Zanda B. (2011) Nature of volatile depletion and genetic relationships in enstatite chondrites and aubrites inferred from Zn isotopes. *Geochim. Cosmochim. Acta* **75**, 297–307.

Münker C., Pfänder J., Weyer S., Büchl A., Kleine T. and Mezger K. (2003) Evolution of planetary cores and the Earth-Moon system from Nb/Ta systematics. *Science* **301**, 84–87.

Nakamura T. (2005) Post-hydration thermal metamorphism of carbonaceous chondrites. *J. Mineral. Petrol. Sci.* **100**, 260–272.

Nakato A., Nakamura T., Kitajima F. and Noguchi T. (2008) Evaluation of dehydration mechanism during heating of hydrous asteroids based on mineralogical and chemical analysis of naturally and experimentally heated CM chondrites. *Earth, Planets Sp.* **60**, 855–864.

Nanne J. A. M., Nimmo F., Cuzzi J. N. and Kleine T. (2019) Origin of the non-carbonaceous–

carbonaceous meteorite dichotomy. *Earth Planet. Sci. Lett.* **511**, 44–54.

Nebel O., Mezger K. and van Westrenen W. (2011) Rubidium isotopes in primitive chondrites: Constraints on Earth's volatile element depletion and lead isotope evolution. *Earth Planet. Sci. Lett.* **305**, 309–316.

Newsom H. E., White W. M., Jochum K. P. and Hofmann A. W. (1986) Siderophile and chalcophile element abundances in oceanic basalts, Pb isotope evolution and growth of the Earth's core. *Earth Planet. Sci. Lett.* **80**, 299–313.

Norman M. D., Garcia M. O. and Bennett V. C. (2004) Rhenium and chalcophile elements in basaltic glasses from Ko'olau and Moloka'i volcanoes: Magmatic outgassing and composition of the Hawaiian plume. *Geochim. Cosmochim. Acta* **68**, 3761–3777.

Noronha B. A. and Friedrich J. M. (2014) Chemical compositions and classification of five thermally altered carbonaceous chondrites. *Meteorit. Planet. Sci.* **49**, 1494–1504.

Norris C. A. and Wood B. J. (2017) Earth's volatile contents established by melting and vaporization. *Nature* **549**, 507–510.

O'Neill H. S. C. (1991) The origin of the Moon and the early history of the Earth - A chemical model. Part 1: The Moon. *Geochim. Cosmochim. Acta* **55**, 1135–1157.

O'Neill H. S. C. and Palme H. (2008) Collisional erosion and the non-chondritic composition of the terrestrial planets. *Philos. Trans. R. Soc. A Math. Phys. Eng. Sci.* **366**, 4205–4238.

Olesik J. W. (2014) *Inductively Coupled Plasma Mass Spectrometers*. 15th ed., Elsevier Ltd.

Orthous-Daunay F. R., Quirico E., Beck P., Brissaud O., Dartois E., Pino T. and Schmitt B. (2013) Mid-infrared study of the molecular structure variability of insoluble organic matter from primitive chondrites. *Icarus* **223**, 534–543.

Palk C., Andreasen R., Rehkämper M., Stunt A., Kreissig K., Coles B., Schönbächler M. and Smith C. (2018) Variable Tl, Pb, and Cd concentrations and isotope compositions of enstatite and ordinary chondrites—Evidence for volatile element mobilization and decay of extinct205Pb. *Meteorit. Planet. Sci.* **53**, 167–186.

Palme H., Hezel D. C. and Ebel D. S. (2015) The origin of chondrules: Constraints from matrix composition and matrix-chondrule complementarity. *Earth Planet. Sci. Lett.* **411**, 11–19.

Palme H., Lodders K. and Jones A. (2014a) *Solar System Abundances of the Elements*. 2nd ed., Elsevier Ltd.

Palme H. and O'Neill H. S. C. (2014) *Cosmochemical Estimates of Mantle Composition*. 2nd ed., Elsevier Ltd.

Palme H. and Rammensee W. (1981) The cosmic abundance of molybdenum. *Earth Planet. Sci. Lett.* **55**, 356–362.

Palme H., Spettel B. and Hezel D. (2014b) Siderophile elements in chondrules of CV chondrites. *Chemie der Erde* **74**, 507–516.

Paniello R. C., Day J. M. D. and Moynier F. (2012) Zinc isotopic evidence for the origin of the Moon. *Nature* **490**, 376–379.

Pizzarello S., Schrader D. L., Monroe A. A. and Lauretta D. S. (2012) Large enantiomeric excesses in primitive meteorites and the diverse effects of water in cosmochemical evolution. *Proc. Natl. Acad. Sci. U. S. A.* **109**, 11949–54.

Pourmand A., Dauphas N. and Ireland T. J. (2012) A novel extraction chromatography and MC-ICP-MS technique for rapid analysis of REE, Sc and Y: Revising CI-chondrite and Post-Archean Australian Shale (PAAS) abundances. *Chem. Geol.* **291**, 38–54.

Pringle E. A. and Moynier F. (2017) Rubidium isotopic composition of the Earth, meteorites, and the Moon: Evidence for the origin of volatile loss during planetary accretion. *Earth Planet. Sci. Lett.* **473**, 62–70.

Pringle E. A., Moynier F., Beck P., Paniello R. and Hezel D. C. (2017) The origin of volatile element depletion in early solar system material: Clues from Zn isotopes in chondrules. *Earth Planet. Sci. Lett.* **468**, 62–71.

Pringle E. A., Moynier F., Savage P. S., Badro J. and Barrat J. A. (2014) Silicon isotopes in angrites and volatile loss in planetesimals. *Proc. Natl. Acad. Sci. U. S. A.* **111**, 17029–17032.

Rehkämper M. and Halliday A. N. (1997) Development and application of new ion-exchange techniques for the separation of the platinum group and other siderophile elements from geological samples. *Talanta* **44**, 663–672.

Render J., Fischer-Gödde M., Burkhardt C. and Kleine T. (2017) The cosmic molybdenum-neodymium isotope correlation and the building material of the Earth. *Geochemical Perspect. Lett.*, 170–178.

Righter K., Danielson L., Drake M. J. and Domanik K. (2013) Partition Coefficients at High Pressure and Temperature. In *Treatise on Geochemistry: Second Edition* Published by Elsevier Inc. pp. 449–477.

Righter K., Nickodem K., Pando K., Danielson L., Boujibar A., Righter M. and Lapen T. J. (2017a) Distribution of Sb, As, Ge, and In between metal and silicate during accretion and core formation in the Earth. *Geochim. Cosmochim. Acta* **198**, 1–16.

Righter K., Pando K., Humayun M., Waeselmann N., Yang S., Boujibar A. and Danielson L. R. (2018) Effect of silicon on activity coefficients of siderophile elements (Au, Pd, Pt, P, Ga, Cu, Zn, and Pb) in liquid Fe: Roles of core formation, late sulfide matte, and late veneer in shaping terrestrial mantle geochemistry. *Geochim. Cosmochim. Acta* **232**, 101–123.

Righter K., Pando K., Marin N., Ross D. K., Righter M., Danielson L., Lapen T. J. and Lee C. (2017b) Volatile element signatures in the mantles of Earth, Moon, and Mars: Core formation fingerprints from Bi, Cd, In, and Sn. *Meteorit. Planet. Sci.* **22**, 1–22.

Robin-Popieul C. C. M., Arndt N. T., Chauvel C., Byerly G. R., Sobolev A. V. and Wilson A. (2012) A new model for barberton komatiites: Deep critical melting with high melt retention. *J. Petrol.* **53**, 2191–2229.

Rochette P., Gattacceca J., Bonal L., Bourot-Denise M., Chevrier V., Clerc J.-P., Consolmagno G. J., Folco L., Gounelle M., Kohout T., Pesonen L., Quirico E., Sagnotti L. and Skripnik A. (2008) Magnetic classification of stony meteorites : 2 . Non-ordinary chondrites. *Meteorit. Planet. Sci.* **43**, 959–980.

Rocholl A. and Jochum K. P. (1993) Th, U and other trace elements in carbonaceous chondrites: Implications for the terrestrial and solar system Th/U ratios. *Earth Planet. Sci. Lett.* **117**, 265–278.

Rospabé M., Benoit M., Ceuleneer G., Hodel F. and Kaczmarek M. A. (2018) Extreme

geochemical variability through the dunitic transition zone of the Oman ophiolite: Implications for melt/fluid-rock reactions at Moho level beneath oceanic spreading centers. *Geochim. Cosmochim. Acta* **234**, 1–23.

Rouxel O., Ludden J., Carignan J., Marin L. and Fouquet Y. (2002) Natural variations of Se isotopic composition determined by hydride generation multiple collector inductively coupled plasma mass spectrometry. *Geochim. Cosmochim. Acta* **66**, 3191–3199.

Rubie D. C., Jacobson S. A., Morbidelli A., O'Brien D. P., Young E. D., de Vries J., Nimmo F., Palme H. and Frost D. J. (2015) Accretion and differentiation of the terrestrial planets with implications for the compositions of early-formed Solar System bodies and accretion of water. *Icarus* **248**, 89–108.

Rubie D. C., Laurenz V., Jacobson S. A., Morbidelli A., Palme H., Vogel A. K. and Frost D. J. (2016) Highly siderophile elements were stripped from Earth's mantle by iron sulfide segregation. *Science* **353**, 1141–4.

Rubin A. E. (2010) Physical properties of chondrules in different chondrite groups: Implications for multiple melting events in dusty environments. *Geochim. Cosmochim. Acta* **74**, 4807–4828.

Rubin A. E., Scott E. R. D. and Keil K. (1997) Shock metamorphism of enstatite chondrites. *Geochim. Cosmochim. Acta* **61**, 847–858.

Rubin A. E., Trigo-Rodríguez J. M., Huber H. and Wasson J. T. (2007) Progressive aqueous alteration of CM carbonaceous chondrites. *Geochim. Cosmochim. Acta* **71**, 2361–2382.

Rubin A. E. and Wasson J. T. (1987) Chondrules, matrix and coarse-grained chondrule rims in the Allende meteorite: Origin, interrelationships and possible precursor components. *Geochim. Cosmochim. Acta* **51**, 1923–1937.

Russell H. N. (1934) Molecules in the Sun and Stars. *Astrophys. J.* **79**, 317–342.

Russell H. N. (1929) On the Composition of the Sun's Atmosphere. *Astrophys. J.* **70**, 11–82.

Sahijpal S., Soni P. and Gupta G. (2007) Numerical simulations of the differentiation of accreting planetesimals with 26Al and 60Fe as the heat sources. *Meteorit. Planet. Sci.* **42**, 1529–1548.

Sands D. G. and Rosman K. J. R. (1997) Cd, Gd and Sm concentrations in BCR-1, BHVO-1, BIR-1, DNC-1, MAG-1, PCC-1 and W-2 by isotope dilution thermal ionisation mass spectrometry. *Geostand. Newsl.* **21**, 77–83.

Savage B. D. and Sembach K. R. (1996) Interstellar abundances from absorption-line observations with the Hubble space telescope. *Annu. Rev. Astron. Astrophys.* **34**, 279–329.

Schaefer L. and Fegley B. (2010a) Chemistry of atmospheres formed during accretion of the Earth and other terrestrial planets. *Icarus* **208**, 438–448.

Schaefer L. and Fegley B. (2010b) Volatile element chemistry during metamorphism of ordinary chondritic material and some of its implications for the composition of asteroids. *Icarus* **205**, 483–496.

Van Schmus W. R. and Wood J. A. (1967) A chemical-petrologic classification for the chondritic meteorites. *Geochim. Cosmochim. Acta* **31**, 747–765.

Schönbächler M., Carlson R. W., Horan M. F., Mock T. D. and Hauri E. H. (2010) Heterogeneous accretion and the moderately volatile element budget of Earth. *Science (80-*

.). **328**, 884–887.

Schrader D. L., Davidson J., Greenwood R. C., Franchi I. A. and Gibson J. M. (2014) A water-ice rich minor body from the early Solar System: The CR chondrite parent asteroid. *Earth Planet. Sci. Lett.* **407**, 48–60.

Schrader D. L., Franchi I. A., Connolly H. C., Greenwood R. C., Lauretta D. S. and Gibson J. M. (2011) The formation and alteration of the Renazzo-like carbonaceous chondrites I: Implications of bulk-oxygen isotopic composition. *Geochim. Cosmochim. Acta* **75**, 308–325.

Schulze H., Bischoff A., Palme H., Spettel B., Dreibus G. and Otto J. (1994) Mineralogy and chemistry of Rumuruti: the first meteorite fall of the new R chondrite group. *Meteoritics* **29**, 275–286.

Scott E. (1984) Classification, metamorphism, and brecciation of type 3 chondrites from Antarctica. *Smithson. Contrib. Earth Sci* **26**, 73–94.

Scott E. R. D., Keil K. and Stöffler D. (1992) Shock metamorphism of carbonaceous chondrites. *Geochim. Cosmochim. Acta* **56**, 4281–4293.

Scott E. R. D. and Krot A. N. (2014) Chondrites and Their Components. In *Treatise on Geochemistry* Elsevier Ltd. pp. 65–137.

Sears D. W., Hasan R. A., Batchelor J. D. and Lu J. (1991) Chemical and physical studies of type 3 chondrites - XI: Metamorphism, pairing, and brecciation of ordinary chondrites. *Proc. 21st Lunar Planet. Sci. Conf.*, 493–512.

Siebert J., Sossi P. A., Blanchard I., Mahan B., Badro J. and Moynier F. (2018) Chondritic Mn/Na ratio and limited post-nebular volatile loss of the Earth. *Earth Planet. Sci. Lett.* **485**, 130–139.

Silveira E. M., Söderlund U., Oliveira E. P., Ernst R. E. and Leal A. B. M. (2013) First precise U-Pb baddeleyite ages of 1500Ma mafic dykes from the São Francisco Craton, Brazil, and tectonic implications. *Lithos* **174**, 144–156.

Sossi P. A. and Fegley B. (2018) Thermodynamics of Element Volatility and its Application to Planetary Processes. *Rev. Mineral. Geochemistry* **84**, 393–459.

Sossi P. A., Klemme S., O'Neill H., Berndt J. and Moynier F. (2019) Evaporation of moderately volatile elements from silicate melts : experiments and theory. *Geochim. Comochimica Acta* **260**, 204–231.

Sossi P. A., Nebel O., O'Neill H. S. C. and Moynier F. (2018) Zinc isotope composition of the Earth and its behaviour during planetary accretion. *Chem. Geol.* **477**, 73–84.

Stöffler D., Keil K. and Edward R.D S. (1991) Shock metamorphism of ordinary chondrites. *Geochim. Cosmochim. Acta* **55**, 3845–3867.

Stracke A., Palme H., Gellissen M., Münker C., Kleine T., Birbaum K., Günther D., Bourdon B. and Zipfel J. (2012) Refractory element fractionation in the Allende meteorite: Implications for solar nebula condensation and the chondritic composition of planetary bodies. *Geochim. Cosmochim. Acta* **85**, 114–141.

Stracke A., Scherer E. E. and Reynolds B. C. (2014) *Application of Isotope Dilution in Geochemistry*. 2nd ed., Elsevier Ltd.

Takahashi H., Gros J., Higuchi H., Morgans J. W. and Anders E. (1978a) Volatile elements in

chondrites: metamorphism or nebular fractionation? *Geochim. Cosmochim. Acta* **42**, 1859–1869.

Takahashi H., Janssens M. J., Morgan J. W. and Anders E. (1978b) Further studies of trace elements in C3 chondrites. *Geochim. Cosmochim. Acta* **42**, 97–106.

Taylor S. R. and Norman M. D. (1990) Accretion of differentiated planetesimals to the Earth. In *Origin of the Earth* (eds. H. E. Newsom and J. H. Jones). Oxford University Press. pp. 29–43.

Tera F. and Carlson R. W. (1999) Assessment of the Pb-Pb and U-Pb chronometry of the early solar system. *Geochim. Cosmochim. Acta* **63**, 1877–1889.

Tonui E. K., Zolensky M. E., Lipschutz M. E. and Okudaira K. (2001) Petrographic and chemical evidence of thermal metamorphism in new carbonaceous chondrites. *Meteorit. Planet. Sci.* **36**, A207.

Tonui E., Zolensky M., Hiroi T., Nakamura T., Lipschutz M. E., Wang M. S. and Okudaira K. (2014) Petrographic, chemical and spectroscopic evidence for thermal metamorphism in carbonaceous chondrites I: CI and CM chondrites. *Geochim. Cosmochim. Acta* **126**, 284–306.

Trinquier A., Birck J. and Allegre C. J. (2007) Widespread ^{54} Cr Heterogeneity in the Inner Solar System. *Astrophys. J.* **655**, 1179–1185.

Trinquier A., Birck J. L., Allègre C. J., Göpel C. and Ulfbeck D. (2008) 53Mn-53Cr systematics of the early Solar System revisited. *Geochim. Cosmochim. Acta* **72**, 5146–5163.

Vlastélic I., Menard G., Gannoun A., Piro J. L., Staudacher T. and Famin V. (2013) Magma degassing during the April 2007 collapse of Piton de la Fournaise: The record of semi-volatile trace elements (Li, B, Cu, In, Sn, Cd, Re, Tl, Bi). *J. Volcanol. Geotherm. Res.* **254**, 94–107.

Vollstaedt H., Mezger K. and Leya I. (2016) The isotope composition of selenium in chondrites constrains the depletion mechanism of volatile elements in solar system materials. *Earth Planet. Sci. Lett.* **450**, 372–380.

Wai C. M. and Wasson J. T. (1977) Nebular condensation of moderately volatile elements and their abundances in ordinary chondrites. *Earth Planet. Sci. Lett.* **36**, 1–13.

Wang H. S., Lineweaver C. H. and Ireland T. R. (2019) The volatility trend of protosolar and terrestrial elemental abundances. *Icarus* **328**, 287–305.

Wang M.-S. and Lipschutz M. E. (2005) Thermal Metamorphism of Primitive Meteorites - XII. The Enstatite Chondrites Revisited. *Environ. Chem.* **2**, 215–226.

Wang M.-S. and Lipschutz M. E. (2007) Trace elements in primitive meteorites—VII Antarctic unequilibrated ordinary chondrites. *Geochim. Cosmochim. Acta* **71**, 1062–1073.

Wang Z. and Becker H. (2015) Abundances of Ag and Cu in mantle peridotites and the implications for the behavior of chalcophile elements in the mantle. *Geochim. Cosmochim. Acta* **160**, 209–226.

Wang Z. and Becker H. (2017) Chalcophile elements in Martian meteorites indicate low sulfur content in the Martian interior and a volatile element-depleted late veneer. *Earth Planet. Sci. Lett.* **463**, 56–68.

Wang Z. and Becker H. (2013) Ratios of S, Se and Te in the silicate Earth require a volatile-

rich late veneer. *Nature* **499**, 328–331.

Wang Z., Becker H. and Wombacher F. (2014) Mass fractions of S, Cu, Se, Mo, Ag, Cd, In, Te, Ba, Sm, W, Tl and Bi in geological reference materials and selected carbonaceous chondrites determined by isotope dilution ICP-MS. *Geostand. Geoanalytical Res.* **39**, 185–208.

Wang Z., Laurenz V., Petitgirard S. and Becker H. (2016) Earth's moderately volatile element composition may not be chondritic: Evidence from In, Cd and Zn. *Earth Planet. Sci. Lett.* **435**, 136–146.

Warren P. H. (2011) Stable-isotopic anomalies and the accretionary assemblage of the Earth and Mars: A subordinate role for carbonaceous chondrites. *Earth Planet. Sci. Lett.* **311**, 93–100.

Wasson J. T. (2008) Evaporation of nebular fines during chondrule formation. *Icarus* **195**, 895–907.

Wasson J. T. (1972) Formation of ordinary chondrites. *Rev. Geophys.* **10**, 711–759.

Wasson J. T. and Chou C.-L. (1974) Fractionation of moderately volatile elements in ordinary chondrites. *Meteoritics* **9**, 69–85.

Wasson J. T., Isa J. and Rubin A. E. (2013) Compositional and petrographic similarities of CV and CK chondrites: A single group with variations in textures and volatile concentrations attributable to impact heating, crushing and oxidation. *Geochim. Cosmochim. Acta* **108**, 45–62.

Weisberg M. K., McCoy T. J. and Krot A. N. (2006) Systematics and Evaluation of Meteorite Classification. In *Meteorites and the early solar system II* pp. 19–52.

Weisberg M. K., Prinz M., Clayton R. N., Mayeda T. K., Grady M. M., Franchi I., Pillinger C. T. and Kallemeyn G. W. (1996) The K (Kakangari) chondrite grouplet. *Geochim. Cosmochim. Acta* **60**, 4253–4263.

Wildt R. (1933) Kondensation in Sternatmosphären. *Zeitschrift für Astrophys.* **6**, 345–354.

Williams J. P. and Cieza L. A. (2011) Protoplanetary Disks and Their Evolution. *Annu. Rev. Astron. Astrophys.* **49**, 67–117.

Witt-Eickschen G., Palme H., O'Neill H. S. C. and Allen C. M. (2009) The geochemistry of the volatile trace elements As, Cd, Ga, In and Sn in the Earth's mantle: New evidence from in situ analyses of mantle xenoliths. *Geochim. Cosmochim. Acta* **73**, 1755–1778.

Wlotzka F. (1993) A weathering scale for the ordinary chondrites. In *Meteoritics* p. 460.

Wolf R., Richter G. R., Woodrow A. B. and Anders E. (1980) Chemical fractionations in meteorites-XI. C2 chondrites. *Geochim. Cosmochim. Acta* **44**, 711–717.

Wolf S. F., Unger D. L. and Friedrich J. M. (2005) Determination of cosmochemically volatile trace elements in chondritic meteorites by inductively coupled plasma mass spectrometry. *Anal. Chim. Acta* **528**, 121–128.

Wombacher F. and Rehkämper M. (2003) Investigation of the mass discrimination of multiple collector ICP-MS using neodymium isotopes and the generalised power law. *J. Anal. At. Spectrom.* **18**, 1371–1375.

Wombacher F., Rehkämper M., Mezger K., Bischoff A. and Münker C. (2008) Cadmium stable

isotope cosmochemistry. *Geochim. Cosmochim. Acta* **72**, 646–667.

Wombacher F., Ziegler A. and Becker H. (2009) Selenium and tellurium abundances in mafic and ultramafic rock reference samples by ID-ICP-MS. In *Geochimica et Cosmochimica Acta Supplement* Pergamon Press. p. 1450.

Wood B. J., Kiseeva E. S. and Mirolo F. J. (2014) Accretion and core formation : The effects of sulfur on metal – silicate partition coefficients. *Geochim. Cosmochim. Acta* **145**, 248–267.

Wood B. J., Smythe D. J. and Harrison T. (2019) The condensation temperatures of the elements: A reappraisal. *Am. Mineral.* **104**, 844–856.

Wood J. A. (2005) The Chondrite Types and their Origins. **341**, 953–971.

Wulf A. V., Palme H. and Jochum K. P. (1995) Fractionation of volatile elements in the early solar system: evidence from heating experiments on primitive meteorites. *Planet. Space Sci.* **43**, 451–468.

Yabuta H., Alexander C. M. O. D., Fogel M. L., Kilcoyne A. L. D. and Cody G. D. (2010) A molecular and isotopic study of the macromolecular organic matter of the ungrouped C2 WIS 91600 and its relationship to Tagish Lake and PCA 91008. *Meteorit. Planet. Sci.* **45**, 1446–1460.

Yang S., Humayun M., Righter K., Jefferson G., Fields D. and Irving A. J. (2015) Siderophile and chalcophile element abundances in shergottites: Implications for Martian core formation. *Meteorit. Planet. Sci.* **50**, 691–714.

Yi W., Halliday A. N., Alt J. C., Lee D.-C. and Rehkämper M. (2000) Cadmium, indium, tin, tellurium, and sulfur in oceanic basalts: Implications for chalcophile element fractionation in the Earth. *J. Geophys. Res.* **105**, 927–949.

Yi W., Halliday A. N., Lee D. C. and Christensen J. N. (1995) Indium and tin in basalts, sulfides, and the mantle. *Geochim. Cosmochim. Acta* **59**, 5081–5090.

Yi W., Halliday A. N., Lee D. C. and Rehkämper M. (1998) Precise determination of cadmium, indium and tellurium using multiple collector ICP-MS. *Geostand. Newsl.* **22**, 173–179.

Yin Q. (2005) From dust to planets: The tale told by moderately volatile elements. *Chondrites protoplanetary Disk* **341**, 632–644.

Yin Q., Yamashita K., Yamakawa A., Tanaka R., Jacobsen B., Ebel D., Hutcheon I. D. and Nakamura E. (2009) 53Mn-53Cr systematics of Allende chondrules and e54Cr-D17O correlation in bulk carbonaceous chondrites. *Lunar Planet. Sci. Conf. XL* **40**, #2006 (abstract).

Yokoyama T., Nagai Y., Hinohara Y. and Mori T. (2017) Investigating the Influence of Non-Spectral Matrix Effects in the Determination of Twenty-Two Trace Elements in Rock Samples by ICP-QMS. *Geostand. Geoanalytical Res.* **41**, 221–242.

Yokoyama T. and Walker R. J. (2016) Nucleosynthetic Isotope Variations of Siderophile and Chalcophile Elements in the Solar System. *Rev. Mineral. Geochemistry* **81**, 107–160.

Young E. D., Zhang K. K. and Schubert G. (2003) Conditions for pore water convection within carbonaceous chondrite parent bodies - Implications for planetesimal size and heat production. *Earth Planet. Sci. Lett.* **213**, 249–259.

Yu M., Sun D., Tian W., Wang G., Shen W. and Xu N. (2002) Systematic studies on adsorption

of trace elements Pt, Pd, Au, Se, Te, As, Hg, Sb on thiol cotton fiber. *Anal. Chim. Acta* **456**, 147–155.

Zelenski M. E., Fischer T. P., de Moor J. M., Marty B., Zimmermann L., Ayalew D., Nekrasov A. N. and Karandashev V. K. (2013) Trace elements in the gas emissions from the Erta Ale volcano, Afar, Ethiopia. *Chem. Geol.* **357**, 95–116.

Zhang W., Hu Z., Liu Y., Chen L., Chen H., Li M., Zhao L., Hu S. and Gao S. (2012) Reassessment of HF/HNO 3 Decomposition Capability in the High-Pressure Digestion of Felsic Rocks for Multi-Element Determination by ICP-MS. *Geostand. Geoanalytical Res.* **36**, 271–289.

Appendix

Appendix A

Table A1: Performance and acquisition parameters for SF-ICP-MS

Instrumental settings and performance		
RF power	1200 W	
Cool gas	16 L min^{-1}	
Resolution [m/Δm]	LR [400], MR [4700], HR [10000]	
Scanning mode	Triple	
E-scan range	15 %	
Samples per peak	LR: 100 (Li 20); MR 40; HR: 25 (major), 20 (traces)	
Sample time [ms]	LR: 1 - 10; MR: 1 - 2.5; HR: 2 - 50	
Mass window [%]	LR: 10 (Li 120); MR: 80 - 120; HR: 100 - 120	
Search window [%]	LR: 10 (Li 120); MR: 80 - 120; HR: 100 - 120	
Integration window [%]	LR: 10 (Li 50); MR: 50 - 60; HR: 60	
	Glassware	**PFA**
Auxiliary gas	1.05 L min^{-1}	1.05 - 1.10 L min^{-1}
Sample gas	1.25 - 1.28 L min^{-1}	0.91 - 0.92 L min^{-1}
Additional gas	-	0.215 L min^{-1}
BaO^+/Ba^+	0.0015	0.0015
Ba^{++}/Ba^+	0.05	0.05
Sensitivity	~1*10^6 cps for ^{115}In per ng/g In	~2*10^6 cps for ^{115}In per ng/g In

Major elements: 1:10,000 dilution

MR: ^{23}Na, ^{26}Mg, ^{27}Al, ^{32}S, ^{43}Ca, ^{52}Cr, ^{55}Mn, ^{57}Fe, ^{61}Ni, ^{89}Y

HR: ^{39}K, ^{89}Y

Minor and trace elements: 1:2,000

LR: ^{77}Se, ^{85}Rb, ^{86}Sr, ^{89}Y, ^{91}Zr, ^{93}Nb, ^{95}Mo, ^{97}Mo, ^{103}Rh, ^{109}Ag, ^{111}Cd, ^{115}In, ^{118}Sn, ^{125}Te, ^{133}Cs, ^{137}Ba, ^{139}La, ^{140}Ce, ^{141}Pr, ^{146}Nd, ^{147}Sm, ^{151}Eu, ^{157}Gd, ^{159}Tb, ^{163}Dy, ^{165}Ho, ^{166}Er, ^{169}Tm, ^{172}Yb, ^{175}Lu, ^{178}Hf, ^{182}W, ^{185}Re, ^{193}Ir, ^{195}Pt, ^{205}Tl, ^{206}Pb, ^{207}Pb, ^{208}Pb, ^{209}Bi, ^{232}Th, ^{238}U

MR: ^{31}P, ^{47}Ti, ^{51}V, ^{59}Co, ^{63}Cu, ^{66}Zn, ^{89}Y

HR: ^{69}Ga, ^{71}Ga, ^{75}As, ^{89}Y

Table A2: Major and trace element abundances relative to Ivuna and normalized to Fe.

	Orgueil A CI1	Orgueil B CI1	Y-980115 CI-like	Tagish Lake C2	Murchison NC CM2	Murchison CM2
Na	0.49	0.49	0.99	0.15	0.14	0.15
Mg	0.97	0.98	0.97	1.10	1.05	1.07
Al	0.99	0.98	0.95	1.38	1.23	1.19
S	0.85	0.85	1.07	0.64	0.43	0.41
K	0.95	0.93	1.25	0.64	2.72	0.99
Ca	0.83	0.83	0.95	0.57	1.02	1.08
Cr	1.00	1.01	1.00	1.07	1.03	1.04
Mn	0.91	0.91	0.86	0.68	0.73	0.71
Fe	1.00	1.00	1.00	1.00	1.00	1.00
Ni	0.94	0.94	0.96	1.00	0.96	0.96
P	1.00	1.03	1.12	1.17	1.06	0.98
Ti	1.03	1.05	1.04	1.31	1.24	1.25
V	0.99	1.01	1.02	1.28	1.21	1.22
Co	0.96	0.98	0.99	1.00	0.98	0.98
Cu	1.01	1.05	0.94	0.86	0.84	0.83
Zn	1.00	1.01	1.02	0.68	0.50	0.50
Ga	0.98	1.00	0.99	0.75	0.68	0.67
As	1.03	1.05	1.03	0.95	0.95	0.95
Se	1.01	1.04	1.07	0.72	0.53	0.54
Rb	0.80	0.82	1.10	0.66	0.55	0.66
Sr	0.92	0.93	1.02	0.78	1.61	1.06
Zr	1.41	1.27	1.02	1.30	1.21	1.21
Nb	1.17	1.12	1.09	1.35	1.29	1.26
Mo	0.94	0.90	0.92	1.03	1.04	1.08
Rh	0.99	0.99	0.98	1.11	1.05	1.09
Ag	1.03	1.07	1.22	0.70	0.53	0.51
Cd	0.95	0.96	0.02	0.72	0.50	0.51
In	0.97	0.98	0.26	0.69	0.48	0.50
Sn	1.00	1.00	1.01	0.70	0.51	0.57
Te	1.01	1.01	1.03	0.70	0.52	0.53
Cs	0.87	0.88	1.03	0.69	0.54	0.61
Ba	1.34	1.29	1.02	1.00	4.06	1.22
La	1.21	1.61	1.02	1.31	1.42	1.23
Ce	1.16	1.49	1.03	1.30	1.38	1.23
Pr	1.14	1.40	1.03	1.28	1.32	1.24
Nd	1.09	1.30	1.02	1.28	1.29	1.24
Sm	1.05	1.14	1.01	1.27	1.26	1.20
Eu	1.01	1.05	1.00	1.22	1.23	1.20
Gd	1.04	1.15	1.03	1.22	1.22	1.21
Tb	1.05	1.05	1.01	1.22	1.22	1.21
Dy	1.06	1.03	1.00	1.23	1.22	1.19
Er	1.08	1.02	1.01	1.20	1.21	1.20
Tm	1.06	1.01	1.00	1.27	1.21	1.21
Yb	1.06	1.02	1.01	1.22	1.19	1.20
Lu	1.10	1.03	1.03	1.27	1.23	1.21
Hf	1.37	1.24	1.02	1.35	1.24	1.21
W	0.94	0.88	0.98	2.15*	1.05	1.08
Re	0.99	1.01	0.99	1.24	0.82	1.02
Ir	1.00	1.00	0.85	1.29	1.06	1.10
Pt	0.96	1.01	1.05	1.04	1.06	1.09
Tl	1.00	1.01	0.05	0.74	0.52	0.53
Pb	1.06	1.07	1.00	0.70	0.55	0.54
Bi	0.98	0.99	0.22	0.69	0.51	0.52
Th	1.65	2.20	1.02	1.34	1.61	1.24
U	2.33	1.84	1.01	1.25	2.17	1.21

	Mighei CM2	Cold Bokkeveld CM2	Murray CM2	Nogoya CM2	Paris CM2	Jbilet Winselwan CM2
Na	0.62	0.50	0.34	0.73	0.76	0.48
Mg	1.08	1.07	1.09	1.03	1.07	1.02
Al	1.17	1.21	1.26	1.23	1.23	1.19
S	0.56	0.49	0.46	0.55	0.57	0.32
K	0.68	0.93	0.64	1.01	0.83	0.96
Ca	1.27	1.11	1.14	1.05	1.28	0.86
Cr	1.03	1.01	1.03	0.99	1.02	1.05
Mn	0.73	0.73	0.72	0.72	0.72	0.70
Fe	1.00	1.00	1.00	1.00	1.00	1.00
Ni	0.95	0.97	0.98	1.03	0.96	0.97
P	0.97	0.97	0.97	0.98	0.97	0.98
Ti	1.23	1.24	1.24	1.22	1.21	1.24
V	1.37	1.21	1.21	1.18	1.18	1.20
Co	0.97	0.98	0.99	0.98	0.97	0.99
Cu	0.87	0.88	0.85	0.90	0.85	0.83
Zn	0.55	0.51	0.51	0.50	0.53	0.50
Ga	0.69	0.70	0.68	0.68	0.69	0.67
As	0.95	0.99	0.88	0.94	0.86	0.93
Se	0.57	0.55	0.55	0.56	0.56	0.53
Rb	0.57	0.71	0.63	0.73	0.67	0.50
Sr	1.28	1.16	1.10	1.13	1.22	2.97
Zr	1.19	1.21	1.21	1.23	1.17	1.35
Nb	1.32	1.25	1.23	1.27	1.19	1.24
Mo	25*	1.23	1.09	1.06	1.37	1.09
Rh	1.06	1.08	1.08	1.07	1.02	1.20
Ag	0.59	0.69	0.55	0.96	0.55	0.51
Cd	0.60	0.48	0.52	0.43	0.52	0.56
In	0.53	0.48	0.50	0.46	0.51	0.49
Sn	0.61	0.53	0.52	0.54	0.56	0.50
Te	0.57	0.54	0.53	0.50	0.55	0.53
Cs	0.59	0.60	0.58	0.58	0.59	0.58
Ba	1.18	1.27	1.12	1.42	1.14	2.34
La	1.23	1.30	1.21	1.33	1.19	1.25
Ce	1.23	1.29	1.22	1.31	1.19	1.26
Pr	1.22	1.27	1.22	1.27	1.18	1.24
Nd	1.20	1.25	1.20	1.25	1.18	1.22
Sm	1.21	1.22	1.22	1.22	1.20	1.23
Eu	1.17	1.20	1.19	1.18	1.20	1.20
Gd	1.24	1.21	1.33	1.20	1.21	1.49
Tb	1.23	1.21	1.29	1.21	1.16	1.58
Dy	1.22	1.20	1.29	1.20	1.16	1.60
Er	1.16	1.16	1.19	1.19	1.15	1.48
Tm	1.19	1.21	1.20	1.20	1.18	1.29
Yb	1.17	1.20	1.18	1.17	1.16	1.19
Lu	1.19	1.21	1.23	1.23	1.19	1.33
Hf	1.20	1.22	1.21	1.26	1.18	1.35
W	255*	1.25	1.10	1.19	1.17	1.23
Re	1.23	1.13	1.12	1.11	1.13	0.78
Ir	1.18	1.10	1.03	1.13	0.99	1.34
Pt	1.10	1.07	1.06	1.10	1.06	0.97
Tl	0.57	0.51	0.55	0.48	0.55	0.54
Pb	1.85*	1.17*	0.56	1.53*	0.54	0.50
Bi	0.59	0.52	0.51	0.53	0.65	0.50
Th	1.26	1.44	1.24	1.44	1.14	1.38
U	1.23	1.49	1.16	3.01	1.12	1.87

	ALH 85013 CM2	EET 96029 CM2	LON 94101 CM2	LON 94102 CM2	SCO 06043 CM1	MET 01070 CM1
Na	0.76	0.39	0.78	0.21	0.23	0.18
Mg	1.08	1.04	1.08	1.04	1.01	1.04
Al	1.25	1.27	1.22	1.23	1.24	1.22
S	0.53	0.61	0.57	0.48	0.55	0.58
K	0.77	0.63	0.78	0.69	0.40	0.45
Ca	1.19	1.41	1.23	1.11	1.15	0.95
Cr	1.02	1.05	1.03	1.02	1.01	1.01
Mn	0.72	0.74	0.74	0.73	0.71	0.73
Fe	1.00	1.00	1.00	1.00	1.00	1.00
Ni	0.97	1.09	0.97	0.98	0.97	1.00
P	1.00	0.96	0.93	1.00	0.96	1.01
Ti	1.26	1.20	1.21	1.23	1.22	1.23
V	1.20	1.19	1.20	1.19	1.18	1.20
Co	0.96	1.02	0.96	0.99	0.97	0.99
Cu	0.86	0.83	0.87	0.86	0.85	0.90
Zn	0.48	0.51	0.52	0.53	0.50	0.51
Ga	0.68	0.67	0.67	0.72	0.69	0.70
As	0.93	0.89	0.95	0.94	0.88	0.95
Se	0.54	0.60	0.56	0.57	0.56	0.57
Rb	0.68	0.61	0.66	0.68	0.58	0.66
Sr	1.16	1.27	1.09	1.14	1.11	1.06
Zr	1.24	1.15	1.25	1.14	1.21	1.21
Nb	1.25	1.21	1.27	1.24	1.26	1.23
Mo	1.15	1.20	1.04	1.08	1.12	1.09
Rh	1.07	1.08	1.06	1.04	1.06	1.05
Ag	0.48	0.51	0.52	0.54	0.50	0.52
Cd	0.48	0.51	0.51	0.52	0.50	0.50
In	0.47	0.50	0.50	0.51	0.48	0.49
Sn	0.49	0.50	0.51	0.53	0.52	0.56
Te	0.52	0.54	0.55	0.56	0.53	0.54
Cs	0.56	0.59	0.58	0.58	0.56	0.66
Ba	1.09	1.11	1.08	1.11	1.05	1.15
La	1.24	1.24	1.24	1.20	1.27	1.24
Ce	1.25	1.25	1.24	1.22	1.26	1.23
Pr	1.22	1.22	1.23	1.21	1.25	1.24
Nd	1.22	1.22	1.21	1.21	1.23	1.23
Sm	1.25	1.21	1.19	1.22	1.21	1.21
Eu	1.19	1.17	1.16	1.20	1.19	1.19
Gd	1.22	1.19	1.14	1.27	1.17	1.23
Tb	1.24	1.19	1.23	1.20	1.22	1.21
Dy	1.25	1.18	1.22	1.18	1.22	1.22
Er	1.23	1.13	1.21	1.12	1.19	1.17
Tm	1.23	1.19	1.20	1.19	1.20	1.19
Yb	1.21	1.18	1.18	1.20	1.18	1.18
Lu	1.24	1.17	1.26	1.16	1.20	1.21
Hf	1.24	1.17	1.28	1.14	1.24	1.22
W	2.19*	1.05	1.14	1.09	1.10	2.99*
Re	1.17	1.46	1.21	0.99	1.18	1.25
Ir	1.07	1.16	1.18	0.96	1.16	1.14
Pt	1.11	1.39	1.11	1.03	1.11	1.09
Tl	0.49	0.55	0.53	0.56	0.51	0.54
Pb	0.46	0.51	0.51	0.52	0.50	0.51
Bi	0.47	0.52	0.52	0.53	0.50	0.51
Th	1.24	1.19	1.26	1.17	1.33	1.24
U	1.14	1.29	1.16	1.15	1.25	1.18

	GRA 95229 CR2	LAP 02342 CR2	Kainsaz CO3	ALHA 77307 CO3	Allende Smiths. CV3	Allende MS CV3
Na	0.43	0.27	0.59	0.20	0.50	0.45
Mg	1.09	0.90	1.07	0.96	1.22	1.13
Al	1.14	1.18	1.21	1.18	1.61	1.62
S	0.16	0.15	0.26	0.28	0.32	0.31
K	0.49	0.47	0.57	0.56	0.51	0.52
Ca	1.10	1.18	1.19	1.23	1.53	1.62
Cr	1.14	1.15	1.02	1.03	1.08	1.07
Mn	0.62	0.75	0.57	0.61	0.55	0.53
Fe	1.00	1.00	1.00	1.00	1.00	1.00
Ni	0.97	0.90	0.94	0.90	0.97	0.98
P	0.77	0.82	0.94	0.96	0.93	0.91
Ti	1.19	1.38	1.30	1.30	1.62	1.52
V	1.16	1.17	1.28	1.27	1.49	1.50
Co	0.98	0.92	0.97	0.94	0.98	0.94
Cu	0.47	0.55	0.75	0.78	0.62	0.58
Zn	0.14	0.14	0.24	0.31	0.29	0.30
Ga	0.29	0.32	0.53	0.60	0.45	0.43
As	0.57	0.67	0.98	0.94	0.71	0.73
Se	0.19	0.22	0.31	0.40	0.34	0.33
Rb	0.36	0.40	0.47	0.53	0.42	0.35
Sr	1.14	1.26	1.22	1.18	1.55	1.56
Zr	1.17	1.16	1.23	1.22	1.50	1.40
Nb	1.24	1.39	1.26	1.20	1.54	1.44
Mo	1.29	0.89	1.11	1.06	1.29	1.17
Rh	1.15	0.99	1.08	1.11	1.21	1.19
Ag	0.14	0.16	0.27	0.37	0.37	0.32
Cd	0.15	0.15	0.02	0.30	0.54	0.28
In	0.14	0.14	0.23	0.29	0.28	0.28
Sn	0.15	0.16	0.25	0.34	0.35	0.35
Te	0.16	0.18	0.29	0.37	0.32	0.31
Cs	0.26	0.26	0.36	0.39	0.36	0.23
Ba	1.01	1.11	1.09	1.15	1.46	2.04
La	1.25	1.14	1.22	1.15	1.77	2.03
Ce	1.22	1.18	1.22	1.15	1.73	1.82
Pr	1.21	1.21	1.23	1.21	1.77	1.75
Nd	1.19	1.24	1.25	1.27	1.77	1.68
Sm	1.19	1.29	1.27	1.26	1.75	1.64
Eu	1.16	1.24	1.24	1.25	1.55	1.54
Gd	1.18	1.22	1.31	1.27	1.63	1.47
Tb	1.20	1.23	1.27	1.27	1.60	1.45
Dy	1.18	1.20	1.26	1.24	1.57	1.40
Er	1.15	1.20	1.22	1.24	1.47	1.38
Tm	1.18	1.27	1.23	1.26	1.68	1.58
Yb	1.17	1.29	1.23	1.25	1.52	1.43
Lu	1.18	1.23	1.25	1.27	1.50	1.38
Hf	1.21	1.19	1.25	1.24	1.52	1.39
W	1.44	0.99	1.17	1.06	1.41	1.15
Re	1.31	1.19	1.70	1.42	1.25	1.15
Ir	1.31	1.11	1.42	1.26	1.26	1.31
Pt	1.24	1.03	1.23	1.22	1.34	1.40
Tl	0.15	0.16	0.23	0.29	0.35	0.34
Pb	0.15	0.16	0.25	0.33	0.37	0.36
Bi	0.14	0.15	0.27	0.34	0.32	0.30
Th	1.19	1.25	1.20	1.27	1.68	1.76
U	1.18	1.35	1.15	1.21	1.66	1.76

	Vigarano CV3	EET 96026 C4/5	ALH 85002 CK4
Na	0.40	0.46	0.44
Mg	1.08	1.20	0.87
Al	1.47	1.47	1.27
S	0.28	0.11	0.23
K	0.51	0.65	0.40
Ca	1.49	1.37	1.34
Cr	1.05	1.07	1.08
Mn	0.54	0.57	0.54
Fe	1.00	1.00	1.00
Ni	0.95	0.75	1.06
P	0.96	0.90	1.01
Ti	1.54	1.48	1.67
V	1.38	1.38	1.59
Co	0.96	0.90	1.11
Cu	0.61	0.65	0.63
Zn	0.28	0.29	0.22
Ga	0.45	0.41	0.43
As	1.06	0.56	0.79
Se	0.32	0.22	0.33
Rb	0.45	0.54	0.22
Sr	1.46	1.43	1.43
Zr	1.41	1.43	1.44
Nb	1.49	1.63	1.64
Mo	1.46	1.39	0.44
Rh	1.14	1.26	1.41
Ag	0.48	0.28	0.24
Cd	0.09	0.05	0.26
In	0.28	0.09	0.24
Sn	0.38	0.06	0.24
Te	0.33	0.04	0.21
Cs	0.38	0.26	0.24
Ba	1.79	1.29	1.19
La	1.68	1.51	1.42
Ce	1.63	1.50	1.44
Pr	1.65	1.50	1.53
Nd	1.65	1.51	1.58
Sm	1.65	1.51	1.64
Eu	1.49	1.43	1.40
Gd	1.57	1.49	1.69
Tb	1.55	1.47	1.53
Dy	1.51	1.45	1.50
Er	1.38	1.42	1.47
Tm	1.56	1.48	1.56
Yb	1.45	1.42	1.48
Lu	1.42	1.48	1.67
Hf	1.47	1.47	1.43
W	1.53	1.39	1.37
Re	1.31	0.45	1.29
Ir	1.27	1.32	1.30
Pt	1.30	1.19	1.64
Tl	0.33	0.02	BDL
Pb	1.62*	0.03	0.28
Bi	0.31	0.02	0.21
Th	1.61	1.43	1.53
U	2.01	1.37	1.38

*contaminated, BDL = Below Detection Limit

Table A3: Major and trace element abundances in µg/g obtained by SF-ICP-MS for Ivuna compared with literature values: (1) Barrat et al. (2012), (2) Wang et al. (2014), (3) Pourmand et al. (2012), (4) Fischer-Gödde et al. (2010), (5) Lu et al. (2007)

	Ivuna	SD	RSD %	(1) SF-ICPMS	(2) ID SF-ICPMS	(3) MC-ICP-MS	(4) ID-ICP-MS	(5) ID-ICP-MS
n	*16*							
Na	4932	293	6	4900				
Mg	95468	2709	3	95500				
Al[a]	7967	435	5	7840				
S	49686	1650	3		53200			
K	407	25	6	432				
Ca	8957	504	6	9210				
Cr	2575	99	4	2570				
Mn	2040	81	4	2020				
Fe	182348	5600	3	188800				
Ni	11226	416	4	12000				
n	*23*							
P	845	21	2	1020				
Ti	381	6	1	430				435
V	47.5	0.8	2	54.0				
Co	507	13	3	531				
Cu	136	4	3	138	125			
Zn	321	13	4	330				
Ga	8.7	0.5	6	9.67				
As	1.7	0.1	5					
Rb	2.09	0.04	2	2.23				
Zr	3.27	0.07	2	3.48				3.55
Nb	0.251	0.011	4	0.298				0.287
Rh	0.129	0.002	2				0.131	
Ag[b]	0.203	0.006	3		0.199			
Cd	0.696	0.014	2		0.691			
In	0.0797	0.0016	2		0.076			
Sn	1.48	0.033	2					2.01
Te	2.49	0.091	4		2.29			
Cs	0.173	0.003	2	0.192				
Ba	2.20	0.05	2	2.57	2.56			
La	0.189	0.016	8	0.241		0.26665		
Ce	0.503	0.035	7	0.614		0.6809		
Pr	0.0824	0.002	3	0.092		0.103		
Nd	0.428	0.005	1	0.471		0.521		
Sm	0.144	0.005	3	0.155	0.171	0.16675		
Eu	0.0547	0.001	2	0.0597		0.06395		
Gd[c]	0.212	0.010	5	0.213		0.2241		
Tb[b]	0.0356	0.0006	2	0.0388		0.04015		
Dy	0.243	0.004	2	0.26		0.27415		
Er[b]	0.158	0.002	1	0.17		0.17745		
Tm	0.0243	0.0003	1	0.0271		0.02795		
Yb	0.165	0.003	2	0.173		0.18165		
Lu[b]	0.0242	0.0003	1	0.0248		0.02815		
Hf	0.096	0.003	3	0.107				0.11
W	0.0934	0.0039	4	0.1	0.112			
Re	0.0327	0.0015	5				0.0381	
Ir	0.409	0.008	2				0.422	
Pt	0.787	0.023	3				0.871	
Tl	0.136	0.003	2		0.13			
Pb	2.39	0.06	2	2.65				
Th	0.0251	0.0015	6	0.0289				
U	0.0060	0.0002	4	0.0075				

[a] n=12; [b] n=19; [c] n=13

Table A4: Major and trace elements in µg/g obtained by SF-ICP-MS for two Orgueil aliquots compared with literature values. (1) Barrat et al. (2012), (2) Friedrich et al. (2002), (3) Wang et al. (2014), (4) Pourmand et al. (2012), (5) Fischer-Gödde et al. (2010), (6) Wolf et al. (2005), (7) Münker et al. (2003)

	Orgueil A	SD	RSD %	Orgueil B	SD	RSD %	AVG Orgueil	SD	RSD %	(1) SF-ICPMS	(2) Q-ICPMS	(3) ID-ICPMS	(4) MC-ICP-MS	(5) ID-ICP-MS	(6) Q-ICPMS	(7) MC-ICP-MS
n	*10*			*4*												
Na	2621	164	6	2403	33	1	2523	121	5	4800						
Mg	98792	3256	3	94883	1260	1	96735	1851	2	94200						
Al	8602	485	6	8004	122	2	8328	324	4	7920						
S	45778	1558	3	44920	1873	4	45450	529	1			53900				
K	427	29	7	389	10	2	410	21	5	550						
Ca	8105	452	6	7507	191	3	7842	335	4	8440						
Cr	2766	114	4	2660	59	2	2719	59	2	2630						
Mn	2019	82	4	1904	30	2	1966	62	3	1970	1870					
Fe	196473	5904	3	187930	2716	1	192528	4598	2	195200						
Ni	11449	506	4	10918	282	3	11213	294	3	11300						
n	*15*			*5*												
P	913	27	3	897	33	4	905	8	1	1020						
Ti	419	6	1	410	13	3	415	4	1	440	470					
V	50.4	0.7	1	49.9	1.8	4	50.1	0.3	1	52.4	48					
Co	525	16	3	506	9	2	515	9	2	519	489					
Cu	148	5	3	144	3	2	146.1	1.7	1	127	150	134			158	
Zn	345	19	5	329	10	3	337.0	8.0	2	303					293	
Ga	8.98	0.43	5	9.52	0.31	3	9.25	0.27	3	9.48					10.1	
As	1.80	0.13	7	1.86	0.06	3	1.83	0.03	2		1.45					
Rb	1.76	0.05	3	1.75	0.04	2	1.75	0.005	0.3	2.33	2.13				2.4	
Zr	5.02	0.10	2	4.32	0.07	2	4.67	0.35	8	3.52	5.2					4.925
Nb	0.309	0.011	4	0.296	0.004	1	0.302	0.007	2	0.289	0.36					0.35
Rh	0.135	0.003	3	0.131	0.002	2	0.133	0.002	1					0.133		
Ag	0.222[a]	0.007	3	0.217	0.006	3	0.2196	0.0028	1						0.172	
Cd	0.705	0.018	3	0.689	0.023	3	0.6968	0.0082	1			0.695			0.636	

	Orgueil A	SD	RSD %	Orgueil B	SD	RSD %	AVG Orgueil	SD	RSD %	(1) SF-ICPMS	(2) Q-ICPMS	(3) ID-ICPMS	(4) MC-ICP-MS	(5) ID-ICP-MS	(6) Q-ICPMS	(7) MC-ICP-MS
In	0.0829	0.0018	2	0.0798	0.0022	3	0.0813	0.0015	2			0.077			0.073	
Sn	1.56	0.039	3	1.54	0.031	2	1.548	0.008	1		1.5				1.45	
Te	2.67	0.161	6	2.59	0.150	6	2.63	0.041	2		2.5	2.34			2.22	
Cs	0.159	0.003	2	0.156	0.004	2	0.158	0.002	1	0.189	0.191				0.191	
Ba	3.14	0.07	2	2.94	0.08	3	3.04	0.10	3	2.46	2.12	(3.8)				
La	0.259	0.013	5	0.314	0.035	11	0.287	0.027	10	0.235	0.236		0.2471			
Ce	0.657	0.029	4	0.778	0.073	9	0.718	0.060	8	0.6	0.623		0.6326			
Pr	0.1010	0.003	3	0.1189	0.004	3	0.1099	0.009	8	0.091	0.0958		0.0962			
Nd	0.500	0.005	1	0.574	0.007	1	0.537	0.037	7	0.464	0.449	0.156	0.4859			
Sm	0.161	0.005	3	0.172	0.006	4	0.166	0.005	3	0.153	0.151		0.1558			
Eu	0.0592	0.001	2	0.0589	0.002	3	0.0590	0.0002	0.3	0.0586	0.0554		0.0601			
Gd	0.232[c]	0.016	7	0.228[d]	0.013	6	0.230	0.002	1	0.206	0.201		0.2091			
Tb	0.0396[a]	0.0008	2	0.0378	0.0004	1	0.0387	0.0009	2	0.0375	0.039		0.038			
Dy	0.273	0.006	2	0.260	0.003	1	0.266	0.007	3	0.254	0.21		0.2582			
Er	0.180[a]	0.004	2	0.167	0.002	1	0.173	0.007	4	0.166	0.154		0.1669			
Tm	0.0275	0.0004	2	0.0252	0.0002	1	0.0263	0.0011	4	0.0262	0.027		0.026			
Yb	0.186	0.004	2	0.173	0.005	3	0.180	0.007	4	0.168	0.158		0.169			
Lu	0.0281[a]	0.0004	1	0.0256	0.0003	1	0.0269	0.0012	5	0.0246	0.028		0.0252			
Hf	0.141	0.003	2	0.124	0.005	4	0.132	0.009	6	0.107	0.112	0.102				0.1419
W	0.0975	0.0074	8	0.0829	0.0020	2	0.0902	0.0073	8	0.11	0.078					
Re	0.0352	0.0013	4	0.0327	0.0008	3	0.0339	0.0013	4		0.043			0.0374		
Ir	0.436	0.009	2	0.421	0.010	2	0.428	0.007	2		0.435			0.435		
Pt	0.809	0.017	2	0.815	0.028	3	0.812	0.003	0.4		0.75	0.169		0.906		
Tl	0.145	0.002	1	0.142	0.005	4	0.1434	0.0018	1						0.137	
Pb	2.65[b]	0.06	2	2.59	0.07	3	2.62	0.03	1	2.69						
Th	0.0455	0.0022	5	0.0603	0.0053	9	0.0529	0.0074	14	0.0283	0.032					
U	0.0152	0.0004	2	0.0118	0.0008	7	0.0135	0.0017	13	0.007722	0.0081					

[a] n=11; [b] n=14; [c] n=8; [d] n=4

Table A5: Major and trace element abundances in µg/g obtained by SF-ICP-MS for Allende Smithsonian compared with literature values. (1) Jarosewich et al (1987), (2) Barrat et al. (2012), (3) Stracke et al. (2012), (4) Wang et al. (2014), (5) Pourmand et al. (2012), (6) Fischer-Gödde et al. (2010), (7) Wolf et al. (2005), (8) Münker et al. (2003)

	Split 16/4	SD	RSD %	(1)	(2) SF-ICP-MS	(3) ID-ICP-MS	(4) ID-ICP-MS	(5) MC-ICP-MS	(6) ID-ICP-MS	(7) Q-ICP-MS	(8) MC-ICP-MS
n	*10*										
Na	3160	145	5	3413							
Mg	149536	4449	3	148302		149400					
Al	16669	627	4	17359		15900					
S	20756	585	3	21000			20100				
K	270	11	4	332	277						
Ca	17789	798	4	18439		17100					
Cr	3603	93	3	3580		3645					
Mn	1465	37	3	1471	1420	1470					
Fe	237784	5474	2	235680		236500					
Ni	14197	388	3	14200		13723					
n	*14*										
P	1040	34	3	1047	1173	1065					
Ti	806	13	2	899	878	847					
V	92.6	1.6	2	92	95.2	93					
Co	656	18	3	600	616	596					
Cu	111.2	3.3	3	119	99		103			119	
Zn[a]	122.8	4.6	4	110	119	104				116.7	
Ga	5.23	0.30	6	6	5.68					6.152	
As	1.57	0.10	6								
Rb	1.15	0.03	3	1.2	1.18	1.32				1.103	
Zr	6.45	0.12	2	9	6.61	6.25					6.489
Nb	0.503	0.018	4		0.573	0.537					0.519
Rh	0.203	0.003	2						0.174		
Ag[a]	0.097	0.005	6				0.09			0.09989	
Cd	0.491	0.012	3				0.463			0.5039	
In	0.0290	0.0007	3				0.027			0.03018	
Sn	0.669	0.010	2							0.575	
Te	1.04	0.050	5				0.94			1	
Cs	0.080	0.002	2	0.096	0.0881	0.098				0.08568	
Ba	4.21	0.09	2	4	4.53	4.65	4.7				
La[b]	0.471	0.017	4	0.52	0.516	0.461		0.5628			
Ce[b]	1.212	0.035	3	1.33	1.29	1.17		1.407			
Pr	0.1909	0.005	3	0.21	0.201	0.18		0.2184			
Nd	0.998	0.014	1	0.99	1.02	0.906		1.121			
Sm	0.328	0.011	3	0.34	0.329	0.293	0.331	0.3562			
Eu	0.1105	0.002	2	0.11	0.114	0.108		0.1232			
Gd[b]	0.439	0.024	6	0.42	0.417	0.372		0.4433			
Tb[a]	0.0735	0.0014	2	0.081	0.0762	0.0663		0.0801			
Dy	0.499	0.009	2	0.42	0.508	0.442		0.5389			
Er[a]	0.304	0.006	2	0.29	0.31	0.274		0.3135			
Tm	0.0532	0.0007	1	0.055	0.0559	0.0487		0.0557			
Yb	0.327	0.008	2	0.3	0.325	0.303		0.3258			
Lu[a]	0.0470	0.0008	2	0.052	0.0459	0.0419		0.045			
Hf	0.191	0.004	2	0.21	0.202	0.174					0.1905
W	0.171	0.010	6	0.2	0.2						
Re	0.0531	0.0031	6	0.064					0.0605		
Ir	0.674	0.019	3	0.74					0.684		
Pt	1.385	0.038	3						1.357		
Tl	0.0622	0.0018	3	0.0531			0.059			0.06081	
Pb	1.08	0.03	3	1.39	1.27	1.54					
Th	0.0561	0.0037	7	0.063	0.0594	0.0727					
U	0.0132	0.0006	5		0.0152	0.0174					

[a] n=12; [b] n=9

Table A6: Major and trace element abundances in µg/g obtained by SF-ICP-MS for BHVO-2 and BCR-2 compared with data of the GeoReM database (Jochum et al., 2016).

	BHVO-2	SD	RSD %	GeoReM	BCR-2	SD	RSD %	GeoReM
n	*4*				*4*			
Na	14638	310	2	16462	20600	698	3	23146
Mg	42960[a]	122	0.3	43767	20610[a]	276	1	21706
Al	67873[a]	627	1	71131	28291[a]*	583	2	71343
S	166	9	5	164	312	13	4	318
K	3917	230	6	4259	13216	715	5	14727
Ca	73752	3217	4	81476	45728	2108	5	50844
Cr	286	8	3	287	14.8	0.5	3	16
Mn	1284	23	2	1309	1477	30	2	1523
Fe	83902	2390	3	86659	91485	2533	3	96312
Ni	124	2	1	120	13.6	0.1	0.4	12.6
n	*4*				*3*			
P	1062	51	5	1172	1345	16	1	1568
Ti	15109	246	2	16373	11385	98	1	13579
V	309	10	3	318	395	11	3	418
Co	44.0	1.1	2	44.9	36.8	0.3	1	37.3
Cu	127	2	2	129	16.8	0.2	1	20
Zn	105	2	2	104	136	6	4	130
Ga	19.3	0.8	4	21.4	19.4	0.5	2	22.1
As	0.710	0.024	3	0.700	0.809	0.051	6	0.860
Rb	8.45	0.25	3	9.26	43.3	1.2	3	46.02
Zr	154	2	1	171	169	1	0.3	187
Nb	16.4	0.2	1	18.1	10.5	0.1	1	12.4
Sn	1.73	0.02	1	1.78	2.52	0.03	1	2.28
Cs	0.0872	0.0022	3	0.0996	1.01	0.02	2	1.16
Ba	119	2	1	131	599	12	2	684
La	12.0	0.9	8	15.2	19.1	1.6	9	25.1
Ce	31.8	1.8	6	37.5	43.1	3.1	7	53.1
Pr	4.83	0.09	2	5.34	5.85	0.02	0.4	6.83
Nd	22.9	0.5	2	24.3	25.3	0.4	2	28.3
Sm	6.02	0.18	3	6.02	6.17	0.23	4	6.55
Eu	2.00	0.03	2	2.04	1.78	0.04	2	1.99
Gd	6.26[b]	0.28	4	6.21	6.23[a]	0.15	2	6.81
Tb	0.854	0.034	4	0.939	0.890	0.017	2	1.077
Dy	5.16	0.08	2	5.28	5.79	0.07	1	6.42
Er	2.52	0.05	2	2.51	3.33	0.05	2	3.67
Tm	0.312	0.001	0	0.335	0.451	0.001	0.3	0.534
Yb	1.89	0.04	2	1.99	2.94	0.07	2	3.39
Lu	0.265	0.003	1	0.275	0.433	0.002	1	0.505
Hf	4.10	0.12	3	4.47	4.59	0.08	2	4.97
W	0.189	0.002	1	0.251	0.398	0.007	2	0.465
Tl	0.0212	0.0009	4	0.0224	0.279	0.004	2	0.267
Pb	1.47	0.03	2	1.65	14.8	0.03	0.2	10.6
Th	1.07	0.08	8	1.22	4.22	0.26	6	5.83
U	0.357	0.021	6	0.412	1.427	0.031	2	1.683

[a] n=2; [b] n=3; *unreasonably low value

Table A7: Major and trace element abundances in µg/g obtained by SF-ICP-MS for 14 aliquots of Murchison NC.

	Murchison NC							
	Mur Std	Mur O_2 100	Mur O_2 200	Mur O_2 300	Mur O_2 400	Mur O_2 600	Mur O_2 800	Mur O_2 1000
Na	922	998	940	940	943	981	996	1058
Mg	125700	135626	128428	130875	134638	130679	136321	139584
Al	10506	6929	12621	12843	12805	8154	13461	9496
S	27057	28763	26984	27729	26659	*24890*	*9089*	*2225*
K	1408	1533	1414	1393	1513	1504	1583	1610
Ca	12071	12960	12265	12489	12481	12713	13062	13449
Cr	3376	3681	3432	3471	3500	3579	3657	3797
Mn	1893	2053	1927	1915	1957	2009	2020	2120
Fe	229302	249220	232771	235023	239744	241974	246229	252860
Ni	13667	14890	13775	13889	14109	14366	14758	15247
P	1083	1159	1139	1150	1116	1134	1189	1188
Ti	593	633	613	626	611	619	654	661
V	72.5	78.0	74.6	75.8	74.3	76.3	79.1	80.7
Co	613	663	625	629	627	640	662	674
Cu	135	149	139	140	141	143	145	150
Zn	192	210	198	200	201	*202*	*208*	*214*
Ga	7.00	7.44	6.96	7.12	7.02	7.11	7.62	7.51
As	1.93	2.15	2.06	2.06	1.93	1.99	2.10	2.03
Rb	1.42	1.54	1.47	1.46	1.45	1.46	1.54	1.56
Zr	5.67	5.83	5.66	5.86	5.53	6.22	5.64	6.60
Nb	0.405	0.434	0.414	0.422	0.417	0.425	0.448	0.450
Rh	0.163	0.176	0.168	0.170	0.172	0.165	0.169	0.178
Ag	0.127	0.139	0.148	0.129	0.134	*0.136*	*0.151*	*0.122*
Cd	0.435	0.467	0.451	0.444	0.457	*0.459*	*0.468*	*0.463*
In	0.048	0.053	0.049	0.050	0.050	*0.051*	*0.052*	*0.054*
Sn	0.933	1.062	0.958	0.965	0.970	*1.004*	*1.014*	*1.043*
Te	1.52	1.69	1.52	1.56	1.60	*1.59*	*1.72*	*0.58*
Cs	0.112	0.121	0.117	0.119	0.117	0.129	0.123	0.125
Ba	11.1	12.2	11.7	11.8	11.6	11.7	12.1	12.5
La	0.367	0.444	0.387	0.419	0.389	0.387	0.458	0.486
Ce	0.92	1.08	0.97	1.04	0.97	0.98	1.15	1.18
Pr	0.141	0.163	0.146	0.156	0.148	0.148	0.173	0.177
Nd	0.705	0.800	0.723	0.774	0.735	0.743	0.831	0.867
Sm	0.226	0.246	0.230	0.243	0.235	0.236	0.256	0.261
Eu	0.0863	0.0952	0.0899	0.0914	0.0889	0.0905	0.0960	0.0983
Gd	0.302	0.332	0.313	0.320	0.305	0.314	0.333	0.341
Tb	0.0569	0.0617	0.0587	0.0590	0.0579	0.0603	0.0620	0.0636
Dy	0.396	0.424	0.398	0.406	0.398	0.417	0.430	0.435
Er	0.245	0.265	0.253	0.250	0.245	0.270	0.258	0.272
Tm	0.0388	0.0413	0.0395	0.0403	0.0395	0.0400	0.0415	0.0423
Yb	0.256	0.274	0.260	0.263	0.262	0.267	0.273	0.285
Lu	0.0385	0.0408	0.0404	0.0401	0.0389	0.0438	0.0398	0.0424
Hf	0.173	0.179	0.173	0.180	0.168	0.191	0.173	0.195
W	0.117	0.148	0.133	0.120	0.117	0.127	0.134	0.154
Re	0.0365	0.0392	0.0382	0.0385	0.0369	*0.0377*	*0.0194*	*0.0059*
Ir	0.533	0.595	0.564	0.594	0.579	*0.550*	*0.495*	*0.290*
Pt	1.09	1.19	1.14	1.16	1.13	*1.10*	*1.11*	*0.71*
Tl	0.0860	0.0925	0.0887	0.0900	0.0893	*0.0919*	*0.0771*	*0.0580*
Pb	1.57	1.73	1.72	1.64	1.66	*1.70*	*1.70*	*1.66*
Th	0.0519	0.0707	0.0539	0.0609	0.0553	0.0550	0.0622	0.0881
U	0.0450	0.0189	0.0168	0.0221	0.0169	0.0210	0.0175	0.0221

	Mur Ar 200	Mur Ar 300	Mur Ar 400	Mur Ar 600	Mur Ar 800	Mur Ar 1000	AVG	SD	RSD
Na	1060	877	957	1008	1041	941	976	52	5
Mg	145768	119648	135975	142288	147386	144832	135553	7747	6
Al	12924	10888	12586	10882	12177	9990	11161	1905	17
S	26760	24311	27498	*25868*	*14104*	*27691*	26970	1188	4
K	1615	1322	1393	1491	1572	1518	1491	88	6
Ca	13785	11154	12674	13351	14121	13918	12892	775	6
Cr	3853	3138	3531	3697	3952	3876	3610	214	6
Mn	2168	1759	1984	2106	2218	2158	2020	122	6
Fe	261073	214678	241646	254361	270428	256946	244733	13831	6
Ni	15462	12698	14253	14914	15901	15664	14542	855	6
P	1250	1024	1157	1178	1218	1261	1161	61	5
Ti	686	558	630	645	674	691	635	35	6
V	83.4	67.9	76.4	79.5	81.8	84.9	77.5	4.4	6
Co	693	569	641	666	700	705	651	36	6
Cu	155	129	142	148	155	160	145	8	6
Zn	217	181	203	*211*	*135*	*5*	200	10	5
Ga	8.06	6.62	7.22	7.50	7.88	7.51	7.33	0.38	5
As	2.33	1.80	2.03	2.17	2.11	2.06	2.05	0.12	6
Rb	1.66	1.33	1.50	1.53	1.61	1.54	1.50	0.08	5
Zr	6.41	5.29	5.64	5.72	6.23	6.41	5.91	0.38	6
Nb	0.471	0.383	0.432	0.441	0.472	0.469	0.435	0.025	6
Rh	0.185	0.152	0.168	0.175	0.188	0.194	0.173	0.010	6
Ag	0.143	0.121	0.133	*0.139*	*0.142*	*0.039*	0.134	0.008	6
Cd	*0.050*	0.406	0.459	*0.324*	*0.038*	*0.037*	0.445	0.019	4
In	*0.037*	0.046	0.051	*0.052*	*0.019*	*0.001*	0.050	0.002	4
Sn	1.052	0.930	0.986	*1.022*	*0.833*	*0.030*	0.982	0.047	5
Te	1.77	1.44	1.59	*1.64*	*1.59*	*0.30*	1.586	0.097	6
Cs	0.133	0.105	0.119	0.124	0.130	0.119	0.121	0.007	6
Ba	13.0	10.4	11.8	12.3	13.0	13.2	12.0	0.7	6
La	0.426	0.374	0.411	0.418	0.449	0.438	0.418	0.033	8
Ce	1.08	0.93	1.03	1.05	1.11	1.10	1.04	0.08	7
Pr	0.161	0.140	0.156	0.158	0.170	0.166	0.157	0.011	7
Nd	0.806	0.694	0.766	0.777	0.835	0.837	0.778	0.052	7
Sm	0.265	0.216	0.243	0.245	0.263	0.263	0.245	0.015	6
Eu	0.0987	0.0807	0.0920	0.0961	0.1007	0.1014	0.0933	0.0056	6
Gd	0.345	0.290	0.326	0.326	0.345	0.354	0.325	0.018	6
Tb	0.0648	0.0530	0.0597	0.0621	0.0657	0.0650	0.0607	0.0034	6
Dy	0.448	0.369	0.416	0.429	0.453	0.459	0.420	0.024	6
Er	0.277	0.222	0.250	0.262	0.283	0.282	0.260	0.016	6
Tm	0.0439	0.0361	0.0407	0.0419	0.0444	0.0440	0.0410	0.0022	5
Yb	0.294	0.238	0.268	0.281	0.299	0.294	0.272	0.016	6
Lu	0.0438	0.0345	0.0388	0.0407	0.0445	0.0445	0.0408	0.0027	7
Hf	0.197	0.160	0.171	0.176	0.190	0.195	0.180	0.011	6
W	0.183	0.120	0.135	0.141	0.141	0.170	0.138	0.019	14
Re	0.0419	0.0333	0.0409	*0.0396*	*0.0406*	*0.0594*	0.038	0.003	7
Ir	0.633	0.525	0.612	*0.615*	*0.632*	*0.661*	0.579	0.035	6
Pt	1.26	1.02	1.14	*1.21*	*1.25*	*1.30*	1.141	0.066	6
Tl	*0.0366*	0.0802	0.0897	*0.0906*	*0.0031*	*0.0005*	0.088	0.004	4
Pb	1.60	1.58	1.71	*1.72*	*0.29*	*0.02*	1.650	0.059	4
Th	0.0617	0.0644	0.0639	0.0576	0.0657	0.0642	0.0625	0.0087	14
U	0.0209	0.0164	0.0185	0.0196	0.0214	0.0213	0.0213	0.0068	32

Values in italics are not taken into account for calculation of the average.

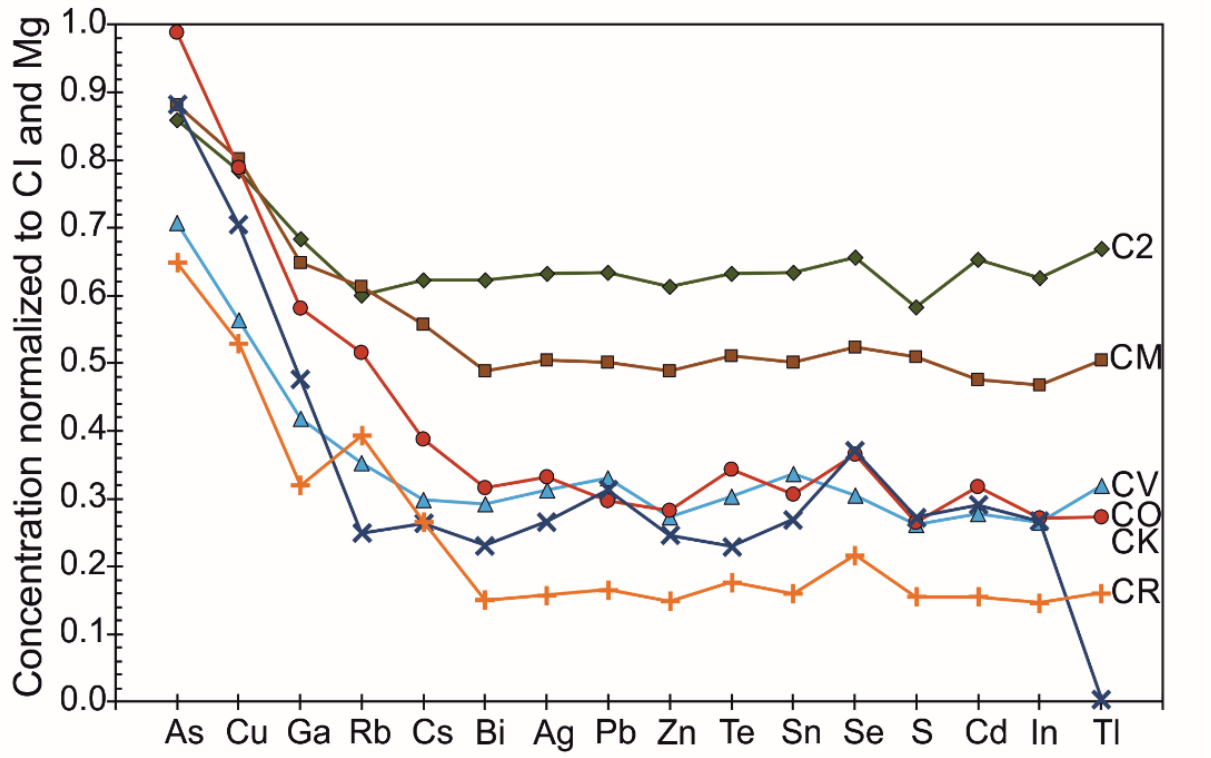

Figure A1: Median volatile element depletion relative to CI and normalized to Mg for comparison to Fe normalized pattern in **Figure 2.6**. Elements are arranged from left to right in order of decreasing 50% T_C (Lodders, 2003; Kiseeva and Wood, 2015). The plateau volatile element level is very similar to that in **Figure 2.6**, except that the CK plateau moves closer to CV and CO level.

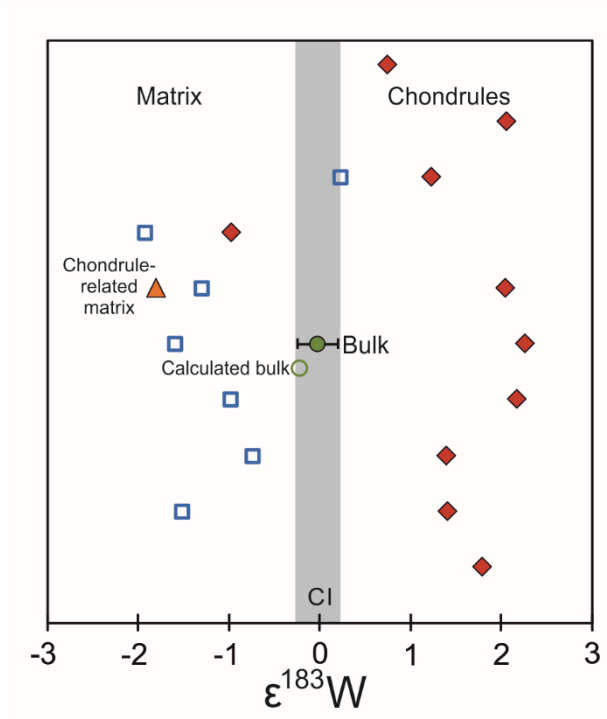

Figure A2: Consistency of the three-component model with $\varepsilon^{183}W$ chondrule-matrix complementarity in Allende (CV3). The chondrule-related matrix should have an approximate W concentration of 520 µg/g and an $\varepsilon^{183}W$ of -1.8, to reproduce bulk Allende $\varepsilon^{183}W$. The $\varepsilon^{183}W$ data for chondrules, bulk matrix and bulk Allende (CV3) was taken from Becker et al. (2015) and Budde et al. (2016b). $\varepsilon^{183}W = 10^4 \times [(^{183}W/^{184}W)_{sample}/(^{183}W/^{184}W)_{terrestrial\ standard\ solution} - 1]$, normalized to $^{186}W/^{184}W$.

Appendix B

Table B1: Average volatile element abundances in carbonaceous chondrites and the BSE.

	CI	%RSD	Source	CM	CV	CR	Source	BSE	%RSD	Source
Mg	96700	2.8	Chapter 2	121000	141000	124000	Chapter 2	221700	1	P&O14
Fe	193000	2.9	Chapter 2	220000	231000	240000	Chapter 2	63000	1	P&O14
Pd	0.56	4	Pa14	0.63	0.71	0.69	L&F98	0.0071	20	P&O14
Si	107000	3	Pa14	127000	157000	150000	L&F98	212000	1	P&O14
Cr	2720	3.6	Chapter 2	3170	3480	3860	Chapter 2	2520	10	P&O14
P	905	2.3	Chapter 2	982	1040	903	Chapter 2	87	15	P&O14
Mn	2040	4	Chapter 2	1770	14004	1830	Chapter 2	1050	10	P&O14
Li	1.45	10	Pa14	1.5	1.7	-	L&F98	1.6	20	P&O14
As	1.83	4.4	Chapter 2	1.81	1.63	1.39	Chapter 2	0.068	30	P&O14
Cu	146	2.6	Chapter 2	140	107	91.3	Chapter 2	30	20	Wa15
K	410	6.2	Chapter 2	384	266	261	Chapter 2	260	15	P&O14
Sb	0.135	14	Pa14	0.13	0.085	0.08	L&F98	0.0054	40	P&O14
Ga	9.25	5.5	Chapter 2	6.81	5.18	3.54	Chapter 2	4.4	5	P&O14
Na	4930	5.9	Chapter 2	3900	2680	2290	Chapter 2	2590	5	P&O14
Ge	32.6	9	Pa14	26	16,0	18	L&F98	1.2	20	P&O14
Rb	2.09	2	Chapter 2	1.58	1.15	1.04	Chapter 2	0.605	10	P&O14
Cs	0.173	1.6	Chapter 2	0.118	0.0804	0.0585	Chapter 2	0.018	50	P&O14
Bi	0.11	7	Pa14	0.07	0.05	-	L&F98	0.003	50	P&O14
Ag	0.22	2.5	Chapter 2	0.133	0.0899	0.04	Chapter 2	0.009	33	Wa15
Pb	2.62	2.2	Chapter 2	1.5	1.07	0.466	Chapter 2	0.185	10	P&O14
Zn	337	3.8	Chapter 2	196	123	61.4	Chapter 2	54	9	P&O14
Te	2.29	1.2	this study	1.42	0.89	0.503	this study	0.011	15	W&B13
Sn	1.55	2.1	Chapter 2	0.921	0.685	0.301	Chapter 2	0.14	30	P&O14
Se	20.6	0.75	this study	12.7	7.95	4.75	this study	0.08	21	W&B13
S	51000	0.67	this study	30800	19800	10100	this study	211	19	W&B13
Cd	0.696	2	Chapter 2	0.422	0.265	0.138	Chapter 2	0.031	19	Wa16
Cl	115	31	Cl17	151	85	70	Cl17	25	36	Cl17*
Br	0.189	38	Cl17	0.123	0.05	0.1	Cl17	0.074	35	Cl17*
In	0.0797	2.1	Chapter 2	0.0474	0.029	0.0149	Chapter 2	0.012	17	Wa16
I	0.057	12	Cl17	0.065	0.035	0.027	Cl17	0.014	79	Cl17*
Tl	0.136	2	Chapter 2	0.0867	0.0593	0.0274	Chapter 2	0.0041	25	P&O14

Pa14 = Palme et al. (2014a), Cl17 = Clay et al. (2017), L&F(98) = Lodders and Fegley (1998), P&O14 = Palme and O'Neill (2014), Wa15 =Wang and Becker (2015), W&B13 = Wang and Becker (2013), Wa16 = Wang et al (2016)

* average of compilation Clay et al. (2017)

Table B2: Sulfur, Se and Te abundances [µg/g] in different carbonaceous chondrites determined by isotope dilution.

Sample	Group	S	2sd	Se	2sd	Te	2sd	Source
Orgueil	CI	45300	680	21.41	0.32	2.285	0.055	A. Bischoff, Univ. Münster, Germany
Ivuna	CI	51000	770	20.56	0.31	2.26	0.054	J.-A. Barrat, UBO, France
Y-980115	CI	61270	920	24.15	0.36	2.405	0.058	NIPR, Japan
SCO 06043	CM1	32290	480	13.26	0.2	1.34	0.032	MWG NASA, USA.
MET 01070	CM1	-	-	13.55	0.2	1.43	0.034	MWG NASA, USA
Paris	CM2	32640	490	12.75	0.19	1.44	0.035	J.-A. Barrat, UBO, France
Murchison	CM2	29170	440	12.5	0.19	1.372	0.033	A. Bischoff, Univ. Münster, Germany
Mighei	CM2	31940	480	13.06	0.2	1.455	0.035	Field Museum, Chicago, USA
Murray	CM2	26060	390	12.47	0.19	1.44	0.035	Smithsonian Institute, USA
Cold Bokkeveld	CM2	27500	410	12.25	0.18	1.435	0.035	NHM London, GB.
Nogoya	CM2	31490	470	11.15	0.17	1.26	0.03	MfN Berlin, Germany.
Allende	CV3	19750	300	8.51	0.13	0.922	0.022	Smithsonian Institute, USA
Vigarano	CV3	-	-	7.4	0.11	0.86	0.021	J. Schlüter, Univ. Hamburg
Acfer 187	CR2	-	-	5.04	0.08	0.539	0.013	A. Bischoff, Univ. Münster, Germany
GRA 95229	CR2	10140	150	4.45	0.07	0.458	0.011	MWG NASA, USA
LAP 02342	CR2	10060	150	5.06	0.08	0.498	0.012	MWG NASA, USA

The 2 sd intermediate precision was estimated from the 2RSD from repeated analyses and digestions of Murchison.

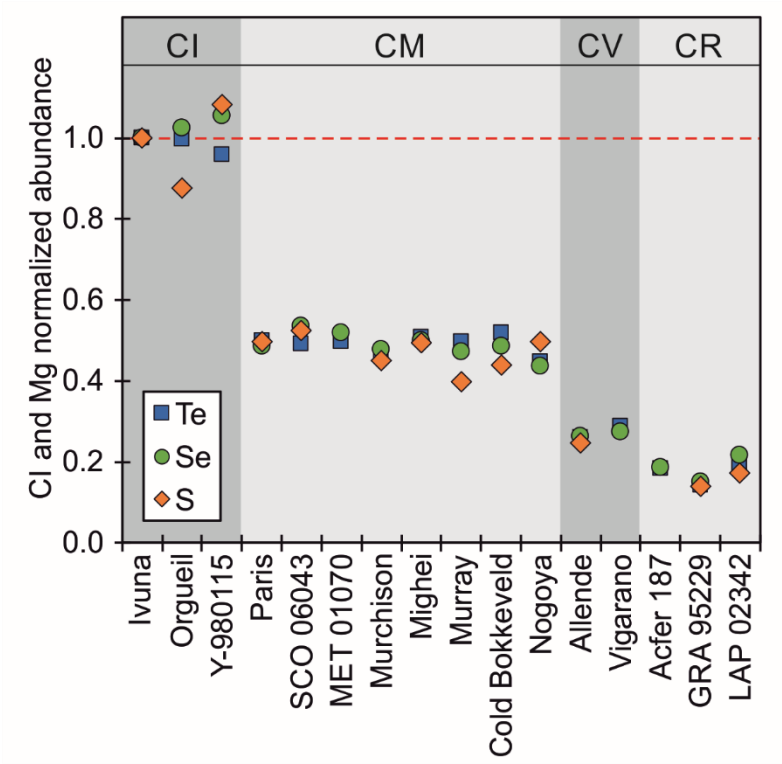

Figure B1: Sulfur, Se and Te abundances in carbonaceous chondrites relative to CI (Ivuna) and Mg normalized.

Appendix C

Table C1: Standard solutions used for spike calibration and mass bias correction.

Element	Company	LOT
Cu	NIST SRM 3114	11017
Zn	NIST SRM 3168a	80123
Ga	NIST SRM 3119a	890709
Ag	Alfa Aesar	154374K
Cd	NIST SRM 3108	60531
	Alfa Aesar	100131010
Sn	NIST SRM 3161a	70330
In	Sigma-Aldrich	MKAA1346V
	Merck	HCO85993
Tl	Merck	HC940537
	Alfa Aesar	8120396

Table C2: Mass fractions of diluted spike solutions

Spike	Spike isotope	Concentration	% (2s)	Source
Cu SSp1	^{65}Cu	40.35 ± 0.15 µg g^{-1}	0.37	Oak Ridge National Laboratory
Cu SSp2	^{65}Cu	4.012 ± 0.015 µg g^{-1}		
Zn SSp1	^{67}Zn	10.356 ± 0.080 µg g^{-1}	0.77	Trace Sciences International
Zn SSp2	^{67}Zn	1.0374 ± 0.0080 µg g^{-1}		
Ga SSp1	^{71}Ga	15.224 ± 0.038 µg g^{-1}	0.25	Oak Ridge National Laboratory
Ga SSp2	^{71}Ga	1.5344 ± 0.0038 µg g^{-1}		
Ag SSp1	^{109}Ag	96.04 ± 0.42 ng g^{-1}	0.43	Oak Ridge National Laboratory
Ag SSp2	^{109}Ag	10.493 ± 0.045 ng g^{-1}		
Ag SSp3	^{109}Ag	0.9486 ± 0.0041 ng g^{-1}		
Cd SSp1	^{110}Cd	98.66 ± 0.49 ng g^{-1}	0.49	Oak Ridge National Laboratory
Cd SSp2	^{110}Cd	9.906 ± 0.049 ng g^{-1}		
Cd SSp3	^{110}Cd	0.9872 ± 0.0048 ng g^{-1}		
In SSp1	^{113}In	30.17 ± 0.12 ng g^{-1}	0.10	Oak Ridge National Laboratory
In SSp2	^{113}In	3.021 ± 0.012 ng g^{-1}		
Sn SSp1	^{117}Sn	148.42 ± 0.57 ng g^{-1}	0.39	Oak Ridge National Laboratory
Sn SSp2	^{117}Sn	14.688 ± 0.057 ng g^{-1}		
Tl SSp1	^{203}Tl	97.22 ± 0.38 ng g^{-1}	0.39	Oak Ridge National Laboratory
Tl SSp2	^{203}Tl	9.718 ± 0.038 ng g^{-1}		
Tl SSp3	^{203}Tl	0.9734 ± 0.0038 ng g^{-1}		

Table C3: Mass spectrometry parameters.

Element	Measured isotopes	Sweeps	Main runs	Uptake time (s)	Rinse time (s)
Cu	^{63}Cu, ^{65}Cu	750	10	60	150
Zn	^{66}Zn, ^{67}Zn	750	10	60	150
Ga	^{69}Ga, ^{71}Ga	750	10	75	180
Ag	^{93}Nb,^{107}Ag, ^{109}Ag	720	10	75	140
Cd	^{105}Pd, ^{110}Cd, ^{111}Cd	720	10	75	180
In	^{113}In, ^{115}In, ^{111}Cd, ^{118}Sn	600	10	75	300
Sn	^{117}Sn, ^{120}Sn, ^{125}Te	720	10	50	120
Tl	^{203}Tl, ^{205}Tl, ^{209}Bi	600	10	75	300

Danksagung

Mein erster und größter Dank gilt *Frank Wombacher*, der wohl beste Doktorvater des gesamten Sonnensystems. Danke, dass deine Tür stets für mich offenstand und ich so viel von dir lernen durfte. Es war und ist mir eine unglaubliche Freude mit dir zusammenzuarbeiten und ich bin sehr dankbar und glücklich, dass ausgerechnet du mein Promotionsbetreuer gewesen bist.

Bei *Carsten Münker* möchte ich mich für die Möglichkeit bedanken meine Doktorarbeit über dieses spannende Thema und in dieser tollen Gruppe zu schreiben. Danke für die vielen Diskussionen und deine permanente Unterstützung und Förderung.

Michael Staubwasser möchte ich dafür danken, dass er sich dazu bereit erklärt hat als Gutachter für diese Arbeit zu fungieren.

Weiterhin möchte ich mich herzlichst bei *Dominik Hezel* bedanken für die so hilfreichen Diskussionen und Aufmunterungen, insbesondere in den teilweise durchaus schwierigen Phasen des 1. Papers. Bei *Claudia Funk* möchte ich mich ganz besonders für die Bereitstellung der S, Se und Te Daten für das 2. Paper bedanken und für deine stets positiven Emails, wenn mal wieder ein Titelvorschlag abgelehnt wurde…

Ein sehr großes Dankeschön geht an die gesamte *Geo-/Kosmochemie AG* inclusive Ehemaliger. Ohne euch wären die letzten 4 Jahre ganz schön langweilig gewesen. Danke, dass ihr mich alle durch diese aufregende Zeit begleitet habt. Dabei möchte ich vor allem meine gesammelten Bürokollegen der letzten Jahre hervorheben - *Julia, Christiane, Alessandro, Luise, Mario* und *Jens* - danke, dass ihr immer mit mir gelacht und auch meine schlechteren Launen ertragen habt. *Christina*, danke, dass du nach Köln gekommen bist und mir über die unzähligen „Coffices“ (und allem was dazu gehört) eine so gute Freundin geworden bist!

Meinen Eltern, Gisela und Frank, sowie meiner Lieblingsschwesti, Maike, möchte ich für alles danken was ich heute bin. Danke für das Fundament und den unerschütterlichen Rückhalt den ihr mir gebt. Danke für euer grenzenloses Vertrauen und eure stets ehrlichen Worte. Ich habe wirklich unverschämtes Glück mit euch :).

Mein letztes Dankeschön gilt dir, Philipp. Du hast buchstäblich alles ertragen in den letzten vier Jahren und bist mit mir durch jede Höhe und Tiefe gegangen. Danke, dass du während der Höhen zusammen mit mir gefeiert hast und mich aus jedem noch so tiefen Loch mit deinem bedingungslosen Glauben an mich wieder herausgeholt hast. Danke, dass du bei mir bist!

Erklärung

Ich versichere, dass ich die von mir vorgelegte Dissertation selbstständig angefertigt, die benutzten Quellen und Hilfsmittel vollständig angegeben und die Stellen der Arbeit – einschließlich Tabellen, Karten und Abbildungen –, die anderen Werken im Wortlaut oder dem Sinn nach entnommen sind, in jedem Einzelfall als Entlehnung kenntlich gemacht habe; dass sie – abgesehen von unten angegebenen Teilpublikationen – noch nicht veröffentlich worden ist, sowie, dass ich eine solche Veröffentlichung vor Abschluss des Promotionsverfahrens nicht vornehmen werde. Die Bestimmungen der Promotionsordnung sind mir bekannt. Die von mir vorgelegte Dissertation ist von PD Dr. Frank Wombacher betreut worden.

Nachfolgend genannte Teilpublikationen liegen vor:

- Braukmüller N., Wombacher F., Hezel D.C., Escoube R., Münker C. (2018) The chemical composition of carbonaceous chondrites: Implications for volatile element depletion, complementarity and alteration. *Geochimica et Cosmochimca* **239**, 17-48.

  Chapter 2

  Appendix A

- Braukmüller N., Wombacher F., Funk C., Münker C. (2019) Earth's volatile element depletion pattern inherited from a carbonaceous chondrite-like source. *Nature Geoscience* **12**, 564-568.

  Chapter 3

  Appendix B

Datum: Unterschrift: